BEYOND JABLONSKI DIAGRAMS IN ORGANIC SYSTEMS: AB INITIO STUDIES OF SUBSTITUTED BENZENE DERIVATIVES

Mireia Segado Centellas

Dipòsit Legal: T. 1703-2011

Mireia Segado Centellas

Beyond Jablonski diagrams in organic systems: *ab initio* studies of substituted benzene derivatives.

Doctoral Thesis

under the direction of Dr. Mar Reguero

departament de Química Física i Inorgànica

Universitat Rovira i Virgili

Tarragona

2011

UNIVERSITAT ROVIRA I VIRGILI

M^a del Mar Reguero de la Poza, professora titular de Química Física, del Departament de Química Física i Inorgànica de la Universitat Rovira i Virgili,

Faig constar que la present memòria, que porta per títol:

Beyond Jablonski diagrams in organic systems:

***ab initio* studies of substituted benzene derivatives.**

ha estat realitzada sota la meva direcció al Departament de Química Física i Inorgànica de la Universitat Rovira i Virgili per la llicenciada en Química Mireia Segado per obtenir el grau de doctora en Química.

Tarragona, juny de 2011

AGRAÏMENTS

En primer lloc m'agradaria agraïr a la meva directora de Tesis, la doctora Maria del Mar Reguero, pels seus consells tant a nivell científic com a nivell personal. Pel suport que ha depositat en mi i en el meu treball, i sobretot per tots els moments que hem compartit durant aquests 4 anys.

També vull agraïr als membres del Grup de Química Quàntica: Prof. Rosa Caballol Lorenzo, Prof. Josep Maria Poblet, Prof. Josep Manel Ricart, Dr. Carles Bo, Dra. Anna M. Clotet, Dr. Joan Igual, Dr. Jordi Carbó, Dr. Xavier López i al Dr. Nuno Guerreiro. En especial m'agradaria agraïr a Dr. Cornelis De Graaf per sempre estar disposat a ajudar-me, a la Dra. Mariangels Carvajal per les converses compartides i al Dr. Antonio Rodríguez Fortea pel seu entusiasme embriagador per la química. M'agradaria fer una menció especial a l'equip informàtic : Elisenda Mas, Moisès Álvarez i José Carlos Ortiz, per la seva paciència i disposició a ajudar.

Des d'aquí vull donar les gràcies a tots aquells que han estat els meus companys. En primer lloc als amics i companys dels cursos de doctorat de Santander: Miquel Huix, Anna Díaz, Juan José Nogueira, Ceila Margarita Fong, Pablo G. Jambrina, Silvia Bouzón i Monica Garcia, per fer que la vida fos somni. En segon lloc als companys de la Universitat: Dra. Susana Romo, Dr. Gerard Novell, Dr. Alberto Roldán, Nadya Antonova, Jorge A. Fernández, David Taratiel, Xavier Aparicio, Sonia Aguado, Núria Alegret, Pablo Aparicio, Jéssica Cid, Alejandro Jimenez, Marc Mulet Gas, Igor Negodaev, John Zapata i Pedro Castro. En especial m'agradaria

agraïr als companys del despatx 202: Pablo Jimenez, Alex Domingo, Zahra Tabooht i Yannick Mercier (Senyor P) per totes les experiències conviscudes i l'estimació que sento vers ells. Al Pablo per la seva vitalitat i per la seva màxima *cada dia surt el sol*, a L' Alex per tot el que m'ha ajudat i per la seva asombrosa claritat d'idees, a la Zahra i el Yannick no acabaria mai de agraïr-lis, però destacaria les converses amb la Zahra fins ben tard al despatx sobre ciència i vida, i amb el Yannick el compartir la vida a Tarragona, mostrant-me la ciutat, preocupant-se per a mi i ensenyant-me tot el que sap. Fora del despatx als amics Rémi Maurice per les nits de karaoke, al Ramón Valencia per ser un piltrafilla i les llargues converses de política, al Gian Giacomo per la seva cuina i a l'Eva Santos per totes les converses sobre filosofia, ciència i política, els espais buits i la seva amistat.

Donar les gràcies al grup de Química Teòrica i Computacional del Centre Superior de Investigacions Científiques de Barcelona, per la seva afectuosa acollida i dedicació per mostrar-me la Química Quàntica.

I would also like to acknowledge here Prof. Domcke and his group for the warm welcome I received in Munich. Thanks to him I have learned more deeply about conical intersections. Also I would like to acknowledge Daniel Opalka for his help, Sai Ramesh for his goodness and Benjami Martorell and Carles Mas pels cafès del matí i els mojitos nocturns.

A la familia i amics vull donar-lis les gràcies per ensenyar-me el què és estimar. A mons pares (els quals poseeixen la qualitat de la bondat) per tots els consells i valors que m'han intentat transmetre. Als amics d'Olesa Sara Ramírez, Raquel Nafria, Montserrat Chicón, Isabel Bodas, Coral Garcia, Mireia Lozano, David Castells, Sergio Garcia, Eva Prats, David Abellan i Marcos Luna, perquè sempre estan i estaran. Als amics de *a line above the sea* per totes les hores que hem passat junts, concerts, experiències compartides i l'afecte mostrat durant tots aquests anys a Tarragona. A *Nadine*, per crear una realitat paral.lela a la casa felicitat. A la gent del 15M per totes les emocions compartides, l'amistad i la lluita per un món millor. A tota la gent que he conegut i estimo a Tarragona. A Tarragona per ser una ciutat màgica on qualsevol nit pot sortir el sol.

I finalment vull donar les gràcies a tots els qui creuen que un altre món es possible.

Mireia Segado

Life is a cage of possibilities

CONTENTS

CHAPTER 1

GENERAL INTRODUCTION

Throughout the centuries [1], mankind has pursued not only to explain the observed facts but also to establish theories and models for the phenomena. Atomic theory, despite being further developed in the early nineteenth century, was founded in the ancient Greece by a philosophical necessity. The first reference found about the limit of indivisible matter was by Leucippus. But this idea was developed by Democritus, who assumed the existence of the atom as an indivisible part of matter.

The Democritus coetanean philosophers ridiculed his thought calling it absurd. They thought it was not possible for a particle to occupy a space if that could not be split, and if it could not be divided, it would not occupy any space and therefore it would not be anything. Thus how is it possible that the matter is made of nothing?

The unity of knowledge has been always one of the hardest ideals pursued by the human thought. Many philosophers have sustained that the meaning of "knowledge" may be the reduction to the unity. In the following lines we will travel across some paths of the evolution of science, and we will see that in every step of the walk the unity turns out as a hidden constant.

In ancient times, light, electricity and magnetism were considered separate phenomena [2]. Focusing on light, greek philosophers contemplated the emission of

light as a process of transference of luminous bodies.

The generalized believe that light was composed by small particles was still prevailing until the first stages of the $XVIII^{th}$ century. With the discoveries of modern scientists, the consideration of the nature of light was divided into two streams: those like Descartes, Huygens and Hooke who considered that the light was a wave phenomenon, and those like Newton and Boyle who argued that light consists of particles emitted by bodies.

Feeling the sense of unity, the relation of the optical phenomena with other areas facilitated the comprehension of the controversial nature of light [3]. In 1819 Hans Christian Oersted demonstrated experimentally the interaction between electric currents and magnets. Subsequent experiences in this topic led to the origin of electromagnetism. More specifically, in 1804 J. C. Maxwell, inspired by the work of Faraday, conceived the electric and magnetic forces as different sides of the same coin, showing that these waves autopropagate at a constant speed, which coincided with the speed of light. Experimental confirmation of Maxwell's theory showed the wave nature of light, and the electromagnetic ether become the light ether.

But it was not enough, it was necessary to study the problem from another perspective, with new eyes. From the study of the black body, Max Planck suggested that the radiation could not be emitted in arbitrary amounts, only in certain packages of energy or quanta. Planck's doubts about the quantum discontinuity were dispelled by Einstein when he introduced the concept of the independent particles called photons, unveiling a new vision of nature, the quantized one [4].

However, recalling the concept of wholeness, in order to understand the nature of light, it was necessary to link waves with particles, connexion made by Joseph Louis Lagrange. In 1772 he reformulated the classic mechanics of Newton trying to show that mechanics can be unified in only one principle. This principle was based on the Lagrangian function (difference between kinetic and potential energy of a system). Lagrange equations are based on the principle of minimum action: among all possible paths with the same fixed initial and final states, the most probable is the one which implies the minimum action [4]. This principle reflects the intimate relationship between the movement of material bodies and the movement of beams of light according to Fermat principle (1657), that generalizes that the effective path of light between two points is the one that runs in the minimum time.

Afterwards in 1883, W. Hamilton showed that the Lagrange equations can be expressed in terms of the Hamiltonian function and finally in 1924 de Broglie formulated the duality of wave and particle.

Following up on these ideas, Schrödinger decided to find a proper wave equation for the electrons [5]. He was guided by William R. Hamilton's analogy between mechanics and optics. The equation he found formulated in terms of the Hamiltonian operator is called the *Time Dependent Schrödinger Equation* (TDSE).

With this last loop of the evolution of science, we get back to the initial question: is it possible that the matter is made of nothing? Nowadays we know that the objective reality is a huge simplification and that we must deal with more abstract concepts. When we observe objects at daily experiences, the physical processes that facilitate the observation have only secondary effects in the observed systems, but in the minimal components of matter the process of observation becomes the dominating perturbation. Hence the natural laws that are formulated in quantum theory do not refer to elementary particles, only to our knowledge of these particles. Then the question of the existence of particles in the space and time may not be questioned in this way, because we observe it only when the particle interacts with other physical system. We can not know how it is, but we can know how it behaves. In the natural science we are not only observers, we are always part of the system.

In this context, we are interested in the phenomena produced by the interaction of light with matter. Photochemistry, in the field of chemistry, is a subdiscipline that studies the reactions or processes in which light is involved. If we use the molecule as a main unit to characterize, parametrize and systematize, we enter into the framework of molecular chemistry, which is the field related to the description of physical and chemical processes that occur with the interaction of light (from the first absorption of photons to the emission of other photons, or the possible production of new products) in terms of molecular and electronic structures.

In our case this study is addressed theoretically using *ab initio* methods, assessing different electronic distribution of the excited states involved, the geometries and energies of the species formed and the mechanism that lead to photochemical transformation and photophysical processes.

Molecular chemistry should be considered as the study of the evolution with time of the nuclear and electronic coordinates following the perturbation caused

by a reaction field. In this case the wave function can be propagated under the Hamiltonian operator according to the time dependent framework. If the potential is time independent, the solutions of the quantum system are superposition of the solutions of the *Time Independent Schrödinger Equation* (TISE).

On the simplest scenario, interaction of light with a molecule results in the formation of an excited state, as a solution of the time dependent Schrödinger equation. In principle there are a lot of possible solutions of the TISE, that means that there are innumerable excited states, each of them with a different electronic distribution what give place to different properties. Thus, each excited state can lead to a chemistry as rich as that of the ground state.

Understanding of the photochemical mechanisms requires the knowledge of the force field that governs the evolution of molecular geometry in the ground and excited states. One of the most standard ways of solving the TISE is the *Born Oppenheimer Approximation* (BOA), where the nuclei are considered stationary relative to electronic motions and therefore the nuclei are represented by point charges moving over a potential created by the electrons. The separation of nuclear and electronic motions allows the description of the molecular electronic energy (E) as a function of nuclear coordinates (Q), E(Q).

The representation of the energy versus the nuclear coordinates gives *Potential Energy Surfaces* (PES) what enables the study of the reactivity of a system in the ground state and different excited states. After the first interaction of the molecule with light, the electronic PES of the state where the transition ends dominates the reaction dynamics until the system is deactivated to another state of lower energy which PES controls then the evolution of the system until the next deactivation. In the last step the lower energy state is the ground state. The deactivation from the first excited state can be radiative, with photon emission (phosphorescence between states of different spin symmetry or fluorescence between states of the same spin symmetry) or non radiative (intersystem crossing between states of different spin symmetry or internal conversion between states of equal spin symmetry).

It becomes clear then, that to study photochemical processes, it is necessary the analysis of the potential energy surfaces of the states involved in the reactivity of each system. We are specially interested in the analysis of the nature of excited states. It is also essential to locate critical points (minima and transition states),

reaction pathways and crossing or interaction points between surfaces, as it is the case of conical intersections, real crossings and avoided crossings.

To study the possible reaction mechanisms the component of the experimental information is important, because in a strictly theoretical way, the study would be not feasible as the light opens endless possibilities of reaction. Thus the theoretical search will be subject in some extent of the constraints of the observer.

Considering that scientific theories are auxiliary functions for realising the scientific proposals, an open questions appears: what is the relationship between theories and observations? There are pure observations, observations that are not biased in some way by the theories? These questions can be grouped into one: it is possible that starting from different assumptions would we observe the same thing? For an analogy, let's think on Kepler and Ptolemy on a hill watching the sunrise. Kepler believes that the sun is fixed and that the earth moves. Ptolemy says that the earth is fixed and rest are moving bodies. Will Kepler and Ptolemy see the same thing in the east?

With this perspective in mind, in the studies carried out in this thesis we have tried not to limit our search to the study of the most chemical intuitive pathways of reaction or to the earliest reported ones. For this reason we have let the system flow into a large cage of possibilities.

This thesis is focused on the theoretical study of several photosensitive molecular systems. First we have studied the photosensitization phenomenon to determine the characteristics that lead a system to be a good singlet oxygen sensitizer. Afterwards, we have studied the intramolecular charge transfer phenomenon in two different families of compounds.

Regarding our first point of study, considerable interest has been focused for several decades on the physical and chemical properties of low lying molecular oxygen states [6]. It is recognized as an important oxidizing intermediate in chemical and biological processes, such as photodegradations [7] defence mechanisms [8] and photocarciogenesis [9], and it is applied in a variety of fields, including organic synthesis [7] and the photodynamic therapy of cancer [8, 10].

The most common way of generating singlet oxygen is photosensitization, that is a process in which the presence of a light-absorbing photosensitizer agent (PS) activates in a substrate reactions that otherwise would not take place [10]. In this

work, the substrate is oxygen in its triplet ground state, which interact with the photosensitizer that leads the oxygen to a singlet state.

1H-phenalenone (or perinaphthenone, often called *Phenalenone*, PN) is an universal reference for the sensitisation of singlet oxygen due to the fact that its quantum yield of singlet oxygen production is close to 1 in a large variety of solvents ranging from water to cyclohexane [11–13].

The singlet oxygen quantum yield (Φ_Δ) is a determinant property of a photosensitizing agent. This quantity is defined as the number of $^1O_2$ molecules generated by each photon absorbed by the PS. Virtually all measurements of Φ_Δ are scaled relative to a reference substance. To understand the effectivity of a given reaction mechanism is of crucial interest to characterize molecules as possible standards and universal references, that open the possibility of making easier the study and development of photosensititzers. In this thesis PN is chosen in order to analyse the properties a molecule needs for being a good photosensitizer.

The second phenomenon studied is the intramolecular charge transfer. The charge separation produced by the charge transfer forms the basis of numerous transformations of chemical and biological systems. This transfer can occur between two different molecules (intermolecular transfer) or between different regions of the same molecule, one donor and other acceptor. *Electron Donor acceptor* (EDA) molecules plays an important role in understanding the processes of charge transfer.

The interest in EDA can be attributed to the ability to control the radiative and non radiative processes in such systems. The fact that the emission properties of these compounds can be controlled by structural changes in the molecule or external parameters such as solvent polarity or temperature is important for applications in the field of the organic materials, for example, as fluorescence markers [14–16] or electrooptical switches [17–19]. In this memory we focus our interest on systems in which the donor part of the EDA system is an alquilamino bounded by a single bond to an aromatic substituted system with acceptor character.

The aminobenzonitriles are the most studied class of EDA molecules [20]. When these compounds are irradiated with ultraviolet (UV) radiation, small structural differences between different members of the family lead to very different fluorescence patterns [20, 21]. In some cases they show only a single band of fluorescence independently of the environmental conditions (either the so-called normal fluorescence

band or the anomalous fluorescence band), in other cases two bands appear, showing the so called dual fluorescence while in other cases the number and type of bands depend on the polarity of the solvent. The origin of the dual fluorescence is associated with the existence of two singlet excited states of different character. One is often called locally excited (LE) because it is formed by an excitation from a π orbital of the aromatic ring to an antibonding orbital located in the same area of the molecule. The other state is characterized by an intramolecular charge transfer (ICT).

The mechanism behind the dual fluorescence phenomenon is highly controversial and has been the subject of many experimental and theoretical studies [22–27]. However the geometrical distortion of the ICT state is not firmly established.

In this thesis an extensive study of the smallest member of the aminobenzonitril family, ABN, is performed. Experimental observations show that in ABN the substitution of four in ring hydrogen atoms by fluorine ones leads to a decrease in the fluorescence and phosphorescence yields. The number of fluorine substituents seems to be an important factor in the opening of a radiationless deactivation channel [28]. This makes the study of the ABN tetrafluor derivative (ABN-4F) an interesting case to be studied theoretically. The comparison of the characteristics of the electronic states of both systems ABN and ABN-4F can answer the questions of which are the regions of the PES that determine the photophysical and photochemical properties.

On the other hand, in spite of the interesting properties of aminopyrimidines as EDA molecules, for some time they have not attracted much attention, probably because the main efforts have been directed towards the aminobenzonitrile family of compounds. However, more recently the discovery of the several possible deactivation pathways for adenine has renewed the interest in aminopyrimidines and some theoretical studies have already been addressed to their deactivation pathways [29, 30], because the members of this family are components of some nucleobases. The pyrimidine monomers are essential in the conservation of the genetic code and it is believed that ultrafast deactivation mechanisms shared by all nucleobases of DNA and RNA are responsible for the photoestability of these molecules.

Due to the substitution of one or several pyrimidine hydrogen by amino or functionalized amino groups, aminopyrimidines are predisposed of undergoing in-

tramolecular charge transfer processes (ICT), because of the ability of the amino group to act as electron donor and to the acceptor character of the aromatic heterocycle. It is interesting to study the ICT mechanism and the competitive photodeactivation pathways in order to rationalise the effect of substituents in the photochemical and photophysical properties of this family of molecules [31, 32].

For a good description of the PES in the studied systems, the type of methods chosen have to deal with equal accuracy with the ground and excited states. For this reason it is indispensable an extended ab initio study conducted from first principles. We have chosen to use the CASSCF/CASPT2 methodology. *Complete Active Space Self Consistent Field* (CASSCF) enables to rapidly characterize the topology of the PES. *Complete active Space with Second Order Perturbation* (CASPT2) theory refine the energy calculations in the geometries found in the first step with the inclusion of dynamic correlation. The indirect interaction of states is taken into account with the *Multi State* (MS)-CASPT2 approach. The applicability and reliability of CASSCF/CASPT2 methodology has been extensively demonstrated in a number of earlier applications [33, 34].

To summarize, this memory is structured as follows: *Chapter 2* include the basic concepts to be considered in photochemical and photophysical studies. *Chapter 3* describes the theoretical methods and some related computational details (*"the eye can not see the sun if it is not used to that"* J. W. von Goethe). *Chapter 4* is dedicated to the study of the photoprocesses that occur in phenalenone that make them able to sensitize singlet oxygen. Also the competitive reactions are studied and compared. *Chapter 5* and *Chapter 6* are devoted to the intramolecular charge transfer (ICT) processes in substituted benzene derivatives that have donor acceptor character. More specifically in *Chapter 5* the central issue is conceptualise the mechanism behind such phenomenon. The model system used are aminobenzonitrile (ABN) and its tetrafluoro counterpart (ABN-4F). Possible ICT and non ICT states and non adiabatic and adiabatic pathways that populate them are also characterized. Thermally activated internal conversion is also studied as competitive channel to emitting processes. In *Chapter 6* the study of substituted aminopyrimidines is presented: 4-aminopyrimidine (APD) , 4-dimethylaminopyrimidine (DMAPD), 4-dimethylamino-5-methylpyrimidine (DMA5MPD) and 4-diethylaminopyrimidine (DEAPD) in gas phase and a polar aprotic solvent are studied here. The nature, donor effect and position of substituents affects their luminescent properties, also

tunned by the solvent. First a exhaustive study of excited states were done. Secondly, in order to rationalise the effect of substituents in the photochemical properties of this family of molecules, the ICT mechanism and competitive deactivation pathways were studied. Finally in *Chapter 7* there are collected the main conclusions extracted from previous chapters.

We have attempted to carry out these scientific studies in the most rigorous manner because the science of the future is built on the present.

CHAPTER 2

MOLECULAR PHOTOCHEMISTRY

Photochemistry is a subdiscipline of the chemistry that studies the relationship between matter and light. If we use the molecule as the main unit to parametrize, characterize and systematize, we get into the framework of molecular photochemistry, that is a field related with the physical and chemical description of the processes that derive from the absorption of photons in terms of the molecular and electronic structures.

According to the formalism of quantum mechanics, the most suitable mathematical object to describe the quantum state of a physical system is the state vector $|\phi\rangle$, which is also called the *ket* vector. The most important feature of the *ket* vectors is that they represent the system in a particular state, and thus they contain all the information about it, which can be obtained by proper manipulation.

In order to study the behaviour of any molecular system, it is not enough to define a state vector or wave function. It is also necessary to observe how this system evolves with time. Newton's laws of motion are no longer valid to describe the systems we are interested in. Its quantum equivalent is represented by the time-dependent Schrödinger equation.

2.1 Schrödinger equation

Developed by Erwin Schrödinger and first published in 1926 [5], the Schrödinger equation is one of the single most important equations in physical sciences and it is the basis of modern quantum mechanics. The partial differential equation describes the state of a chemical system as a wave function which evolves in time:

$$i\hbar\frac{\partial}{\partial t}\psi(\vec{q},t) = \hat{H}\psi(\vec{q},t) \tag{2.1}$$

If we set $\vec{q}$ as a collective coordinate to represent the position of both nuclei and electrons on a molecule ($q = \vec{Q}_{nuc}, \vec{q}_{el}$), the molecular Hamiltonian (expressed in atomic units with $e = me = \hbar = 1$) becomes, if relativistic effect are not considered:

$$\hat{H} = \sum_{i=1}^{N} -\frac{\nabla_i^2}{2} + \sum_{\alpha=1}^{M} -\frac{\nabla_\alpha^2}{2m_\alpha} + \sum_{\alpha>\beta}^{M} \frac{Z_\alpha Z_\beta}{|\vec{R}_\alpha - \vec{R}_\beta|} + \sum_{i>j}^{N} \frac{1}{|\vec{r}_i - \vec{r}_j|} + \sum_{i=1}^{N}\sum_{\alpha=1}^{M} \frac{-Z_\alpha}{|\vec{r}_i - \vec{R}_\alpha|} \tag{2.2}$$

In the case that the molecular Hamiltonian has no time dependence and the system is described with and eigenstate of the Hamiltonian, $\psi(\vec{q},t)$ can be rewritten as a product of two functions in which the space and temporal coordinates can be separated:

$$\psi(\vec{q},t) = \Psi(\vec{q})\Phi(t) \tag{2.3}$$

Manipulating Equation 2.1 it becomes:

$$i\hbar\frac{1}{\Phi(t)}\frac{\partial\Phi(t)}{\partial t} = \frac{\hat{H}\Psi(\vec{q})}{\Psi(\vec{q})} = E \tag{2.4}$$

and from the right terms:

$$\hat{H}\Psi_n(\vec{q}) = E\Psi_n(\vec{q}) \tag{2.5}$$

Equation 2.5 is known as the *Time Independent Schrödinger Equation*, TISE. The method of separation of variables leads to a particular solution of the *Time Dependent Schrödinger Equation* which allows the prediction of time independent variables [35]. Since the early development of quantum chemistry, most of the efforts of theoretical chemist have been placed in solving it in order to obtain the total energy of a molecular system within a stationary state.

2.2 Born-Oppenheimer approximation

Even after the simplification achieved by the time-space separation (Equation 2.3), the solution of TISE still becomes unfeasible. The electron nuclei interaction in Equation 2.2 does not allow the separation of electronic and nuclear coordinates which results in a complex equation. However the limitation can be overcome by starting with the Born representation [36] for the wave function.

The molecular Hamiltonian can be separated into electronic and nuclear contributions:

$$(\hat{T}_N + \hat{H}_{el})\Psi_n(q,Q) = E\Psi_n(q,Q) \tag{2.6}$$

where

$$\hat{H}_{el} = \sum_{i=1}^{N} -\frac{\nabla_i^2}{2} + \sum_{i>j}^{N} \frac{1}{|\vec{r}_i - \vec{r}_j|} + \sum_{i=1}^{N}\sum_{\alpha=1}^{M} \frac{-Z_\alpha}{|\vec{r}_i - \vec{R}_\alpha|} \tag{2.7}$$

$$\hat{T}_N = \sum_{\alpha=1}^{M} -\frac{\nabla_\alpha^2}{2m_\alpha} \quad \hat{V}_{NN} = \sum_{\alpha>\beta}^{M} \frac{Z_\alpha Z_\beta}{|\vec{R}_\alpha - \vec{R}_\beta|} \tag{2.8}$$

Setting kinetic nuclear energy to zero, the clamped nucleus Hamiltonian is obtained. In this electronic Hamiltonian, $\hat{H}_{el}$, the nuclear coordinates act as parameters. For any value of Q, $\hat{H}_{el}$'s eigenvalues $E_{el,i}$ and eigenfunctions Φ_i can be found from:

$$\hat{H}_{el}(q;Q)\Phi_i(q,Q) = E_{el,i}(Q)\Phi_i(q;Q) \tag{2.9}$$

where the set of Φ_i eigenfunctions is complete and orthonormal. These functions can be used as a basis set to expand the wave function of the system:

$$\Psi(q,Q) = \sum_i \chi_i(Q)\Phi_i(q;Q) \tag{2.10}$$

where $\chi_i(Q)$ are nuclear functions that act as the expansion coefficients. This expansion is known as the Born representation, and it is exact as long as it is complete.

Using these functions, the TISE equation can be rewritten,

$$[\hat{H}_N + E_{el,i} - E]\chi_i(Q) = -\sum_{m \neq i} \Lambda_{im}\chi_m(Q) \tag{2.11}$$

$$\Lambda_{im} = \delta_{im}\hat{T}_N - < \Phi_i|\hat{T}_N|\Phi_j > \tag{2.12}$$

where the matrix elements of Equation (2.12) are the non adiabatic coupling vectors which describe the dynamic interaction between the electronic and nuclear motion.

If we now replace the multiconfigurational *ansatz* by a monoconfigurational one:

$$\Psi(q, Q) = \chi(Q)\Phi(q, Q) \tag{2.13}$$

We are in the *Born-Oppenheimer Approximation* (BOA). Now $\hat{\Lambda}$ is the diagonal non adiabatic coupling of the state of interest, $\hat{\Lambda}_{ii}$. Then BO approximation implicitly set Λ_{im} to zero. Moreover [37], if nuclear and electronic couplings are small, it can be reduced to a further approximation called the BO adiabatic approximation when Λ is completely ignored. BO approximation is expected to be accurate if the off diagonal elements of the coupling are negligible, whereas the adiabatic BO will be valid if all coupling elements are negligible.

Thus working with the BO approximation it is possible to set out the electronic and nuclear Schrödinger equations separately:

$$\hat{H}_{el}(q; Q)\Phi_n(q, Q) = E_{el,n}(Q)\Phi_n(q; Q) \tag{2.14}$$

$$[\hat{T}_{NN} + V_{NN}(Q) + E_{n,el}(Q)]\chi_n(Q) = E_n\chi_n(Q) \tag{2.15}$$

The ensemble of V_{NN} and $E_{n,el}$ constitute the potential field, represented by $U_n(Q)$ that acts over the nuclei of the system.

2.3 Matter-radiation interaction

Many systems can exist in different stationary quantum states, each one characterized by an allowed value of the total energy. In this section we shall examine the

laws which governs the passage of a system from one stationary state to another. In particular we shall consider the passage of a system from a lower energy state to a higher energy state by absorption of radiant energy.

When the electromagnetic radiation falls upon a system of charged particles, it creates a time depending perturbation that can induce transitions among the different quantum states of the system, (for more extended information see *chapter 5* of reference [4]).

From comparison of the weak field Hamiltonian to the Hamiltonian in absence of electromagnetic radiation, the operator that represents the distortion or perturbation of the system can be extracted,

$$\delta H = -\frac{\hbar e}{ic}\sum_j \frac{1}{m_j} A_j \nabla_j \tag{2.16}$$

where A_j is the electromagnetic vector potential for particle j. If the particle which is interacting with the radiation has dimensions which are small compared with the wavelength, the initial rate of transition from state k to l state is proportional to the interaction between states, given by:

$$< \psi_n|\delta H|\psi_m >= \frac{1}{\hbar} A(E_n - E_m)|\mu_{nm}| \tag{2.17}$$

E_i is the stationary energy of state i and μ is the *Transition Dipole Moment* (TDM), that can be calculated as:

$$TDM_{n\to m} = \sum_{\alpha=x,y,z} e < \Phi_n \mid \alpha \mid \Phi_m > \tag{2.18}$$

To have maximum transition probability is necessary that resonance takes place between the radiation and the quantum states of the system, but it is also necessary the fulfilment of the selection rules which prevent the TDM integral from being zero.

A classical concept related with the quantum mechanical concept of TDM is the oscillator strength, f. f is proportional to the band intensity in experimental spectra.

In fact the relation with TDM is:

$$f = \frac{2}{3}|TDM_{n\to m}|^2 \Delta E_{nm} \tag{2.19}$$

The value of f calculated theoretically helps to predict the excited state that will be preferentially populated by the absorption of the initial radiation. Regarding *Franck-Condon* (FC) principle[38–40] based on the fact that the electrons move much faster than nuclei, it is assumed that the initial excitation is an electronic vertical transition and the molecular geometry does not change during the change of state. It is also assumed that the geometry of the initial state corresponds to the geometry of the energetic minimum of the ground state.

2.4 Potential energy surfaces

The comprehension of reactivity needs the knowledge of the potential field that governs the evolution of the molecular geometry. The separation of the electronic and nuclear motions within the BO approximation leads to the natural appearance of the potential field $U_n(Q)$. This function correspond to a hypersurface of dimension 3N-6 ((3N-5) for linear molecules) different for each electronic state n. These surfaces are called *Potential Energy Surfaces* (PES) or adiabatic potential energy hypersurfaces [41, 42].

The PES is probably one of the major achievements of the BO approximation, because many chemical processes can be rationalized in terms of the dynamics of the nuclei on a single BO adiabatic PES. In particular, thermal reactions are assumed to go along only the ground state PES. On the other hand, reactions involving excited states demand the analysis of the excited state PES.

Photochemistry is characterized by the involvement of excited states on reactivity. In the context of the BO approximation, the photochemical processes that occur along only one PES are considered adiabatic processes. In contrast, a process that starts on a PES and ends up in another PES is classified as non adiabatic process. Non adiabatic chemical processes are very common in photochemistry and photobiology and, although they can be understood within the BO approximation framework, they can not be properly studied in it.

Photochemical reaction paths

In general it is assumed that the molecule is initially in equilibrium in its ground state, usually of singlet character, that is represented by S_0 (0 surface of singlet character). After the radiation absorption process that is controlled by the selection rules and the Franck-Condon principle, the molecule is on a vibrational and electronic excited state. A representation of all photophysical processes that can occur from this excited state including radiationless and radiative deactivation mechanisms, is depicted in the *Jablonki diagram* (Figure 2.1).

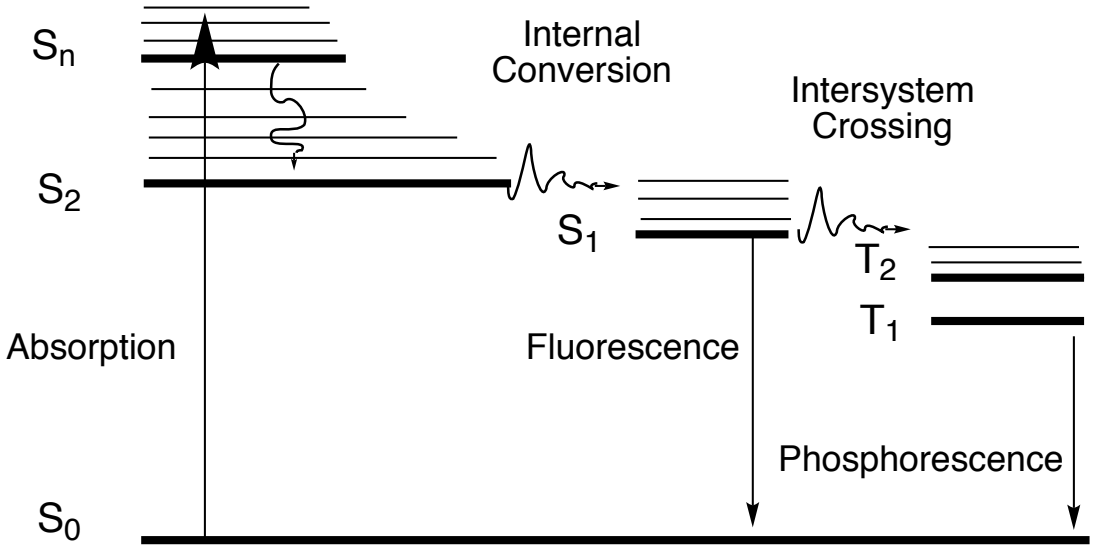

Figure 2.1: Jablonski diagram.

Electronic singlet states are represented by S_1, S_2, S_3 .. in increasing order of energies, and different multiplicity states, that we will suppose triplets, are represented by T_1, T_2, T_3... The vibrational relaxation (VR), internal conversion (IC), quenching and intersystem crossing (ISC) are processes that contribute with different efficiency (depending on the molecule, on the excited state and on the environment) to the deactivation of excited states.

When more than one process can occur, the particular evolution of the system is determined by the probability of each competitive process. A process with high probability is associated with fast dynamics. In high energy excited states, the most probable process is the radiationless deactivation , while the probability of

this photophysical process notably decreases when the system reaches the lower excited states of each symmetry. Chemical processes, then, become competitive only on the low lying excited states and therefore in general for mechanistic studies the attention is focused on low lying excited states because it is there where the chemical processes will most probably take place.

Thereupon after initial absorption, the PES corresponding to the lowest energy state populated after the initial excitation, controls the evolution as far as the next deactivation occurs. In the last stage the system must be in its ground state. The deactivation from the first excited state can be radiative, emitting photons (phosphorescence from a triplet to a singlet state or fluorescence from a singlet state to another singlet), or non radiative (intersystem crossing between states of different spin symmetry or internal conversion between states of the same spin symmetry). Regarding the photophysical processes of fluorescence and phosphorescence, it is interesting to recall Kasha's rule, a principle that states that photon emission occurs in appreciable yield only from the lowest excited state of a given multiplicity [43].

From the computational point of view [44], once we have a correct description of the low energy excited states that can be involved in the reactivity of interest, we can approach the study of the photochemical and photophysical processes in two stages. In the first stage we will localize and optimize the critical points on PES of the states of interest: minima, *Transition State* (TS) structures and surface crossings.

The minima and TS (adiabatic pathways) can be studied with the same procedures than in thermal reactions. However, the crossing zones between different potential energy surfaces need special methods of study because the BO approximation is not valid in these cases. In a second stage we connect the critical points located previously computing interpolated and/or *Minimum Energy Paths* (MEP) between them.

The picture thus obtained of the PES is very detailed but at the same time limited to a static point of view as opposite to the real trajectories that the system with non zero kinetic energy would follow. To get a more realistic simulation, dynamical calculations should be done, but this is out of the scope of our photochemical studies.

The information that can be drawn from the critical points and paths obtained are schematized as follows:

- Optimization of minima in ground and excited states:
  · Absorption
  · Emission (fluorescence and/or phosphorescence)
- Optimization of TSs and MEPs:
  · Adiabatic reactions
- Optimization of minimum energy surface crossing points:
  · Non adiabatic reactions

2.5 Surface crossings

In the previous section we have given an overview of the general aspects of the photochemistry reaction paths and highlighted the role of the surface crossings. Now we will present a description of these surface crossings in simple theoretical terms, focusing in two aspects: *a)* the interaction between crossing states and *b)* the nuclear coordinates associated with the intersection. These two elements generate some characteristics surface topologies.

As we have already commented, the BO approximation and BO adiabatic approximation holds for the vast majority of chemical situations. However in the presence of fast nuclear vibrations the electrons are unable to instantaneously adapt to the rapid changes of the nuclear positions. This leads to a significant coupling between the nuclear and electronic motions that is called vibronic coupling [45]. This coupling is the ultimately responsible for the breakdown of the adiabatic picture.

In diatomic molecules the PES of two states will only intersect if the states differ in symmetry or multiplicity of spin [46]. But the two PES of a polyatomic molecule can intersect even if the states belong to the same symmetry and spin multiplicity. This affirmation, first proved in 1929 by Neuman and Wigner [47], opens the question of how the states intersect in polyatomic molecules.

According to the treatment of Longuet-Higgins [48, 49], if we consider two functions ψ_1 and ψ_2 (depend on nuclear coordinates, Q) that belong to a complete set

of orthonormal electronic functions, the energies $E_1(Q)$ and $E_2(Q)$ of the states ψ_1 and ψ_2 will be the two eigenvalues values of the matrix,

$$\begin{pmatrix} H_{11} & H_{12} \\ H_{21} & H_{22} \end{pmatrix} \tag{2.20}$$

In each point Q, $E_1(Q)$ and $E_2(Q)$ will be sorted out by an amount

$$\left\{ (H_{11} - H_{22})^2 + 4 \mid H_{12} \mid^2 \right\}^{\frac{1}{2}} \tag{2.21}$$

Therefore in a crossing, where E_1(Q) and E_2(Q) must be equal, two conditions must be fulfilled,

$$H_{11} = H_{22} \tag{2.22}$$

$$H_{12}(= H_{21}) = 0 \tag{2.23}$$

Equation 2.22 constitutes the condition for real or avoided crossing, while equation 2.23 assures that the crossing is real, as opposite to avoided.

A conical intersection occurs when two states of the same spin and spatial symmetry are degenerate. The two conditions 2.22 and 2.23 must be fulfilled. These requirements reduce the dimension of the space of the CI by two, so the CI is a hyper-surface of dimension 3N-6(5)-2. Thus there is a hypersurface of dimension 3N-8(7) where the states are degenerate. From the point of view of the chemical reactivity, the system can evolve modifying 3N-8(7) coordinates without breaking the degeneration.

The two coordinates that split the degeneration are usually represented by X_1 and X_2 and they expand the called bifurcation space. It can be demonstrated [50] that these coordinates are the *gradient difference* vector (X_1, related with the equation 2.22) and the vector of coupling among states (*derivative coupling*, X_2, related with the equation 2.23):

$$X_1 = \frac{\partial(E_i - E_j)}{\partial Q} \tag{2.24}$$

$$X_2 =< \Psi_i|\frac{\partial \hat{H}}{\partial Q}|\Psi_j > \tag{2.25}$$

The representation of the energy of the crossing states with respect to the branching space coordinates shows the form of double cone, here the reason of the name of *conical intersection* given to this topological feature.

In the vicinity of a conical intersection the local topography can be represented by four conical parameters as function of the two branching coordinates [51], $\vec{X_1}$ and $\vec{X_2}$.

Denoting g and h as the lengths of $\vec{X_1}$ and $\vec{X_2}$, and defining:

$$d_{gh} = \sqrt{(g^2 + h^2)} \tag{2.26}$$

The following parameters are defined:

$$\Delta_{gh} = \frac{(g^2 - h^2)}{d_{gh}^2} \tag{2.27}$$

$$\vec{S_{IJ}} = \frac{\partial}{\partial R}\frac{(E_i + E_j)}{2} \tag{2.28}$$

$$\frac{S^x}{d_{gh}} = \frac{\vec{s_{ij}}\vec{X_1}}{g^2} \tag{2.29}$$

$$\frac{S^Y}{d_{gh}} = \frac{\vec{s_{ij}}\vec{X_2}}{h^2} \tag{2.30}$$

The cylindrical symmetry of a doble cone is taken as reference. The first parameter Δ_{gh} removes the cylindrical symmetry of the pitch. The second parameter S_{IJ} characterize the verticality of the pitch. Finally two parameters S^X/d_{gh} and S^Y/d_{gh}) describe the orientation of the cone axis (S^X/d_{gh}, S^Y/d_{gh}).

If the S^{IJ} and Δ_{gh} vanish, then the symmetry is kept through out displacements along $\vec{X_1}$ and $\vec{X_2}$. Non vanishing Δ_{gh} removes the cylindrical symmetry of the picth, making it different along x and y. Non vanishing S_{IJ} produces a tilt in the cone axis.

Then in order to understand the effect of the different parameters near the crossing points different basic cones are described:

- **TYPE a)** Vertical symmetric double cone. Only d_{gh} is non zero.
- **TYPE b)** Vertical asymmetric double cone. Only d_{gh} and Δ_{gh} are non zero.
- **TYPE c)** Tilted symmetric double cone. $\Delta_{gh} = 0$.

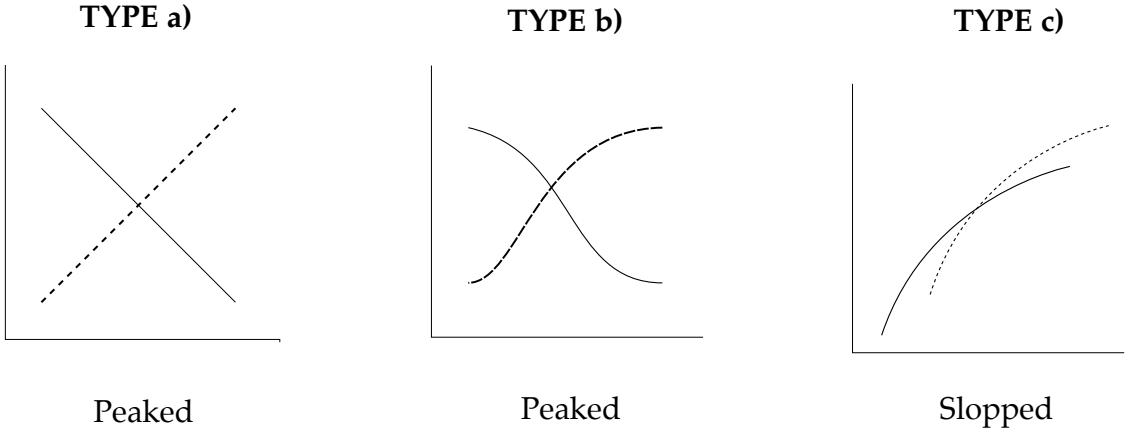

Figure 2.2: Schematic representation of the different type of conical intersections.

The main distinction can be drawn between tilted (sloped) and peaked conical intersections, as shown in Figure 2.2.

In the vicinity of a CI there is a region where $H_{11} = H_{22}$ but H_{12} has a small but non-negligible value. Hence the energies of the states are:

$$E_1 = H_{11} - H_{12} \tag{2.31}$$
$$E_2 = H_{11} + H_{12}$$

so the energy difference among states, is:

$$E_2 - E_1 = 2H_{12} \tag{2.32}$$

In this situation an avoided crossing appears. Through this crossing, the system can change its wave function adiabatically, and the energy of the CI is a higher bound for the TS of the adiabatic path originated by the avoided crossing in the lower PES.

In the case that two states of different symmetry are degenerate, a real crossing appears. In this case only one condition is necessary i.e. $H_{11} = H_{22}$, since H_{12} is zero for reasons of symmetry, and the dimension of the space is 3N-7. When the states are of different spatial symmetry but same spin, the customary nomenclature is somehow ambiguous, and in this work we will continue talking about conical intersections. When the states involved are of different spin symmetry, in this thesis singlet and triplet, we refer to *Singlet Triplet Crossings* (STC). The fact that H_{12} is zero implies that the probability of a change of state in a real crossing is in principle zero, but at these points the *Spin Orbit Coupling* (SOC) must be taken into account. If it is not negligible, H_{12} will be different from zero and, as in the case of the vicinity of a CI, an avoided crossing will appear. Thus, the adiabatic change of the wave function gives rise to an efficient ISC. The energy of the STC will be a higher bound for the barrier of the ISC process.

Usually and in particular in low-energy processes, transition from one state to other is expected to take place in the region of the lowest energy point of the hyperline of degeneracy, which is also referred to as the *minimum in the crossing seam* (MXS). These are the most interesting points on the hypersurfaces because it is there where the probability of surface change is greater [52]. On top, its energy corresponds to the minimum energy necessary to follow the channel opened by the crossing, and its geometry gives a hint of the proximity of this channel to the region of the initially populated PES.

Given the importance of surface crossing (STCs and CIs), a lot of interest has been placed in the computation of the geometries of these critical points. The algorithms to locate and optimize them can be grouped in three families: i) techniques that minimize a Lagrangian including the constraints to maintain the degeneracy of states, ii) gradient projection techniques and iii) methods using penalty functions.

In this thesis we used GAUSSIAN03 and MOLCAS7.0 to optimize surface crossings. The algorithm employed in Molcas is based on a modified version of the method suggested by Anglada and Bofill [53] that uses a Lagrange multiplier optimization scheme in a conjunction with a space division of internal coordinates. Non adiabatic coupling terms are not considered. On the other hand Gaussian uses the analytical Newton-Lagrange algorithms proposed in reference [50] that does not require the determination of the Lagrange multiplier.

CHAPTER 3

COMPUTATION AND METHODOLOGY

The resolution of the electronic time independent Schrödinger equation allows the evaluation of molecular properties. By solving the electronic Schrödinger equation on selected fixed geometries (thus assuming the validity of the adiabatic BO approximation), it is possible to obtain information about the topology of a concrete electronic state.

The exact solution of the electronic time independent Schrödinger equation can be obtained for one electron systems. However as the number of electrons within a molecule increases, the resulting electron-electron repulsion makes quantum mechanical calculations much heavier and rapidly unfeasible. In this case, the only realistic alternative is to obtain approximate solutions of the electronic Schrödinger equation. To this end, three major approaches have been developed in quantum chemistry: *i)* semiempirical methods, *ii) ab initio* methods and *iii)* electronic density functional methods.

In our studies we have to deal with chemical processes that involve not only electronic ground state, but also the electronic excited states. Hence, the careful choice of the best suited computational method for the specific system and electronic state

is a very important step in the study. In our calculations we have employed *ab initio* methods, specifically *Complete Active Apace Self Consistent Field* (CASSCF) and CASSCF with *second order perturbation theory*, CASPT2 methods.

In this chapter a few selected methods will be briefly summarized to help in the understanding of the following studies. For a more complete description of the wide range of quantum chemical methods the interested reader may find all desired information in the specialized text books [54, 55].

The tools to model photochemical processes are now available in standard quantum chemistry program packages. In this thesis all the calculations were carried out using the MOLCAS-7.0 [56] and GAUSSIAN-03 [57] sets of programs. Some details of the particular methodology used and optimization algorithms provided by these programs are also discussed in the rest of this chapter.

3.1 Hartree-Fock (HF) theory

A common approach to find the approximate solutions of the Schrödinger equation is to expand the N-electron wave function in antisymmetrized products $\phi(k)$ of one-electron functions χ.

$$\Psi = \sum_k C_k \phi_k \tag{3.1}$$

$$\phi_k = det(\chi_a(1)\chi_b(2)\cdots) \tag{3.2}$$

ϕ_k are normally referred to as Slater determinants. This wave function depends on the coordinates of each electron and also in the position of the nuclei. Writing the wave function in this manner the requirement of Pauli principle is fulfilled. In principle the exact wave function is given as a complete (i.e. infinite) expansion of all Slater determinants that can be generated from a complete one-electron space. This is not possible and therefore approximations have to be made in all practical applications.

The *Hartree Fock* method in its most elementary form considers a single determinant *ansatz* for the approximation of a N-electron state function Ψ.

The Hamiltonian $\hat{H}$ is usually taken to be the clamped-nuclei BO one. Owing to the variational principle, the expectation value of Equation 3.3 is always higher than the exact ground state energy.

$$\frac{<\Psi|\hat{H}|\Psi>}{<\Psi|\Psi>} = \epsilon_{HF} \tag{3.3}$$

The best approximated energy will be the lowest one, so the best function to describe the system will be the one that provides the lowest energy. The entities to be varied in order to find a energy minimum are the single electron orbitals themselves. In doing this minimization one obtains an expression for the best HF spin orbitals.

The equation for the spin orbitals under orthonormality takes the form:

$$f|\chi_a>=\sum_{b=1}^{N}\epsilon_{ab}|\varphi_a> \tag{3.4}$$

$$f_1 = h_1 + \sum_b J_b(1) - K_b(1) \tag{3.5}$$

f_1 is the Fock operator, h_1 is the core Hamiltonian for one electron (describing the kinetic energy and the nuclear attraction of an electron), to which is added the sum over all the spin orbitals of the *Coloumb* and *Exchange* operators J_b and K_b. For any electron χ_b interacting with electron χ_a these operators are defined by:

$$J_b(1)\chi_a(1) =< \chi_b(2)|\frac{1}{r_1 - r_2}|\chi_b(2) > |\chi_a(1) > \tag{3.6}$$

$$K_b(1)\chi_a(1) =< \chi_b(2)|\frac{1}{r_1 - r_2}|\chi_a(2) > |\chi_b(1) > \tag{3.7}$$

Physically the *Coulomb* operator describes the repulsion between electrons and the *Exchange* operator describes the modification of the energy due to the effects of Pauli principle. $\hat{J}$ and $\hat{K}$ depend on the set of one electron functions χ and hence the equations need to be solved in an iterative scheme until self consistency is obtained.

It is necessary to point out that any single determinant wave function formed from a set of spin orbitals χ_a retains a certain degree of flexibility in the spin orbitals (as can be seen in Equation 3.4). Hence the spin orbitals can be mixed among them-

selves without changing the expectation value E_0 because for a single determinant wave function, any expectation value is invariant under an unitary transformation of the spin orbitals. Thus the spin orbitals that make the total energy stationary are not unique.

The HF equations in a canonical form lead to:

$$f_1\chi_a(1) = \epsilon_a\chi_a(1) \tag{3.8}$$

The unique set of spin orbitals obtained from a solution of this eigenvalue equation is called the set of canonical spin orbitals.

Another set of orbitals often used are *localized* orbitals. There are not an unique of define them, but in general they are obtained looking for minimizing the overlap between orbitals located on different nuclei. This kind of orbitals, in the context of the *complete active space* approximation (see next subsection) will be used in the study of the intramolecular charge transfer processes exposed in (*Chapter 5* and *Chapter 6*).

In 1951 Roothan [58] and Hall [59] independently suggested expanding the spin orbitals in a known basis set of the form:

$$\chi_i = \sum_{\alpha}^{M} c_{\alpha i}\varphi_\alpha(1) \tag{3.9}$$

This defines the molecular orbitals using a *Linear Combination of Atomic Orbitals* (LCAO). It turns the *Hartree Fock* equations into a matrix equation, the so called Roothan equation, where χ are the basis functions and $c_{\alpha i}$ are the coefficients which are calculated by *Self Consistent Field* (SCF) method. The variational parameters are now the *molecular orbitals* (MO) coefficients instead of the orbitals themselves. The Hartree Fock matrix equation can be expressed as:

$$FC = SCE \tag{3.10}$$

where F is the Fock matrix, C the collection column vectors C_i, S the overlap matrix of the basis functions χ and E the eigenvalue matrix, which can be diagonalized by an unitary transformation of the orbitals to yield the orbital energies.

Summing up, the HF method essentially describes the movement of a single electron in the field of the nuclei and the average field of the other electrons with an expectation value E_0 which is not just the sum of orbital energies.

$$E_o = \sum_{a}^{N} < a|h|a > + \frac{1}{2} \sum_{a}^{N} \sum_{b}^{N} < ab||ab > \tag{3.11}$$

It typically recovers more than 99 per cent of the exact, non relativistic energy but the remaining error is, unfortunately, still large on the chemical energy scale. Energy differences may, however, be more accurate through error cancellation.

3.2 Correlation energy

In the context of *ab initio* methods the *Correlation Energy* (E_{corr}) is defined as:

$$E_{corr} = \xi_o - E_o \tag{3.12}$$

which describe the difference between the non relativistic energy of the system (ξ_o) and the Hartree Fock energy (E_o), obtained in the limit that the basis set approaches completeness.

The objective of post HF methods is to incorporate this correlation energy in order to obtain in a certain base the exact energy. Electron correlation is sometimes divided into *dynamic* and *non dynamic* (static) correlation. Static correlation is important for systems where the state is well described only with more than one (nearly) degenerate determinant, this case is quite common in the field of study of this thesis, the excited states of organic molecules.

Post HF Methods

We will comment now briefly the *post HF* methods used along the studies presented here.

3.2.1 Complete Active Space SCF (CASSCF) theory

The first step in generalizing the *HF* method for any arbitrary state is to allow higher flexibility on the wave function. The exact ground state or excited state wave function (biased to the basis set) can be described as a linear combination of all possible determinants given by the occupation by the electrons of the system of any set of orbitals of the basis set, given place to the *Full Configuration Interaction*(FCI). Unfortunately even in calculations involving small molecular species the number of determinants is extremely large and therefore the wave functions are usually truncated. The wave function is then expressed as a linear combination of a finite set of determinants. In this so called *MultiConfigurational Self Consistent Field* (MCSCF) method [60], the *ansatz* for the N-electron wave function is:

$$\Psi(x_1, ...x_N) = \sum_I C_I |\Phi_I > \tag{3.13}$$

As a consequence, in the open shell systems, a single Slater determinant is not always sufficient for obtaining eigenfunctions of $\hat{S}^2$ and it is necessary to use linear combinations of Slater determinants. These linear combinations that fulfil the spin and the spatial symmetry requirements are usually referred to as *configuration state functions* (CSF), easily constructed with the unitary group approach and its graphical representation.

The variation parameters in the MCSCF method are the CSF coefficients C_I and the coefficients $c_{\alpha i}$ of Equation 3.9 which are both varied in order to minimize the energy in contrast with *Configuration Interaction* methods that only optimize the coefficients C_I. MCSCF is computationally more expensive but enables more accurate results with fewer CSF.

One of the most difficult steps in the MCSCF method is to find a good set of χ which give a balanced description for the state(s) of interest. A systematic although not very economic way, is based on the subdivision of the orbital set into three subspaces.

- the set of inactive orbitals which are doubly occupied in all CSF
- the set of active orbitals which have variable occupation numbers in the various CSFs

- the set of virtual (external) orbitals which are unoccupied in all CSF.

The multiconfigurational character is then introduced by a full configuration interaction within the active space. Therefore, this method has the acronym *Complete Active Space Self Consistent Field*, CASSCF [61, 62].

The optimization of such a CASSCF wave function is a highly non linear problem [62, 63]. Some of the solutions are sensible approximations to accessible states of the system while others simply represent saddle points or other stationary points in the (c,C) variational space and sometimes it is hard to distinguish them from sensible solutions. However, efficient programs of the CASSCF method exist.

An iteration of the CASSCF optimization can be usually divided into two different parts. In the first part CI coefficients are obtained and in the second part the orbital optimization is performed. To this date, in most MCSCF calculations, the first part is done only in a small portion of the time spent in the second part. There are two approaches to the orbital optimization: the *Newton Raphson* (NR) and the *super Configuration Interaction* (super-CI) method.

In the super-CI method [62, 63], the starting point is the fulfilment of the condition of the generalized Brioullin's Theorem [64]. A unnormalized Brioullin state $|pq\rangle = (\hat{E}_{pq} - \hat{E}_{pq})|0\rangle$ is defined and the secular problem has to be solved with this states as the basis set to obtain a wave function $\Psi = |0\rangle + \sum_{p,q} X_{pq}|pq\rangle$. The generalized Brillouin theorem is fulfilled at convergence, that is, when all coefficients X_{pq} are zero.

The NR method looks for the unitary transformation $U = exp(X)$ of the initial orbital set which minimizes the energy, taking the derivative of the Taylor expansion of the energy up to second order in matrix elements of X [62, 63].

There are two accelerating devices of the MCSCF convergence that have been used in this thesis. The first one is the *level shift* (LS) technique [65]. Oscillating convergence in an SCF calculation is usually an oscillation between wave functions that are close in energy or a mixing of states. Thus oscillating convergence can often be helped by level shifting, which artificially raises the energies of the virtual orbitals, and it may or may not help in cases of random convergence. This is applicable to both the super-CI and the approximate Newton-Raphson methods.

In second place, we can use of a convergence acceleration method which is de-

signed to reduce the number of iterations necessary to converge to a solution. Most MCSCF programs do not actually compute orbitals from the previous iteration orbitals in the way that is described in introductory descriptions of the SCF method. The method of choice is usually Pulay's DIIS method (Direct Inversion of the Iterative Subspace, [66, 67]). Some programs also give the user the capability to modify the DIIS method, such as putting in damping factors.

In Molcas, the orbital optimization in the *Reduced Active Space* SCF (RASSCF) modul program is performed using the super-CI method (the reader is referred to the reference [60] for more details). A *quasi Newton* (QN) update method is used in order to improve convergence. By default, dynamic damping is used during the first few iterations. When the change in the density between two subsequent iterations drops below a certain threshold the second order update/C2-DIIS procedure kicks in. A level shift of 0.1 mH is the default value.

In Gaussian the default SCF algorithm uses a combination of two DIIS extrapolation methods: EDIIS and CDIIS. EDIIS [68] uses energies for extrapolation, and it dominates the early iterations of the SCF convergence process. CDIIS, which performs extrapolation based on the commutators of the Fock and density matrices, handles the latter phases of SCF convergence. In some cases with difficult convergence damping factors are used. The default level shift value is 0.1 mH.

CASSCF calculations can be beneficially performed for the average of several states which leads to the *state average* CASSCF formalism, SA-CASSCF. Where such *state averaged* wave function *ansatzs* are employed, we shall refer to these as SAz-CAS methods, where z is the number of states over which the average is taken. Convergence problems of the CASSCF wave function can be expected in situations of near degeneracy of states, and it is specially severe when the states have different character. A good solution in these cases is the state averaging.

It is important to point out that CASSCF wave functions are not designed to recover large fractions of correlation energy. Rather, The CASSCF method is designed to describe multiplet and near degeneracy situations usually in a reasonable and consistent way to *zero order* and therefore to provide a good starting point for the treatment of electron correlation energy.

3.2.2 Complete active space with 2^{nd} Order Perturbation Theory (CASPT2)

The most straightforward way to improve the HF result is to include the effects of dynamic electron correlation through many body perturbation theory. Based on a single HF determinant, a division of the Hamiltonian was proposed by Moller and Pleset [54].

In $\hat{H} = \hat{H}^0 + \hat{V}$, the zero order part of the Hamiltonian (or unperturbed $\hat{H}$) is defined by $\hat{H}^0 = \sum_i F(i)$ while the perturbation, $\hat{V}$ is known as the fluctuation potential since it creates fluctuations of the electrons with respect to the mean field description of HF.

If the perturbation is small we can expect that E_i be reasonably close to E_i^0 and hence we wish to systematically improve the eigenvalues of H_0 to converge onto the total Hamiltonian, $\hat{H}$. The exact eigenfunctions and eigenvalues are expanded in a power series in λ, so that:

$$E_i = E_i^{(0)} + \lambda E_i^{(1)} + \lambda^2 E_i^{(2)} + \cdots \tag{3.14}$$

$$|\Phi >= |\Psi_i^{(0)} > + \lambda |\Psi_i^{(1)} > + \lambda^2 |\Psi_i^{(2)} > + \cdots \tag{3.15}$$

In the Moller Pleset method up to second order, MP2, the first order correction to the energy $E^{(1)}$ is $\langle \Psi | \hat{H}' | \Psi \rangle$ and the first order correction to the function $\Psi^{(1)}$ is $\Psi^{(1)} = \sum_j c_j \Phi_j$, where $E_0 = E^0 + E^1$. $E^{(1)}$ cancels the double counting of the electron-electron repulsions, given the correct HF energy E_0. MP2 leads to the following estimates of the total correlation energy:

$$E_{MP2} = E_{HF} + \sum_{j \neq 0} \frac{\langle \Psi^{(0)} | \hat{V} | \Phi_j \rangle \langle \Phi_j | \hat{V} | \Psi^{(0)} \rangle}{E^{(0)} - E_j} \tag{3.16}$$

Since the perturbation operator do not contain more than two body terms, according to Slater's Rules, $\hat{V}$ can only couple to the HF determinant with double excitations so, according to Brioullin's theorem, single excited determinants will not contribute to the correlation energy.

The generalization of the MP2 theory from a single HF determinant to a multiconfigurational reference function turns surprisingly difficult. The most widely used method of this kind is the CASPT2 approach with a CASSCF wave function as the starting point developed and extensively applied by Roos and co-workers [60, 69]. In general it is impossible to unambiguously partition the BO Hamiltonian into a zero order Hamiltonian and a perturbation, and consequently many different version of the method exist.

The configuration space, in which the wave function is expanded, can be decomposed in four subspaces V_0, V_K, V_{SD} and $V_{TK...}$, where:

- (1) V_0 is the one dimensional space spanned by the CASSCF reference wave function.
- (2) V_K is the space spanned by the orthogonal complement to $|0\rangle$ in the restricted full CI subspace used to generate the CASSCF wave function.
- (3) V_{SD} is the space spanned by all single and double replacement states generated from V_0 and not included in 1 and 2.
- (4) $V_{TK...}$ is the space which contains all higher excitations.

In defining the zeroth order Hamiltonian, we want three conditions to be fulfilled. The first and most important condition is that the perturbation expansion converges rapidly. Second, the zeroth order Hamiltonian should preferably be equivalent to the Moller Pleset Hamiltonian in the limiting case of a closed shell reference function. Third, it should be possible to make an efficient computational implementation of the method. These conditions can be fulfilled for a zeroth order Hamiltonian of the following form:

$$\hat{H}_0 = \hat{P}_0\hat{F}\hat{P}_0 + \hat{P}_K\hat{F}\hat{P}_K + \hat{P_{TQ..}}\hat{F}\hat{V_{TQ...}} \tag{3.17}$$

where $\hat{P}_0$ is the projector onto V_0, $\hat{P}_K$ is the projector onto V_K..., and $\hat{F}$ is the one particle operator. With this choice of $\hat{H}_0$, we also achieve that only vectors belonging to V_{SD} will contribute to the first order wave function and the second order energy. The remaining operator to be defined is the one particle operator $\hat{F}$. The

freedom in choosing this operator is reduced since we want it to reproduce the results from closed shell MP2, so $\hat{F}$ is defined as a spin averaged Fock operator:

$$\hat{F} = \hat{h} + \sum_{tu} D_{tu}(\hat{J}_{tu} - \frac{1}{2}\hat{K}_{tu}) \tag{3.18}$$

where the first order density matrix of the MCSCF $|0\rangle$ was introduced: $D_{ut} = \langle 0|E_{tu}|0\rangle$. The operator E_{tu} is known as orbital replacement operator or generator of the unitary group and is given by:

$$E_{tu} = \sum_{\alpha} a^{+}_{u\alpha} a_{t\alpha} \tag{3.19}$$

In second order perturbation theory, the first order wave function $|1\rangle$ is determined by:

$$(\hat{H}^0 - E^0)|1> + (\hat{V} - E^1)|0> = 0 \tag{3.20}$$

$|1\rangle$ is expanded on a set of first order interaction space (FOIS):

$$|1\rangle = \sum_{I} C_I |\Psi_I\rangle \quad |\Psi_I\rangle \, \epsilon \, V_{SD} \tag{3.21}$$

The first order wave function gives the second order energy:

$$E_{MRPT2} = E_{CASSCF} + <0|\hat{V}|1> \tag{3.22}$$

CASPT2 becomes usually unmanageable even for moderate size molecules. There is a way around this problem by making use of the principle of internal contraction. In this methods, the FOIS of the multireference wave function is expanded by acting with the excitation operators onto the entire wave function together [70]. For example:

$$|1\rangle = \sum_{pqrs} c_{pqrs} E_{pq} E_{rs} |0\rangle \tag{3.23}$$

where the CI coefficients are fixed by the preceding CASSCF calculation. The set of excited state CSFs is not linearly independent and not orthogonal, which creates additional technical challenges.

In CASPT2 calculations three problems may overcome.

- The first problem is that CASPT2 had systematic errors [71]. These systematic errors have recently been considerably reduced by the introduction of a modified zeroth order Hamiltonian [72]. The method introduces a shift (the *Ionization Potential Electron Affinity* (IPEA) shift) that modifies the energies of active orbitals such that they become closer to ionization energies when excited from and closer to electron affinities when excited out of. In this thesis the IPEA is a fixed shift parameter of 0.25.

- The Second problem is the possible inclusion of intruder states. A number of methods have been developed to avoid this problem. There are two different cases: a large interaction matrix between intruder states and the reference state that indicates that it's necessary to include that state in the reference wave functions, and a second case where the intruder state does not have a large interaction with the reference wave function, but intrudes because E_o is similar to E_j. Hence the intruder state can be shift up artificially by adding an arbitrary value to the expectation value of $\hat{H}$ [73]. In this thesis the imaginary level shift technique [74]is used, so intruder states are projected onto the imaginary energy axis.

- The third problem appears when the CASSCF wave function is not a good zero order reference wave function. The CASSCF states that are orthogonal to the reference state are part of the secondary space. However these states do not contribute in the second order treatment, since by definition they not interact with the reference state via the total Hamiltonian $\hat{H}$. In some instances strong mixing occurs between the reference state and and one or more CASSCF states of the secondary space. The solution is to use the *Multi State* CASPT2 approach (MS-CASPT2) [75]. It uses a multidimensional reference space and constructs an effective Hamiltonian which is computed perturbatively, permitting the CASSCF states to interact via non diagonal terms. The diagonal terms are the *single state*, SS-CASPT2 energies.

$$H_{12}^{eff} = \delta_{12}E_1 + < \Psi_1|\hat{H}|\Psi_2 > \tag{3.24}$$

The MS-CASPT2 introduces the interaction between CASSCF roots via the first order correction to them. After symmetrization the effective Hamiltonian is diagonalized and MS-CASPT2 energies and *Perturbed Modified CAS Configuration Interaction* (PM-CAS-CI) functions (linear combination of CASSCF states) are obtained.

3.3 Spin Orbit Coupling

The *spin orbit coupling* (SOC) Hamiltonian ($\hat{H}_{SO}$) acts as a small, but sometimes vital element to the Hamiltonian of the total system. Providing that the coupling is small, the spin orbit interaction can be treated as a perturbation of a non relativistic spin pure wave function and written:

$$\hat{H} = \hat{H}_{el} + \hat{H}_{SO} \tag{3.25}$$

In first order approximation transitions between pure singlet and pure triplet states are forbidden due to the orthonormality of the spin wave functions. However Spin Orbit Coupling arising from the interaction between spin and orbital angular momenta allows mixing between the singlet and the triplet manifolds providing a mechanism for intersystem crossing.

For non zero SOC matrix values, the two interacting states must obey El-Sayed's rule [76]. That states that angular momentum must be conserved.

The development of the calculation of SOC starts at the full microscopic *Breit-Pauli* or *no pair spin orbit* Hamiltonians formed by one and two electrons parts. Employing such an operator straight forward in the usual LCAO approach requires the evaluation of up to four-center spin orbit coupling elements. Even for medium sized molecules this procedure is very time consuming.

The strategy used in this thesis is the definition of an effective one electron spin orbit operator which includes both the direct and the exchange interactions between the outer valence and the core electrons, but handles the screening of the one electron terms by the two electron contributions by means of an average over the electrons which are active in a configuration interaction procedure. In other

words, we introduce a mean field approximation for an effective one electron spin orbit Hamiltonian [52, 77]. This implies that the spin other orbit contributions have been contracted by a fixed atomic density matrix.

On the basis of several CASSCF wave functions (spin free), the computing of the Hamiltonian matrix elements and the following diagonalization, provides a set of non interacting linear combination of CASSCF functions, the spin orbit states [78].

3.4 Polarizable Continuum models (PCM)

In recent years there has been a considerable effort in developing theoretical methods that allow to approach quantum chemistry to the limit of experimental accuracy in the gas phase. However, most chemical processes occur in condensed phase, and solute-solvent interaction can have a dramatic effect in molecular properties [79]. Recently efforts have been invested in the development of computational strategies to allow the use of *ab initio* methods with models of solvation [80]. The family of polarizable continuum models has become very popular, that can be described as an *Apparent Surface Charge* (ASC) approach . In this work we have used a continuum model of solvation in conjunction with the CASSCF and CASPT2 methods.

In PCM, the solvent is represented either as a polarizable dielectric or as a conductor. They differ in the boundary conditions. The version used in this thesis is the conductor model and the formalism is described in ref. [81]. It works very well for polar solvents. The solut is placed in a cavity formed by interlocking spheres centered on solute atoms or atomic groups [82]. The cavity is mapped in terms of finite elements ("*tesserae*"), used to approximate the surface integrals as finite sums.

The formal derivation of the model is based on the use of a partitioning of the Hamiltonian, by the definition of a effective fixed nuclei Hamiltonian $\hat{H}_M$ for the solute M:

$$\hat{H}_M(q,Q) = \hat{H}_M^{(0)}(q,Q) + \hat{V}_{int} \tag{3.26}$$

$\hat{H}_M$ depends on the coordinates of the electrons (q) and parametrically on coordinates of the nuclei (Q). Here $\hat{H}_M$ is the usual electronic Hamiltonian in vacuo, according to the BO approximation, and $\hat{V}_{int}$ is the interaction potential.

In $\hat{V}_{PCM}$ (interaction potential PCM operator), solute solvent interactions are reproduced by a set of point charges placed in surface tesserae, whose magnitude depend on solute nuclei and electronic density. These solvatation charges polarize the electronic distribution and modify the potential energy surface. This problem has to be solved iteratively.

When applied to electronic transitions, non equilibrium solvation effects can be included, where the solvation charge is separated on each point of the surface into two components: *a)* a fast component, in equilibrium with the solute electronic density. It is the charge due to the electronic component of solvent polarization and *b)* a slow component, that is the charge from the orientational components. In electronic transition calculations the slow part is delayed based on the sudden change of electronic density.

The last consideration in PCM calculations is in the case of state average CASSCF calculations, where special attention should be paid to the definition of solvatation charges (which depends on the electronic density).

CHAPTER 4

PHOTOSENSITIZATION BY PHENALENONE

4.1 Introduction

For several decades, considerable interest has been focused on the physical and chemical properties of low lying molecular oxygen states [6]. Molecular oxygen, characterized by a ground state of triplet character and two singlet excited states close in energy, has special properties in its magnetic and spectroscopic behaviour, energy transfer and chemical reactivity.

Molecular oxigen description by molecular orbital theory predicts that its ground state is a triplet. The electron configuration of $^3\Sigma_g^-$ symmetry is an open shell with 6 electrons and 4 orbitals, $(\pi_x)^2(\pi_y)^2(\pi_x^*)^1(\pi_y^*)^1$. Two excited singlet states are located close in energy; the first is described by two equivalent Δ_g^+ configurations: $(\pi_x)^2(\pi_y)^2(\pi_x^*)^2$ and $(\pi_x)^2(\pi_y)^2(\pi_y^*)^2$ and the second by a $^1\Sigma_g^+$ one: $(\pi_x)^2(\pi_y)^2(\pi_x^*)^1(\pi_y^*)^1$, with energies of 0.98 eV and 1.63 eV respectively.

The most common way of generating singlet oxygen is photosensitization, that is, through a process in which the presence of a light-absorbing photosensitizer

agent (PS) activates in a substrate reactions that otherwise would not take place [10]. There are two types of photosensititzation mechanisms:

- **Mechanism type 1:** An excited state of PS (PS^*) oxidizes or reduces the substrate at the same time that PS is reduced or oxidized.

$$PS \overset{h\nu}{\rightarrow} PS^*$$
$$PS^* + R \rightarrow R_{ox} + PS_{red}$$
$$PS^* + R \rightarrow R_{red} + PS_{ox}$$

- **Mechanism type 2:** An excited state of the PS (PS^*) transfers energy to the substract, leading to an excited state of the substract plus the deactivated PS.

$$PS \overset{h\nu}{\rightarrow} PS^*$$
$$PS^* + R \rightarrow R^* + PS$$

In the case of molecular oxygen, the mechanism of photosensititzation is *type 2*, an energy transfer from the excited state of a photosensitizer (PS) to the ground state of molecular oxygen, O_2 ($^3\Sigma_g^-$), in a process where the angular momentum must be conserved (Figure 4.1). There are several possible reactions between different excited states of the PS and the molecular oxygen that yield different molecular oxygen excited states. The characteristics that a PS must have to be a efficient are: *a)* an excited triplet state that is sufficiently long-lived; *b)* the ability to be extensively populated by the way of an efficient intersystem crossing (ISC); *c)* significant overlap between its emission spectrum and $^1O_2$ absorption spectrum; *c)*.

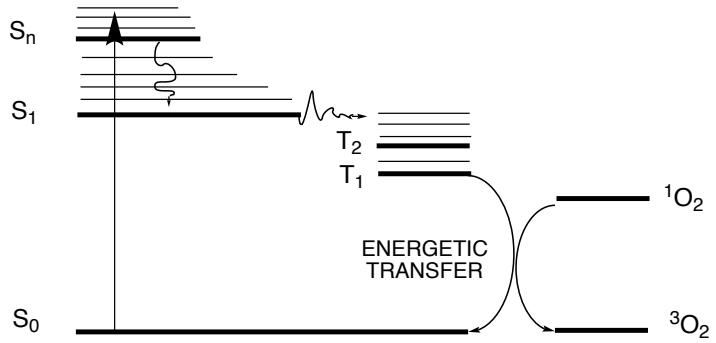

Figure 4.1: Schematic ilustration of singlet oxygen production by photosensitization

Singlet oxygen photosensitization is highly favoured in nature, because *i)* the excitation energy of both singlets are lower than the energy of many organic triplets, in most cases the difference is small enough to make the process fast and large enough to make it irreversible, *ii*) the very small size of the molecular oxygen allows for a particularly rapid diffusion in many media, and *iii)* due to the high atmospheric oxygen concentration, hardly any other intermolecular process is able to compete with oxygen quenching.

On the other hand, in many cases, energy transfer results in the formation of both singlet states, O_2 ($^1\Sigma_g^+$) and O_2 ($^1\Delta_g$). However, the spin-allowed $^1\Sigma_g^+ \rightarrow ^1\Delta_g$ deactivation occurs with extremely high rate constants in the condensed phase, and with a unit of efficiency in any solvent; thus all molecular oxygen that is in O_2 ($^1\Sigma_g^+$) state will be recovered as O_2 ($^1\Delta_g$).

The first excited state of molecular oxygen O_2 ($^1\Delta_g$, from here on represented by $^1O_2$), has a rich chemistry and a large number of photophysical aplications [6]. It is recognized as an important oxidizing intermediate in chemical and biological processes, such as photodegradations [7], defence mechanisms [8] and photocarciogenesis [9], and it is applied in a variety of fields, such as organic synthesis [7] and the photodynamic therapy of cancer [8, 10].

The *singlet oxygen quantum yield* (Φ_Δ) is a determinant property of a photosensitizing agent. This quantity is defined as the number of $^1O_2$ molecules generated by each photon absorbed by the PS. The production of $^1O_2$ by photosensitization involves four steps: *(1)* light absorption by the photosensitizer, *(2)* formation of the photosensitizer's triplet state; the quantum yield of this process is the intersystem crossing efficiency or triplet yield (Φ_T), *(3)* trapping of the photosensitizer in the triplet state by molecular oxygen within its lifetime; the fraction of trapped triplet states in a given system is designated by f_T and *(4)* energy transfer from the photosensitizer triplet state to molecular oxygen. The probability of this energy transfer is S_Δ.

Globally, the probability of this sensitizing process schematized in Figure 4.1 is

$$\Phi_\Delta = \Phi_T \cdot f_T \cdot S_\Delta$$

Virtually all measurements of Φ_Δ are scaled relative to a reference substance. The study and characterization of molecules as possible standards and universal

references is of crucial interest to understand the effectivity of a given reaction mechanism because it provides the possibility of comparison of some measurable properties, making the study and development of new *type 2* photosensitizers an easier task.

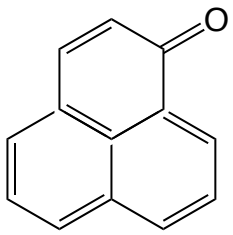

Figure 4.2: Phenalenone

1H-phenalen-1-one (or perinaphthenone, often called *Phenalenone*, PN) is an universal reference for the sensitization of singlet oxygen due to the fact that its quantum yield of singlet oxygen production is close to 1 in a large variety of solvents ranging from water to cyclohexane (see Tabla 4.1) [11–13].

Table 4.1: Quantum yield of singlet oxygen production (Φ_Δ) of PN in different solvents.

PS	**solvent**	$\Phi\Delta$
PN	Toluen	0.97±0.06
PN	Cyclohexane	0.91±0.03
PN	1,4-dioxane	0.99±0.05
PN	N,N-dimetilacetamide	0.87

PN is present in the environment as atmospheric and water pollutant [83, 84]. Some plants produce secondary metabolites (metabolites that are not involved in primary essential mechanisms) containing its skeleton [85–88] that play a significant role in some defence mechanism of plants. Plants defend themselves from the pathogen infections or mechanical injury by a number of mechanisms, including the induction by light of the biosynthesis of secondary defence metabolites. These compounds, termed phytoalexins because they are synthetized at the moment of stress, represent a very economical way to counteract hazard, because the carbon and energy resources are diverted to phytoalexins synthesis only at the early period of attack and only at its location.

PN cromophores are not in principle phototoxic for plants, but they respond to pathogen attack with a process that has the capability of, using solar energy, producing singlet oxygen by photosensititzation [89] that is letal for pathogen agents. A curious fact is that the PN derivatives with high quantum yields of singlet oxygen

production are typically phytoalexins, whereas those derivatives with low quantum yields are phytoanticipints (they are also present in healthy plants) [90].

The mechanism of defence triggered by PN arouses interest in the field of prospective applications because it can be used as a model for developing novel crop protection strategies [89, 90]. PN is also used as a standard for the production of singlet oxygen in photodynamic therapy (PDT), a medical procedure used to destroy unwanted tissue (in general, of localized tumours). The knowledge of the mechanism of photosensitization can help in the further development of PDT as a technique for cell death or cell signalling [91].

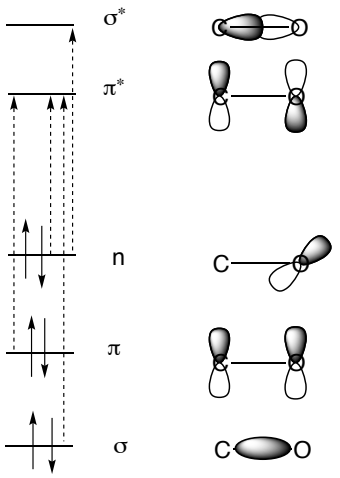

Figure 4.3: Orbital energy diagram and qualitative contour diagram of molecular orbitals of formaldehide

PN possesses a conjugated carbonyl group and an extended π network of conjugated C=C double bonds that are responsible for its photophysical and photochemical properties. Aromatic ketones exhibit low-lying electronic excited configurations of $(n - \pi^*)$ character arising from the excitation of an electron from the lone pair of the O and others of $(\pi - \pi^*)$ character, both of singlet and triplet multiplicity [92]. The relative energies and interplay among these states depend on the peculiarities of each system. The simplest example of a carbonil compound is formaldehide, which expectation values in the orbital energy level diagram are shown in Figure 4.3. This example is interesting as an example of ordering of orbital energies in this kind of compounds.

The absorption spectrum of PN shows a band at about 358 nm due to the transition to the second singlet excited state of $^1(\pi - \pi)$ character [11]. The possible subsequent deexcitation processes are internal conversion, fluorescence and intersystem crossing that should yield the triplet state capable of photosensitization. The interest in a detailed knowledge of the mechanism of production of singlet oxygen by PN is evident. This mechanism has already been studied experimentally [93–95] and theoretically [11, 93, 96] thus, many aspects of this process are already known. However, a number of questions remain to be elucidated.

On the basis of studies by Darmanyan and Foote [97] it has been accepted that, like in other monoketones, the triplet $^3(\pi - \pi^*)$ state in PN reacts by a *type 2* mechanism leading to an efficient energy transfer to molecular oxygen, whereas the triplet $^3(n - \pi^*)$ state leads to a hydrogen abstraction from the solvent [97]. We can schematize then the following processes in PN:

- Generation of the reactive triplet species

$$^1PN^* \rightarrow {}^3PN^*$$

- Energy transfer to molecular oxygen

$$^3PN^* + {}^3O_2 \rightarrow {}^1PN + {}^1O_2^*$$

- Solvent hydrogen abstraction

$$^3PN^* + R - H \rightarrow PNH^{\cdot} + R^{\cdot}$$

From the high quantum yields of singlet oxygen production by PN (larger than 0.6 in any solvent), it has been concluded that the lowest-lying triplet state of PN must have $(\pi - \pi^*)$ character [12]. Later studies [11, 13] suggest that the population of this state is due to the existence of a very efficient intersystem crossing with a quantum yield close to 1.

Very recently, a study of the excited states of PN based on Time-Dependent Density Functional Theory (TDDFT) calculations has been published [96]. The authors located the ground and some excited state minima and computed the absorption and emission spectra, although the fluorescence did not satisfactorily reproduce the experimental data. The aim of the TDDFT study was not to describe in detail all the steps of the photochemistry of PN but to accurately calculate the spin orbit coupling effects and the intersystem crossing rates. Due to the monoconfigurational character of TDDFT, the results of our study that we present here differ in some points from those of ref. [96].

Scope

In this work, we will determine the sequence of processes that leads to populating the triplet state of PN responsible for the oxygen photosensitization to understand the factors underlying the high efficiency of singlet oxygen production by PN. The role of the other excited states, especially the $^3(n-\pi^*)$ state, will also be investigated, given that PN shows a certain extent of degradation under some conditions that is attributed to hydrogen abstraction from the solvent [13, 98, 99].

In a second objective for prospective developments of new photosensititzers of singlet oxygen, we have also studied and rationalized all the possible photochemical and photophysical processes that can occur from the first absorption in PN due to the possibility that they be favoured in other systems, and then compete with the main favoured reactions mentioned before.

This work is an extensive *ab initio* study conducted from first principles using the CASSCF/CASPT2 methodology. We pay special attention to the analysis of the nature of the states involved.

With this methodology, we have characterized the potential energy surfaces of the ground state and the four lower excited states, i.e., the singlet and triplet $(n-\pi^*)$ and $(\pi-\pi^*)$ states. Minima, conical intersections and singlet-triplet crossing points were optimized, and oscillator strengths and spin orbit interactions were calculated where necessary. Reaction pathways were also obtained, and linear geometric interpolations were performed between the critical points of maximum interest. These results provide values of vertical and non vertical excitation energies and detailed information about the mechanism for populating the triplet state manifold. The various reactive pathways of phenalenone in the gas phase are thus completely characterized, and we have obtained a sound theoretical basis for a better understanding of its spectroscopic properties and a plausible interpretation of its photochemical behaviour.

4.2 Computational Details

This study was conducted by adhering to the CASSCF/CASPT2 protocol. The *ab initio* multiconfiguracional CASSCF method [61] was used in all the geometry

optimizations of minimum energy points, conical intersections (CI) and singlet-triplet crossings (STC) [53]. The energetics was then refined with the MS-CASPT2 method, [100] which introduces the effect of the dynamic electron correlation into the calculation. Only in one particular case (see below), the geometry had to be optimized at the MS-CASPT2 level, with an extra computational cost.

In general, the active space used to describe the excited states of both $(n - \pi^*)$ and $(\pi - \pi^*)$ character was a (16,15), i.e. an active space with 16 electrons and 15 active orbitals that comprises the valence π molecular orbitals and π electrons plus the oxygen lone pair (see Figure 4.4). A d-polarized split-valence basis set 6-31G* [101] was used for all optimizations, with control calculations to check how the enlargement of the basis sets affected the stability of the results.

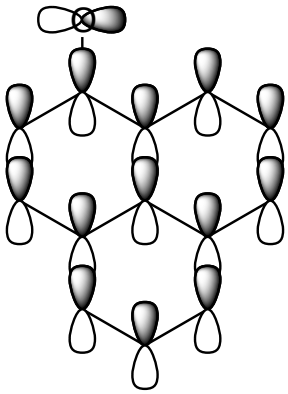

Figure 4.4: Atomic representation of the orbitals of the (16,15) active space.

The reference wave functions and the molecular orbitals were obtained by state average CASSCF calculations constrained in general to *Cs* symmetry including all the states of interest for a given symmetry. Symmetry was imposed because of the prohibitive size of the CASSCF/CASPT2 calculations in a system with 22 atoms and an active space of (16,15), which is essential because of the structure of the PN's conjugated rings.

We consider the symmetry plane of the *Cs* punctual group as the molecular plane of PN. By the character table the orbitals are classified in irreducible representations a′ and a″. The orbitals of σ character and the lone pair orbital of the exocyclic oxygen n_o are of a′ character, while those of π character are of a″ symmetry.

The description of states is obtained analyzing the direct product of the different

irreducible representations of the orbitals involved in the possible excitations. A $(a') \rightarrow (a'')$ electronic excitation leads to electron states described by the irreducible representation A″. On the other hand $(a'') \rightarrow (a'')$ excitations lead to electronic states described by the irreducible representation A′.

For the reasons detailed in the next paragraph, some calculations for non planar geometries were also run. In those cases, given that the lose of the *Cs* symmetry made that the (16,15) calculations require computational resources not available, a smaller active space had to be used. To reduce it, the occupation numbers of pseudo natural orbitals were analyzed in order to extract the orbitals with occupations close to 0 and 2. Eventually, a (12,12) active space was defined. The details of the reduction of the active space for each calculated excited state without symmetry restriction are showed in Figure 4.5.

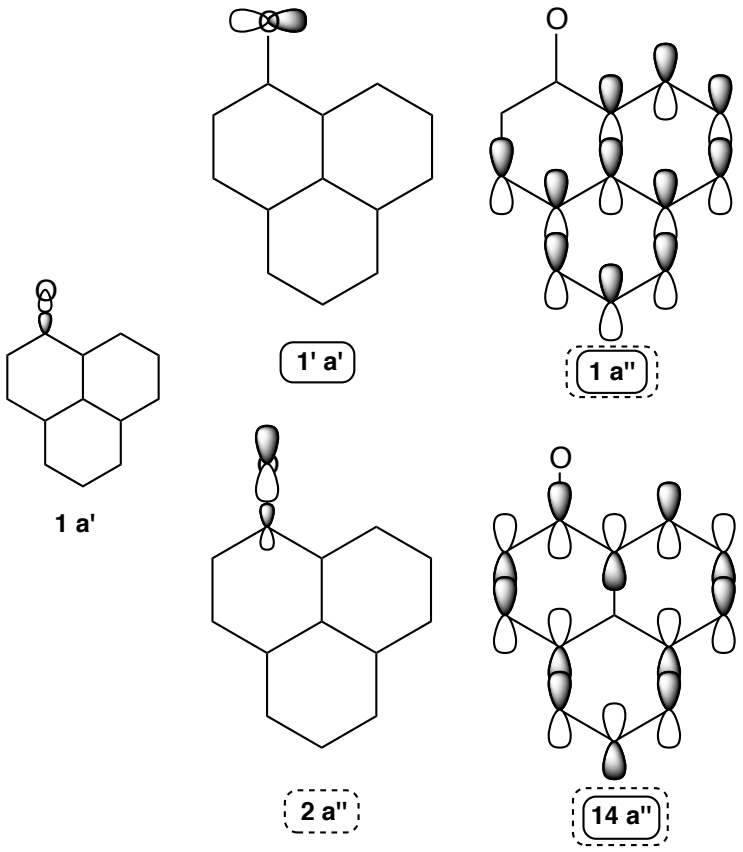

Figure 4.5: Orbitals eliminated from the (16,15) active space. In solid line are drawn those from A′ states and in dashed lines those from A″ states. 1 a′ is the orbital that tends to substitute the n_O orbital (1′ a′) in the CASSF(16,15) calculations of A′ states.

Calculations without symmetry constrains and with a (12,12) active space were run for two reasons. First, a set of calculations was performed to ascertain that the critical points that we had located under the *Cs* point group symmetry were indeed planar even without geometrical restrictions. With this aim the planar optimized geometries were distorted to break the planarity, and the geometry optimizations were rerun. In all cases, the final optimized geometry returned to planarity, providing the same structures as those obtained under *Cs* symmetry restrictions. In fact, these were the results expected considering the rigidity of the conjugated rings of PN [102].

A second group of calculations was performed to look for non radiative deactivation pathways at non planar geometries. The experience of the group in the study of other cyclic systems [103, 104] indicated that probably those critical points involved very distorted geometries, although in the case of the PN it would imply very high energies.

In the calculations regarding the states of $(\pi - \pi^*)$ character (of A' symmetry) with a (16,15) active space, the n orbital of the oxygen (n_O) (a') is doubly occupied, giving place to a predictable frequent problem. In the standard CAS(16,15) calculations this orbital, included initially in the active space, rotates to the inactive space being replaced by a σ (a') orbital that is incorporated in the active space with an occupation of 1.99. To minimize the effect of this problem, in these cases a (14,14) active space was used, after removing the n_O orbital. Test calculations showed that this change in the active space does not lead to substantial differences in the optimized geometries or in the energies.

The final electronic energies of the CASSCF optimized structures were calculated at the CASPT2 level using an atomic natural orbital-type (ANO-L) basis set contracted to C,O[4s3p1d]/H[2s1p] [105]. ANO-L basis sets were designed to treat correlation and polarization effects optimally. The lack of diffuse functions in the basis set used is of no importance, given that the present study focuses the attention on the valence state transitions where Rydberg states are expected to have a marginal influence [106].

The imaginary level shift technique [107] was used to prevent intruder states from appearing. A shift parameter of 0.3 au was selected after testing.

CASSCF wave functions were used as reference functions in the single-state CASPT2 (SS-CASPT2) treatment and the coupling among states via dynamic correlation was taken into account through the multi state CASPT2 treatment [75]. The resulting PM-CAS-CI wave functions were also obtained. The analysis of the natural orbital occupancies of these functions provided the necessary information to characterize the nature of the different electronic states. Carbon and oxygen 1s core electrons were kept frozen in this step.

The number of states included in the state averaged CASSCF reference wave functions of the MS-CASPT2 treatment can be an important parameter in some calculations. This is the case for the singlet states of A' symmetry of the system studied here, due to the large interaction of the CASSCF wave functions at the MS-CASPT2 level. To determine the optimum number of CASSCF states to be averaged for the stability of CSF composition of states and energies, test calculations were run at the ground state geometry, including 5, 6 and 7 roots (see more details in the Appendix of this chapter). Due to the non negligible coupling of the $^1(\pi - \pi^*)$ CASSCF states found, MS-CASPT2 level of calculation is necessary for a good description of the $^1(\pi - \pi^*)$ PES. Therefore the search of the $^1(\pi - \pi^*)$ minimum had to be done at the MS-CASPT2 level with an average of the five lowest-lying CASSCF states and using a reduced (12,12) active space. The high computational cost of this calculation makes it affordable only for the specific cases were it is indispensable, but not to be chosen as the standard method of work.

The CAS state interaction (CASSI) protocol [78] and the PM-CAS-CI functions were used to compute transition dipole moments and oscillator strengths, which are proportional to the transition probability (in both absorptions and radiative emissions). An effective one electron spin orbit Hamiltonian matrix based on atomic mean field integrals (AMFI) was computed, also using the CASSI protocol, to calculate the spin orbit coupling, SOC, of the crossing singlet and triplet states at the minimum energy points of the single triplet crossings [52, 77].

Minimum energy paths (MEPs) [108] and linear interpolation reaction coordinates paths were calculated between critical points of interest on several surfaces to ascertain the viability of the proposed reaction mechanisms.

4.3 Results and discussion

The photochemical process studied can be framed in different stages: the initial excitation, the immediately successive relaxation and the subsequent secondary processes. In analogy to this division, we have structured this section in three subsections. In the first subsection, we collect the results of the calculation of the absorption spectrum, which is related to the initial photoexcitation. In the second section, we show the stable structures found at the PES of the different excited states involved in the process. The data obtained in these first two steps suggest possible reaction paths, which are studied in the third subsection. The information in these three subsections forms a global picture that allows us to suggest a sound hypothesis about the mechanism of populating the sensitiser state of PN.

4.3.1 Franck Condon region and nature of excited states

From the computational point of view, then, the first step in this work must be to locate the minimum energy species of phenalenone in the ground state (called FC geometry, discussed in detail in the next subsection) and to calculate the energies of the excited states at this geometry.

In principle, it would be necessary to consider only the states with energy equal to or smaller than that of the sample irradiation energy (355 nm, 3.49 eV); however, due to the possible interaction via dynamic correlation of states of the same symmetry, higher states were also included in the initial calculations to obtain a good description of the states and absorption spectra.

A preliminary study was done in order to check the effect of basis set and the optimize number of average states involved in the calculations. Test calculations were run with 6-31G* and ANO-L basis set. Calculations including 5, 6 and 7 averaged states were done to select the number of roots for a good description of states. This study, that can be found in the Appendix of this chapter, leads us to develop subsequent work using 6-31G* for geometry optimizations and ANO-L basis set to refine the energies at the critical points. The number of roots included are five for the singlet states of A' ($\pi - \pi^*$) character (including the ground state), one for the singlet state of A'' ($n - \pi^*$) character, three for the triplet states of A'

($\pi - \pi^*$) and one for triplet state of A'' ($n - \pi^*$) character.

Vertical spectrum

Table 4.2 shows the values of excitation energies, dipole moments and oscillator strengths obtained in the FC zone with different levels of aproximation. The MS-CASPT2/ANO-L results are the most accurate ones, so they will be used to discuss the absortion spectra of PN. We obtain an energy interval of study of 5.36 eV at FC zone, at MS-CASPT2 level.

Table 4.2: Absorption energies (in eV), oscillator strengths (f) and dipole moments (μ in Debyes) for PN computed with ANO-L basis set and an active space of 16 electrons and 15 orbitals.

Estados	CASSCF	SS-CASPT2	μ	f	MS-CASPT2	μ	f
$1^1A'$ (GS)	0.00	0.00	3.5		0.00	4.10	
$1^1A''$	3.22	3.32	0.8	$<10^{-3}$	3.36	0.80	$<10^{-3}$
$2^1A'$	3.94	3.96	3.8	0.0100	3.48	6.63	0.2012
$3^1A'$	4.89	4.29	4.8	0.0779	4.00	3.95	0.0180
$4^1A'$	5.27	4.18	5.7	0.1801	4.79	3.59	0.0163
$5^1A'$	5.60	5.01	4.0	0.0208	5.36	3.64	$<10^{-3}$
$1^3A'$	2.36	2.53	3.47	$<10^{-3}$	2.56	3.47	$<10^{-3}$
$2^3A'$	3.50	3.64	3.51	$<10^{-3}$	3.68	3.51	$<10^{-3}$
$3^3A'$	3.97	3.89	3.83	$<10^{-3}$	3.93	3.83	$<10^{-3}$
$1^3A''$	3.09	3.20	0.7	$<10^{-3}$	3.24	0.7	$<10^{-3}$

Of the first six states, only the first one is of ($n - \pi^*$) character; consequently, for reasons of symmetry, it does not interact with any other state, and its wave function and energy are the same at the SS- as at the MS-CASPT2 level (the change in the relative energy is due to the change in energy of the ground state). In contrast, the states of A' symmetry strongly interact and even produce qualitative changes, as shown by the difference between the SS- and MS-CASPT2 results.

At this last level, the first singlet excited state has ($n - \pi^*$) character ($1^1A''$) and is located 3.36 eV above the ground state. This excited state can be interpreted as a promotion of an electron from the oxygen non bonding lone pair orbital to the ring (see Figure 4.6). Consequently there is a charge transfer from the exocyclic

heteroatom to the ring, that creates a reduction of the polarity that is reflected in the decrease of dipole moment from the ground state $1^1A'$ (4.10 D) to $1^1A''$ state (0.80 D).

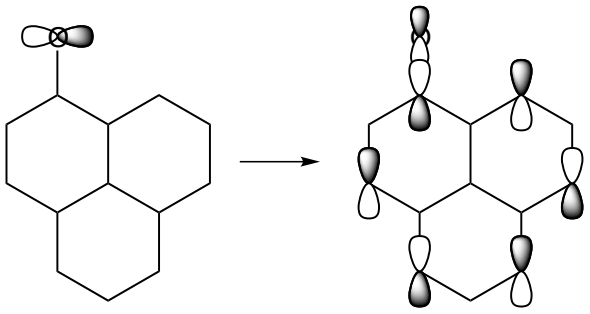

Figure 4.6: Excitation that characterize the CSF with the most significant weight in the CASSCF and PM-CAS-CI wave functions of $^1(n-\pi^*)$ and $^3(n-\pi^*)$ states.

The computed value of the oscillator strength, smaller than 10^{-3}, indicates that the transition from the ground state will not occur. This transition in not forbidden by selection rules (the symmetry group is *Cs*) but the low intensity calculated shows that the carbonyl local environment, which has essentially C_{2v} symmetry, determines the selection rule [109]. In this situation the *n* orbital is essentially of *p* character, therefore the overlap of the orbitals involved in the transition is given approximately by the product $\pi_z^* \cdot p_x$ yielding a negligible transition dipole moment [110].

The second singlet excited state is of $(\pi-\pi^*)$ character (A' symmetry). The composition of the A' PM-CAS-CI functions in terms of the CASSCF functions, collected in Table 4.3, shows that this excited state is described by a combination of the $3^1A'$ and $4^1A'$ CASSCF states with coefficients 0.64 and 0.73 respectively. The dramatic change in the description of this state when the coupling among states is considered (at the MS-CASPT2 level of calculation), precludes a correct description of this state at the CASSCF level, which provides a good approximation in other cases. The nature of this state must be interpreted in terms of PM-CAS-CI wave functions, which describe it as a monoexcitation between two molecular orbitals spread over the entire PN structure, but having opposite bonding/antibonding interactions among neighbour atoms (more details exposed in the next subsection: $(\pi-\pi^*)$ *coupling via dynamical correlation*). This state is characterized by a larger dipole moment, as shown in Table 4.2. The high value of the oscillator strength

indicates that this transition is highly probable.

Table 4.3: Eigenvalues (in Hartrees) and eigenvectors of the effective hamiltonian matrix of the 5 low-lying MS-CASPT2 states obtained with average of 5 states.

5 average states						
State		$1^1A'$ (GS)	$2^1A'$	$3^1A'$	$4^1A'$	$5^1A'$
Eigenvalues		-573.93820	-573.81020	-573.79131	-573.76223	-573.74126
		Eigenvectors				
$^1A'$	GS	0.9948	-0.0986	-0.0022	-0.0164	-0.0157
$^1A'$	$2\,^1(\pi-\pi^*)$	-0.0122	-0.1582	0.9799	0.1135	-0.0390
$^1A'$	$3\,^1(\pi-\pi^*)$	-0.0811	-0.6432	-0.0509	-0.6173	-0.4426
$^1A'$	$4\,^1(\pi-\pi^*)$	-0.0577	-0.7304	-0.1436	0.3988	0.5322
$^1A'$	$5\,^1(\pi-\pi^*)$	0.0138	0.1337	0.1279	-0.6682	0.7203

The third excited $(\pi-\pi^*)$ state, $3^1A'$, is located 4.00 eV above the ground state and have a small oscillator strength (0.018) and a dipole moment of 3.95 D. The next $4^1A'$ and $5^1A'$ states, with excitation energies of 4.79 eV and 5.36 eV respectively, are characteritzed by low oscillator strenghts, negligible when compared to that of the lowest $^1(\pi-\pi^*)$ excited state. Therefore, it is reasonable to assume that they will not be populated at the initial excitation and will not be involved in the photochemical process studied. For this reason, they are not analysed further in this work, although they are included in the A' calculations due to the composition of the PM-CAS-CI wave functions in terms of the CASSCF functions.

Thus, the theoretical results predict that the first excited $^1(\pi-\pi^*)$ state will be the one populated by the initial excitation. In fact, its excitation energy of 3.48 eV concurs with the experimental values of the maximum of the absorption band of PN, 3.46 eV in toluene [111, 112] and 3.35 eV in methylcyclohexane [93], and it also agrees with the experimental evidence that assigns a $(\pi-\pi^*)$ character to the absorption. The comparison between the theoretical results (in gas phase) and the experimental ones in solution is possible due to the low dielectric constants of the solvents (2.38 for toluene and 2.03 for methylcyclohexane) and to the similar dipole moments of the states involved in the transition (4.1 D and 6.63 D for the ground and excited states, respectively).

The characterization of the low-lying triplet states of a sensitiser is a key point in rationalizing the efficiency of the intersystem crossing and the quantum yield of singlet oxygen production. The energy of the triplets relative to the first singlet

excited states is determinant to explain the role of the triplets in the reaction mechanism. Consequently, the first five triplet states of PN were characterized in the FC zone.

The first triplet state has $^3(\pi - \pi^*)$ character (A' symmetry) and is 2.56 eV above the ground state. This state is described by the excitation showed in Figure 4.7; both orbitals are of π character and are delocalized in the rings. The calculated dipole moment of 3.47 D is in agreement with the neutral character of the state. It is 0.8 eV more stable than the first singlet excited state $^1(n - \pi^*)$, but there is a negligible spin orbit coupling between them (less than 10^{-8}). Therefore, an intersystem crossing in the Frank Condon area can be ruled out.

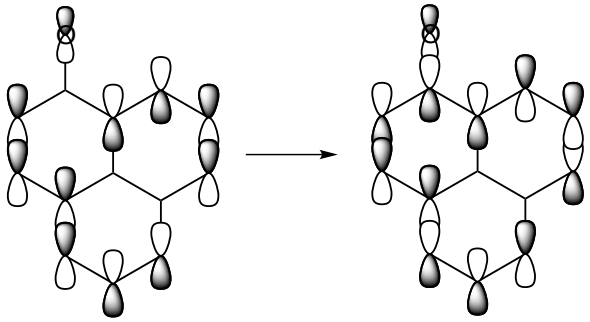

Figure 4.7: Excitation that characterize the CSF with the most significant weight in the CASSCF and PM-CAS-CI wave functions of $^3(\pi - \pi^*)$ states.

The second low-lying triplet state has $(n - \pi^*)$ character (A" symmetry) and is 3.24 eV above the ground state. It is only 0.12 eV more stable than the first singlet $^1(n - \pi*)$ excited state but the spin orbit coupling between them is negligible, in agreement with El-Sayed rules, despite these two states are very close in energy. Therefore, an intersystem crossing can also be ruled out in this case. This state is described in terms of excitations like the $^1(n - \pi^*)$ state (see Figure 4.6), with a decrease of the dipole moment relative to the ground state of 0.7 D.

The next triplet excited states are of $^3(\pi - \pi^*)$ character, more energetics than the sample irradiation energy and the bright $^1(\pi - \pi^*)$ excited state. The second $^3(\pi - \pi^*)$ is located at 3.68 eV, only 0.2 eV above the bright state with a calculated dipole moment of 3.51 D. The third excited state is located at 3.83 eV and has a dipole moment of 3.93 D. The analysis of PM-CAS-CI wave functions show that these states do not interact via dynamical correlation. The computed spin orbit couplings between these triplet and singlet states $(n - \pi^*)$ and $(\pi - \pi^*)$ are negligible.

$(\pi - \pi^*)$ coupling via dynamical correlation

The description of the valence states in molecules with π orbitals show different difficulties, one of them is the inclusion of dynamic correlation. It is necessary to include it because correlation affects in different extent to different types of states (neutral/ionic, valence/rydberg), so it changes not only the absolute energies, but also the relative ones.

In our case the most important correlation effect is given by the intravalence correlation, described by the mixture of diferent CSFs that only differ on the distribution of the electrons in the π valence states. With the aim of analysing the dynamic correlation in PN and the relation with the coupling of A' states at MS-CASPT2 level, we analysed the wave functions of the SA-CASSCF states of A' character and the PM-CAS-CI wave functions. The more important CSF are showed in Figure 4.8.

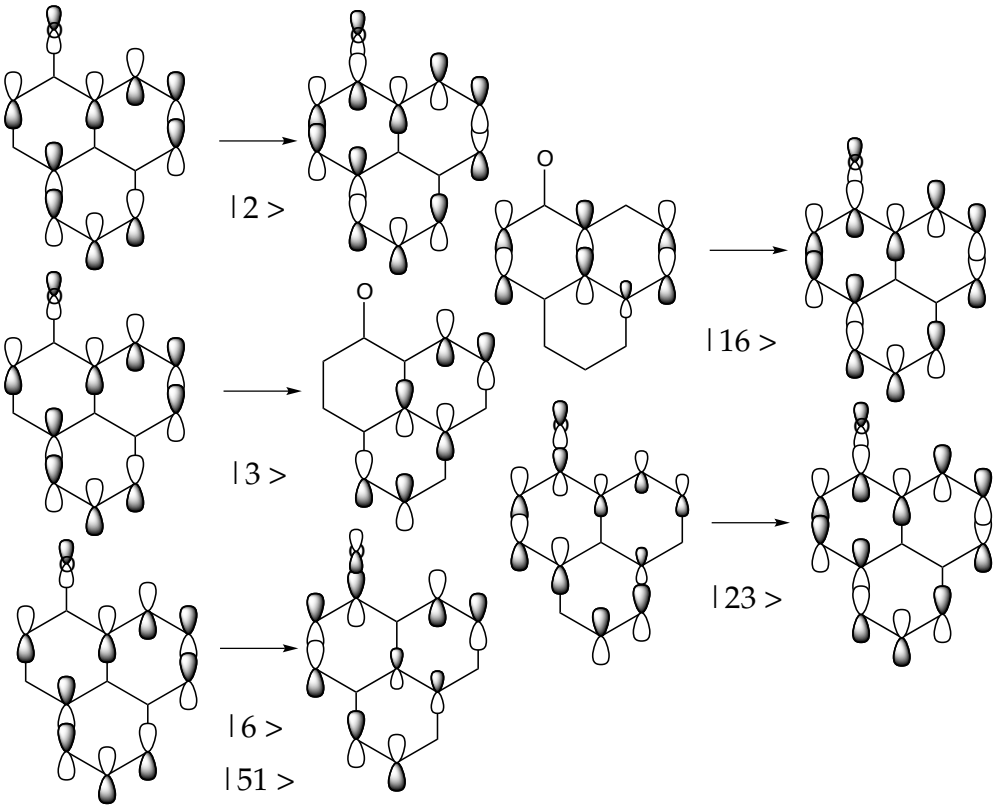

Figure 4.8: Excitations that characterize the CSF with significant weights in the CASSCF and PM-CAS-CI wave functions of the low-lying A' states of PN. CSF |51> corresponds to a biexcitation.

Let's first analyse the SA-CASSCF state functions in terms of CSF given by the following linear combination (only main contribution showed):

$$2^1A' = 0.47 \mid 3\rangle + 0.39 \mid 9\rangle - 0.48 \mid 16\rangle$$
$$3^1A' = 0.47 \mid 2\rangle - 0.25 \mid 6\rangle - 0.2 \mid 23\rangle + 0.35 \mid 51\rangle$$
$$4^1A' = 0.60 \mid 2\rangle - 0.22 \mid 6\rangle + 0.27 \mid 23\rangle - 0.31 \mid 51\rangle$$
$$5^1A' = -0.36 \mid 9\rangle - 0.49 \mid 16\rangle$$

The states $3^1A'$ and $4^1A'$ are formed by the same CSF with different coefficients. It is interesting to point out that CSF $|2\rangle$ correspond to an ionic configuration, as showed by the electronic density difference between the orbitals involved in the monoexcitation described by this CSF. This density difference represented in Figure 4.9, shows a partial charge transfer. For this reason, state $4^1A'(\mu = 6.04$ D) with a large contribution of $|2\rangle$ has a larger dipole moment than $3^1A'$ ($\mu = 4.97$ D), with a smaller coeficient.

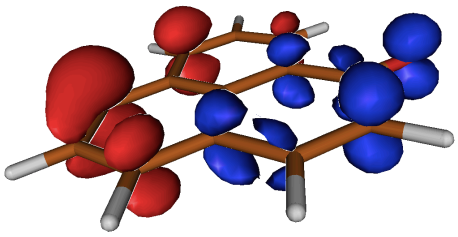

Figure 4.9: Density difference of $|2\rangle$ CSF's excitation.

When dynamic correlation is included, we allow the interaction of the CASSCF wave functions to give place to the PM-CAS-CI functions. The composition of the PM-CAS-CI wave functions in terms of the SA-CASSCF wave functions obtained were given in Table 4.3. In terms of the CSF, the PM-CAS-CI are:

$$2^1A' = -0.78 \mid 2\rangle$$
$$3^1A' = 0.46 \mid 3\rangle + 0.34 \mid 9\rangle - 0.52 \mid 16\rangle$$
$$4^1A' = 0.20 \mid 3\rangle 0.43 \mid 9\rangle + 0.45 \mid 16\rangle - 0.25 \mid 51\rangle$$
$$5^1A' = -0.23 \mid 6\rangle - 0.20 \mid 16\rangle + 0.35 \mid 23\rangle - 0.43 \mid 51\rangle$$

The $2^1A'$ PM-CAS-CI state is a combination of $3^1A'$ and $4^1A'$ CASSCF states.

This state is composed basically by only one CSF $\mid 2\rangle$, that give place to a large dipole moment of 6.63 D. It has been shown previously [113] that in the ionic configurations the dynamic correlation effect is larger due to the σ net polarization. Consequently when correlation is included in the calculations, ionic states are preferentially stabilized relative neutral states. This has been also the case in PN, where the ionic state becomes the lowest energy excited state in the MS-CASPT2 treatment.

The $3^1A'$ PM-CAS-CI state is basically given by the $2^1A'$ CASSCF wave function, so their wave functions are very similar. The $4^1A'$ and $5^1A'$ PM-CAS-CI states are also combination of the $3^1A'$ and $4^1A'$ wave functions and a non negligible contribution of the $5^1A'$ state.

The dynamic correlation affects in different degree the different CSF that describe the several ($\pi - \pi^*$) states. If the dynamic correlation is extracted, the neutral and ionic CSF, separated in energy in the correlated calculations, can become degenerated resulting that in the SA-CASSCF description the states can be a linear combination of both CSF. The combination of these two configurations that will be represented by ϕ_k and ϕ_l, is rised when the matrix element H_{kl} increases and the value of $H_{kk} - H_{ll}$ decreases. If we have to configurations of the same energy, then they split by configuration interaction, obtaining from the CI matrix positive and negative states.

Our hypothesis is that in the case of PN, ionic configuration $\mid 2\rangle$ and neutral configurations become close together in energy without inclusion of dynamic correlation at CASSCF level. This degenerancy give place to a new interaction between them at CASSCF level. In fact, if we analyze in more detail the composition of the $3^1A'$ and $4^1A'$ SA-CASSCF state, we observe that they are qualitatively they are the positive and negative combination of the same CSFs,that can be schematized in the following way:

$$\Phi = \frac{|2\rangle \pm (|23\rangle - |51\rangle)}{\sqrt{2}}$$

Thus it is necessary not only to include the dynamic correlation by the SS-CASPT2 treatment, it is also necessary the inclusion of the interaction of SA-CASSCF states with the MS-CASPT2 treatment.

4.3.2 Equilibrium geometries

The natural evolution of a system over a PES (without considering inertia) is relaxation towards the nearest minimum (relative or absolute) that corresponds to a stable species in the state of the PES. The effective reach of the minimum depends on the possible alternative processes that compete with the relaxation towards this minimum. In any case, the evolution over a PES from the static point of view follows the gradient of the surface, which will, in general, lead to the nearest minimum.

The geometrical optimizations of the ground state and the $^1(n-\pi^*)$, $^1(\pi-\pi^*)$, $^3(\pi-\pi^*)$ and $^3(n-\pi^*)$ excited states were run with *Cs* symmetry restriction. This election was based on computational reasons and chemical behaviour evidences. The first reason is the high computational cost of the CASSCF/CASPT2 methodology applied to a system of 22 atoms and an active space of 16 electrons and 15 orbitals. From the chemical point of view, the reason for mantaining the active space and impose symmetry restrictions is the rigidity of PN given by the π conjugation of the rings and the exocyclic oxygen. Previous studies have shown that less rigid molecules mantain the planar symmetry in the critical points of the deactivation mechanism that populates triplet states [102].

Small flexible ketones like acrolein (with a conjugated C-C double bond) can show torsioned $^3(\pi-\pi^*)$ stable structures [102], but they are not related to pathways of populating the triplet mainfold, but to non radiative deactivation pathways (by crossing with the ground state PES at torsioned geometries). In fact, acroleine shows low phosphorescence yield and a short triplet lifetime. As the rigidity of the monoketones increases, the triplet lifetime increases too [114]. The reason explain in ref. [115], is that the rigid systems do not need torsioned geometries to populate the triplet state, but the torsion is necessary to reach the non radiative deactivation pathway.

Consequently, we optimized the geometries of the lowest singlet and triplet states of PN under the constraint of C_1 symmetry. Neverthless, the correctness of this restriction was confirmed by optimization of non planar geometries performed with a smaller active space (where the orbitals with occupancies close to 0 or 2 were extracted). The geometries always recovered the planarity, what confirmed that working with a larger active space and symmetry constraints was adequate.

The optimized geometries are shown in Figure 4.11 (atom labelling in Figure 4.10). The energetics obtained at CASSCF and MS-CASPT2/ANO-L level for the minimum energy structures are collected in Table 4.4.

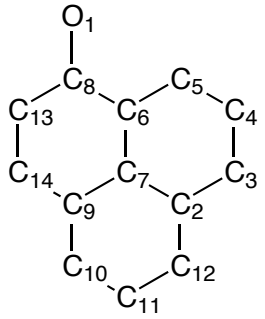

Figure 4.10: Atom labelling for PN.

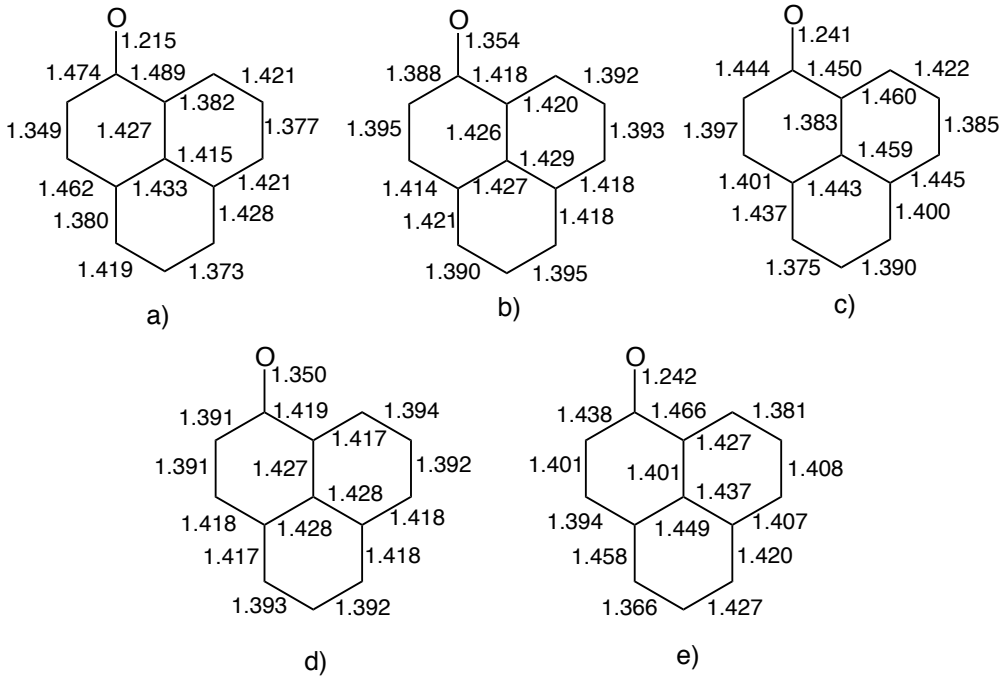

Figure 4.11: Optimized geometries calculated at CASSCF(16,15) level for a) S_0; b) $^1(n-\pi^*)_{min}$; c) $^1(\pi-\pi^*)_{min}$ (at MS-CASPT2(12,12) level) ; d) $^3(n-\pi^*)_{min}$; e) $^3(\pi-\pi^*)_{min}$. All distances in Angstroms.

Ground state

The equilibrium ground state geometry is characterized by a O_1-C_8 distance of 1.215 Å, typical of the double bond of carbonil [116]. The C_3-C_4, C_5-C_6, C_9-C_{10}, C_{11}-C_{12} and C_{13}-C_{14} distances are in a range of C-C distances closer to the double bond than to the single one.

Table 4.4: Energy (in eV) and dipolar moments (in D) obtained at CASSCF(16,15) and MS-CASPT2(16,15) level with (ANO-L) basis set. All optimitzations are done using 6-31G plus polaritzation with CASSCF(16,15) with the exception of $^1(\pi-\pi^*)$ state at MS-CASPT2(12,12) level.

Estat	CASSCF	MS-CASPT2	μ
(GS)	0	0	4.1
$^1(n-\pi*)$	2.41	2.72	1.39
$^1(\pi-\pi*)$		2.97	6.45
$^3(\pi-\pi*)$	1.88	2.12	1.47
$^3(n-\pi*)$	2.36	2.67	3.37

$^1(n-\pi^*)$ *state*

The minimum of the lowest lying singlet excited state $^1(n-\pi^*)$ is 2.72 eV more energetic than the ground state minimum. The CASSCF natural orbital occupancies confirm the $^1(n-\pi^*)$ character of the excitation; the occupancy is 1.00 for the n_O orbital and 1.002 for the π^* orbital with antibonding character over O_1 and C_8. Its electronic configuration corresponds to an open shell with two unpaired electrons, one on the n orbital of the oxygen and the other on the carbon skeleton. Consistently, the C=O bond (1.354 Å) is longer than in the ground state (1.215 Å). The decrease in the π polarization due to the longer C=O distance and the nature of the excitation induces a decrease in the dipole moment with respect to the ground state: from 4.10 D to 1.39 D. There is an electronic redistribution in the π system that delocalize the double bonds among the C_8-C_{13}-C_{14}, C_3-C_4-C_5 and C_{10}-C_{11}-C_{12} atoms. The vertical energy difference calculated from this minimum to the ground state is 1.98 eV. This transition has a very low oscillator strength, smaller than 10^{-9}, resulting in a negligible probability of fluorescence emission from this species.

$^1(\pi-\pi^*)$ *state*

As explained previously, an accurate description of the bright $^1(\pi-\pi^*)$ state is only possible at the MS-CASPT2 level because this state is described by a combination of the $3^1A'$ and $4^1A'$ CASSCF functions. This situation makes necessary the use of the MS-CASPT2 method, not only for the energy calculation but also for the geometry optimization. To make this calculation feasible, we performed a

symmetry constrained numerical MS-CASPT2 optimization using a (12,12) active space.

The $^1(\pi - \pi^*)$ minimum obtained (see c) of Figure 4.11) is 2.97 eV more energetic than the ground state minimum. It is characterized by a double bond C_8-O_1 distance of 1.241 Å, 0.062 Å larger than the ground states and with a reduction of the distance among the carbons adjacent to oxygen, C_6-C_8-C_{13} atoms, according to the excitation to an orbital of antibonding character between carbon and oxygen and bonding among C_6-C_8-C_{13}.

The most interesting feature of this minimum is that at this geometry, not very different from the ground state equilibrium geometry, the $^1(\pi - \pi^*)$ state is only 0.04 eV higher in energy than the $^1(n - \pi^*)$ one. In fact, to explore this area in more detail, the 3rd and 4th CASSCF A' states were also optimized, and the MS-CASPT2 energies were calculated at the geometries obtained (represented in the following by $^1(\pi - \pi^*)$-r3 and $^1(\pi - \pi^*)$-r4). These are not, in principle, critical points at the MS-CASPT2 level, but the geometries obtained were very near the MS-CASPT2 optimized minimum (geometries of $^1(\pi - \pi^*)$-r3 and $^1(\pi - \pi^*)$-r4 are collected in Figure 4.12), and the energetics produced a very interesting result for our study (Table 4.5). At these geometries, the $^1(\pi - \pi^*)$ and the $^1(n - \pi^*)$ are inverted, the first being lower in energy than the second (0.02 eV at the $^1(\pi - \pi^*)$-r4 and 0.06 eV at $^1(\pi - \pi^*)$-r3).

Table 4.5: Vertical energies (in eV relative to ground state minimum) of the two excited states at $^1(\pi - \pi^*)$, $^1(\pi - \pi^*)$-r4 and $^1(\pi - \pi^*)$-r3 geometries calculated at MS-CASPT2(16,15)/ANO-L level.

	Geometry		
State	$^1(\pi - \pi*)$	$^1(\pi - \pi*) - r4$	$^1(\pi - \pi*) - r3$
$^1(\pi - \pi*)$	2.97	3.13	3.06
$^1(n - \pi*)$	2.93	3.15	3.11

This indicates that the $^1(\pi - \pi^*)$ and the $^1(n - \pi^*)$ can be considered degenerate in this region. In this situation, the possibility of emission from the $^1(\pi - \pi^*)$ minimum must be considered. The calculated oscillator strength at this geometry, 0.19, indicates that the probability of this transition is not negligible. Thus, fluorescence emission can take place from this species. Nevertheless, to predict the intensity of this band, the lifetime for the emitting species must also be considered. If the spe-

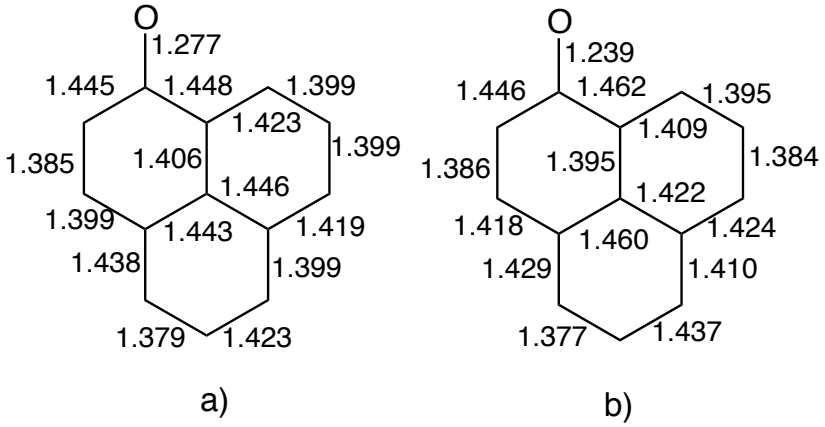

Figure 4.12: Optimized geometries calculated at CASSCF(16,15) level for: a) $^1(\pi - \pi^*) - r3$ and b) $^1(\pi - \pi^*) - r4$ states.

cies is very short-lived (equilibrium geometry described by a shallow minimum), the probability of the emission will be low. This point will be discussed in the next subsection, where the reaction paths (and their barriers) are obtained. The calculated vertical energy difference to the ground state from the $^1(\pi - \pi^*)$ minimum, of 2.75 eV, is in very good agreement with the experimental value of the fluorescence band in methylcyclohexane, 2.64 eV [93]. The vertical transition energies of $^1(\pi - \pi^*)$-r3 and $^1(\pi - \pi^*)$-r4 are 2.81 eV and 2.87 eV respectively.

As far as we know, this $^1(\pi - \pi^*)$ species had never been proposed up to now as that responsible for the fluorescence of PN. Previous studies [96] propose the emission from $^1(n - \pi*)$ state, but the emission from this species (1.98 eV given in ref. [96]), is not in good agreement with the fluorescence experimental frequency. Our results are supported by the good agreement between the experimental data of frequency of emission and the vertical energy difference provided here.

$^3(\pi - \pi^*)$ *and* $^3(n - \pi^*)$ *states*

The minima of the first and second triplet excited states, of $^3(\pi - \pi^*)$ and $^3(n - \pi^*)$ character, are at 2.12 eV and 2.67 eV respectively over the ground state minimum. The characteristics (minimum energy geometry, dipole moment, and electronic configuration) of the $^3(\pi - \pi^*)$ species are similar to those of the ground state (although some bonds in the carbon skeleton are elongated) while the $^3(n - \pi^*)$ species is similar to the $^1(n - \pi^*)$.

The bond distances of the $^3(n-\pi^*)$ minimum are similar to those of the $^1(n-\pi^*)$ minimum, with a C_8-O_1 distance of 1.350 Å. The CASSCF natural orbital occupancies are similar to those of the $^1(n-\pi^*)$ minimum, so the $^3(n-\pi^*)$ state can be described, like $^1(n-\pi^*)$, as an open shell state.

On the other hand the minimum $^3(\pi-\pi^*)$ is characterized by orbital occupancies that differ from the ground state in a major occupancy of the antibonding orbitals leading to an increase of the carbon ring distances and mantaining, like the ground state, a C_8-O_1 distance (of 1.242 Å) characteristic of a double bond.

Concerning luminescent deactivation, according to Kasha's rules, it will take place from the first triplet excited state. The emission energy from the $^3(\pi-\pi^*)$ minimum is calculated to be 1.72 eV, which concurs well with the experimental data of 1.70-1.91 eV for the phosphorescence of PN in cyclohexane [93] and methylcyclohexane-ethyliodide [94]. Also in this case the similar dipole moments of the states involved in the transition (3.70 D for the ground state and 3.37 D for the $^3(\pi-\pi^*)$), makes possible the comparison of the theoretical results (in gas phase), with the experimental data, measured in low polar solvents. The comparison with the previous TD-DFT prediction, of 1.52 eV [96], differs both from our results and from the experimental data.

In order to analyse the band intensity, we also calculated the electronic transition dipole moment of spin-mixed states obtaining a SOC lower than $10^{-3}\ cm^{-1}$ and a transition oscillator strength lower than 10^{-8}, which explain the weakness of the phosphorescence band of PN.

It is interesting to compare the geometrical parameters obtained with the TD-DFT ones reported in reference [96]. The ground state geometry obtained in both works is almost identical, with differences in the bond distances on the order of 0.01 Å. The changes in the geometries when PN is excited follow the same trends in both works; however, whereas the changes are the same for the states with $(\pi-\pi^*)$ character (the excited geometries are as similar as those of the ground state), in the case of the states with $(n-\pi^*)$ character, the changes in CASSCF geometries are, in general, larger. The largest divergence, of approx. 0.05 Å, appears in the C-O bond distance. Despite the small geometry differences for the $(\pi-\pi^*)$ states, the energy differences of these species are the most significant.

In general, the comparison with the available experimental data supports the

veracity of the obtained equilibrium geometries.

4.3.3 Reaction mechanims

The results from the previous sections suggest possible reaction paths for the photochemistry of phenalenone that are explored in this section. The corresponding calculations and the conclusions are presented here. The schematic profile of the low-lying PES of PN is shown in Figure 4.13 and the scheme of possible reaction paths outlined in Figure 4.14. They were drawn to help explaining this part of the study. In Figure 4.14 the energetics is also collected; the data associated with the arrows correspond to the barriers of the processes (relative to the preceding species), whereas the data below the species are the energies relative to the ground state minimum. The bold arrows indicate the most probable events.

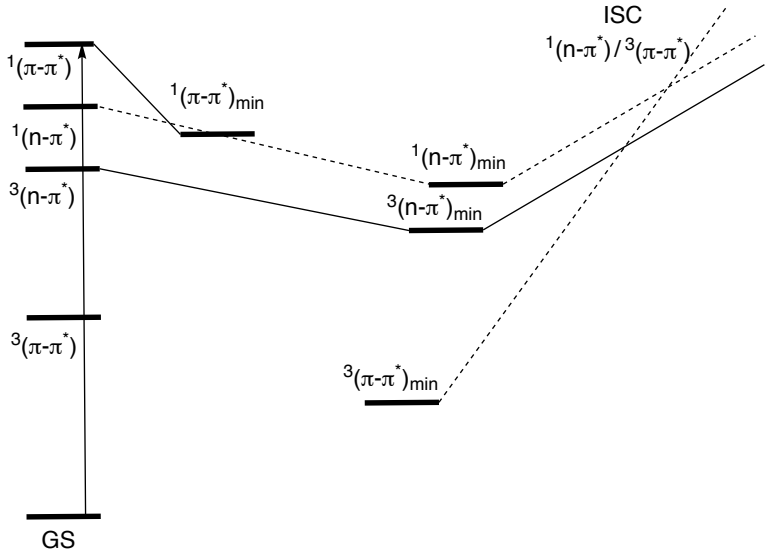

Figure 4.13: Schematic profile of the low-lying PES of the phenalenone.

First steps of deactivation

As stated earlier, the initial absorption populates the $^1(\pi - \pi^*)$ state. At this point, several processes are possible, represented by A, B and C in Figure 4.14. Let's analyse them one by one.

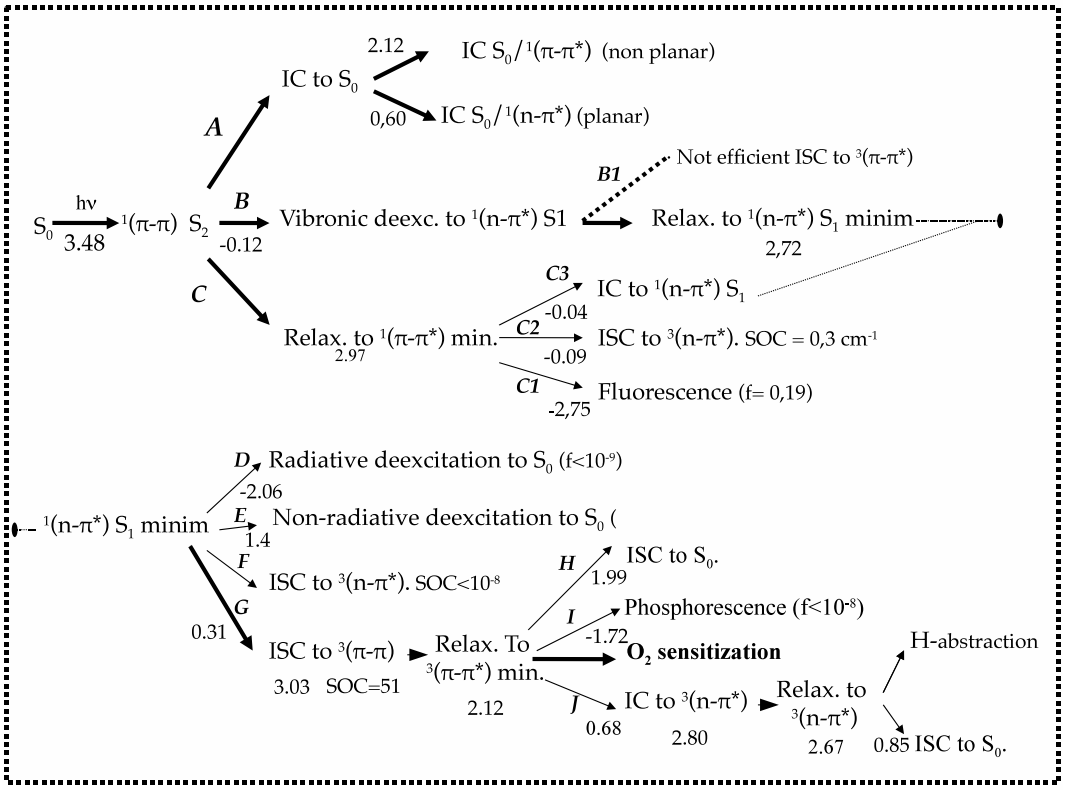

Figure 4.14: Schematic representation of the possible photoprocesses of PN.

PATH A – First, we have considered the possibility of non-radiative deactivation via IC to the ground state (path A in Figure 4.14). To investigate this possibility, we looked for CIs between the ground and the first excited state.

An useful information about the potential energy surface topology can be obtained from the analysis of the electronic configurations of the states that can be involved in the CI. The different assignement of occupied orbitals correspond to different electronic configurations and description of states. Based on the comparison of the orbitals occupied on the $(\pi - \pi^*)$ and the ground states, it is expected to find the same energy for both states where the orbitals π and π^* have similar energies.This is favored by the torsion of the π orbitals or by enlarging the bond distances. Previous studies of our group in other cyclic systems suggest that this degenerancy can be achived more easily with the torsion of the π orbitals at no planar structures. Thus the $S_0/^1(\pi - \pi^*)$ IC was looked for without symmetry restrictions, using a (12,12) active space selected as explained in the computational details.

A conical intersection was found between the ground and the $^1(\pi - \pi^*)$ state at a geometry with a bend phenyl ring and a non-conjuged C-O bond of 1.180 Å of length similar to that of the C-O bond of carbon monoxide (Figure 4.15). Table 4.6 shows the most relevant CSF of the CASSCF and PM-CAS-CI wave functions of the $\pi - \pi^*$ state at this geometry. The $^1(\pi - \pi^*)$ CASSCF state in this CI have only a contribution of 0.76 of $|2\rangle$, like the PM-CAS-CI wave function of the bright state at the FC zone.

It is interesting to point out that, at non planar structures, CASSCF states do not mix at MS-CASPT2 level, as shown in Table 4.7. It can be due to the lost of degenerancy between different electronic $\pi - \pi^*$ valence electronic configurations in non planar distorsioned geometries at CASSCF level. Then the description of the lowest $(\pi - \pi^*)$ state is the same at the CASSCF and at the MS-CASPT2 level. Therefore, the geometry of the lowest energy point of this CI, optimized at the CAS-SCF level, is reliable enough. The energy of this structure, 5.28 eV over the ground state minimum (calculated at the MS-CASPT2(12,12) level), makes this deactivation path inaccessible.

Table 4.6: Most relevant CSF of CASSCF and PM-CAS-CI wave functions at the $S_0/^1(\pi - \pi^*)$ CI optimized geometry.

Method	CSF	coeficient
CASSCF	|2>	0.78
MS-CASPT2	|2>	0.78

Table 4.7: Eigenvalues (in Hartree) and eigenvectors of the effective hamiltonian matrix of the 5 A′ low-lying MS-CASPT2(12,12) states, at the $S_0/^1(\pi - \pi^*)$ CI geometry.

	6-31G*			
States	$1^1A'$ (GS)	$2^1A'$	$3^1A'$	$4^1A'$
	Eigenvectors			
$1^1A'$ (GS)	0.9606	0.1848	0.2030	0.0100
$2^1A'$	0.1691	0.9801	-0.0913	0.0454
$3^1A'$	0.0428	-0.0358	0.1846	0.9811
$4^1A'$	-0.2149	-0.0608	-0.9116	0.1755
$5^1A'$	0.0226	0.0105	0.2918	0.0659

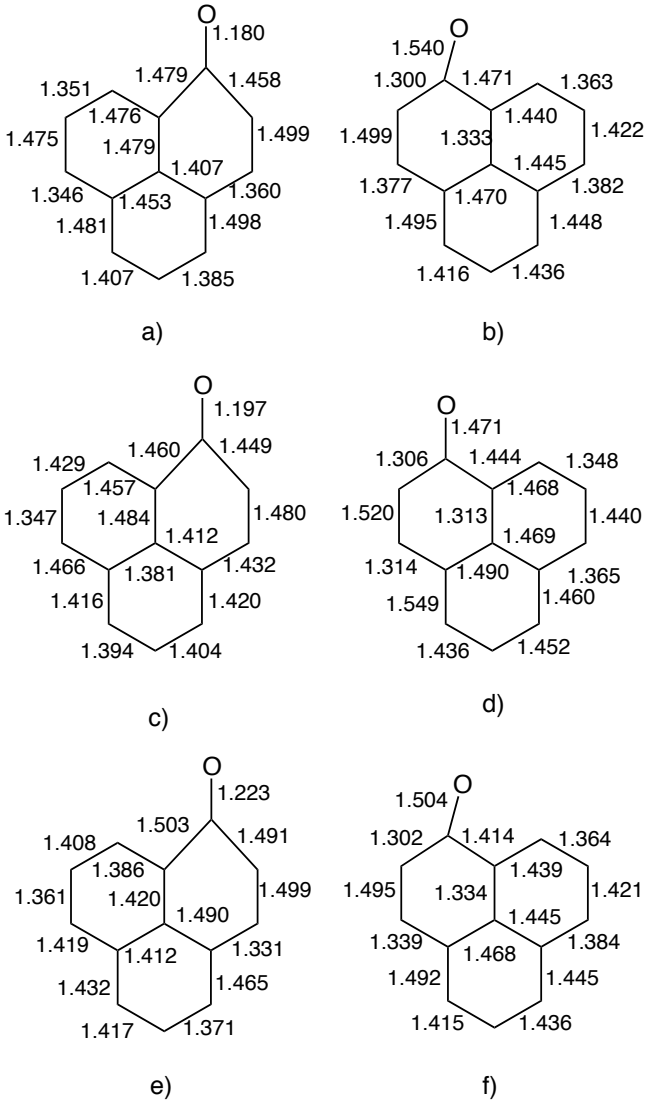

Figure 4.15: Geometries of S_0/S_1 conical intersections and $S_0/$ T1 ISC. a) $S_0/^1(\pi - \pi^*)$ non-planar CI ; b) $S_0/^1(n - \pi^*)$ planar CI; c) $S_0/^3(\pi - \pi^*)$ non-planar ISC; d) $S_0/^3(\pi - \pi^*)$ planar ISC; e) $S_0/^3(n - \pi^*)$ non-planar ISC; f) $S_0/^3(n - \pi^*)$ planar ISC

On the other hand, when the CI was looked for under *Cs* symmetry restrictions, a planar CI between the ground and the $(n - \pi^*)$ state was located (geometry shown in Figure 4.15). It is characterized by a enlarged C-O distance of 1.504 Å, that destabilizes $^1(\pi - \pi^*)$, $^1(n - \pi^*)$ and ground states. The energy of this crossing, 4.08 eV relative to the ground state minima, is 0.60 eV above the initial excitation indicating that the probability of this process is very low.

To investigate the possibility of an ISC at these first stages of the reaction, we calculated the SOC between the singlet at triplet excited states at the FC geometry. The values obtained were in all cases smaller than 10^{-8} cm^{-1}, what rules out any ISC at this region.

PATH B – After the population of the $^1(\pi - \pi^*)$ state by the photoexcitation at the FC region, another possible path is a direct deexcitation to the $^1(n - \pi^*)$ state, more stable by only 0.12 eV, via vibronic coupling due to the fact that vibrational transitions are faster than nuclear movements.

If this happens, once on the $^1(n - \pi^*)$ surface, neither the non-radiative nor the radiative deexcitation to the ground state are fast processes due to the large energy difference and the small oscillator strength between these two states. Consequently, the system will preferentially relax towards a more stable geometry on this surface, if it were accessible (B1 in Figure 4.14). To corroborate the accessibility of path B1, the minimum energy path (MEP) from the FC zone on the $^1(n - \pi^*)$ PES was calculated. It shows a barrierless path that leads directly to the $^1(n - \pi^*)$ minimum enlarging the C-O distance from 1.215 Å to 1.355 Å, turning out the double bond in a single bond.

During the relaxation pathway, the system can cross with the triplet states PES producing a possible intersystem crossing. To take into account or rule out this possibility, the energy of the $^3(\pi - \pi^*)$ state along the MEP was also calculated, together with the spin orbit coupling of those states.

Along the MEP, the curves $^1(n - \pi^*)$ and $^3(\pi - \pi^*)$ do not cross and the SOC values are below 10^{-8} along the entire path indicating that an intersystem crossing to the $^3(\pi - \pi^*)$ will not occur along this process, and the minimum $^1(n - \pi^*)$ could be populated.

PATH C – Another alternative exists: the immediate relaxation over the $^1(\pi - \pi^*)$, which will lead to the $^1(\pi - \pi^*)$ minimum. From this point, again, there are several competing reactions. Vertical energies of some closer excited states are showed in Table 4.8. One possibility is that the system decay radiatively to the ground state, emitting fluorescence (C1 in Figure 4.14). As seen before, the probability of this decay is not negligible (oscillator strength 0.19), but the actual occurrence will depend on the lifetime of the emitting species that, from the point of view of

the topology of the PES, is related to the height of the barriers of the paths leaving the $^1(\pi - \pi^*)$ minimum.

Table 4.8: Vertical energies (relative to ground state minimum) of four excited states at $^1(\pi - \pi^*)$ geometry calculated at MS-CASPT2(16,15)/ANO-L level.

State	$^1(\pi - \pi*)$
$^1(\pi - \pi*)$	2.97
$^1(n - \pi*)$	2.93
$^3(n - \pi*)$	2.88
$^3(\pi - \pi*)$	2.14

One of them is the intersystem crossing to the triplet manifold (C2 in Figure 4.14). We calculated the SOC between the $^1(\pi - \pi^*)$ and the $^3(n - \pi^*)$ states at the F. C. region and at the $^1(\pi - \pi^*)$ minimum. The obtained values, smaller than 10^{-8} cm^{-1} and 0.3 cm^{-1}, respectively, and a difference energy of 0.09 eV between $^3(n - \pi*)$ and $^1(\pi - \pi^*)$ in the $^1(\pi - \pi^*)$ minimum indicate that this ISC will not be the most probable process at this stage.

We also must consider a possible IC to the $^1(n - \pi^*)$(C3 in Figure 4.14). Considering that at the r3 and r4 geometries the $^1(\pi - \pi^*)$ state is lower in energy than the $^1(n - \pi^*)$ state, it is clear that the $^1(\pi - \pi^*)$ minimum is surrounded by an extensive conical intersection between these singlet states. The small energy difference between the $^1(\pi - \pi^*)$ minimum and the r3 and r4 geometries indicates that this CI is very accessible and, being the minimum of the $^1(n - \pi^*)$ state more stable by 0.25 eV that the $^1(\pi - \pi^*)$ one, the IC will be by far the most probable process for PN at this stage. The accessibility of this path predicts a short lifetime for the $^1(\pi - \pi^*)$ species; thus, despite the large oscillator strength to the emission to the ground state, the fluorescence quantum yield for this emission is predicted to be very low. This is in good agreement with the low fluorescence quantum yield of 10^{-4} derived from experimental measurements reported in ref. [11].

Population of triplet states

Once the system is on the $^1(n - \pi^*)$ minimum, which is attained through path B1 or through path C3, it can evolve again along different paths. The probability of radiative deactivation (D in Figure 4.14), as demonstrated earlier, is very low due to the small value of the oscillator strength (smaller than 10^{-9}). Radiationless

deactivation from this minimum to the ground state (E in Figure 4.14), as stated above, is also ruled out due to the high energy barrier of 1.40 eV relative to the minimum that is necessary to overcome to reach the CI with the ground state.

Considering the experimental evidence that the formation of triplet PN is very efficient and based on theoretical considerations, the most effective pathway must be the deactivation from the $^1(n-\pi^*)$ to a triplet state through a crossing point where the SOC between these states must be large.

In order to find the points with this characteristics, STC optimization were run between $^1(n-\pi^*)$, $^3(\pi-\pi^*)$ and $^3(n-\pi^*)$ and calculations with the RASSI protocol were realized to obtain the SOC values.

A point of degenerancy between the $^1(n-\pi^*)$ and $^3(\pi-\pi^*)$ states (STC) was located near the $^1(n-\pi^*)$ minimum. The geometry depicted in Figure 4.16 a) is the point of minimum energy of the hypersurface of dimension 3N-7 (because H_{12} is equal to zero by spin symmetry). This geometry is located at 3.03 eV above the ground state and only 0.31 eV above the $^1(n-\pi^*)$ minimum. The necessary distorsion that takes the system from $^1(n-\pi^*)$ minimum to the STC is mainly elongation of the C=O bond from 1.355 Å to 1.393 Å, and in the carbon eskeleton the most notable difference is the C_1-C_2 bond distance of 1.388 Å that decreases to 1.378 Å. These geometrical changes destabilize more the $^3(\pi-\pi^*)$ state than the $^1(n-\pi^*)$ state, reducing the $^1(n-\pi^*)$ -$^3(\pi-\pi^*)$ energy gap and opening the ISC channel (G in Figure 4.14).

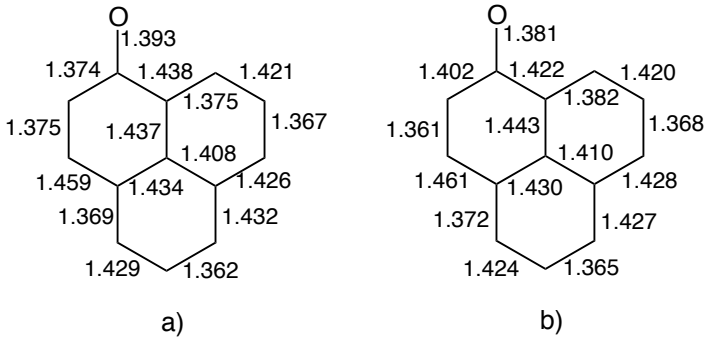

Figure 4.16: Optimized geometries obtained at the CASSCF(16,15) level for a) $^3(\pi-\pi^*)/^1(n-\pi^*)$ STC and b) $^3(\pi-\pi^*)/^3(n-\pi^*)$ CI . All distances in Angstroms.

This point of degenerancy is energetically accessible, but corresponds to a real crossing, and do not allow, if the states do not really interact, the population of

the triplet state. The value obtained for the SOC at this STC point, of 51 cm^{-1}, is large for this kind of organic systems. The new wave function of the state of lower energy obtained taken into account the SOC is a linear combination of the former wave functions with similar weights. It indicates that the crossing in fact becomes avoided and that there exists an adiabatic path from the $^1(n-\pi^*)$ minimum, passing through a TS, to the $^3(\pi-\pi^*)$ surface. This means that the path for the ISC is open and the probability of producing an ISC is high.

In contrast, no crossing point was found between the $^1(n-\pi^*)$ and $^3(n-\pi^*)$ states. These surfaces remain parallel in this region due to their similar electronic configurations, which differ only in the spin coupling of two electrons in different regions of the space. Moreover, to know the probability of a direct $^1(n-\pi^*) \rightarrow {}^3(n-\pi^*)$ ISC, we calculated the SOC between both states at their minimum energy geometries. The values obtained were smaller than 10^{-8} (in agreement with El-Sayed rules), what rules out, at this level of calculation, the existence of an ISC to the $^3(n-\pi^*)$ state (path F in Figure 4.14).

The topology of the surfaces of the $^1(n-\pi^*)$, $^3(\pi-\pi^*)$ and $^3(n-\pi^*)$ states determined at the CASSCF level in this region must be confirmed using calculations in which the dynamic correlation is considered. For this reason, we calculated the CASPT2 energy profiles of the $^1(n-\pi^*)$, $^3(\pi-\pi^*)$ and $^3(n-\pi^*)$ states along a path interpolated between the $^1(n-\pi^*)$ minimum and the optimized crossing point. The results are plotted in Figure 4.17.

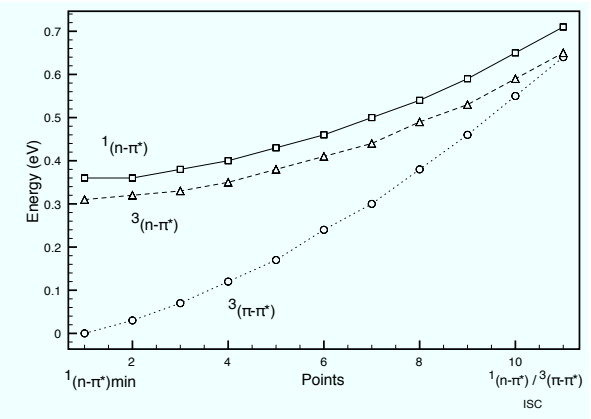

Figure 4.17: Energy profiles of the $^3(\pi-\pi^*)$, $^3(n-\pi^*)$ and $^1(n-\pi^*)$ PES linearly interpolated between the $^1(n-\pi^*)$ minimum and the $^3(\pi-\pi^*)/^1(n-\pi^*)$ STC. Energies calculated at the CASSCF(12,12)/CASPT2/6-31G(d) level.

The characteristics of the ISC path are the same at the CASPT2 level as those found at the CASSCF level. When the energies of the $^1(n-\pi^*)$, $^3(\pi-\pi^*)$ and $^3(n-\pi^*)$ states are calculated at the CASPT2(16,15) level at the STC point optimized at the CASSCF level, it is found that these three states are still practically degenerate. The energy of this point, 0.31 eV above the $^1(n-\pi^*)$ minimum (MS-CASPT2(16,15)/ANO-L value), is an upper bound for the value of the barrier to the ISC. This low barrier indicates that the ISC is, in fact, accessible considering the remaining excitation energy, so the population of the $^3(\pi-\pi^*)$ must be very efficient. Due to the triple degeneracy found, we calculated the spin orbit interaction between $^1(n-\pi^*)$, $^3(\pi-\pi^*)$ and $^3(n-\pi^*)$. The resulting spin orbit states, shown in Table 4.9, confirm the efficiency of the $^1(n-\pi^*)/^3(\pi-\pi^*)$ ISC and definitively rule out the ISC to the $^3(n-\pi^*)$ state. The population of the $^3(\pi-\pi^*)$ via ISC will be the preferentially followed path.

Table 4.9: Spin orbit states resulting from the spin orbit interaction of the $^3(\pi-\pi^*)$, $^3(n-\pi^*)$ and $^1(n-\pi^*)$ states at the minimum energy point of the $^3(\pi-\pi^*)/^1(n-\pi^*)$ STC.

Spin orbit States	Spin free states $^1(n-\pi^*)$	$^3(n-\pi^*)$	$^3(\pi-\pi^*)$
		weights	
1	0.0085	0.9915	0.0000
2	0.0085	0.9915	0.0000
3	0.0000	1.0000	0.0000
4	0.4998	0.0000	0.5002
5	0.0000	0.0085	0.9915
6	0.0000	0.0085	0.9915
7	0.5002	0.0000	0.4998

On the $^3(\pi-\pi^*)$ surface, the system will relax again to reach the minimum energy structure on this state. The $^3(\pi-\pi^*)$ species is considered to be responsible for the molecular oxygen sensitisation, and we have shown above that its minimum is efficiently populated. To determine if this species is also long-lived (another condition necessary to be an effective sensitiser), we must also study the possible competitive reaction paths from this minimum to corroborate that there is no effective depopulation mechanism.

First, we looked for possible ISC to the ground state to analyse the possibility

of a radiationless deactivation (Path H in Figure 4.14). We found two minimum energy points on the STC with the ground state which geometries are depicted in Figure 4.15. One of them is a planar structure with a large 1.471 Å C-O distance and shorter distances than the ground state minimum in C_8-C_{13}, C_{14}-C_9, C_2-C_3 and C_4-C_5. The second structure is a non planar minimum characterized by a C-O distance of 1.197 Å similar to the C-O double bond, and the bend of the C_6-C_8-C_{13} atoms. The energies of these crossing points of 4.11 eV for the planar structure and 4.41 eV for a bent one are significantly higher than the initial vertical excitation, so these deactivation paths can be ruled out.

Another possible process from the $^3(\pi - \pi^*)$ minimum is phosphorescence (path I in Figure 4.14). As we have mentioned above, the small oscillator strength of this transition (less than 10^{-8}) predicts a very low quantum yield for phosphorescence, in agreement with the low intensity found experimentally [94]. Consequently, we predict a large lifetime of the $^3(\pi - \pi^*)$ species that provides the capacity of interacting with molecular oxygen.

Finally, due to the interesting feature shown by the profiles in Figure 4.17 that show that the $^3(\pi - \pi^*)$ and $^3(n - \pi^*)$ states are degenerate and the participation of the $^3(n - \pi^*)$ state in hydrogen abstraction reactions, we looked for a conical intersection between both triplet states. The CI originated is in fact a real crossing for planar geometries, given that in this case the $^3(\pi - \pi^*)$ and $^3(n - \pi^*)$ have different spatial symmetry (A' and A''). Consequently H_{12} is equal to zero and the dimension of the degeneracy subspace is 3N-7.

It is interesting to point out that in the case of PN, the adiabatic path that there exist in the surroundings of any CI must run along non planar geometries. The reason is that the avoided crossing that creates the adiabatic path appears when H_{12} is different from zero, and in this case it will only happen when the $^3(\pi - \pi^*)$ and $^3(n - \pi^*)$ states will not belong to different spatial symmetries (A' and A''), i.e., when the system looses the planarity. But the evolution of the system from the initial excitation is expected not to loose the planarity, so the system will not have kinetic energy accumulated in the out of plane movements and the internal conversion from the $^3(\pi - \pi^*)$ to the $^3(n - \pi^*)$ is expected to happen through the CI. We located the minimum energy point of degeneracy between these two surfaces at the CASSCF level. Its geometry is depicted in Figure 4.16 *b*) and has an energy of 2.80 eV above the ground state.

The relative population of the triplets depends (without taken into account dynamic aspects) on the thermodynamic equilibrium between both minima. The $^3(\pi-\pi^*)$ minimum is 0.55 eV more stable than the $^3(n-\pi^*)$ one, the barrier of the non-adiabatic pathway from $^3(n-\pi^*)to^3(\pi-\pi^*)$ is of 0.13 eV high and for the reverse process is 0.68 eV. Therefore the equilibrium is displaced towards the $^3(\pi-\pi^*)$, although the population on the $^3(n-\pi^*)$ minimum (path J on Figure 4.14) is possible under certain circumstances.

These results show that the $^3(\pi-\pi^*)$ is not only the most stable excited species but that it is also characterized by a deep well surrounded by relatively high barriers (0.81 eV to the ISC, 0.68 eV to the IC), which makes the $^3(\pi-\pi^*)$ species long-lived and explains the fact that PN has a large quantum yield for the sensitisation of singlet oxygen [117] formed from the $^3(\pi-\pi^*)$ state.

Radiationless deactivation pathways from the $^3(n-\pi^*)$ minimum were also explored. We found two minimum energy points of degeneracy with the ground state (Figure 4.15 e) and f)), one with a planar structure, 4.08 eV $^3(\pi-\pi^*)$ high and a non planar one, 3.52 eV high. In this case the non planar STC is less energetic than the planar one despite the rigidity of the system, probably due to the very long C-O distance, 1.50 Å, of the planar structure. Anyway these energies are high enough to ruled out a radiationless deactivation from the $^3(n-\pi^*)$ state. The radiative deactivation is neither possible: according Kasha's rules this state is not the first triplet excited state and have low probability of emission as shown by its low oscillator strength for the transition to ground state. PN in its $^3(n-\pi^*)$ state is then capable of abstracting hydrogen from the solvent, as suggested by previous experimental studies [97].

It is interesting to analyse the observed dependency on the temperature of the extension of the H-abstraction reaction, i.e., the dependence on the temperature of the population of the $^3(n-\pi^*)$ [95], as opposed to the population of the $^1(n-\pi^*)$ minimum, which is not temperature dependent. After the initial excitation of 3.48 eV, the highest energy point on the path to the $^1(n-\pi^*)$ minimum is the S_1/T_1 ISC, located at 3.03 eV relative to the ground state minimum, whereas the barrier between the $^3(n-\pi^*)$ and the $^3(\pi-\pi^*)$ minimum is only 2.80 eV. In principle, the latter process should not be temperature-dependent. However, another factor different from the absolute energies should be taken into account, i.e., the dispersion of energy of the excited PN to the environment and the relative barriers of

the processes. The molecules in high vibrational states are "hot" molecules that are not in thermodynamic equilibrium with he environment. In these case, the release of energy to the surroundings is in the form of "fast" heat with a vibrational relaxation of about 10^{-11} seconds [11]. The processes that lead to the $^3(\pi - \pi^*)$ population are all fast events, and the intermediate species $^1(\pi - \pi^*)$ and $^1(n - \pi^*)$ have very short lifetimes because their minima are very shallow. At these stages "fast" heat represents only a small proportion of the excess of excitation energy. On the other hand, the $^3(\pi - \pi^*)$ species has an appreciable lifetime [118] and therefore thermal equilibration via vibrational relaxation can occur during the lifetime of these species, loosing the system its excess excitation energy. The surmounting of the subsequent barrier to reach the $^3(n - \pi^*)$ surface, then, must be thermally activated and becomes temperature-dependent.

4.4 Summary

The computational study by means of *ab initio* calculations presented here explains the photophysical and photochemical processes that make phenalenone a very efficient singlet oxygen sensitizer. From the mechanistic point of view, the features of the PES of the states involved in the photoreactivity of PN provide a sound basis to make a hypothesis about the different steps of the mechanism for populating the triplet state responsible for sensitizing singlet oxygen. In addition, the magnitudes found are comparable with experimental data, which supports the veracity of the mechanism proposed in this study. This mechanism can be summarized as follows:

- Excitation to the $^1(\pi - \pi^*)$ state by means of the initial absorption. The theoretical data of 3.48 eV agrees with the experimental data of 3.46 eV.

- Possible geometrical relaxation over the $^1(\pi - \pi^*)$ PES to a minimum energy point. The radiative deexcitation from this minimum is calculated to be allowed (oscillator strength of 0.19, emission energy 2.75 eV), but the short lifetime of this species predicts a low probability of luminescence. Our results are in good agreement with the experimental data of 2.64 eV for the emission energy and a quantum yield of fluorescence of 10^{-4}.

- Deactivation via an IC to the $^1(n-\pi^*)$ state at a geometry near the $^1(\pi-\pi^*)$ minimum in an almost barrierless process.
- ISC to the $^3(\pi-\pi^*)$ state through an avoided crossing only 0.31 eV above the $^1(n-\pi^*)$ minimum. Due to the low barrier and high SOC this ISC is predicted to be very efficient.
- Geometrical relaxation over the $^3(\pi-\pi^*)$ PES to the nearest minimum. Phosphorescence from this minimum is predicted to show a wavelength of 1.72 eV, in agreement with the experimental data of 1.70 eV.
- Possible internal conversion to the $^3(n-\pi^*)$ PES. This channel explains the PN's capacity of hydrogen abstraction as this reaction is triggered from the $^3(n-\pi^*)$ state. The equilibrium between both triplet species will depend on the temperature, given that the $^3(\pi-\pi^*)$ minimum is long-lived enough to reach the thermal equilibrium with the environment, loosing the excess of excitation energy.
- Radiationless deactivation processes are ruled out on the basis of the high energies of the crossings between the excited states with the ground state.

The high efficiency of the mechanism of $^3(\pi-\pi^*)$ population and the low efficiency of the processes of deactivation from this minimum explain why PN is so suitable as a singlet oxygen sensitizer. From the computational point of view, the CASSCF/CASPT2 protocol proved to be suitable for conducting such a study. It was shown that the interaction of states must be included via dynamic correlation (in the multi-state CASPT2 calculations) if the excited states of phenalenone are to be accurately described.

A1 Appendix: Description of electronic states

In these preliminary study the number of states considered was 8 for the $^1(\pi-\pi^*)$ states, 2 for $^1(n-\pi^*)$ states, 2 for $^3(n-\pi^*)$ states and 3 for $^3(\pi-\pi^*)$ states. The energies at the FC geometry at the CASSCF, SS-CASPT2 and MS-CASPT2 level using 6-31G* basis set, (used for geometry optimizations) and ANO-L basis set (used to refine energies at the critical points obtained) are shown in Table 4.10.

Table 4.10: Vertical energies (in eV) CASSCF and MS-CASPT2 using a 6-31G plus polarization and ANO-L basis set. The state with the highest oscillator strengths is in bold.

	6-31G*		ANO-L	
State	CASSCF	MS-CASPT2	CASSCF	MS-CASPT2
$1^1A'$(GS)				
$2^1A'$	**3.97**	**3.57**	**3.93**	**3.30**
$3^1A'$	4.94	4.07	4.87	4.00
$4^1A'$	5.34	4.92	5.26	4.78
$5^1A'$	5.67	5.27	5.61	5.20
$6^1A'$	5.78	5.88	5.72	5.80
$7^1A'$	6.48	6.3	6.43	6.07
$8^1A'$	6.72	6.51	6.65	6.42
$1^1A''$	3.09	3.28	3.25	3.29
$2^1A''$	5.55	5.61	5.68	5.60
$1^3A'$	2.37	2.57	2.36	2.56
$2^3A'$	3.52	3.72	3.50	3.68
$3^3A'$	4.00	4.01	3.97	3.93
$1^3A''$	3.13	3.27	3.12	3.22
$1^3A''$	5.65	5.81	5.61	5.71

The ordering of states in the FC zone is the same with both basis sets, but the energy difference between the first singlet excited states of A' and A'' symmetry is 0.29 eV with the 6-31G* basis set while it reduces to 0.01 eV with the ANO-L basis set, so the $(\pi-\pi^*)$ is more stabilized with the latter basis set. This correction is significant enough to indicate that it is convenient to refine the energetics of our results with the ANO-L basis set. On the other hand, the analysis of the correlated wave functions shows the same trends in both basis set, reason why we can consider the qualitative description of different states at MS-CASPT2/6-31G* level accurate

enough.

To study the possible interaction between CASSCF states, PM-CAS-CI wave functions obtained in the MS-CASPT2 treatment are analysed separately for $^1(\pi - \pi^*)$, $^1(n - \pi^*)$, $^3(\pi - \pi^*)$ and $^3(n - \pi^*)$ states (see Tables 4.11, 4.12 , 4.13 and 4.14).

Table 4.11: Eigenvectors of the diagonalization of the effective Hamiltonian matrix in the MS-CASPT2 treatment with an state average of 2 $^1(n - \pi^*$ states. Large values in bold.

	6-31G*		ANO-L	
States	$1^1A''$	$2^1A''$	$1^1A''$	$2^1A''$
$1^1A''$	**0.9988**	0.0483	**0.9997**	-0.0242
$2^1A''$	0.0483	**0.9988**	0.0242	**0.9997**

Table 4.12: Eigenvectors of the diagonalitzation of the effective Hamiltonian matrix in the MS-CASPT2 treatment with an state average of 2 $^3(n - \pi^*$ states.

	6-31G*		ANO-L	
States	$1^3A''$	$2^3A''$	$1^3A''$	$2^3A''$
	Eigenvectors			
$1^3A''$	0.9996	0.0278	0.9994	0.0333
$2^3A''$	0.0277	0.9996	0.0333	0.9994

Table 4.13: Eigenvectors of the diagonalitzation of the effective Hamiltonian matrix in the MS-CASPT2 treatment with an state average of 3 $^3(\pi - \pi^*$ states.

6-31G*

States	$1^3A'$	$2^3A'$	$3^3A'$
	Eigenvectors		
$1^3A'$	0.9985	-0.0545	-0.0008
$2^3A'$	0.0545	0.9984	0.0055
$3^3A'$	0.0005	-0.005	0.9999

ANO-L

States	$1^3A'$	$2^3A'$	$3^3A'$
	Eigenvectors		
$1^3A'$	0.9982	0.0604	0.0009
$2^3A'$	-0.0604	0.9982	-0.0020
$3^3A'$	-0.0010	0.0019	0.9999

Table 4.14: Eigenvectors of the diagonalization of the effective Hamiltonian matrix in the MS-CASPT2 treatment with an state average of 8 $^1(\pi - \pi^*)$ states. Largest values in bold.

6-31G*

States	$1^1A'$ (GS)	$2^1A'$	$3^1A'$	$4^1A'$
		Eigenvectors		
$1^1A'$ (GS)	**0.996**	-0.083	-0.005	0.003
$2^1A'$	-0.009	-0.157	**0.984**	0.068
$3^1A'$	-0.053	**-0.538**	-0.065	**-0.627**
$4^1A'$	0.062	**0.771**	0.130	-0.286
$5^1A'$	-0.013	-0.116	-0.093	**0.664**
$6^1A'$	-0.034	-0.136	-0.030	0.279
$7^1A'$	-0.002	-0.091	-0.033	-0.004
$8^1A'$	-0.009	0.213	0.007	0.045

ANO-L

States	$1^1A'$ (GS)	$2^1A'$	$3^1A'$	$4^1A'$
		Eigenvectors		
$1^1A'$ (GS)	**0.996**	-0.083	-0.005	0.003
$2^1A'$	-0.009	-0.157	**0.984**	0.068
$3^1A'$	-0.053	**-0.538**	-0.065	**-0.627**
$4^1A'$	0.062	**0.771**	0.130	-0.286
$5^1A'$	-0.013	-0.116	-0.093	**0.664**
$6^1A'$	-0.034	-0.136	-0.030	0.279
$7^1A'$	-0.002	-0.091	-0.033	-0.004
$8^1A'$	-0.009	0.213	0.007	0.045

The results of $^1(n - \pi^*)$, $^3(\pi - \pi^*)$ and $^3(n - \pi^*)$ show small extradiagonal terms in the effective Hamiltonian matrix of the MS-CASPT2 treatment and coefficients close to one in the diagonal terms. Therefore, these states do not interact and can be described correctly at the CASSCF level. On top of that, for the singlet and triplet states of A" symmetry, the second excited states are much higher in energy than the irradiative energy (5.60 eV the $^1(n - \pi^*)$ state and 5.71 eV the $^3(n - \pi^*)$ state). For these reasons, only one A" state was included in the study in both cases. On the other hand the three lowest triplet states of A' symmetry show very small energy difference, not much higher than the lowest singlet A' state. Consequently although not interaction was observed in the PM-CAS-CI wave function, three of the $^3(\pi - \pi^*)$ states were included in the CASSCF calculations.

A different case is that of the $^1(\pi - \pi^*)$ states that interact via the total Hamilto-

nian giving place to PM-CAS-CI wave functions that are linear combination of SA-CASSCF ones. For these reason, to accurately describe the $^1(\pi - \pi^*)$ states, it is necessary to include higher excited states and to use the MS-CASPT2 treatment in the description of the lowest $^1(\pi - \pi^*)$ state.

To determine the optimum number of CASSCF states to be averaged, test calculations were run at the ground state geometry, including 5, 6 ,7 and 8 roots with contracted ANO-L basis type (Tables 4.15, 4.16 and 4.14).

Table 4.15: Eigenvalues (in Hartrees) and eigenvectors of the effective Hamiltonian matrix of the 5 low-lying MS-CASPT2 states obtained with state average of 5 and 6 states.

5 average states

State		$1^1A'$ (GS)	$2^1A'$	$3^1A'$	$4^1A'$	$5^1A'$
Eigenvalues		-573.93820	-573.81020	-573.79131	-573.76223	-573.74126
		Eigenvectors				
$^1A'$	GS	0.9948	-0.0986	-0.0022	-0.0164	-0.0157
$^1A'$	$2\,^1(\pi - \pi^*)$	-0.0122	-0.1582	0.9799	0.1135	-0.0390
$^1A'$	$3\,^1(\pi - \pi^*)$	-0.0811	-0.6432	-0.0509	-0.6173	-0.4426
$^1A'$	$4\,^1(\pi - \pi^*)$	-0.0577	-0.7304	-0.1436	0.3988	0.5322
$^1A'$	$5\,^1(\pi - \pi^*)$	0.0138	0.1337	0.1279	-0.6682	0.7203

6 average states

State		$1^1A'$ (GS)	$2^1A'$	$3^1A'$	$4^1A'$	$5^1A'$
Eigenvalues		-573.93826	-573.8109	-573.79116	-573.76214	573.74558
		Eigenvectors				
$^1A'$	GS	-0.9944	-0.1023	-0.0023	-0.0122	-0.0204
$^1A'$	$2\,^1(\pi - \pi^*)$	0.0111	-0.1431	0.9834	0.1037	-0.0188
$^1A'$	$3\,^1(\pi - \pi^*)$	-0.0788	0.6283	0.0443	0.6047	0.4285
$^1A'$	$4\,^1(\pi - \pi^*)$	-0.0625	0.7378	0.1286	-0.3450	-0.5399
$^1A'$	$5\,^1(\pi - \pi^*)$	-0.0123	0.1383	0.1194	-0.6933	0.5312
$^1A'$	$6\,^1(\pi - \pi^*)$	0.0274	-0.1033	-0.0111	0.1533	-0.4917

In the case of an average of 5 A' states, the first excited state of A' character ($2^1A'$) is described in the PM-CAS-CI wave function with contributions of 0.64 of the 3^{rd} CASSCF state and 0.73 for the 4^{th} CASSCF state. To describe correctly this state is necessary to include CASSSCF' states ($3^1A'$) and ($4^1A'$) in the MS-CASPT2 treatment, but $4^1A'$ PM-CAS-CI state is given by a linear combination of the ($3^1A'$), ($4^1A'$) and ($5^1A'$) CASSCF states with coefficients -0.61, 0.40 y -0.67 respectively, so in fact to get a good description at the MS-CASPT2 level of the first A' excited state,

Table 4.16: Eigenvalues (in Hartrees) and eigenvectors of the effective Hamiltonian matrix of the 5 low-lying MS-CASPT2 states obtained with state average of 7 states.

7 average states						
State		$1^1A'$ (GS)	$2^1A'$	$3^1A'$	$4^1A'$	$5^1A'$
Eigenvalues		-573.93828	-573.81208	-573.79121	-573.76200	-573.74597
			Eigenvectors			
$^1A'$	GS	-0.9944	-0.1021	0.0004	-0.0110	0.0203
$^1A'$	$2\,^1(\pi-\pi^*)$	0.0108	-0.1219	-0.9860	0.1004	0.0230
$^1A'$	$3\,^1(\pi-\pi^*)$	-0.0781	0.6244	-0.0324	0.6047	-0.4211
$^1A'$	$4\,^1(\pi-\pi^*)$	-0.0625	0.7352	-0.1051	-0.3318	0.5522
$^1A'$	$5\,^1(\pi-\pi^*)$	-0.0136	0.1517	-0.1190	-0.6954	-0.5016
$^1A'$	$6\,^1(\pi-\pi^*)$	-0.0286	0.1072	-0.0089	-0.1731	-0.5093
$^1A'$	$7\,^1(\pi-\pi^*)$	-0.0027	0.0982	-0.0364	0.0159	-0.0757

we need to include 5 roots in the state averaging at the CASSCF level. To check if this number of root is enough we run the same calculations including 6 and 7 roots. The results showed that the inclusion of a larger number of roots hardly change the composition and the energies of the PM-CAS-CI functions. Consequently, 5 states were considered in the subsequent calculations of the singlet A' states.

The outcome of these initial calculations permitted us to limit the extension of our study to the first five states, i.e., the ground state and the $(\pi-\pi^*)$ and $(n-\pi^*)$ singlet and triplet low-lying excited states.

CHAPTER 5

CHARGE TRANSFER IN AMINOBENZONITRILES

5.1 Introduction

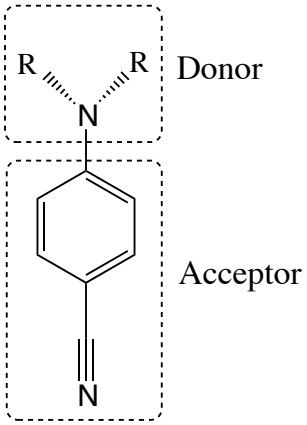

Figure 5.1: Donor and acceptor parts of ABN family of EDA compounds.

The family of the aminobenzonitriles is one of the most investigated classes of electron donor acceptor (EDA) compounds (see Figure 5.1), being considered the prototype of this kind of systems [20].

Under UV excitation, the members of this family can show different luminescent patterns, i.e., a normal fluorescent band, an anomalous band (anomalously red shifted) or dual fluorescence [20, 21].

The fact that the emission properties of these compounds can be controlled by structural changes in the molecule or external parameters such as solvent polarity or temperature is important for applications in the field of organic materials, for example, as fluorescence markers [14–16] or electrooptical switches [17–19]. The interest focused on the excited states of this systems is therefore cognitive and applied.

The original hypothesis of dual fluorescence was proposed by Lippert in 1959 [119]. He suggested that solvent polarity induced the reversal of the two lowest excited S_1 and S_2 states that where directly populated after the initial excitation. Since then, a huge amount of experimental and theoretical studies have been devoted to the ABN family to determine the nature of the emitting species and explain the photochemistry of these compounds (to avoid a long list of publications we just mention here the review of ref. [20]).

It is now generally accepted that the normal fluorescence band is generated by a locally excited (LE) state while the anomalous band corresponds to emission from a intramolecular charge transfer (ICT) state. Some general rules have also been proposed to predict the appearance of an anomalous fluorescence band, like the need of a small energy gap between the lowest singlet excited states (LE and ICT) at the Franck Condon region, $\Delta E(S_1,S_2)$ [24, 120] to favour the existence of a low energy ICT species. Anyway, there still exist a lively debate about some points of the dual fluorescence phenomenon regarding the structure of the emitting species and the detailed mechanism of the ICT reaction.

Concerning geometrical parameters of the ICT species of aminobenzonitriles, four different types of molecular structures have been proposed (Figure 5.2). Three of these differ mostly in the orientation of the amino group relative to the plane of the phenyl ring. The twisted ICT model, where the amino group is in a twisted position relative to the benzene ring, was proposed by Grabowski and co-workers [22]. In the planar ICT (PICT) suggested by Zachariasse [23–25], the amino group lies in the benzene plane. The wagged ICT (WICT) suggested by Zachariase et al [26, 27] involves a rehybridization of the amino nitrogen from planar sp^2 to pyramidal sp^3. The fourth model, the rehybridized ICT RICT [121, 122] involves a rehybridization of the cyano carbon atom from sp to sp^2 entailing a bend cyano group.

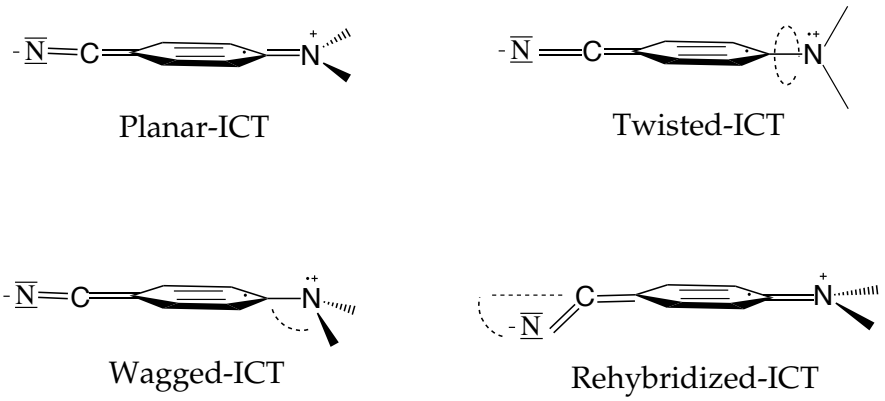

Figure 5.2: Different types of structures proposed for ICT minima

Concerning the reaction mechanisms related with the dual fluorescence phenomenon, these is still a controversy. In the last decade three different type of mechanism have been proposed (Figure 5.3):

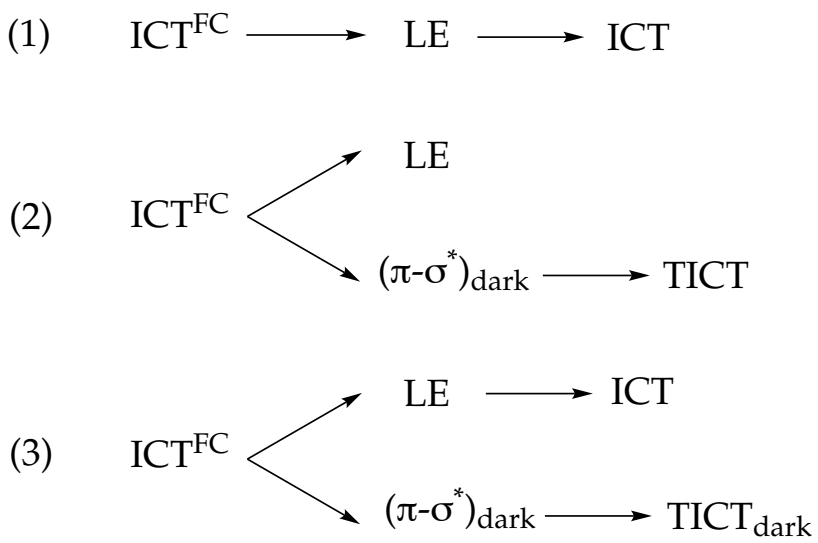

Figure 5.3: Different mechanism proposed for the ICT reaction.

Mechanism 1- [103, 123] After the excitation to the S_2 (ICT) state, the system relaxes through a near conical intersection where the S_2/S_1 internal conversion takes place. In fact, the S_2/S_1 CT-LE radiationless decay can occur at any point of the extended conical intersection *seam* that runs almost parallel to the amino torsion coordinate. The lowest energy point on this conical intersection seam corresponds to a pyramidal structure where the amino group is untwisted, so the branching at the CI favours the formation of the LE state. The two emitting S_1 species are also

adiabatically linked along the amino torsion reaction coordinate. Thus, the S_1 LE-TICT equilibration and dual fluorescence will be controlled by the adiabatic and non adiabatic paths.

Mechanism 2- [124, 125] Upon the population of the FC-ICT state, a rapid switch leads to a bifurcation into the LE state and the $(\pi - \sigma^*)$ state [126], a dark state. In this mechanism the minimum corresponding to the TICT species is assumed to be populated from the $(\pi - \sigma^*)$ state. In the cases of absence of ICT reaction, it is attributed to the higher energy of TICT relative to the $(\pi - \sigma^*)$ minimum. The authors of this hypothesis also pointed out that the primary energetic requirement for the formation of the ICT state is the presence of a $(\pi - \sigma^*)$ state that lies in between the $(\pi - \pi^*)$ and ICT states.

Mechanism 3- This mechanism has been proposed for DMABN based on the results exposed in ref. [127, 128]. After the first excitation the system splits into two excited states, a dark TICT state formed by the dark $(\pi - \sigma^*)$ state and a fluorescence ICT state formed from the LE state. That is, the authors then suggest the existence of two ICT states and point out that these ICT and TICT states are non communicating.

Taken into account that structural changes in the donor or acceptor moieties with the addition of further substituents can modify the interplay between LE and ICT surfaces, is not strange that the studies of different system will lead to different hypothesis about the CT mechanism. On top of this diversity, theoretical and experimental studies not always lead to the same conclusions, so the debate about the photochemistry of the ABN family is still very lively.

Among the aminobenzonitrile compounds, the most studied ones have been the 4-(dimethylamino) benzonitrile (DMABN) and the 4-aminobenzonitrile (ABN) because of their similar architecture and their different behaviour. In the fluorescence spectra of DMABN in non polar solvents, the emission from the ICT state just starts to become observable on the red edge of the fluorescence band of the locally excited LE state [119] [20]. Upon increasing solvent polarity, the efficiency of the ICT reaction becomes progressively larger and DMABN exhibit dual fluorescence in polar enough solvents as acetonitrile or water [129, 130] . As opposite, ABN only shows normal band in gas phase as well as in polar solvents [129, 130].

Compounds where the amino group is enforced to be twisted show only the CT fluorescence band supporting the TICT hypothesis [20, 103, 131] but other rigid de-

rivatives that can twist only partially, and still show the anomalous band, support the PICT structure as the emitting species [25]. However bicyclic but still slightly flexible molecules, as 1-*tert*-butyl-6-cyano-1,2,3,4-tetrahydroquinoline (NTC6) and 1-methyl-7-cyano-2,3,4,5-tetrahydro-1H-1-benzazepine (NMC7), are also able to twist and they can very well adopt a stable TICT structure [132] Up to now, for DMABN and ABN theoretical results supports almost exclusively the TICT model with the amino group in a perpendicular position to the benzene ring. However recent studies [127] in DMABN proposed another ICT structure partially twisted (pTICT), as the emitting ICT species.

Modification of the electronic structure of the amino moiety, also exerts a strong influence on the ICT reaction. Most of the 4-aminobenzonitriles with a tertiary amino group undergo ICT reaction, but this generally does not occur for molecules that have a secondary amino substituent [129] [133] . Further on, ICT has never been reported for aminobenzonitriles with a primary group such as ABN.

ICT reaction can also be modulated by modification in the benzonitrile moiety. For example, the charge transfer process can be enhanced by enlarging the acceptor character of the acceptor moiety by adding additional acceptor substituents. The addition of more -CN substituents to the bezonitrile has a mesomeric effect that leads to a modification of the S_1 and S_2 surfaces. These possible changes can be avoided by the introduction of substituents with a predominantly inductive influence, leaving the nature of S_1 and S_2 largely intact. This could be achieved, for example, by fluoro substituents. It has been shown by comparison of the reduction potentials of benzonitrile and fluorobenzenes [134] that it is necessary up to six F atoms to increase the electron acceptor character as much as a with a single nitrile group. The small electron affinity of F make possible to enlarge the acceptor character of benzene moiety step by step [135], leading to a more controlled process.

Thus, Zachariasse et al. [28] investigated the introduction of a fluorine atom into different positions of the benzene ring in 4-aminobenzonitrile derivatives, and stated that there is no indication of ICT emission in alkane solvents and that the internal conversion (IC) that provides a radiationless deactivation path is enhanced by the fluoro substituent. Neither the introduction of two F-substituents in the phenyl ring of ABN (in the 2,5-difluoro-4-aminobenzonitrile) are sufficient to induce an ICT reaction [136]. However, for the tetrafluoro-aminobenzonitrile derivatives, unlike ABN and DMABN, the fluorescence spectra, both in polar and non polar

solvents, consist only of ICT emission while the fluorescence band from the LE cannot be detected. [136] [28][137]. This evidences the faster population of the CT excited state in these derivatives as compared to their non fluorinated counterparts. It means that fluoro substituent could decrease the energy gap $\Delta E(S_1,S_2)$, making the 2,3,5,6-tetrafluoro-4-ABN (ABN-4F) the first donor/acceptor molecule with a primary amino group for which ICT emission is observed [136].

Regarding other competitive photochemical reaction paths, Zachariasse and coworkers [138] have observed that the fluorescence decay time and quantum yield strongly decrease with increasing the temperature in DMABN and ABN in alkane solvents. They have established that DMABN and ABN undergo efficient thermally activated IC. Thus, IC becomes the dominant deactivation pathway of the first excited singlet state S_1 at high temperatures.

The number of fluorine substituents seems to be also an important factor in the opening of the IC channel, enhancing the accessibility to a conical intersection leading to the electronic ground state. The internal conversion yield in n-hexane at 25° is considerable larger for ABN-4F ($\approx$1.00) and 2,3,5,6-tetrafluoro-4-aminobenzonitrile (DMABN-4F) (0.92) than for ABN (0.10) and DMABN (0.10). Thus, in the tetrafluorinated aminobenzonitriles, both the IC channel and the induced ICT emission are enhanced as compared with non substituted ones [28, 136, 139].

Scope

Our group developed some years ago a computational study on two members of the aminobezonitrile family, in particular on ABN and DMABN and set the main milestones to explain the photochemistry of these compounds [103]. A path involving the PES of the LE and twisted ICT excited states was located and the corresponding LE and TICT species suggested as the responsible of the normal and anomalous emissions. Recent experimental findings, though, suggest the involvement of a $(\pi - \sigma^*)$ excited state in the CT mechanism, what made necessary a revision of the results previously reported by the group. We present here a new study of the photochemistry of ABN, focused firstly on the ICT reaction mechanism. We also extend the scope of our study to include the analysis of other competitive reaction channels on the singlet manifold like is radiationless deactivation through internal

conversion. Furthermore we studied also the tetrafluoro substituted ABN where the ICT fluorescence and the radiationless deactivations are enhanced. We expect to get a more general view of all the possible radiative and radiationless channels in aminobenzonitrils by comparison of the results obtained for ABN and ABN-4F (see Figure 5.4).

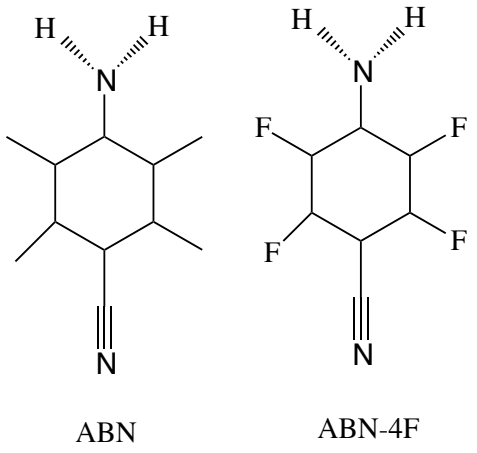

Figure 5.4: Structure of ABN and ABN-4F.

The steps of this study will be basically the following:

- Firstly we present the study of the nature of excited states of the parent system (ABN). We resolve the question of the nature of the lowest excited states and locate the corresponding minima.
- The information collected in the previous step suggests possible ICT reaction paths, that are studied afterwards.
- The internal conversion enhanced by the increase of temperature in ABN is investigated. We looked for crossing of the singlet excited states with the ground state.
- Finally, to understand how the substitution of the four hydrogen atoms in the benzene ring of ABN by fluorine atoms can modify the luminescence behaviour of these compounds, we have studied the ABN-4F centering our study on the areas of the PES of the ground and excited states that have been shown to be crucial in the study of ABN.

5.2 Computational information

The ground state and the low lying singlet excited states of ABN and ABN-4F have been studied using the MS-CASPT2/CASSCF strategy already described. The 12 electrons and 11 orbitals that constitute the active space include the benzene π and π^* orbitals, the amino nitrogen lone pair, and the four π and π^* orbitals of the cyano group (see Figure 5.5). Full geometry optimizations were performed without any symmetry constraint using the d-polarized split-valence basis set 6-31G* [101]. Numerical frequency calculations were run to determine the nature of the stationary points.

Due to the stabilizazing effect of dynamic correlation in intramolecular charge transfer states, optimizations in the study of the ICT mechanism in ABN were carried out when using more flexible basis set, the Dunning correlation consistent polarized valence double [9s4p1d/3s2p1d] for carbon and nitrogen atoms, and [4s1p/2s1p] for hydrogen atoms, designated cc-pVDZ basis set [140].

Conical intersections were optimized using the algorithm described in ref [50]. State averaged orbitals were used, and the orbital rotation derivative correction to the gradient (which is usually small) was not computed. This gives the lowest energy point on the crossing, but it must not be forgotten that decay can take place away from the minimum energy point on the crossing, depending on the kinetic energy of the system.

VB structures have been determined exploiting the results of the computation of the second order exchange density matrix P_{ij} and the diagonal elements of the electronic density matrix. The elements of P_{ij} have a simple physical interpretation, which is related to the spin coupling between the electrons localized in the orbitals residing on the atoms i and j. An illustration of the meaning of these matrix elements can be found in reference [141]

In ABN-4F, in order to take into account the involvement of $\pi - \sigma^*_{C-F}$, states a bigger active space was used after tested. It adds to in the previous active space an additional σ^* orbital that comprises the totally symmetric combination of antibonding C−F σ^* orbitals (Figure 5.5).

To incorporate the effect of the dynamic valence electron correlation on the relative energies of the lower excited states, we performed second order multiconfigura-

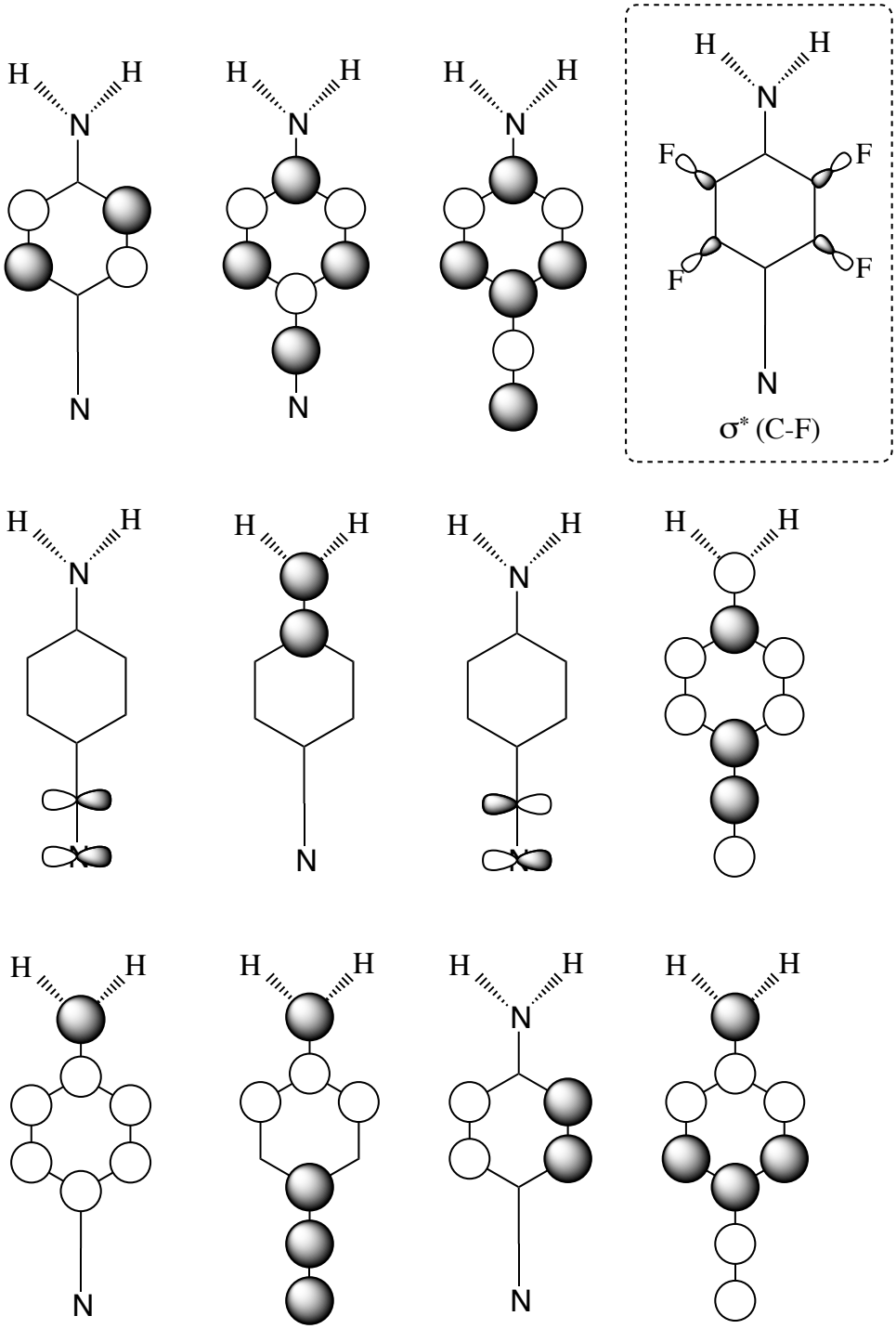

Figure 5.5: Schematic representation of the orbitals included in the CAS(12,11). The additional orbital incorporated in the case of ABN-4F in the CAS(12,12) calculations is drawn framed in dashed lines.

tional perturbation theory calculations (CASPT2) based on the CASSCF(12,11) reference function [60]. CASPT2 single point energies were calculated at the CASSCF/cc-pVDZ geometries. All valence electrons were correlated. All CASPT2 computations have been performed using the completed Fock matrix in the definition of the zero order Hamiltonian, together with an imaginary level shift of 0.2 in order to avoid the incorporation of intruder states[74]. Interaction of CASSCF states via dynamic correlation is taken into account with MS-CASPT2 treatment [75].

The CAS state interaction (CASSI) protocol [78] and the PM-CAS-CI functions were used to compute transition dipole moments and oscillator strengths to compare transition probability in both absorptions and radiative emissions.

Minimum energy paths (MEPs) [108], intrinsic reaction coordinates (IRCs) [142] path and linear interpolated internal reaction coordinate (LIIRC) paths were calculated between critical points of interest (stationary points and conical intersections) on several surfaces to ascertain the viability of the proposed reaction mechanisms.

The CASSCF calculations were carried out with the Gaussian 03 system of programs [57], while the CASPT2 computations were performed with the MOLCAS 7.0 program package [56].

5.3 Model system ABN

5.3.1 FC region

Ground state

From the computational point of view, the first step in this work must be to locate the minimum energy species of ABN at the ground state. This has been done by carrying out CASSCF (12,11) optimization using the cc-pVDZ basis set. This optimized ground state (GS) geometry of ABN is in good agreement with the X-ray crystal structures reported in [143] as well as with results from previous calculations [144, 145]. The atom labelling and definition of angles are given in Figure 5.6 and the molecular structure is shown in Figure 5.7.

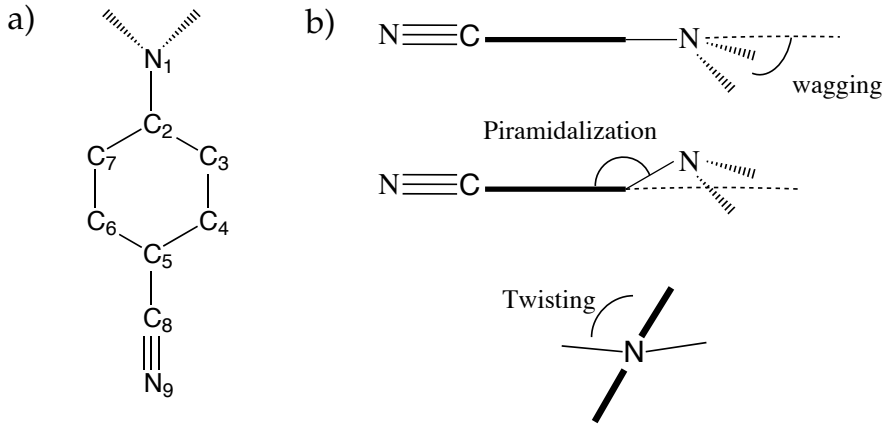

Figure 5.6: a) Atom labelling in ABN. b) Definition of the wagging, pyramidalization and twisting angles.

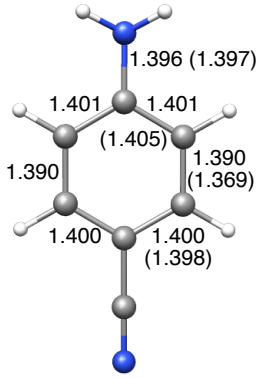

Figure 5.7: Optimized ground state geometry of ABN. In parenthesis experimental geometrical parameters of reference [143].

The S_0-GS minimum belongs to the *Cs* point group with a *kekulé* nature of the phenyl ring and a pyramidal amino group. The molecule is completely planar, with the exception of this NH_2 group. Its pyramidalization corresponds to an inversion of the amino group and can be quantified by measuring the pyramidalization angle ϕ. We found ϕ = 43.0° for ABN, slightly larger than the experimental value ϕ = 34.84°.

The computed bond lengths for ABN are also slightly larger than the X-ray data, with a standard error of 0.015 Å [143]. The N_1-C_2 bond length is somehow larger in comparison with the crystal structure. Concerning benzene bond distances, C_2-C_3 are the largest and C_3-C_4 the shortest, what agrees qualitatively with experimental findings, but the computed C_3-C_4 distance is larger in comparison. Serrano et al.

[146] suggested that measured bond lengths are too small because it is often observed that in the solid phase this type of bond length are underestimated [130].

Nature of excited states

It is convenient to have identified, at the FC geometry, all the excited states involved in the reaction. In principle, we need to consider only the excited states between the ground state and the bright state, but some of the higher excited states can be stabilized along reaction path to be studied and get involved in the reaction mechanism. These states must be also included in the initial calculations at the FC zone.

On the top of this it is convenient to include, in the CASSCF step, more excited states than the strictly necessary in principle. First to consider the different effect of dynamic correlation in excited states at SS-CASPT2 level, and second to allow for possible interactions of the states of interest with higher excited states that can appear when we take into account the dynamic correlation at the MS-CASPT2 level. For these reasons in these study we included 13 states in an average procedure at the CASSCF step (SA13-CASSCF) to characterize the nature of the excited states. The analysis of the influence of the number of states averaged on the results can be found in the Appendix of this chapter.

But before describing the nature of the excited states, it is convenient to say a few words about the nomenclature used often in the literature related with ICT in the aminobenzonitrile family.

The L_a and L_b nomenclature, used to design sometimes the CT and LE states at the FC geometry, was introduced by Platt [147] in order to define excited states in no substituted aromatic hydrocarbons. The lowest excited state is the transition forbidden L_b state, while the second excited state is the L_a state. Despite this nomenclature is often used for the description of EDA systems, when the symmetry is broken by substitution this classification loses their validity.

In substituted benzene EDA molecules, the three low lying electronic states expected in general are: a locally excited (LE) state (excitation localized mainly in the benzene ring) and two states of CT character derived from a transfer from an electron from the covalently linked donor group to the π^* orbital system of ben-

zene. The nomenclature of these two CT states, based on anion radical, helps to classify them according to the Jahn Teller distortion of the benzene ring when the anion radical is formed at accepting the transferred electron. In MO language the extra electron may be placed in one of the two degenerated π^* orbitals 3a or 3b shown in Figure 5.8. Placing an extra electron in orbital 3a of benzene results in a node between the central carbon atoms 2 and 3 and between 5 and 6 leading to an antiquinoid structure (AQ). Placing an electron in 3b results in a shortening of the C_2-C_3 and C_5-C_6 bond lengths leading to the quinoid structure (Q).

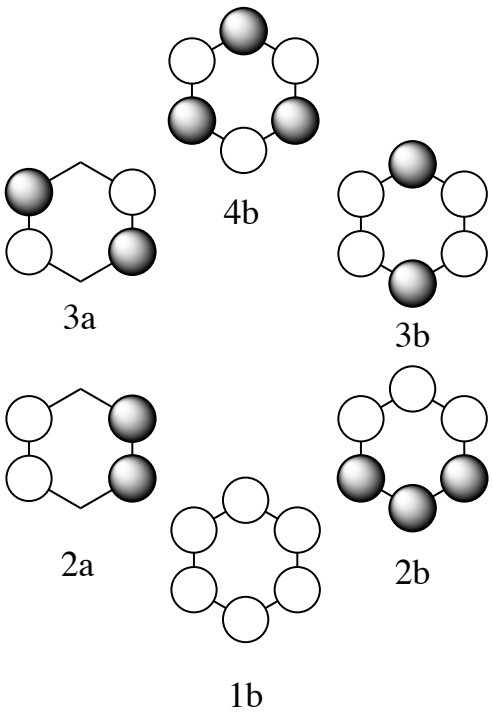

Figure 5.8: The 6 π orbitals of benzene labelled as in C_2 symmetry

Apart from the LE, CT(Q) and CT(AQ) states, other types of monoexcitations have been found in the detailed analysis of the lowest excited states of ABN performed in this work. These are represented in Figure 5.9.

The names adopted for the states derived from these excitations are collected in Table 5.1. The characterization and labelling of states was made by analysing the contribution of the CSF in each wave function, the difference density plot between excited states and the ground state, and the occupation numbers of the natural orbitals of each state.

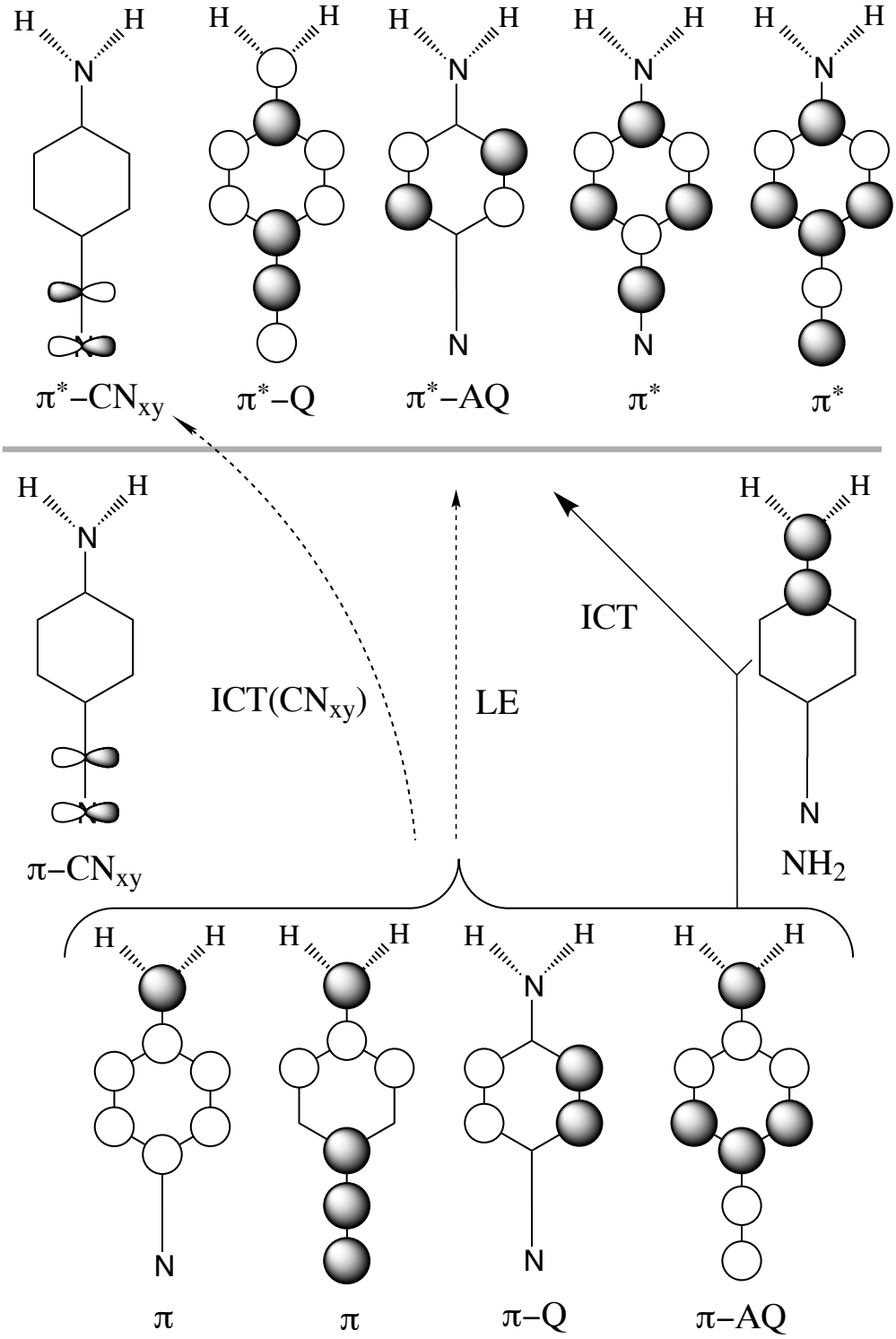

Figure 5.9: Scheme of excitations. Orbitals under the horizontal line are doubly occupied in the ground state, while orbitals above the line are empty.

Table 5.1: Nomenclature adopted for the excited states derived from the different types of monoexcitations represented in Figure 5.9.

STATES	LABEL	EXCITATIONS
Locally excited	LE	π-Q+π-AQ $\rightarrow$ π^*-Q+π^*-AQ
ICT : From amino group to benzonitrile	ICT(Q)	π-AQ $\rightarrow$ π^*-Q
ICT: From amino group to ring	ICT(AQ)	π + π-AQ + π-Q $\rightarrow$ π^*-AQ
From cyano group	CN_{xy}	CN_{xy}; $\rightarrow$ π^*-Q
ICT : To antibonding cyano group orbital	ICT(CNxy)	CN_{xy} + π-AQ $\rightarrow$ CN^*_{xy}
From amino and cyano to Ring	D+A $\rightarrow$ R	*a*)π-AQ + π-Q $\rightarrow$ π^*-AQ b) π $\rightarrow$ π^*-Q

Table 5.2 shows the relative energies, dipole moments and oscillator strengths obtained at different levels of calculation for the thirteen lowest excited states of ABN in the ground state geometry.

Table 5.2: Vertical energies (in kcal·mol^{-1}) and dipole moments (μ in Debyes) of the 13^{13} lowest states of ABN, obtained with a SA13-CASSCF wave function at several levels of calculation.

State	CASSCF	SS-CASPT2	μ	PM-State	MS-CASPT2	μ
S_0	0	0	5.33	S_0	0	6.77
LE	108.41	108.68	5.13	LE	106.25	6.3
ICT(Q)	155.1	124.19	10.07	ICT(Q)	121.21	9.76
D+A $\rightarrow$ R (b)	174.3	167.23	4.57	ICT(AQ)'	144.99	8.32
ICT(AQ)	175.38	160.35	6.83	ICT(AQ)	160.33	6.97
CN_{xy}	190.78	177.91	2.22	D+A $\rightarrow$ R (b)	171.06	4.99
ICT(AQ)	201.23	162.63	6.31	CN_{xy}	179.28	2.74
D+A $\rightarrow$ R (a)	203.77	165.18	5.03	D+A $\rightarrow$ R (a)	183.77	3.31
D+A $\rightarrow$ R (b)	205.9	193.12	4.16	ICT(CN)	186.23	6.26
ICT(CN)	211.68	184.49	6.51	ICT(Q)	191.99	5.43
S_{11}	225.8	197.29	5.91	$S_1$1	209.18	4.36
S_{12}	231.17	211.56	3.12	$S_1$2	211.09	1.69
S_{13}	234.86	209.54	1.40	$S_1$3	216.96	3.18

In all levels of calculation the first excited state is of LE character with a dipole moment around 6.30 D. This state is composed by two monoexcited CSF, with excitations π-Q $\rightarrow$ π^*-Q and π-Q $\rightarrow$ π^*-AQ. In principle it could be though that this excitation is not completely localized in the ring, given that there exist a contribution of the lone pair of the N of the amino group in π-Q and π^*-AQ orbitals. But

if we calculate the difference of electronic density between the ground state and the LE state, plotted schematically in Figure 5.10, or calculate the occupation of the localized orbitals of these states (see Figure 5.11), we observe that the reduction of the occupation of the amino nitrogen is only 0.025, what confirms the LE character of this state.

The second excited state is ICT(Q). The difference in electronic density with ground state depicted in Figure 5.10 shows that this state is characterized by a charge transfer mainly from the amino group to the carbon of the ring bonded to the cyano group, according with its calculated high dipole moment of 9.76 D. This state is labelled as ICT(Q) because the main excitation (from the GS) is a monoexcitation of the type π-AQ $\rightarrow$ π^*-Q with a coefficient of 0.7. Furthermore, in order to analyse the quantitative charge transfer character of this state, a calculation with atomic localized orbitals was done. The occupation numbers of the localized orbitals depicted in Figure 5.11 show that the transfer is not a full charge transfer because the occupation number of the amino nitrogen is only reduced from 1.878 to 1.543.

The first ICT(AQ) state is the third excited PM-CAS-CI state. This state is derived basically, like all ICT(AQ) states, from an excitation of the type π + π-AQ + π-Q $\rightarrow$ π^*-AQ. Its characteristic difference of electron density with the ground state is depicted in Figure 5.10.

Another type of electronic state is the labelled CN_{xy}. It is placed as the 5^{th} excited state at CASSCF level and 6^{th} at MS-CASPT2 level. Its wave function is characterized by a contribution of 0.82 of the CSF given by the monoexcitation $CN_{xy} \rightarrow \pi^*$-Q. Therefore there is a transfer of electronic density from the cyano π in plane orbital to the benzene ring with a reduction of the dipole moment to 2.74 D (to be compared with the ground state dipole moment of 6.77 D).

There are also two more ICT states labelled as $D + A \rightarrow R$. Their electronic configurations involve a transfer of electron density from the amino group and from the cyano group π orbitals to the ring, as can be observed in the plot of the density difference of Figure 5.10.

The ICT (CN) state is of special importance on the study of the deactivation mechanism studied here. This state is the one called ($\pi - \sigma^*$) in previous studies, and to elucidate its role in the ICT mechanism has been one of the reasons to study

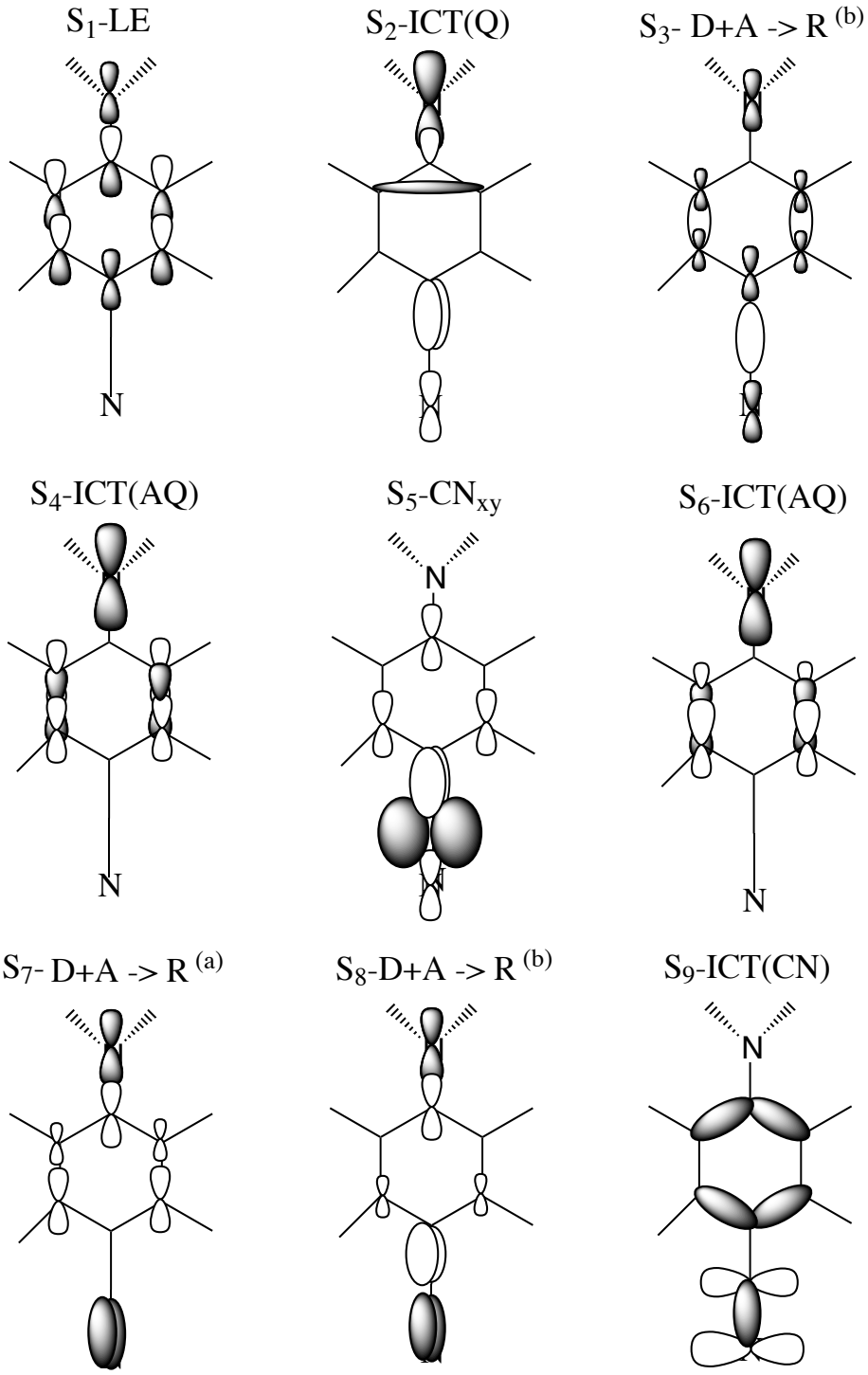

Figure 5.10: Schematic representation of the electronic density difference between first low lying excited states and the ground state. The loss of the electronic density is coloured in black and the gain of electronic density in white.

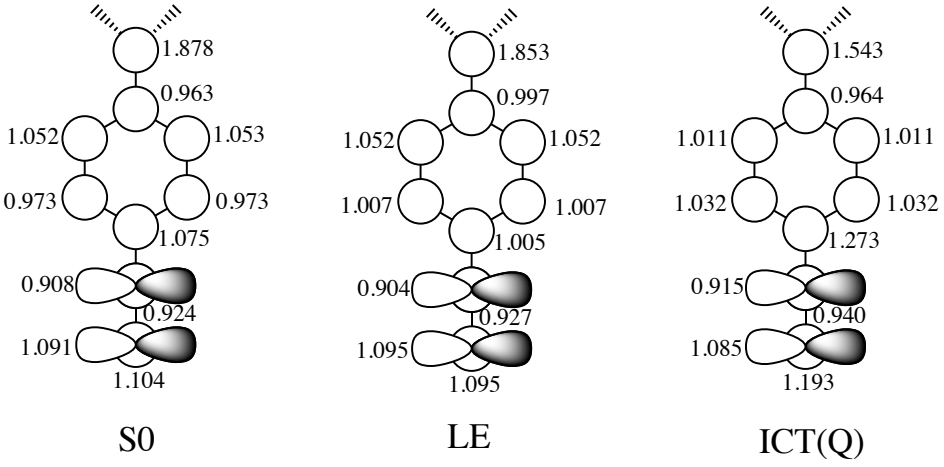

Figure 5.11: Occupation numbers of the localized orbitals of S_0 LE and ICT states in the FC zone.

again the photochemistry of ABN. It is characterized by a charge transfer from the aminobenzene ring to the cyano group (as showed by the plot of difference density). This state is composed mostly by two CSF: one is a promotion of an electron from the $\pi - AQ$ to CN^*_{xy} orbitals and the other is from CN_{xy} to CN^*_{xy} orbitals. The computed dipole moment is of 6.26 D, indicating a transference of charge. The reason to rename it is that the orbital where the excitation take place to, is in fact mostly composed by the antibonding in plane π orbital of the cyano group, instead of by a σ^* orbital.

In principle, all the states involved in the reactivity of interest are included in the set of states described up to here. Nevertheless, given that in the MS-CASPT2 step higher states can get coupled with these ones and modify their description and energies, three additional states were included in the average at the CASSCF level. The detailed description of these, though, is not possible because of the computational limitations of the MOLCAS package. Nevertheless, MS-CASPT2 results show that in this case the higher states do not interact with the lower states (see Appendix of this chapter), so their characterization is not essential in this study.

It can be interesting to comment on the denomination of *charge transfer state*. While the conventional meaning indicates a transfer of charge corresponding almost to a full electron from the amino moiety to the phenyl ring, we have found some other excited states that should also be considered as ICT states, but with different origin or destination of the transferred charge. While some states show a transfer

from the amino to the cyano substituent, with the corresponding large increase of the dipole moment, other surprising states has also been found with transfer from the cyano group to the phenyl ring, which leads to a decrease of the dipole moment.

From the experimental point of view a distinction between *charge transfer* and *electron transfer* has been stated at some point [20] according to the following three criteria: *i)* The excited state dipole moments should correspond to a full separation of charges. *ii)* the transition dipole should be very small, corresponding to an overlap forbidden transition in fluorescence *iii)* the absorption spectrum of the excited state should match the sum of the spectra of the cation radical D^+ and anion radical A^-.

From our point of view a clear-cut distinction can not be established, but the criterion we have followed to design as "CT" to a given state has tried to be made clear in the description made in this section.

Letś turn to the results of the vertical energies at the ground state minimum of ABN, focusing in the results for the lowest LE and ICT excited states, that can be compared with the energies of the maximum band of the experimental absorption spectra.

Abortion spectra

Table 5.3 shows the CASSCF/CASPT2 energies computed at SA13-CASSCF/ CASPT2 level in gas phase.

Table 5.3: Character of states, vertical energies (in kcal·mol^{-1}), oscillator strengths (f), and dipole moments (μ in Debyes) at the GS geometry of ABN obtained at different levels of calculation, based on a SA13-CASSCF reference wave function.

State	CASSCF	SS-CASPT2	μ	PM-State	MS-CASPT2	μ	f
S_0	0.00	0.00	5.33	S_0	0.00	6.77	
LE	108.41	108.68	5.13	LE	106.25	6.30	0.0709
ICT (Q)	155.10	124.19	10.07	ICT	121.21	9.76	0.6231

Let us first analyse the CASSCF results. At this level, the CT state is located above the LE state and it is characterized by a high dipole moment. Although the CASSCF results agree qualitatively with the experimental data in non polar solvents

[24, 28, 139], the energetics are highly overestimated, particularly for the CT state, where the disagreement is larger than 40 kcal·mol $^{-1}$ with the experimental value in hexane of 109.4 kcal·mol^{-1} [136].

In order to obtain more accurate results, the energies were recalculated with the CASPT2 method to include the dynamic correlation. As can be seen from the results shown in Table 5.2, the dynamic electron correlation has a different quantitative effect on the LE and CT states. For both states, the MS-CASPT2 excitation energies are smaller than the CASSCF ones, but the LE state undergoes a smaller stabilization, of around 2.16 kcal·mol^{-1}, whereas the CT state is stabilized by around 33.89 kcal·mol^{-1}. Moreover SS-CASPT2 and MS-CASPT2 energy differences are small, given that there is no mixing of both CASSSCF states via dynamic correlation. A direct consequence of this discriminatory effect of the dynamic electron correlation is that the energy gap between the two excited states is smaller, what can have important consequences in the ICT mechanism.

The computed dipole moments in gas phase for ABN vary with the inclusion of interaction of states via dynamic correlation. For the ground state, the dipole is computed to be 5.40 D at CASSCF level, slightly lower than the estimated 6.60 D in non polar solvents [26, 136]. At MS-CASPT2 level it is increased to 6.77 D, in agreement with the experimental value. This can be attributed to a major contribution of the charge transfer CSF in the ground state in the PM-CAS-CI wave function, reflected in an increase of the weight of ionic states.

The coupling between the amino group and the benzene ring was also analysed. In Table 5.4 is shown the coupling between the non bonding pair of the amino group nitrogen and the π system of benzene ring, as defined by the values of the second order exchange density matrix (P_{ij}) between the p orbitals of C_2 and N_1 (see Figure 5.6 for labelling). Surprisingly, this value is larger in the ICT state than in the ground and LE states, in agreement with Zachariasse claim that the amino group is strongly coupled to the benzonitrile fragment [148].

The large computed oscillator strength between the ground and the CT states indicates that the CT is the initially promoted state. It will carry most of the energy after absorption due to the allowed character of the transition. The oscillator strengths are in good agreement with experiments predicting a weak $S_0 \rightarrow S_1$ band and a stronger $S_0 \rightarrow S_2$ absorption.

Table 5.4: Second order exchange density matrix between p orbitals of C_2 and N_1 (see Figure 5.6 for labelling) in the FC zone of ABN.

States	P_{ij}
GS	0.057
LE	0.045
ICT	0.28

Figure 5.12 show the orientation of transition dipole moments of the first and second excited states. This results are also in good agreement with experiments [20]. In order to analyse the polarization of the transition dipole moment in major detail, the composition of the LE and CT wave functions in terms of CSF that compose LE and CT is crucial. Despite the calculations are done without symmetry restrictions, we can consider that the molecule in its ground state is in idealized symmetry *Cs*. Then in the following discussion, molecular orbital's symmetry are exposed in parenthesis after orbitals name.

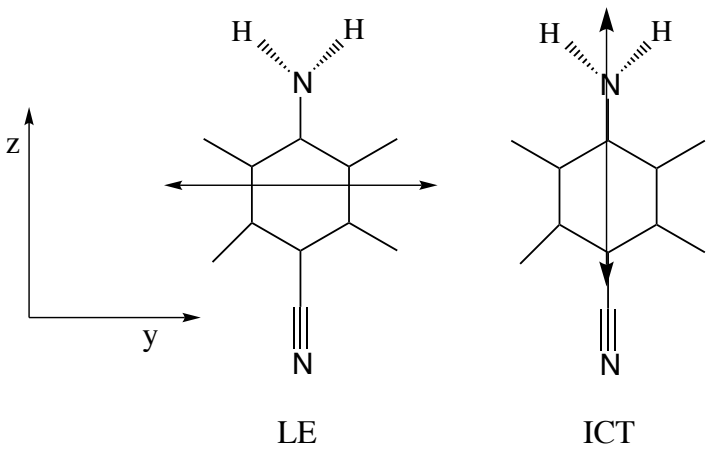

Figure 5.12: Orientation of transition dipole moments of S_1-LE and S_2-ICT states.

The LE wave function is composed mainly by two monoexcited configurations, one with a weight of 0.44 of a promotion from π-AQ (A') to π^*-AQ (A'') (leading to a A''-CSF) and the other with a weight of 0.29, of a promotion from π-Q (A') to π^*-Q (A'). According to experimental and theoretical results the LE transition is polarized in an axis perpendicular to the ground state polarization. It can be attribute to a major contribution of the A'' -CSF to the LE wave function leading to a non zero value in the transition dipole moment (TDM) in the x and y directions.

Contrary, the CT is characterized by an excitation with a weight of 0.78 from π-AQ (A') to π^*-Q (A') (leading to a A'-CSF). Then this state have the same symmetry as ground state, that is parallel polarized in the z axis, and the TDM is larger.

5.3.2 Minima of the excited states

The next step in this study is to locate the minima of the excited states that could be involved in the ICT process. These will not only be those that can be populated after the initial excitation, but we have to consider all those that have an energy similar or lower than the one of the initial excitation of 121 kcal·mol^{-1}.

To avoid limiting our search with preconceived ideas (regarding the models of ICT structures commented in the introduction of this chapter), we explored the PES of the lowest excited states of ABN. The outcome of this search is described now.

Minima from the ICT(AQ) and CN_{xy} excited states were not found at low energies. In the case of ICT(AQ) state, all the optimizations evolve to quinoidal ICT(Q) geometries, and the obtained conical intersection between ICT(Q) and ICT(AQ) was very high in energy (commented in more detail in the next subsection). From the calculations we concluded that the population of ICT(AQ) is not probable. In the case of the CN_{xy} state, its relaxation coordinate stabilizes more the ICT(CN) state, leading to a crossing of these two surfaces. The ICT(CN) become lower in energy and the probability of ICT(CN) being involved in the ICT mechanism increases. The minima obtained for other states are depicted in Figure 5.13.

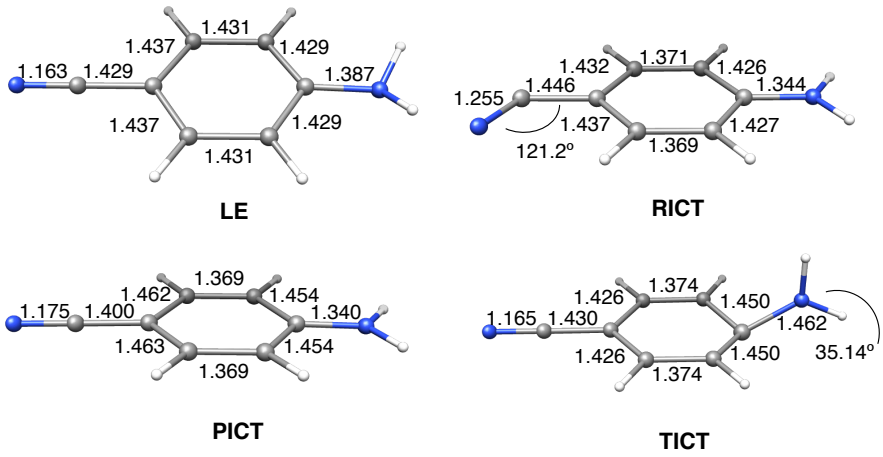

Figure 5.13: Optimized structures of excited state minima of ABN.

These geometries were obtained at the CASSCF(12,11)/cc-PVDZ level without state averaging. As it will be explained latter, this is an important point. The energetics of this structures were then recalculated at the SA-CASSCF(12,11)/MS-CASPT2/cc-PVDZ level, averaging two or three states as shown in Table 5.5. It should be pointed out that the RICT species corresponds to the structure of the minimum of the ICT(CN) state, named $(\pi - \sigma^*)$ in previous works.

Table 5.5: CASSCF, SS-CASPT2 and MS-CASPT2 energies relative to the S_0 minimum (in kcal·mol^{-1}), dipole moments (in Debye) and state nature of the characterized ABN minima optimized at CASSCF/cc-pVDZ level. The number of states averaged in the CASSCF reference wave function corresponds to the number of states shown in each minimum.

Minimum	Nature	CASSCF	SS-CASPT2	Dipole	Nature	MS-CASPT2
LE	S_0	4.13	2.01	5.37	S_0	2.01
	LE	104.22	102.73	5.1	**LE**	**102.40**
RICT	S_0	40.86	31.02	4.86	S_0	31.02
	LE	147.04	134.62	4.55	**ICT**	**122.14**
	ICT	152.77	122.15	10.45	LE	134.64
TICT	S_0	39.14	33.26	3.82	S_0	33.26
	LE	133.85	125.86	4.56	**ICT**	**112.94**
	ICT	160.93	125.87	10.76	LE	138.80
PICT	S_0	13.26	4.94	6.71	S_0	3.74
	LE	116.22	105.74	5.93	LE	105.74
	ICT	146.15	115.79	11.23	**ICT**	**116.99**

The calculation of the CT states shows two problems:

1. When performing the calculation of the SA-CASSCF level averaging with the same weights the S_0, LE and ICT states, the averaged orbitals are better suited to describe the LE state (given that it is similar to the S_0 state) than to describe the ICT states. For this reason these later states are artificially destabilized relative to the LE states (although the energy of those are also higher) at the SA-CASSCF level, compared to the results obtained without state averaging.

   In the case of the excited states at the TICT minimum, the situation is more complicated given than there is another factor influencing the results as will

be explained below.

2. The dynamic correlation decreases preferentially the energy of the ICT states, stabilizing them relative to the LE states. This fact is reflected in the non negligible change between the results at SA-CASSCF level and at the SS-CASPT2 level, where the ICT states are very stabilized relative to the LE state. This stabilization is even larger when the coupling among states is allowed in the calculation, resulting in a further stabilization of the ICT states at the MS-CASPT2 level.

At the TICT minimum the relation between the LE and ICT states is quite complex. To try to analyse the situation, let's assume that these states are correctly described by the PM-CAS-CI functions at the MS-CASPT2 level. When the coupling among states is not allowed in the energy calculation, these states become practically degenerated (see SS-CASPT2 energies in Table 5.5) and the states mix. When the electron dynamic correlation is excluded from the calculation (at the SA-CASSCF level) the energy gap between these states increases artificially, destabilizing preferentially the ICT state. The effect of the averaged orbitals, better fitted to describe the LE state, destabilized even further the ICT states, resulting in a very incorrect description of the situation at SA-CASSCF level.

The mixing of the LE and ICT states is reflected in the composition of the PM-CAS-CI wave functions of the SA3-MS-CASPT2 calculation run at the TICT minimum geometry, shown in Table 5.6: the perturbed modified functions of the 2^{nd} and 3^{rd} roots are a combination with almost equal weights of the CASSCF functions assigned to the LE and ICT states. It means that at the SA-CASSCF level these state are not correctly described.

Table 5.6: Eigenvectors of the SA3-MS-CASPT2 effective Hamiltonian matrix diagonalization in TICT optimized geometry at CASSCF/cc-pVDZ level.

3 state averaged			
States	1 (GS) PM-CI	2 PM-CI	3 PM-CI
GS	1.0000	0.0000	0.0000
2	-0.0000	**0.7072**	**-0.7069**
3	-0.0000	**0.7069**	**0.7072**

The question of the correctness of the geometry optimization performed at CASSCF level is the arisen, although it was performed without state averaging. Despite the TICT and RICT minima are optimized as second roots at the CASSCF/cc-pVDZ level with the Gaussian03 program, in SA2-CASSCF(12,11) and SA3-CASSCF(12,11) single points calculations done in Molcas7.0, the ICT states lie high in energy, as third roots. Table 5.7 shows CASSCF calculations performed without state averaging with both packages. In the case of Molcas calculations, the low computed dipole moments and the analysis of wave functions demonstrate that in all optimized minima, the corresponding S_1 state is of LE character in disagreement with gaussian results. It can be attributed to the different implementations of the CASSCF algorithm in both packages, probably the root flipping can be enhanced because LE and CT states are very close in energy.

Table 5.7: CASSCF energies relative to the S_0 minimum (in kcal·mol^{-1}) and dipole moments (in Debye) of the most important characterized minima for the ABN molecule on Molcas and Gaussian suite of programs.

Geom	S_1 State	S_1 E_{CASSCF}	μ
		Gaussian	
LE	LE	104.22	5.41
TICT	ICT(Q)	128.07	**11.53**
RICT	ICT(CN)	141.45	**12.42**
		Molcas	
LE	LE	104.22	5.41
TICT	LE	129.28	**4.50**
RICT	LE	140.85	**4.63**

Then, given the controversy that still goes on about the TICT structure, we reoptimized this geometry at the MS-CASPT2 level. The structure obtained, quite similar to that obtained at the CASSCF level, is shown in Figure 5.14 and energies are shown in Table 5.8.

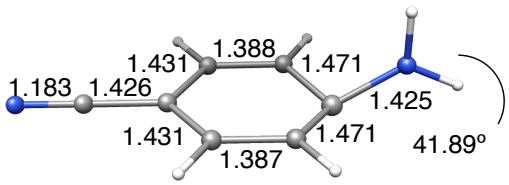

Figure 5.14: TICT minimum optimized at SA3-MS-CASPT2/cc-pVDZ level.

Table 5.8: CASSCF, SS-CASPT2 and MS-CASPT2/cc-pVDZ energies relative to the S_0 minimum (in kcal·mol^{-1}) and dipole moments (in Debye) in the ABN TICT minimum optimized at the MS-CASPT2/cc-pVDZ level.

Minimum	CASSCF	Dipole	SS-CASPT2	MS-CASPT2	Nature	Dipole
TICT	49.03	3.85	41.05	41.04	S_0	3.85
	134.99	5.13	122.78	110.16	ICT	**10.16**
	164.69	10.46	129.59	142.21	LE	5.44

The main differences are a larger pyramidalization angle (6° larger), a smaller N_1-C_2 bond distance (0.04 Å shorter) and a slightly larger C-C distances at the phenyl ring. The energy is only 3 kcal·mol^{-1} lower (at MS-CASPT2 level) than that of the previous optimized geometry. Like before the PM-CAS-CI wave functions of the 2^{nd} and 3^{rd} roots combine almost with equal weights the CASSCF functions assigned to LE and ICT states (Table 5.9). The charge transfer character of the 2^{nd} MS-CASPT2 state is assessed by its high dipole moment and by the determinant with the largest weight in the MS-CASPT2 eigenfunction (the coefficient is equal to 0.88) that corresponds to a monoexcitation from the lone pair of the amino N atom to the $\pi^* - Q$ orbital.

Table 5.9: Eigenvectors of the PM-CAS-CI in the ABN TICT minimum optimized at the MS-CASPT2/cc-pVDZ level.

States	1 (GS) PM-CI	2 PM-CI	3 PM-CI
		Eigenvectors	
1-CASSCF	-1.0000	0.0000	0.0000
2-CASSCF	-0.0000	**-0.7786**	**0.6274**
3-CASSCF	0.0000	**0.6274**	**0.7786**

It has to be pointed out that the mixture of states at the MS-CASPT2 level is not present at the other excited state minima (LE, RICT and PICT), as demonstrated by the composition of the PM-CAS-CI eigenfunctions shown in the Annex of this chapter.

To sum up, we can say that we have located minima on the S_1 PES corresponding to the LE, TICT, and RICT excited states (at 102.40, 110.15 and 122.14 kcal·mol^{-1} respectively) and a minimum on the S_2 PES corresponding to a PICT structure

(116.99 kcal·mol^{-1}). The next step of this work must be to study which of these minima can be populated.

5.3.3 Pathways of population of the excited state minima

The investigation of the connection between different excited states and the different structures in them, implies the search of CI and TS and the determination of paths along the critical points of interest. The first task was performed using a cc-pVDZ basis set, but the computational cost of the second task made advisable the use of the smaller $6-31G^*$ basis set.

Deactivation pathways to the S_1 surface.

The first step in this part of our study is to calculate the minimum energy path from the FC geometry on the S_2 surface. The calculated MEP leads directly to the PICT shallow minimum. From there several pathways are accessible.

Pathway ICT(Q)→ LE – In a previous work developed by our group at the CASSCF/6-31G* level [103] a S_2/S_1 conical intersection between the CT and LE states, accessible from FC zone, was located, which explains the appearance or absence of dual fluorescence based on LE ⇆ TICT model equilibrium. In the present study this CI between CT/LE state was found (geometry shown in Figure 5.15) at 114.79 kcal·mol^{-1} (Table 5.10), 11.4 kcal·mol^{-1} below the FC excitation energy, so it is accessible.

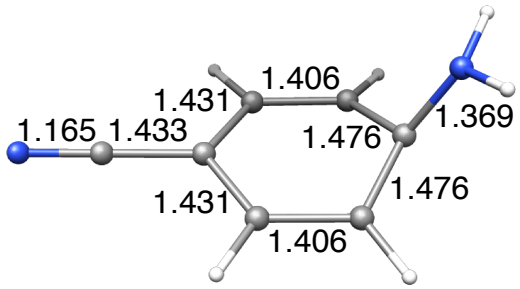

Figure 5.15: Geometrical parameters of the S_2/S_1 ICT(Q)/LE CI. Distances in angstroms.

Table 5.10: MS-CASPT2/cc-pVDZ energies relative to the S_0 minimum (in kcal·mol^{-1} of the conical intersections optimized at CASSCF/cc-pVDZ level. Calculations performed with a) SA2-CASSCF, b) SA9-CASSCF reference functions. The energies listed correspond to the average of the energies of the two state crossing at the CASSCF optimized geometries.

Geom	$E_{MS-CASPT2}$
S_3/S_2 CI	
CT-Q/RICT	128.07$^{(a)}$
CT-Q/CT-AQ	146.87$^{(a)}$
	138.86$^{(b)}$
S_2/S_1 CI	
CT-Q/LE	114.79$^{(a)}$

The branching space is dominated by skeletal deformations of the phenyl ring coupled with C-N stretch (see Figure 5.16). Thus the branching does not involve either the amino group twist or the pyramidalization coordinates and thus the S_2/S_1 degeneracy will be preserved along the torsional coordinate. In fact, the S_2/S_1 CT/LE radiationless decay can occur at any point of the extended conical intersection seam that results almost parallel to the amino torsional coordinate.

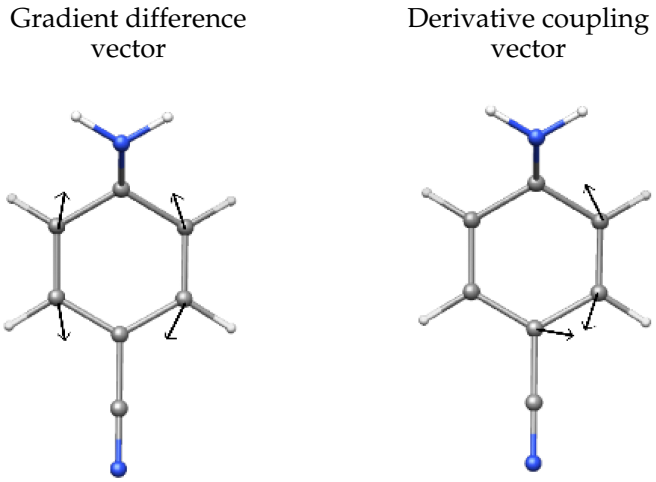

Figure 5.16: Branching space of CI S_2/S_1 between the ICT(Q) and LE states optimized at SA2-CASSCF/cc-pVDZ level.

The lowest energy point obtained on this conical intersection seam corresponds to a pyramidal structure where the amino group is untwisted; however, the seam is accessible for a large range of torsional angles so, if the decay takes place at large torsional angles, the probability of forming the S_1-TICT species enlarges, but in this ultrashort reaction a large amplitude twist of 90° is unlikely to occur in a solvent environment . When the minimum energy point of the CI was recalculated at CASPT2 level, it was still degenerated at SS-CASPT2 level (see Annex of this chapter), but mixing of states at MS-CASPT2 level splitted the energy of the two states (see Table 5.11).

Table 5.11: Eigenvectors of the diagonalization of the SA2-MS-CASPT2 effective Hamiltonian matrix in ICT(Q)/LE CI geometry optimized at CASSCF/cc-pVDZ level.

2 state averaged		
States	2 PM-CI	3 PM-CI
2-SA2-CASSCF	0.6684	-0.7438
3-SA2-CASSCF	-0.7438	-0.6684

A path between the FC and the ICT(Q)/LE CI geometries was calculated. Figure 5.17 shows that there is no barrier to access the CI so this first step in the deactivation process is barrierless.

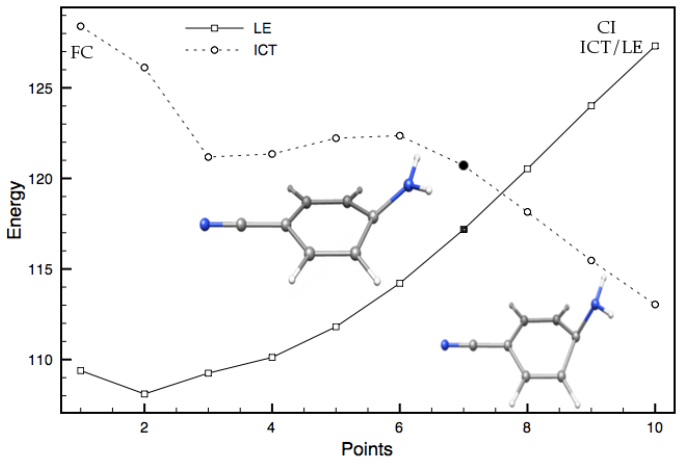

Figure 5.17: Profiles of the S_1 and S_2 excited states (LE and ICT) along the LIIRC path from the FC region to the geometry of the S_2/S_1 CI optimized at CASSCF level. Energies in kcal·mol^{-1} calculated at the MS-CASPT2/6-31G* level.

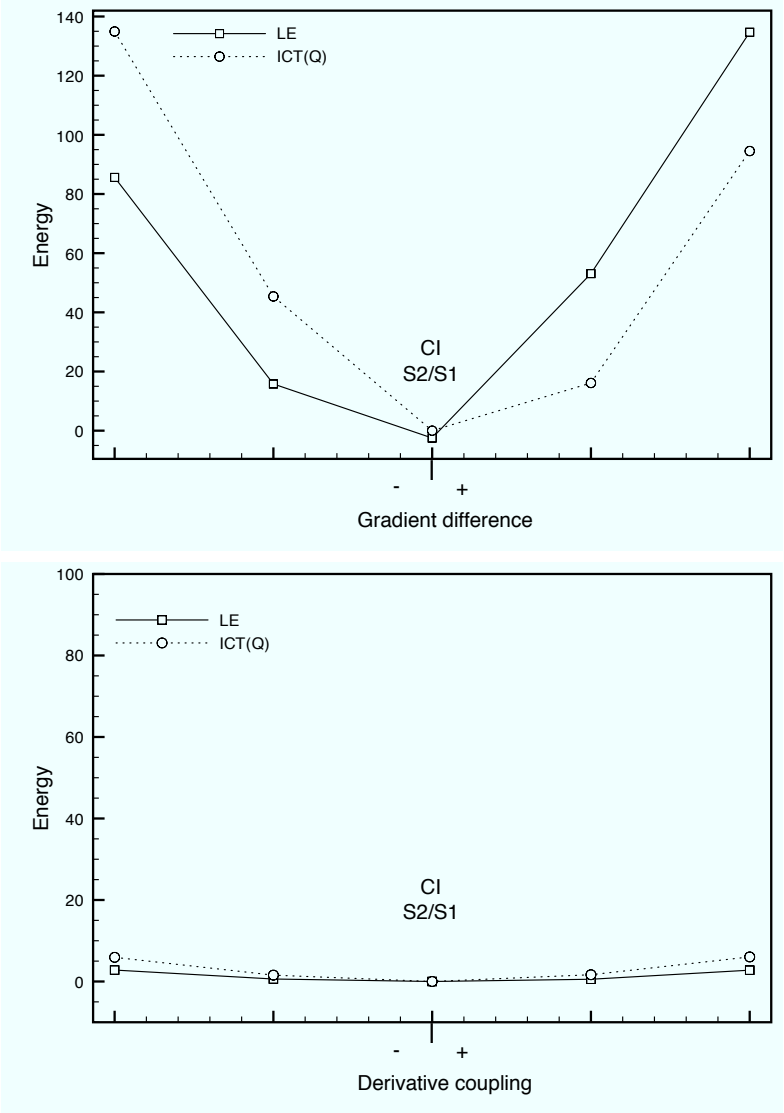

Figure 5.18: Energy plot of the Taylor expansion of the PES of the LE and ICT states at the LE/ICT CI, as a function of the gradient difference (GD) and the derivative coupling (DC) vectors.

It is interesting to comment the effect of the dynamic correlation in this crossing between two states that are affected in different extend by the dynamical correlation, stabilizing in major degree the upper state of CT character. As can be seen from the LIIRC path (see Figure 5.17), the decreasing of $\Delta E(S_1, S_2)$ with the inclusion of correlation, moves the position of the crossing to an earlier step of the path, to a point 6 showed in Figure 5.17. Its geometry is less pyrimidalized favouring the relaxation, after the crossing, towards the planar LE minimum. In spite that

the dynamic correlation tends to stabilize the ICT states, in ABN, it favours the population of the LE minimum.

But the actual evolution of the system when it reaches the CI also depends on the topology of the surfaces involved in the crossing in the neighbourhood of the CI. The zones near the CI have to be analysed in major detail. An inspection of the effect of the coordinates that remove the degeneracy have been done by means of a Taylor expansion as a function of the gradient difference and derivative coupling vectors. The plot of the energies (Figure 5.18) obtained show that the effect of the derivative coupling near conical intersection is negligible compared with the gradient difference effect.

Then two MEPS were computed starting from the CI geometry slightly modified by adding and subtracting the vector of the gradient difference. One of the MEPs relaxes to the LE minimum despite the other one relaxes to a S_1/S_0 conical intersection, that will be analysed later.

Pathway mediated by the ICT(CN) PES – From the S_2 (ICT) state, there is an accessible S_3/S_2 CI at 128.07 kcal·mol^{-1} (Figure 5.19), only 1.88 kcal·mol^{-1} higher in energy than the FC excitation (Table 5.27). At the geometry optimized at CASSCF level, the states are also degenerated at the MS-CASPT2 level. This CI involves a change of hybridation of the cyano group leading to a bent geometry. In the minimum energy crossing point the angle is of 145.46°.

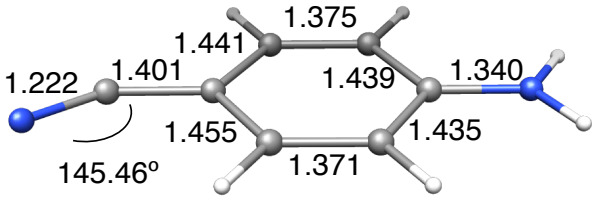

Figure 5.19: Geometrical parameters of the S_3/S_2 ICT(Q)/ICT(CN) CI. Distances in angstroms.

In the same way than before, a LIIRC path between FC and the RICT minimum (minimum energy structure of the ICT(CN) PES) was computed (see Figure 5.20). In this case the process along the LIIRC on S_2 is not barrierless 6.86 kcal·mol^{-1}, and the energy of the CI can be considered as the activation energy barrier, of 1.88

kcal·mol^{-1}. After reaching this ICT(Q)/ICT(CN) conical intersection, the ICT(CN) state is populated and the system could relax to RICT minimum.

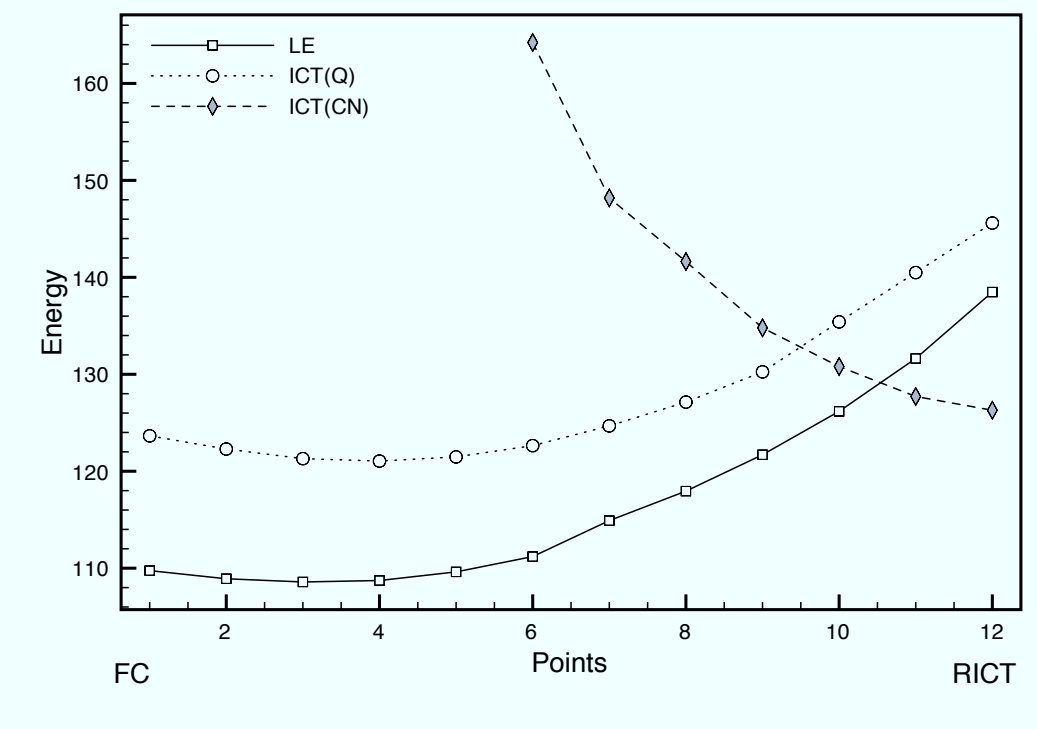

Figure 5.20: Profiles of the PES of LE, ICT(Q) and ICT(CN) excited states along the LIIRC path from the FC region to the RICT geometry optimized at CASSCF level. Energies in kcal·mol^{-1} calculated at the MS-CASPT2/6-31G* level.

Other pathways – In order to determine the possible involvement of the ICT(AQ) states in the deactivation mechanisms, a conical intersection S_3/S_2 between ICT(AQ) ICT(Q) was looked for. We found its minimum energy point 20.68 kcal·mol^{-1} (at SA3-CASSCF level) above the FC excitation energy. As commented in the Appendix of this chapter, the coupling of ICT(AQ) states at MS-CASPT2 level produces a new state ICT(AQ)' lower in energy and characterized by almost only the $\pi - Q \rightarrow \pi^* - AQ$ excitation. To describe properly this ICT(AQ) state, the energy of this S_3/S_2 CI was recalculated at SA9-CASSCF/MS-CASPT2 level. On the crossing, the ICT(AQ) state shows then the same nature than in FC region, with a contribution of 0.67 of $\pi - Q \rightarrow \pi^* - AQ$ excitation, and the crossing energy decreases. Nevertheless it is still 12.67 kcal·mol^{-1} higher in energy than the FC excitation, 24.07 kcal·mol^{-1} above the ICT/LE CI and 10.16 kcal·mol^{-1} above ICT(Q)/ICT(CN) conical intersection, so this ICT(AQ)/ICT(Q) is the least favourable.

Topology of the S_1 potential energy surfaces

We now turn to describe the topology of the S_1 surface. Given that all the LE, TICT and RICT minima are located on this surface, it is convenient to determine the adiabatic and non adiabatic paths that connect those minima.

Equilibrium LE-TICT – We have already describe in the previous subsection the CI that connects the LE and TICT minima. But this point corresponds to an upper limit for the energy of the TS of the adiabatic path, created in the neighbourhood of the CI due to the adjacent avoided crossing. We located at the CASSCF level the transition state, denoted $TS_{LE-TICT}$, connecting these stable species. The geometry obtained is shown in Figure 5.21.

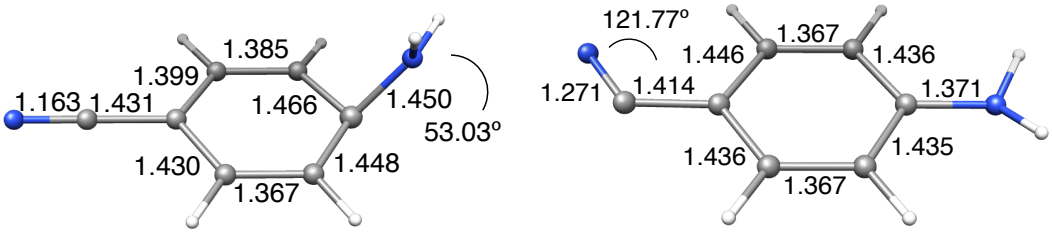

TS LE-TICT CI S_2/S_1 ICT(CN)/LE

Figure 5.21: Geometrical parameters of some critical points on the S_1 PES of ABN.

At the MS-CASPT2/cc-pVDZ level, the reaction LE $\rightarrow$ TICT on the S_1 PES of ABN is an endoergic process, by 7.76 kcal·mol^{-1}, with an activation barrier of 9.26 kcal·mol^{-1} (see Table 5.12). The barrier of the opposite process, TICT $\rightarrow$ LE, is reduced to 1.45 kcal·mol^{-1}. This structure is similar to the TICT minimum, so in this TS calculations a state average of three states was also necessary. With this SA3-CASSCF reference wave function, it is observed a mixing of CASSCF states at the MS-CASPT2 level (Table 5.12).

Thus, the S_1 $LE \rightarrow TICT$ equilibration will be controlled by *(a)* the position along the amino group twist coordinate where the S_2/S_1 CT/LE radiationless decay occurs and *(b)* the adiabatic S_1 torsional reaction path, where the reaction coordinate is dominated by the amino group twist, but also involves the quinoid/antiquinoid benzene ring skeletal deformations together with C-N stretching and the pyramidalization of the carbon atom in the C(NH_2) group. Figure 5.22 shows the profile of this reaction.

Table 5.12: CASSCF and MS-CASPT2/cc-pVDZ energies (in kcal·mol^{-1}), dipole moments and eigenvectors of the PM-CAS-CI wave functions in the $TS_{LE-TICT}$ optimized geometry of ABN.

CASSCF	MS-CASPT2	Dipole	States	1 (GS) PM-CI	2 PM-CI	3 PM-CI
	TS (LE-TICT)				Eigenvectors	
56	46.16	5.11	1-CASSCF	-0.9856	-0.1674	-0.0224
140.6	111.66	**9.17**	2-CASSCF	-0.0494	**-0.4133**	**0.9092**
155.49	137.04	3.93	3-CASSCF	-0.1615	**0.8951**	**0.4156**

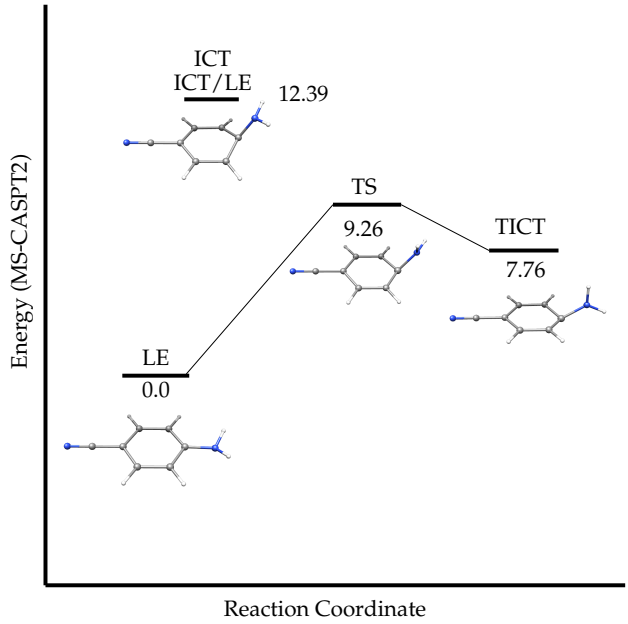

Figure 5.22: Schematic potential energy profile of the adiabatic path between the LE and TICT minima for ABN. Energies are in kcal·mol^{-1}.

Therefore in ABN the equilibrium lies in favour of LE, as the TICT minimum was found at considerably higher energy with a low reaction barrier toward LE in the adiabatic and non adiabatic paths. The minimum energy point of the CI has a pyramidal untwisted geometry. These characteristics explain why it is difficult to populate the TICT state from LE state and why the population of TICT will not be detectable.

Following the study of the S_1 topology, we looked for the non adiabatic pathways connecting the RICT minimum with the LE and TICT minima.

RICT-LE equilibrium – First of all, a CI between LE and RICT states was found, which geometry is shown in Figure 5.21. It is placed at an average energy of 127.48 kcal·mol^{-1} relative to the ground state minimum and 5.35 kcal·mol^{-1} above the RICT minimum (see Figure 5.13). Given the different effect of dynamic correlation in both states, an interpolated path between the RICT and LE minima was calculated at the MS-CASPT2 level (showed in Figure 5.23). In this way the barrier found from RICT to LE is very low, of about 3.7 kcal·mol^{-1}, and the LE minima is favoured in energetic grounds. Hence from this result we can deduce that, if the RICT minimum is populated, it will be quickly depopulated in favour of the LE minimum.

Table 5.13: CASSCF and MS-CASPT2/cc-pVDZ energies (in kcal·mol^{-1}), dipole moments (in Debyes) and eigenvectors of the PM-CAS-CI wave functions in the ICT(CN)/LE CI optimized geometry of ABN.

CASSCF	MS-CASPT2	Dipole	States	2 PM-CI	3 PM-CI
				Eigenvectors	
149.15	118.77	9.54	2-SA2-CASSCF	-0.6700	-0.7423
149.5	136.2	5.34	3-SA2-CASSCF	-0.7423	0.6700

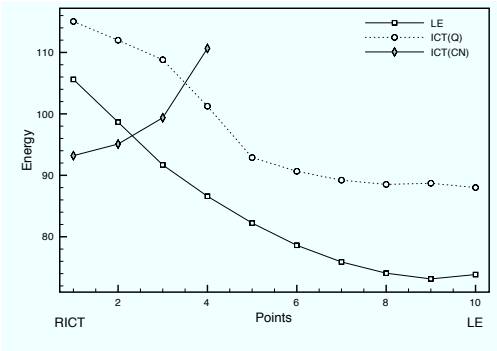

Figure 5.23: Profiles of the LE, ICT(Q) and ICT(CN) excited states along the LIIRC path from the RICT to the LE minima geometries. Energies in kcal·mol^{-1} calculated at the MS-CASPT2/6-31G* level.

RICT-TICT equilibrium – The RICT/TICT conical intersection was not found. Instead, we calculated the LIIRC linking the TICT and RICT minima. The profiles obtained at the MS-CASPT2/6-31G* level are shown in Figure 5.24. The $RICT \rightarrow TICT$ process shows a low barrier of about 5.29 kcal·mol^{-1}.Then, from the RICT minimum, the TICT minimum could be populated.

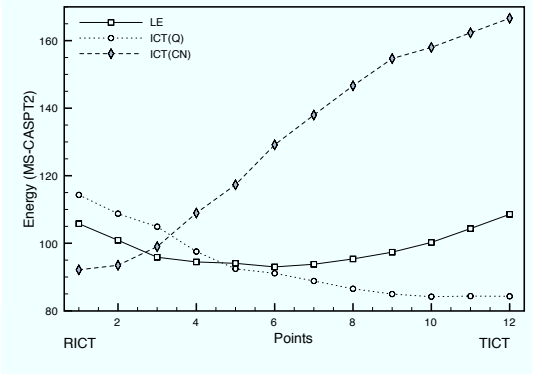

Figure 5.24: Profiles of the LE, ICT(Q) and ICT(CN) excited states along the LIIRC path from the RICT to TICT minimum. Energies in kcal·mol^{-1} calculated at the MS-CASPT2/6-31G* level.

These results show that there is a thermodynamic equilibrium between TICT, LE and RICT minima, given that all are connected and communicated on the S_1 PES.

5.3.4 Transient absorptions

From the experimental point of view, the population of the excited state minima can be checked by means of *excited state absorption* (ESA) spectra. The results and interpretation of these experiments, though, are not free of disagreements and controversy. Anyway, it is interesting to analyse the results of these experiments to have a reference for comparison of our computational results.

Most of the ESA experiments have been done for DMABN, that shows a different luminescent behaviour than ABN, but for this reason to compare results of both systems can be interesting. The complete set of computational results for *transient absorption* (TA) calculations are collected in Table 5.14. The experimental results and the tentative assignment of experimental bands based in our results are collected in Table 5.15.

Table 5.15 shows that the band observed in ABN at 295 nm and attributed to a LE transition [123, 130] could be assigned (based on the results of the Table 5.14 to a transition from the LE species or from the RICT one. The band at 320 nm, that appear both in the ESA spectra of DMABN and ABN, is attributed in the first one to a transition from the TICT intermediate [128] and in the second one to the LE species [123].

Table 5.14: Most intense (f > 0.01) MS-CASPT2/cc-pVDZ transient absorption energies (TA) and oscillator strengths of PM-CAS-CI in the ABN minima optimized at MS-CASPT2/cc-pVDZ level. The SA15-CASSCF is the reference function in the perturbation treatment.

Minimum	PM-CAS-CI states	TA (kcal·mol^{-1})	TA (nm)	f
LE	$2 \rightarrow 4$	41.35	691	0.03435
	$2 \rightarrow 7$	66.66	429	0.07506
	$2 \rightarrow 12$	100.72	284	0.14685
	$2 \rightarrow 14$	111.98	255	0.00803
RICT	$2 \rightarrow 5$	50.32	568	0.17767
	$2 \rightarrow 13$	98.78	289	0.21404
TICT	$2 \rightarrow 3$	24.83	1191	0.049620
	$2 \rightarrow 9$	86.32	331	0.014827
	$2 \rightarrow 15$	133.00	215	0.026930
PICT	$2 \rightarrow 4$	46.55	614	0.04750
	$2 \rightarrow 9$	76.17	375	0.02668
	$2 \rightarrow 13$	110.65	258	0.01891
	$2 \rightarrow 15$	116.11	246	0.01349

Table 5.15: Comparison of maximum band frequencies of ESA spectra of ABN and DMABN compared with theoretical results obtained at MS-CASPT2(12,11)/cc-pVDZ level and assignment of bands.

DMABN λ(nm) state	ABN λ(nm) state	Theoretical Results λ(nm) state f
300 LE	295 LE	284 LE 0.147 289 RICT 0.214
320 TICT	320 LE	330 TICT 0.015
349 LE		
420 TICT *only in polar solvent*		
450 LE	450 LE	429 LE 0.075
535 LE		
		Â£ 568 RICT 0.178 ?
> 660 LE > 680 RICT	> 650 RICT > 650 LE	
		Â£ 691 LE 0.034 ?

The band at 450 nm attributed in both DMABN and ABN to a LE transition [123], is obtained at 429 nm. The agreement, not as good as in previous cases, is nevertheless quite satisfactory (the energy difference correspond to 3 kcal·mol^{-1} approximately).

The most controverted band and the one obtained theoretically with the largest error is the band above 650 nm (680 nm for DMABN). From experimental evidences some authors assign this band to a LE transition, given than its decay time is the same than that of the 450 nm band (also assigned to a LE transition) [123, 130]. Other authors assign this band to the RICT specie [128]. Moreover Zachariasse has found similar bands in DMABN analogues without the cyano group [149], ruling out the possibility of assignment to the RICT transition and supporting further the assignment to a LE transition. On the other hand, this band blue shifts as the polarity of the solvent increases, fact related to solutes with large dipole moment, what supports the assignment to a RICT species transition [128] . The band at 450 nm does not shift with solvent polarity, argument that is used to support the hypothesis that this band can not be assigned to the same transient than that of the 650 nm band [128]. Consequently this argument indicates that the 650 nm band is not originated at the LE minimum. On top of this, the 650 nm band also blue shifts with increasing pump prove delay times, what is consistent with stabilization of the highly polar RICT (ICT(CN) state) species by reorientation of solvent molecules. Also, the decay time of this band is very short for DMABN in acetonitrile, but very long for ABN and DMABN in n-hexane, where the ICT reaction does not take place [124].

From the theoretical point of view, previous TDDFT results for ABN [124] assign this band to a transition from the RICT species, calculated at 571 nm, because only a $(\pi - \sigma^*) \rightarrow (\pi - \sigma^*)$ transition was obtained above 500 nm.

In this work we obtain two transitions that could be assigned to the 650 nm band; one at 568 nm that correspond to a ICT(CN) $\rightarrow$ ICT(CN) transition from the RICT intermediate and the other at 691 nm that correspond to a LE $\rightarrow$ ICT(Q) transition from the LE intermediate. The first band is coincident with the one obtained at TDDFT level. It is possible that the second one has not been found with TDDFT calculations due to the difficulties of this method to describe charge transfer states. Comparing our results with the experimental maximum of the band in n-hexane (approx. 650 nm), we can not assign the experimental band to one specific transition

on energetic grounds, given than the energy differences are similar (both of the order of 5 kcal·mol^{-1}). The relation between polarity of the species and shift of the bands could help.

We have to take into account first that the shift of a transition with different solvent polarity is not related only with the character of the initial state, it depends on the dipole moments of both states involved in the transition.

The band from the RICT specie (calculated at 568.2 nm) corresponds to an excitation from state 2 ($\mu = 13.76D$) to state 5 ($\mu = 9.2$). State 2 will be more stabilized with polar solvents than state 5, leading to an increase of the energy difference between both states, and to a shortening of the wavelength with a shifting of the spectra towards blue. Then, despite the energy does not fit well with experimental results, the behaviour with the solvent is in agreement, given that a blue shift is observed for this transition when the polarity of the solvent is increased.

On the other hand, the other LE transition is characterized by a promotion from state 2 ($\mu = 6.78D$) to state 4 ($\mu = 8.38D$) calculated at 691 nm. In polar solvent the upper state will be stabilized preferentially, decreasing the energy difference and consequently shifting the band to red. This is not in agreement with experimental results despite the vertical energies are in better agreement.

These arguments support the assignment of the 650 nm band to a transition from the RICT transient, supporting mechanism 2 that proposes the ICT(CN) state as intermediate of the ICT reaction. Nevertheless the wideness of the experimental band does not allow to rule out completely the contribution of a transition from the LE species to this band.

As a whole, our results support the hypothesis of the involvement of the ICT(CN) state and the population of the RICT species in the photochemistry of ABN, playing the role of an intermediate in the path of population of the LE minimum.

5.3.5 Deactivation pathways

Radiative deactivation

The emission properties of the system depend on the population of each minima, the probability of emission (related to f) and the competing radiationless deactiva-

tion pathways to S_0. These last ones lie high in energy , as will be shown in next subsections, so they will only be competitive at high temperatures. Here we focus on energies of possible emitting species and oscillator strengths (collected in Table 5.16) to predict the luminescent properties of ABN.

Table 5.16: MS-CASPT2/cc-pVDZ energies relative to the S_0 (in kcal·mol^{-1}) and oscillator strengths calculated of the characterized S_1 ABN minima optimized at CASSCF/cc-pVDZ level for LE and RICT minima and at MS-CASPT2/cc-pVDZ level for TICT minimum.

State	MS-CASPT2	f
LE	102.4	0.0069
RICT	122.14	0.0010
TICT	110.21	0.0060

In agreement with experimental results, our calculations show that the RICT state is a dark state , given its high energy and its low computed oscillator strength, f =0.001. On the other hand LE and CT states have f one order of magnitude higher, but the LE oscillator strength is larger, f= 0.007 in comparison with that of the TICT state of 0.006, and it is significantly more stable than TICT species. Thus the lack of ICT fluorescence in the gas phase must be attributed to the LE state energy relative to the TICT state, that displaces the population of the S_1 excited state to the LE minimum.

The only band observed in ABN is in good agreement with our mechanistic results, and also with the computed vertical energy emission for this state of 93.7 kcal·mol^{-1}, compared with the 90.0 kcal·mol^{-1} obtained experimentally in hexane [136].

Thermally activated radiationless deactivation

Since the fluorescence intensity of ABN strongly decreases upon increasing the temperature (ϕ_f = 0.021 and 0.009, at 25°C and 284°C in n-hexane respectively) [139], in this subsection we discuss the possible non radiative decay channels competing with the photochemical reaction path of the S_1 emission. We will restrict our study to the singlet manifold, so we will study the possible paths for internal conversion from S_1 to the ground state.

Figure 5.25 summarize a schematic profile of the different channels for S_1-S_0 internal conversion in ABN. It also displays the structures of the minimum energy points of the S_0/S_1 conical intersections located corresponding to the funnel for the internal conversion, as well as the transition states of the paths leading from the S_1-LE minimum to the CIs, when they exist.

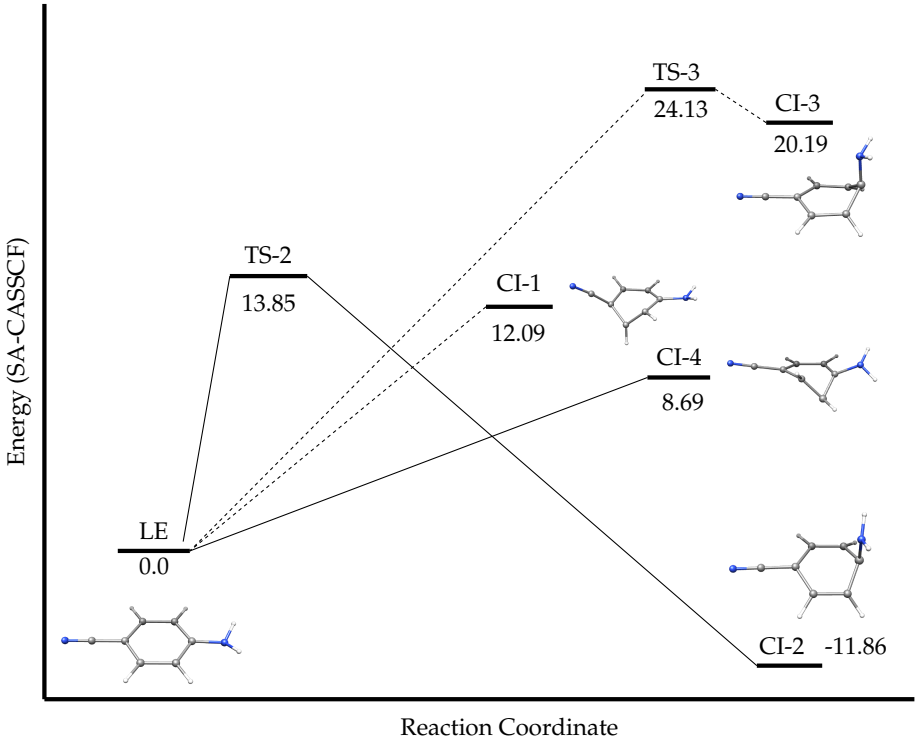

Figure 5.25: Schematic potential energy profiles regarding the S_0/S_1 internal conversion for ABN. MS-CASPT2 energies in kcal·mol^{-1}.

The energies of the S_0/S_1 CI and TS obtained at different computational levels are collected in Table 5.17, their molecular structures in Figure 5.26.

We have found four different reaction pathways through where the internal conversion can take place. All computed S_1/S_0 CI are of LE/S_0 character except C2 which is of CT/S_0 character. Because the distortion needed to take the system from the S_1-LE minimum to the funnel (mainly the folding or pyramidalization of different carbon atoms of the benzene ring) is strongly unfavourable energetically for the ground state, the energy gap between S_1 and S_0 is rapidly reduced along the coordinate, opening up internal conversion deactivation channels.

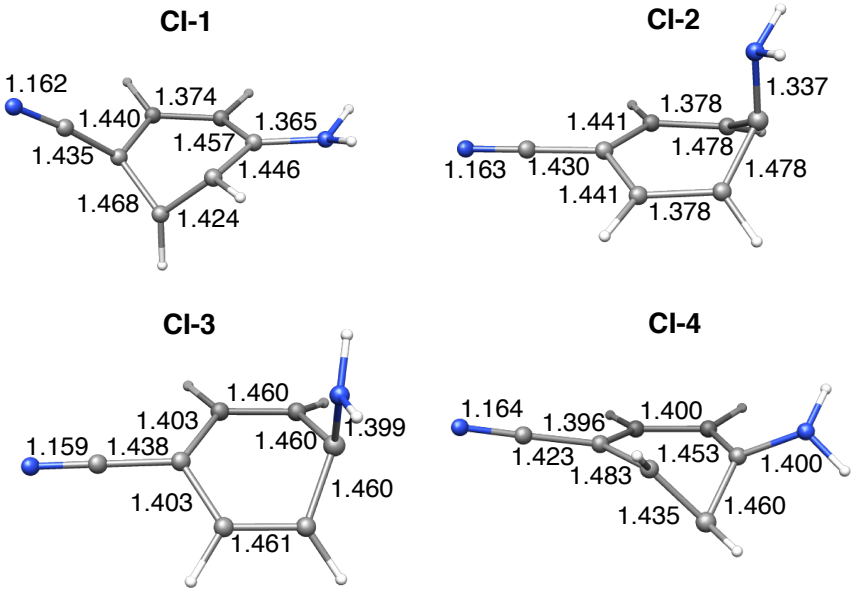

Figure 5.26: Geometrical parameters of the S_1/S_0 CIs for ABN optimized at CASSCF(12,11)/6-31G* level.

Table 5.17: MS-CASPT2/cc-pVDZ energies relative to the S_0 minimum of the critical points involved in the radiationless deactivation S_1/S_0 of ABN located at CASSCF/cc-pVDZ level.

Critical Points	$E_{MS-CASPT2}$
S_1/S_0 CI	
C1	114.49
C2	90.54
C3	122.59
C4	111.09
Transition states	
TS2	116.25
TS3	126.53

To characterize the radiationless deactivation mechanism is necessary to determine if the paths from the LE intermediate, which minimum is the one ultimately populated on the S_1 PES, to the different possible funnels have or does not have barriers. For this reason we looked for TSs along those paths.

We only located TSs in the paths corresponds to CI-2 and CI-3. To check if the absence of the TS in the paths to CI-1 and CI-4 was a computational problem or a

real absence of barrier, we analysed the shape of the CIs in more detail.

Let's recall that the peaked or slopped nature of a conical intersection (Figure 5.27) can be characterized by the values of the parameters Δ_{gh}, $\frac{S^x}{d_{gh}}$ and $\frac{S^y}{d_{gh}}$ (as explained in *Chapter 2*). The larger the values, the more degree of slopped character of the CI.

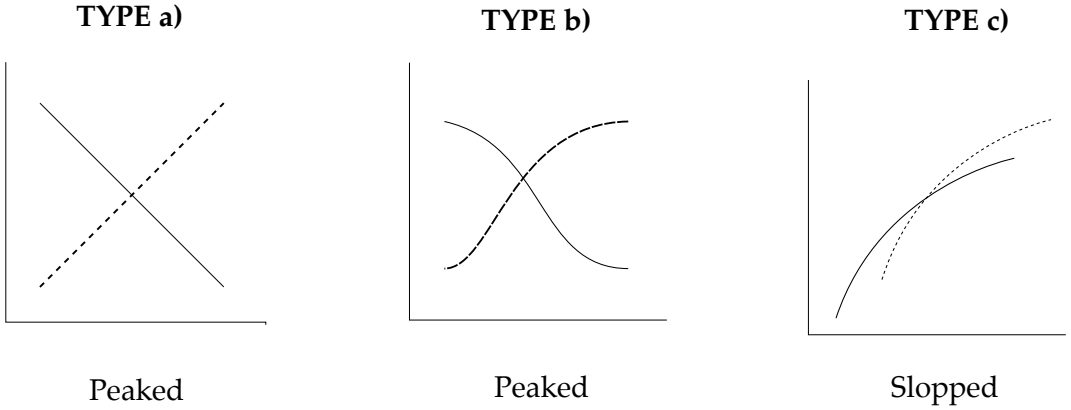

Figure 5.27: Schematic representation of the different type of conical intersections.

To reach a peaked CI along the upper surface it is expected to have to overcome a previous barrier, while in a slopped CI the crossing point will probably be the only critical point of the upper surface. For this reason we calculated Δ_{gh}, $\frac{S^x}{d_{gh}}$ and $\frac{S^y}{d_{gh}}$ for the four S_1/S_0 conical intersections found for ABN. The values obtained are shown in Table 5.18.

Table 5.18: Values of the parameters that describe the topology of a CI at the crossing points of the different radiationless deactivation channels of ABN.

Critical Points	CI-1	CI-2	CI-3	CI-4
Δ_{gh}	-0.14	-0.09	0.35	0.69
Sx/d_{GH}	-0.64	-0.46	0.61	-0.16
Sy/d_{GH}	-0.28	0.05	0.03	0.77

The most slopped conical intersection is CI-4 and the less slopped one is CI-2, followed not very close by CI-3. The more symmetric conical intersections are CI-1 and CI-2, as shown the small values of Δ_{gh}.

The absence of TS in the path to reach CI-1 and CI-4 and the presence in the case of CI-2 and CI-3 are explained by the different topology of the intersections as

evidenced by the values of the Table 5.18. The high energy of TS-2 is in agreement with the more pronounced peaked nature of CI-2 as compared with TS-3 and CI-3.

To check further the absence of TS in the paths to CI-1 and CI-4, we calculated the profile of the S_0 and S_1 surfaces at the CASPT2/6-31G* level by linear interpolation between the S_1-LE minimum and the corresponding S_0/S_1-CI. The results are showed in Figures 5.28 and 5.29.

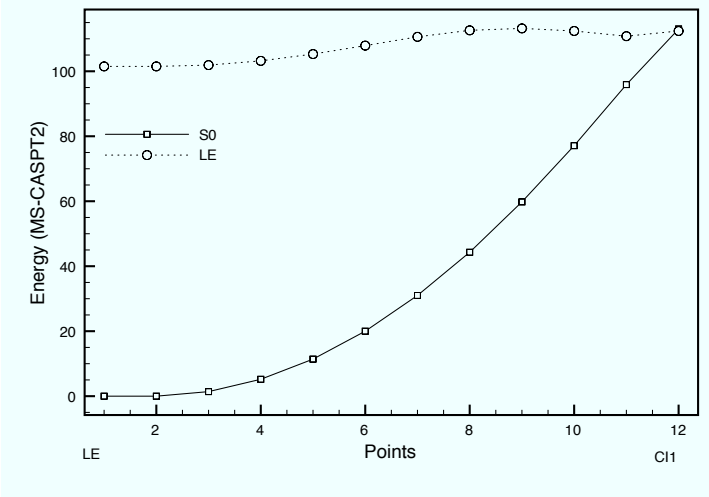

Figure 5.28: Profiles of the S_0 and S_1 potential energy surfaces along the LIIRC path between LE minimum and CI-1.

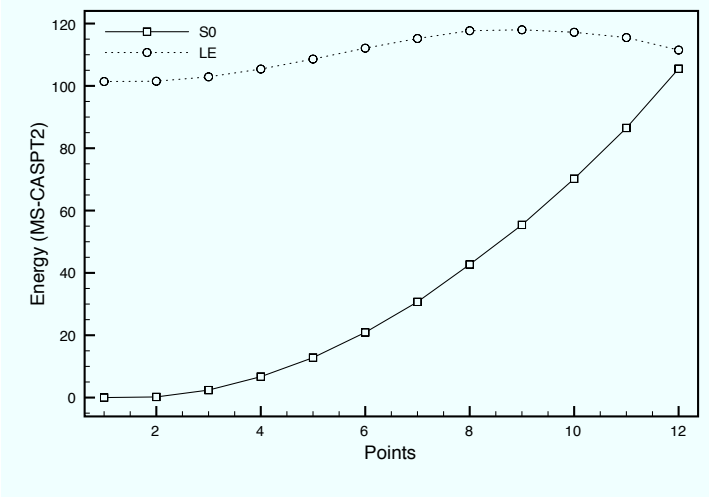

Figure 5.29: Profiles of the S_0 and S_1 potential energy surfaces along the LIIRC path between LE minimum and CI-4.

From these results, we can see that the S_0/S_1 conical intersection is almost the highest energy point in each S_1 profile, thus, its energy can be considered as the energy of the barrier of the internal conversion pathway.

As pointed out in ref. [139], the internal conversion activation energy measured experimentally corresponds to the barrier that has to be overcome to bring the system to the S_0/S_1 CI. The lowest activation barrier at the CASPT2 level is 8.69 kcal·mol^{-1}, corresponding to CI-4, in surprising good agreement with the 8.3 kcal·mol^{-1} estimated in [139] in n-hexane.

The large activation barriers found for the internal conversion in ABN explain that in this system this decay channel only becomes important above room temperature.

5.4 ABN tetrafluoro counterpart

F-substitution in the benzene ring of aminobenzonitriles leads to a decrease of the fluorescence quantum yield, by the opening of the internal conversion channel and enhancing the accessibility to a conical intersection connecting the excited state populated by the initial excitation and the electronic ground state.

Since 4-aminobenzonitrile and 2,3,5,6-tetrafluoro-4-aminobenzonitrile (ABN-4F) differ in the kind of emission spectra and in the fluorescence quantum yield, in the following section we present a study about the LE -ICT equilibration and the S_1/S_0 internal conversion as a competitive reaction path for the ICT emission in ABN-4F at the CASSCF/CASPT2/6-31G* level.

5.4.1 FC region

Ground state and absorption spectra

First of all the ground state geometry was optimized (geometry depicted in Figure 5.30). In this case a piramidalization angle θ of 40.0° was found and the bond distances were slightly smaller than those found for ABN. In this case, though, there are no experimental X-ray crystal structures neither previous theoretical res-

ults to compare. The computed dipole moment in the gas phase is 6.09 D, in good agreement with the value of 6.18 D obtained in non polar solvents [136].

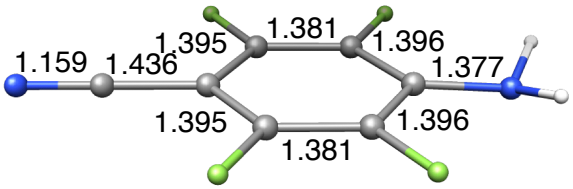

Figure 5.30: ABN-4F ground state geometrical parameters

Table 5.19 shows the energies of the lowest excited states of ABN-4F. The order of the states is the same than in ABN and in agreement with experimental results. The ICT is the most populated state after the first excitation with an oscillator strength of 0.57 (higher than for ABN). It is computed at 126.23 kcal·mol^{-1} above ground state, while experimental results [136] place the maximum of absorption band at 111.5 kcal·mol^{-1}.

Table 5.19: Vertical energies (in kcal·mol^{-1}), oscillator strengths, and dipole moments (μ in Debyes) for ABN-4F obtained at different levels of calculation based on the SA3-CASSCF reference function.

State	CASSCF	SS-CASPT2	μ	PM-State	MS-CASPT2	μ	f
S_0	0	0	5.43	S_0	0	6.09	
LE	115.83	112.59	5.12	LE	113.14	5.10	0.001
ICT(Q)	154.33	125.13	10.68	ICT(Q)	126.23	10.54	0.569

The energy gap between LE and CT in FC zone is 4 kcal·mol^{-1} smaller in ABN-4F than in ABN, which can be related with the larger efficiency of the ICT reaction in ABN-4F.

5.4.2 Minima on S_1

We located on the S_1 PES minima corresponding to the LE, ICT(Q) and ICT(CN) (LE, TICT and RICT) structures. Energies and geometries are shown in Table 5.20 and Figure 5.31.

Table 5.20: MS-CASPT2/cc-pVDZ energies relative to the S_0 minimum (E) (in kcal·mol^{-1}), dipole moments (in Debye) and oscillator strengths of the S_1 minima of ABN-4F obtained at CASSCF/6-31G* level. Calculated a) without state averaging and b) with the SA3-CASSCF reference function.

Minima	MS-CASPT2	Dipole	f
LE a	106.92	5.37	0.00347
RICT[a]	124.19	12.59	0.00128
TICT[a]	124.69	10.82	-
TICT[b]	112.28	10.47	0.00735

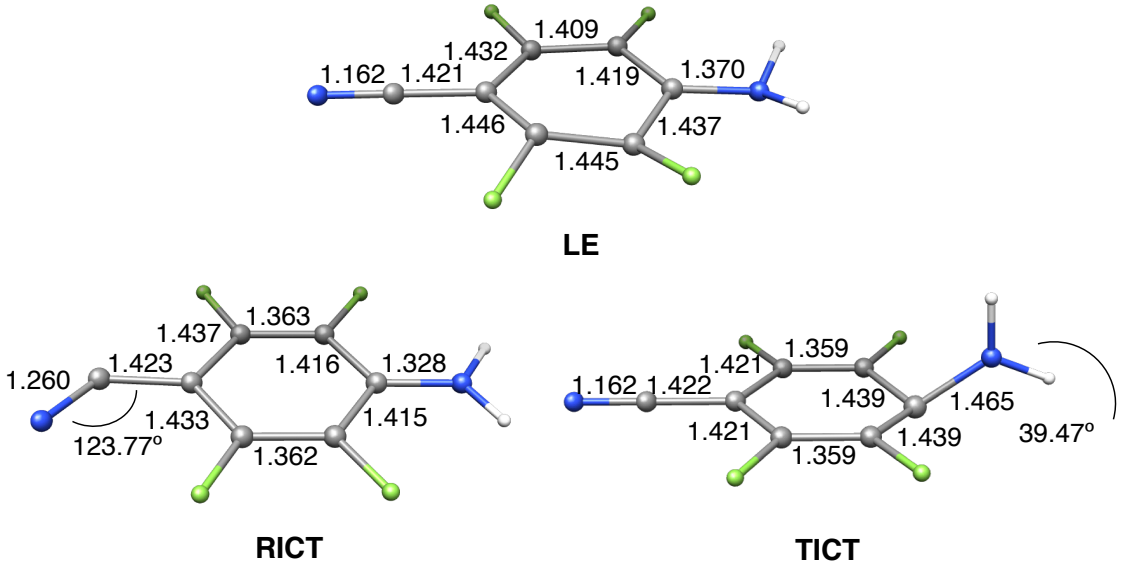

Figure 5.31: Geometrical parameters of S_1 minima of ABN-4F optimized at CASSCF/6-31G* level.

In ABN-4F, the S_1-LE structure has an anti-Kekulé benzene moiety with the hydrogen atoms of the amino group slightly out of the plane, like in the ground state structure. The computed dipole moment is 5.37 D. The most important feature of this structure is that, since the fluorine atoms enhance the tendency of non planar folding, the fluorine atoms lye almost 23° out from plane of the benzene ring.

Some fluoro substituted compounds show low energy excited states characterized by excitations from π molecular orbitals to σ^*_{C-F} . In order to check the involvement of these ($\pi - \sigma^*_{C-F}$) states in this minimum and its effect on the out of plane distortion, a single point with a more extended active space (12,12) with inclusion of the totally symmetric combination of C-F σ^* orbitals was done. The results con-

Table 5.21: CASSCF, SS-CASPT2 and MS-CASPT2/cc-pVDZ energies relative to the S_0 minimum (E), vertical energies (both in kcal·mol^{-1}), dipole moments (in Debye) and oscillator strengths of the characterized ABN-4F minima optimized at CASSCF/6-31G*. All single point CASSCF calculations were done with the state averaged procedure except labelled *r2*.

Minimum	Nature	CASSCF	SS-CASPT2	Dipole	MS-CASPT2	Dipole
LE	S_0	14.16	13.07	5.39	13.06	5.57
	LE	109.55	107.7	5.16	107.7	5.34
	r2-LE	108.67	106.92	5.37		
RICT	S_0	38.7	27.46	5.34	27.46	4.77
	ICT	150.42	126.84	10.05	126.84	9.23
	LE	169.11	144.05	6.04	144.05	4.25
RICT	r2-ICT	146.87	124.19	12.59		
TICT	S_0	43.33	37.13	3.34	37.13	3.17
	LE	135.99	120.48	4.87	112.28	10.47
	ICT	156.12	127.12	10.02	135.31	5.2
	r2-ICT	121.43	124.69	10.82		

firm that the ($\pi - \sigma^*_{C-F}$) state is not involved in the description of this state and the LE minimum has a pure LE character.

Concerning the TICT structure, the C(NH_2) group is pyramidalized as well as twisted, with a quinoidal distribution in the benzene ring and a N-phenyl bond length enlarged by 0.088 Å compared with the ground state. The computed dipole moment of 10.47 D for S_1-TICT is in good agreement with the (13.6$\pm$ 0.6) D estimated by Zachariasse for the ICT emitting species.(26) The PM-CAS-CI wave function of this ICT state has a main contribution (of 0.88) of the excitation $\pi - Q \rightarrow \pi^* - Q$.This structure is also of ICT character in second root without state averaging calculations in molcas package. According to the ICT in ABN-4F states are more stabilized.

Concerning the RICT minimum is characterized by a cyano bend angle of 123.77° and a quinoidal distribution of the ring. Its charge transfer character is observed by the high computed dipole moment of 12.59 D.

5.4.3 Mechanistic overview

Deactivation from S_2 to S_1

To study higher excited states, we also performed a SA13-CASSCF based calculation of the absorption spectra, whose results are shown in Table 5.22. The state characterization have placed at MS-CASPT2 level the LE state as first excited state, the ICT(Q) as the second excited state, ICT(AQ)' as the third excited state at 18.9 kcal·mol^{-1} above ICT(Q) (similar to ABN results where it was 22.79 kcal·mol^{-1} above) and the ICT(CN) state as the seventh excited state.

Table 5.22: Vertical energies (in kcal·mol^{-1}), oscillator strengths, and dipole moments (μ in Debyes) of SA13-CASSCF results for ABN-4F.

State	CASSCF	SS-CASPT2	μ	MS-CASPT2	μ	f
1	0	0.00	5.38	0.00	6.50	
2	114.3	112.32	5.12	113.66	5.20	0.00000
3	154.83	124.72	10.57	123.06	9.94	0.64008
4	175.77	165.45	4.52	141.96	9.24	0.44381
5	184.38	159.94	7.69	162.58	6.75	0.16081
6	188.88	175.74	1.99	168.89	7.14	0.62365
7	206.91	197.56	3.55	177.09	2.07	0.00000
8	210.73	183.66	6.40	185.12	6.33	0.00000
9	211.51	167.08	7.16	195.07	3.39	0.07440
10	212.58	175.86	4.58	196.08	5.47	0.00177
11	226.54	199.00	5.96	198.70	6.18	0.00834
12	241.46	225.94	2.90	222.30	6.30	0.00596
13	245.38	207.95	9.72	228.97	2.79	0.01001

For ABN-4F we performed a study similar to that of ABN. We first studied the possible paths of the deactivation from S_2 to S_1 and then the possible mechanisms of deactivation from S_1. In this study the geometry optimizations were all run with the 6-31G* basis set given that some test calculations on CIs (the critical points more sensitive to the basis set) showed that the results hardly change with the enlargement of the basis set (see Table 5.23).

We first computed the minimum energy path (MEP) from Franck-Condon region. In ABN-4F it leads directly to a S_2/S_1 conical intersection that resembles very much the one found in ABN (energy in Table 5.23 and geometry in Figure

Table 5.23: CASSCF, SS-CASPT2 and MS-CASPT2/cc-pVDZ energies relative to the S_0 minimum (E, in kcal·mol^{-1}), dipole moments (in Debye) of some critical points of ABN-4F located at CASSCF/6-31G* level.

Critical Points	CASSCF	SS-CASPT2	Dipole	MS-CASPT2
		Conical S_3/S_2		
ICT-Q/ICT(CN)	157.71	130.55	10.98	130.29
	157.84	131.41	11.50	131.67
		Conical S_2/S_1		
ICT-Q/LE	129.82	109.69	8.29	109.5
	130.97	117.9	4.84	118.08
ICT(CN)/LE	153.82	128.04	8.64	128.04
	154.56	142.59	4.19	142.59
		Transition States		
LE-TICT	148.99	112.50	9.67	112.59

5.32). Unlike ABN, no PICT structure has been found for ABN-4F. The reason for not being able to locate the planar ICT structure in this system could be the strong steric hindrance between the fluorine atoms of the phenyl ring and the amino group and also for the shallowness of the S_2 surface in this region. The S_2/S_1 CI where the MEP leads has ICT(Q)/LE character and is placed 12.44 kcal·mol^{-1} below the excitation energy.

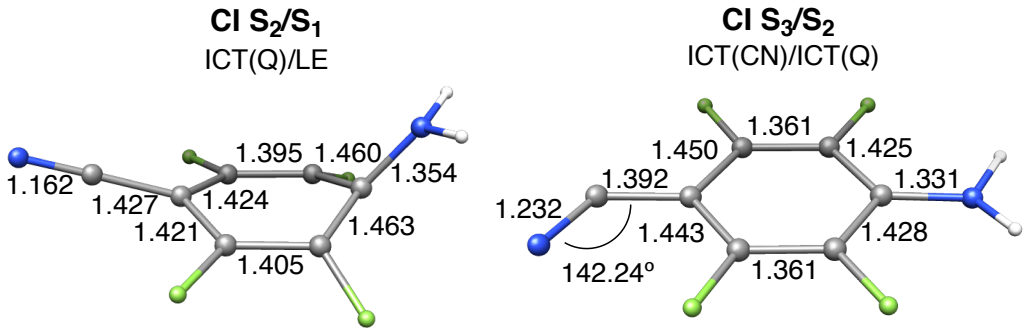

Figure 5.32: Geometrical parameters of the S_2/S_1 CI and S_3/S_2 CI

The most important point to make is that in both, ABN and ABN-4F, the branching space (shown in Figure 5.33) does not involve either the amino group twist or the pyramidalization coordinates and thus the S_1/S_2 degeneracy will be preserved

along the amino group torsion). Thus, S_2/S_1 internal conversion can take place over the full range of torsion angles, and both the S_1-LE and the S_1-TICT minima could be populated after internal conversion at any point of the seam. These results are in good agreement with the experiments of ultrafast dynamics reported by Fuss in different aminobenzonitrile derivatives [150–152] .They investigated a number of such compounds by transient ionization in the gas phase, initially exciting the higher-lying L_a like (S_2) state. They found the same relaxation path for all compounds: from S_2, the wave packet passes through a conical intersection in less than 100 fs. From there, a part of it reaches the S_1 (LE) state directly, whereas another part temporarily populates the ICT state. They observed also a temporary population of the ICT state in ABN, where equilibrated ICT population cannot be detected even in strongly polar solvents [152].

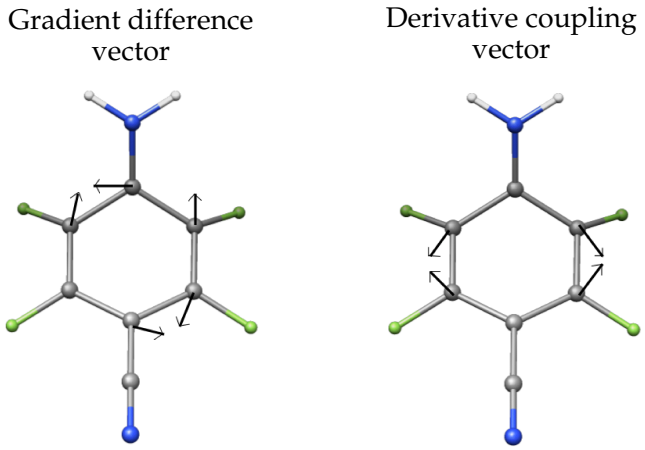

Figure 5.33: Branching space coordinates of the S_1/S_2 conical intersection located in ABN-4F

We also studied the ($\pi - \sigma^*$) mediated mechanism. The S_3/S_2 conical intersection between the ICT(CN) and ICT(Q) states is about 7.92 kcal·mol^{-1} higher than the initial absorption (see Table 5.23). If this CI is reached, the RICT minimum will be populated. Hence depending on the vibrational energy in bending coordinates following photoexcitation, this CI can be accessed. Following the relaxation on the ICT(CN) surface this state crosses the LE. The geometry of this CI has been optimized at CASSCF level. When the energy of the ICT(CN) and LE states are recalculated at the CASPT2 level, the energies of these states are far from degenerate (energy difference of 14.55 kcal·mol^{-1}, average energy 135.31 kcal·mol^{-1}), so a good

approximation of the energy of this CI can not be done at this level of calculation.

Globally, these results show that the most probable path to populate the minima of the S_1 PES in ABN-4F is through the CT/LE CI.

Radiative processes

We assume that, like in ABN, the minima located on the S_1 surface are all connected. The species that will emit and the quantum yield of fluorescence depend, consequently on the population and the oscillator strength of each minima.

As commented in the previous subsection, the most stable minima is the LE one, followed by the TICT structure, only 4 kcal·mol^{-1} higher in energy. RICT structure is the most inestable one so if its populated, it will be depopulated quickly. The difference between LE and TICT energies is smaller in the tetrafluoro counterpart than in the parent system by about 7 kcal·mol^{-1}.

The path linking adiabatically the LE and TICT minima was also studied. The barrier of the $LE \rightarrow TICT$ process calculated is 5.7 kcal·mol^{-1} high, while the barrier of the backward process is only 0.3 kcal·mol^{-1} high (see Figure 5.34). Since after the initial excitation the wave packet goes through the ICT/LE conical intersection and can relax along both states, both the LE and the TICT minima can be populated, although the thermodynamic equilibrium will favour the LE species. But in ABN-4F the oscillator strength for deactivation to the ground state system is larger for the ICT state in the TICT minimum than for the LE state in the LE minimum. For this reason, although the population of the TICT minimum is less favoured by kinetic factors, our results predict that ICT emission could be observed in ABN-4F in gas phase. The energy of this emission computed at CASPT2/cc-pVDZ level of 75.1 kcal·mol^{-1} agrees satisfactory with the 71.3 kcal·mol^{-1} measured experimentally in n-hexane [139].

Nevertheless, in ABN-4F the fluorescent quantum yield is very small, what indicates than there must exist a radiationless deactivation path very efficient. The possibility of this process along the singlet manifold will be studied in the next subsection.

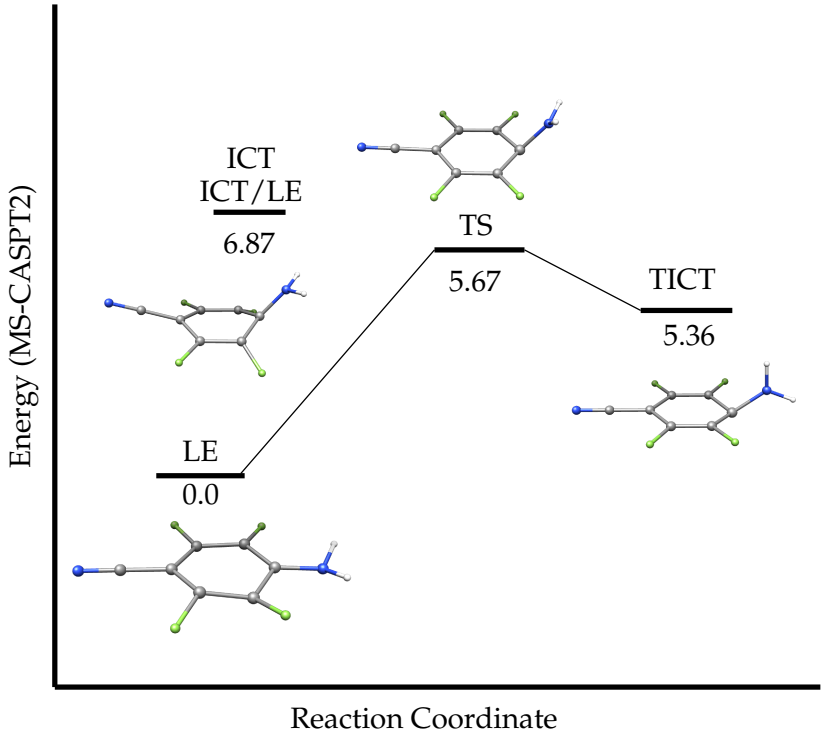

Figure 5.34: Schematic potential energy profile regarding the LE/TICT equilibration obtained at the CASSCF(12,11)/6-31G* level for ABN-4F. Depicted energies are MS-CASPT2 energies in kcal·mol^{-1}.

Radiationless deactivation: characterization of internal conversion channels

We discuss here the possible non radiative decay channels by internal conversion to the ground state from S_1 as a competing photochemical reaction path of the LE - ICT reaction. Figure 5.35 summarize a schematic potential energy profile for different deactivation channels through which the S_0/S_1 internal conversion can take place. In Table 5.24 CI S_1/S_0 energies are collected, while their molecular structures are depicted in Figure 5.36. All the CI structures, like in ABN, correspond to different bending of the phenyl ring and puckering of different C atoms out of the ring plane.

Like for ABN, all the S_1/S_0 crossings are of LE/S_0 character except CI-2 that is ICT(Q)/S_0, but all crossings lie lower in energy than in ABN. The parameters that describe the topology of the conical intersections are showed in Table 5.25. From them we can deduce that CI-1 and CI-3 are more slopped than CI-2 and CI-4.

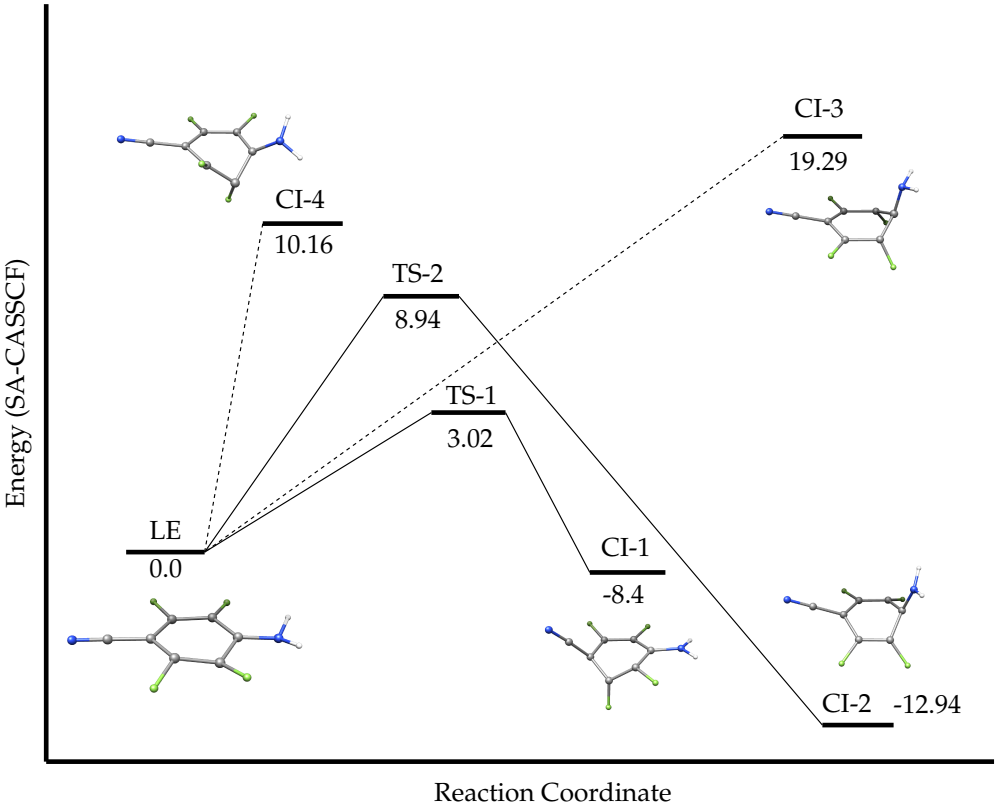

Figure 5.35: Schematic potential energy profiles regarding the radiationless deactivation mechanism obtained at the CASSCF(12,11)/6-31G* level for ABN-4F. Depicted energies are MS-CASPT2 energies in kcal·mol^{-1}.

Table 5.24: MS-CASPT2/cc-pVDZ energies relative to the S_0 minimum (in kcal·mol^{-1}) of the radiationless deactivation critical points of ABN-4F obtained at CASSCF/6-31G* level.

Critical Points	MS-CASPT2
S_1/S_0 CI	
C1	98.52
C2	93.98
C3	126.21
C4	117.08
Transition states	
TS1	103.9
TS2	115.86

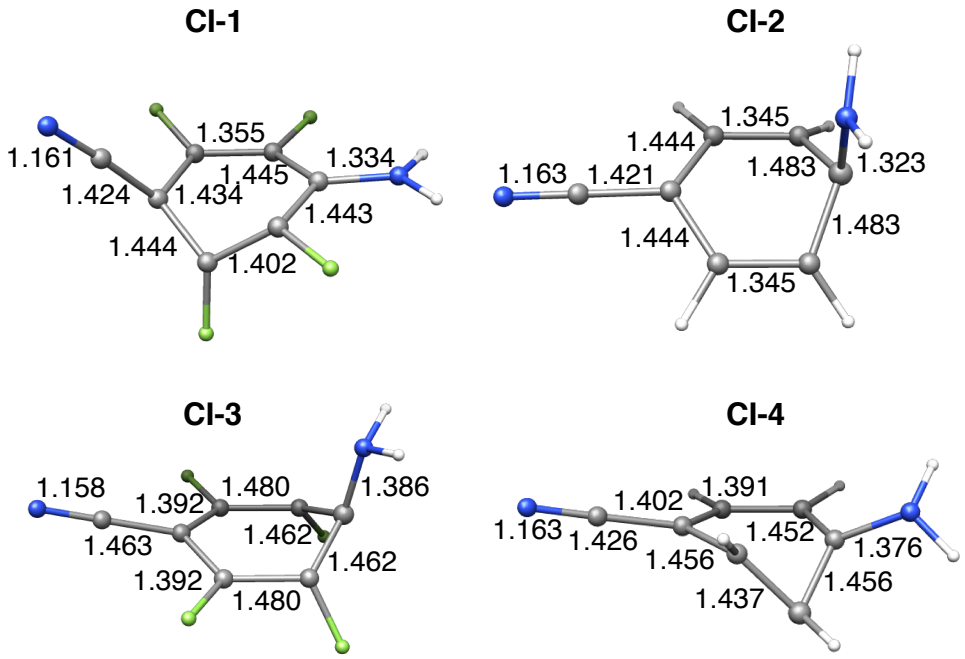

Figure 5.36: Geometrical parameters of the S_1/S_0 CIs optimized for ABN-4F.

Table 5.25: Values of the parameters that describe the topology of the CIs at the crossing points of the different radiationless deactivation channels of ABN-4F.

Critical Points	C1	C2	C3	C4
Dgh	0.87	0.25	-0.21	0.38
Sx/dGH	0.03	0.38	0.99	-0.31
Sy/dGH	-1.06	0.09	0.00	-0.21

In order to characterize activation barriers, transition states of the path from the LE minimum to the conical intersections were looked for. Only TS for the paths to CI-1 and CI-2 were found. The energies of the CI and the TS collected in Table 5.26 show that being optimized the geometries of critical points at CASSCF/6-31G* level, at the CASPT2 level it is difficult to establish accurately the height of the barriers of the processes studied.

To get a better estimate of some of these barriers, we calculated a profile of the S_0 and S_1 surfaces along the path from the LE minimum to the CI-1, CI-3 and CI-4 at the SA2-CASSCF/CASPT2/6-31G* level (see Figure 5.37, 5.38 and 5.39). For CI-1 (Figure 5.37), we observe that the S_1 surface is very flat, so the activation barrier

for this internal conversion channel is only about 2.7 kcal·mol^{-1}. Consequently we can consider this process barrierless, especially if we take into account the large amount of energy that the system retain from the initial excitation to the S_2 state. This is in good agreement with the slopped character assigned to CI-1. This result agrees satisfactory with the 3.0 and 4.6 kcal·mol^{-1} estimated for the 2-fluoro-4-(1-azetidinyl)benzonitrile (P4CF2) and 3-fluoro-4-(1-azetidinyl)benzonitrile (P4CF3) monofluorinated derivatives in cyclopentante [28].

Table 5.26: CASSCF, SS-CASPT2 and MS-CASPT2/cc-pVDZ energies relative to the S_0 minimum (E), vertical energies (both in kcal·mol^{-1}) and dipole moments (in Debye) of the critical points involved in the radiationless deactivation of ABN-4F obtained at CASSCF/6-31G* level.

Critical Points	Nature	CASSCF	SS-CASPT2	Dipole	MS-CASPT2
		S_1/S_0 CI			
C1	LE	111.99	90.92	7.45	88.61
	S_0	112.82	106.12	4.44	108.42
C2	ICT	107.2	89.63	10.88	89.1
	S_0	108.96	98.34	4.06	98.87
C3	LE	127.8	124.47	4.76	124.47
	S_0	127.83	127.95	5.04	127.95
C4	LE	127.68	114.81	6.43	111.92
	S_0	128.22	119.35	4.99	122.24
		Transition States			
TS1		113.02	102.96	6.82	103.9
TS2		121.49	114.69	5.53	115.86

As a consequence of the fact that the non radiative decay from S_1 to the ground state is almost a barrierless process in ABN-4F, internal conversion becomes the dominating process in this system. Thus, after population of the S_1-LE minimum, the system quickly will reach the S_0/S_1 CI-1, with a passage through the cone to the ground state like sand in a funnel, avoiding the normal fluorescence emission and ICT emission. Thus during the adiabatic ICT reaction from the LE state, the full 90° twist motion is strongly quenched by an ultrafast radiationless deactivation path via a conical intersection, characterized by out of plane deformations of the phenyl group. The addition of fluorine atoms drops the energy of the S_0/S_1 conical

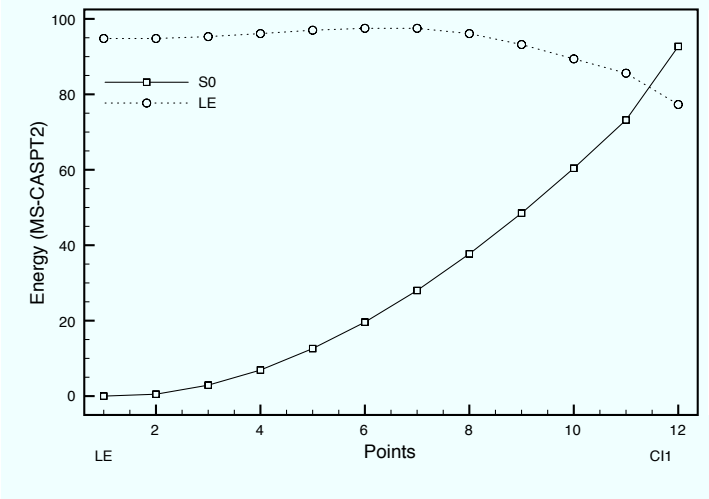

Figure 5.37: Profiles of the S_0 and S_1 potential energy surfaces along the LIIRC path between LE minimum and CI-1.

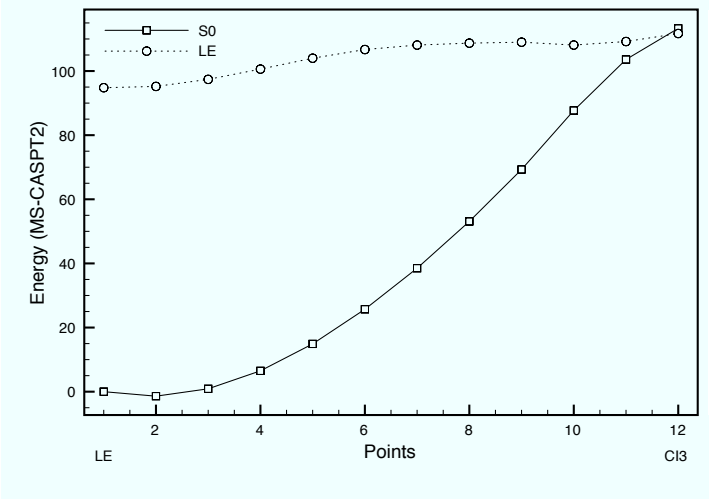

Figure 5.38: Profiles of the S_0 and S_1 potential energy surfaces along the LIIRC path between LE minimum and CI-3.

intersections due to the high electron affinity of fluorine, that leads to preference of sp^3 over sp^2 hybridization.

These results explain the fact that for ABN-4F the ICT fluorescence quantum yield in n-hexane is only 6.10^{-5} [139] and no emission from LE species could be detected.

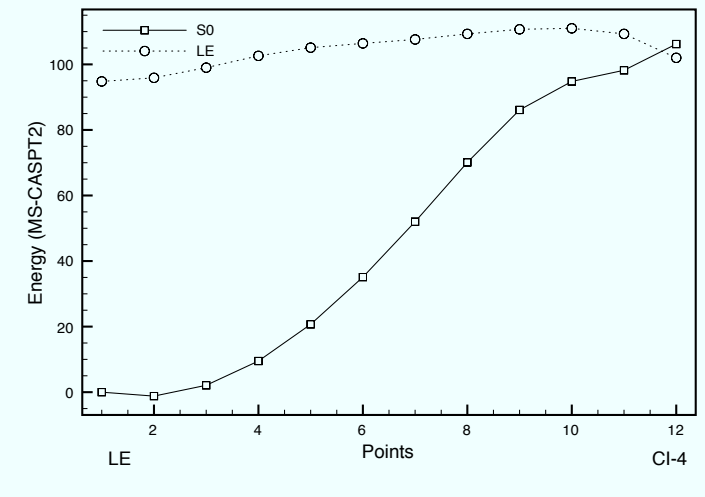

Figure 5.39: Profiles of the S_0 and S_1 potential energy surfaces along the LIIRC path between LE minimum and CI-4.

5.5 Summary

We have characterized for ABN and ABN-4F the low lying excited states: LE, ICT(Q), ICT(AQ), CN_{xy} and ICT(CN). According to our results only LE, ICT(Q) and ICT(CN) can be populated after the initial excitation. Initially the ICT(Q) state is populated. From there two different pathways along two different coordinates were found, an LE/ICT pathway and a pathway mediated by the ICT(CN) PES. The LE/ICT path involve a ICT(Q)/LE conical intersection and a thermodynamical equilibrium between both LE and ICT minima. On the other hand the ICT(CN) pathway comprises as a first step a conical intersection between ICT(Q)/ICT(CN) and a thermodynamic equilibrium between ICT(CN), LE and ICT(Q) minima, called RICT, LE and TICT respectively. The results show that all the obtained S_1 minima (LE, RICT, TICT) are connected and communicating. The population of the minima can be checked by means of excited state absorption spectra, although these results are not free of controversy expenses of controversy.

The topology of the potential energy surfaces in ABN-4F do no change in comparison with its counterpart ABN, what change are the energetics of the different species. A direct consequence of the F-substitution in the benzene ring is that the energy gap between the two excited states LE and CT is smaller in ABN-4F than in ABN, which may be one of the reasons why the ICT reaction is more efficient in the

first molecule.

In ABN the two LE/ICT and the ICT(CN)-mediated pathways are both energetically accessible, but the LE/ICT one is the most favoured. In the case of ABN-4F is obtained that only the ICT/LE pathway is energetically accessible. Actually, in both molecules the key to explain the different luminescence behaviour is the comparison of the energetics for the adiabatic and non adiabatic paths connecting the LE and ICT minima, and for the activation of different non radiative deactivation channels to the ground state.

In ABN-4F, F-substitution in the benzene ring leads to a decrease of the fluorescence quantum yield, opening the internal conversion channel and enhancing the accessibility to a conical intersection towards the electronic ground state. The internal conversion becomes the dominating process. Our results show that, after population of the locally excited minimum, the system will lead to a S_0/S_1 CI in an almost barrierless process. Since the passage through the cone of the conical intersection is like sand in a funnel, the normal fluorescence band from S_1-LE will not be observed. Moreover, the S_1-LE $\rightarrow$ S_1-TICT is an endoergic process by 5.36 kcal·mol^{-1}, with an activation barrier of 5.67 kcal·mol^{-1}, and a backward reaction barrier of 0.31 kcal·mol^{-1}. Then, after temporarily population of the S_1-TICT species, a small amount of the wave packet could be emitted radiatively to the ground state, explaining the low ICT fluorescence quantum yield (only 6.10^{-5}) in this system. On the other hand, the large activation barriers found in ABN explain that internal conversion in this molecule only becomes an important decay channel above room temperature. Moreover, the S_1-LE $\rightarrow$ S_1 TICT is an endoergic process by 7.76 kcal·mol^{-1}, with an activation barrier of 9.26 kcal·mol^{-1}, then the equilibrium is displaced towards S_1 -LE, from where the normal fluorescence band will be produced. We found that the ICT emission in ABN-4F takes place from a twisted structure. The RICT minimum is higher in energy in both system and its pobability of emission is low. Thus concerning the emission properties for these systems, we explain why in ABN-4F it is observed only the ICT anomalous band, computed in the gas phase at 75.1 kcal·mol^{-1}, while in ABN only the LE normal fluorescence band of 93.7 kcal·mol^{-1} is observed. The calculated emission energies are in good agreement with the available experimental data.

A2 Appendix: Influence of the number of states averaged on the description of the excited states at the GS geometry of ABN

It can be interesting to analyse the evolution of the excited states energies as the number of states averaged increases. Tables 5.27 to 5.31 show the results of averaging 3, 4, 5, 9 and again 13 states. The composition of the PM-CAS-CI wave functions in terms of CASSCF states are shown in Tables from 5.32 to 5.36.

Table 5.27: Vertical energies (in kcal·mol^{-1}), oscillator strengths (f), and dipole moments (μ in Debyes) of SA3-CASSCF ABN.

State	CASSCF	SS-CASPT2	μ	PM-State	MS-CASPT2	μ	f
S_0	0.00	0.00	5.40	S_0	0.00	6.08	
LE	109.78	108.65	5.13	LE	109.26	5.19	0.004482
ICT	153.43	124.98	10.25	ICT	126.19	10.29	0.449645

Table 5.28: Vertical energies (in kcal·mol^{-1}), oscillator strengths (f), and dipole moments (μ in Debyes) of SA4-CASSCF ABN.

State	CASSCF	SS-CASPT2	μ	PM-State	MS-CASPT2
S_0	0.00	0.00	5.39	S_0	0.00
LE	108.73	108.58	5.20	LE	107.99
ICT(Q)	153.71	125.24	10.20	ICT(Q)	126.36
ICT(AQ)	174.06	159.60	6.96	ICT(AQ)	161.30

Table 5.29: Vertical energies (in kcal·mol^{-1}), oscillator strengths (f), and dipole moments (μ in Debyes) of SA5-CASSCF ABN.

State	CASSCF	SS-CASPT2	μ	PM-State	MS-CASPT2
S_0	0.00	0.00	5.34	S_0	0.00
LE	108.64	108.83	5.14	LE	108.41
ICT(Q)	154.09	124.80	10.14	ICT(Q)	121.95
ICT(AQ)	174.95	159.96	6.87	**ICT(AQ)**	**161.88**
AQ →Q (s+d)	175.60	168.01	4.88	AQ→Q (s+d)	173.12

Table 5.30: Vertical energies (in kcal·mol^{-1}), oscillator strengths (f), and dipole moments (μ in Debyes) of SA9-CASSCF ABN.

State	CASSCF	SS-CASPT2	μ	PM-State	MS-CASPT2
S_0	0.00	0.00	5.35	S_0	0.00
LE	108.50	108.82	5.14	LE (+AQ)	106.03
ICT(Q)	154.57	124.52	10.10	ICT(Q)	121.57
AQ→Q (s+d)	174.58	167.49	4.68	**ICT(AQ)**	**145.77**
ICT(AQ)	175.44	160.09	6.84	ICT(AQ)	160.62
CNxy	195.73	179.30	1.79	AQ→Q (s+d)	171.62
ICT(AQ)	201.21	161.55	6.62	CNxy	180.46
D+A → R (a)	203.91	165.51	5.12	ICT(AQ)	186.07
D+A → R (b)	209.45	195.40	3.61	D+A → R (b)	200.90

Table 5.31: Vertical energies (in kcal·mol^{-1}), oscillator strengths (f), and dipole moments (μ in Debyes) of SA13-CASSCF ABN.

State	CASSCF	SS-CASPT2	PM-State	MS-CASPT2	μ	f
S_0	0	0	S_0	0	6.77	
LE	108.41	108.68	LE	106.25	6.3	0.0709
ICT(Q)	155.1	124.19	ICT(Q)	121.21	9.76	0.6231
AQ→Q (s+d)	174.3	167.23	ICT(AQ)'	144.99	8.32	0.3406
ICT(AQ)	175.38	160.35	ICT(AQ)	160.33	6.97	0.7065
CN_xy	190.78	177.91	D+A → R (b)	171.06	4.99	0.0187
ICT(AQ)	201.23	162.63	CN_xy	179.28	2.74	0.0000
D+A → R (a)	203.77	165.18	D+A → R (a)	183.77	3.31	0.0853
D+A → R (b)	205.9	193.12	ICT(CN)	186.23	6.26	0.1682
ICT(CN)	211.68	184.49	ICT(Q)	191.99	5.43	0.0003
$S_1$1	225.8	197.29	$S_1$1	209.18	4.36	0.0002
$S_1$2	231.17	211.56	$S_1$2	211.09	1.69	0.0001
$S_1$3	234.86	209.54	$S_1$3	216.96	3.18	0.0163

When 5 or less states are included in the state average of the reference function of the MS-CASPT2 treatment, the eigenvectors of the effective Hamiltonian show diagonal elements near to one (see Tables 5.32, 5.33 and 5.34). Therefore, these states do not interact via dynamic correlation. However this is not the case for the calculations with 9 and 13 state averaged, where some eigenfunctions show several eigenvectors with similarly large values.

Table 5.32: Eigenvectors of the MS-CASPT2 effective Hamiltonian matrix diagonalization of the first three low-lying states of ABN obtained with a SA3-CASSCF reference function.

3 state averaged			
States	1 (GS) PM-CI	2 PM-CI	3 PM-CI
	Eigenvectors		
GS	0.99759596	0.00001452	-0.06929860
2	-0.00001301	1.00000000	0.00002232
3	-0.06929860	0.00002136	-0.99759596

Table 5.33: Eigenvectors of the MS-CASPT2 effective Hamiltonian matrix diagonalization of the first four low-lying states of ABN obtained with a SA4-CASSCF reference function.

4 state averaged				
States	1 (GS) PM-CI	2 PM-CI	3 PM-CI	4 PM-CI
		Eigenvectors		
GS	0.99778520	-0.00001459	0.06651832	0.00000577
2	-0.00001377	-0.98919301	0.00000218	-0.14661920
3	-0.06651832	-0.00000696	0.99778520	0.00006801
4	-0.00000329	-0.14661920	-0.00006867	0.98919301

Table 5.34: Eigenvectors of the MS-CASPT2 effective Hamiltonian matrix diagonalization of the first five low-lying states of ABN obtained with a SA5-CASSCF reference function.

5 state averaged					
States	1 (GS) PM-CI	2 PM-CI	3 PM-CI	4 PM-CI	5 PM-CI
			Eigenvectors		
GS	-0.99690300	0.00003935	-0.07861796	0.00035001	-0.00187210
2	-0.00000956	-0.98900078	0.00028234	0.14791000	0.00010049
3	0.07471662	-0.00022228	-0.95432086	0.00014364	0.28929060
4	-0.00033023	-0.14791010	-0.00027874	-0.98900061	-0.00045680
5	-0.02453019	0.00010050	0.28825467	-0.00053021	0.95723938

The strong combination at the MS-CASPT2 level of the 5^{th} and 8^{th} CASSCF wave functions (evident in the composition of the 4^{th} PM-CAS-CI wave function in Tables 5.35 and 5.36) stabilized the MS-CASPT2 state in such a way that it becomes the the 3^{rd} excited state with an energetic stabilization of approximately 15 kcal·mol^{-1}. This big difference can be attributed to a different description of the state. Hence besides from the different effect of dynamic correlation on the SA-CASSCF states,

Table 5.35: Eigenvectors of the MS-CASPT2 effective Hamiltonian matrix diagonalization of the first nine low-lying states of ABN obtained with a SA9-CASSCF reference function.

9 state averaged					
States	1 (GS) PM-CI	2 PM-CI	3 PM-CI	4 PM-CI	5 PM-CI
			Eigenvectors		
1 CAS (GS)	-0.99539182	0.00000203	-0.09190022	0.00002075	0.02487752
2 CAS	-0.00001214	-0.94939018	0.00003425	**-0.31335357**	-0.00003027
3 CAS	-0.08404290	0.00000436	0.95124261	0.00011261	0.13587424
4 CAS	-0.02755961	0.00009883	0.26782767	-0.00039209	-0.23687613
5 CAS	-0.00002999	0.22252342	-0.00002268	**-0.71958882**	-0.00003805
6 CAS	-0.00000042	0.00042294	0.00000151	-0.00250996	-0.00000615
7 CAS	-0.02761376	0.00000565	0.05079175	0.00012051	-0.95195684
8 CAS	0.00000353	0.22167864	0.00002323	**-0.61967329**	0.00004487
9 CAS	-0.02469524	0.00001519	0.11126717	0.00002239	-0.13633479

States	6 PM-CI	7 PM-CI	8-PM-CI	9-PM-CI
			Eigenvectors	
1 CAS (GS)	0.00573080	-0.00000020	-0.00002376	0.00988592
2 CAS	-0.00004509	-0.00048121	-0.02162381	-0.00000156
3 CAS	-0.20957170	0.00000061	-0.00003443	0.16028776
4 CAS	0.90825110	-0.00000620	0.00023576	-0.21558809
5 CAS	-0.00046656	0.00102690	0.65777956	0.00018191
6 CAS	0.00000456	0.99998686	-0.00445003	-0.00000098
7 CAS	-0.21391992	-0.00000506	-0.00013483	0.21136247
8 CAS	-0.00010016	-0.00499955	-0.75288683	-0.00003742
9 CAS	-0.29217261	-0.00000025	0.00006681	-0.93971152

we have to take into account the possibility of a different description of the states at CASSCF and MS-CASPT2 levels, due to the possibility of interaction of CASSCF wave functions opened by the MS-CASPT2 treatment.

Let's have a more detailed look at the results obtained averaging 13 states. The 4^{th} low lying PM-CAS-CI state obtained in MS-CASPT2 calculations is composed mainly by two SA-CASSCF states with coefficients of 0.72 and 0.59 for the 5^{th} and 8^{th} SA-CASSCF state respectively (Table 5.36). The PM-CAS-CI wave function is composed mainly by one monoexcited CSF characterized by a promotion of an electron from a π-Q to π^*-AQ orbitals with a coefficient of 0.74. This state is labelled as ICT(AQ)'.

Table 5.36: Eigenvectors of the MS-CASPT2 effective Hamiltonian matrix diagonalization of the first thirteen low-lying states of ABN obtained with a SA13-CASSCF reference function.

States	1 (GS) PM-CI	2 PM-CI	3 PM-CI	4 PM-CI	5 PM-CI
			Eigenvectors		
1 CAS (GS)	-0.99429638	0.00000723	0.09304361	-0.00000601	-0.02460428
2 CAS	-0.00001376	-0.94762062	-0.00005447	0.31857252	0.00002210
3 CAS	-0.08567606	0.00002108	-0.94748997	-0.00011078	-0.15418784
4 CAS	-0.02601176	0.00008001	-0.26178071	0.00027605	0.22853804
5 CAS	-0.00001099	0.22842259	-0.00001205	**0.72391563**	0.00007189
6 CAS	0.00000009	-0.00020790	-0.00000001	-0.00146180	-0.00000476
7 CAS	0.02679503	-0.00001742	0.05391693	0.00005186	-0.93291830
8 CAS	0.00000411	0.21576213	-0.00002968	**0.59652683**	-0.00013633
9 CAS	0.03414364	0.00000516	0.14169256	0.00007685	-0.22862948
10 CAS	-0.00000017	-0.00013869	-0.00000002	-0.00005514	-0.00000012
11 CAS	-0.03839197	0.00000053	0.04574575	0.00006116	-0.02798341
12 CAS	0.00000041	-0.05731424	0.00003552	-0.13642291	-0.00007024
13 CAS	0.00003550	-0.00000014	0.00000386	0.00000008	-0.00009300

States	6 PM-CI	7 PM-CI	8-PM-CI	9-PM-CI	10-PM-CI
			Eigenvectors		
1 CAS (GS)	-0.01695697	0.00000139	0.00001553	-0.00000610	0.03812681
2 CAS	0.00002451	0.00028845	0.01665144	0.00032233	0.00001614
3 CAS	0.19712521	0.00000441	0.00004792	-0.00001862	0.12918456
4 CAS	-0.88983646	-0.00001953	-0.00022980	0.00005232	-0.29426354
5 CAS	0.00037199	-0.00017239	-0.59037769	-0.00587838	0.00023905
6 CAS	-0.00000985	0.98668496	-0.00346912	0.16259803	-0.00000938
7 CAS	-0.17994398	-0.00001196	-0.00025958	0.00002800	-0.22153679
8 CAS	0.00002701	0.00238591	0.76573352	0.00793322	-0.00017411
9 CAS	-0.31083298	0.00000813	0.00010094	-0.00007433	0.60357148
10 CAS	-0.00001066	0.16262464	0.00985726	-0.98663865	-0.00016287
11 CAS	0.20011986	-0.00003195	-0.00019731	0.00012485	-0.69418247
12 CAS	0.00003569	-0.00044681	0.25440072	0.00290532	-0.00021242
13 CAS	0.00033307	0.00001869	0.00000015	0.00002943	-0.00035063

The description at the CASSCF level of the MS-CASPT2 states is a good approximation for the lowest states of ABN at the FC region, with the exception of the 4^{th} and 8^{th} states, that couple via dynamic correlation. This conclusion, obtained at the FC region, is expected to be also of application for geometries close to FC zone.

CHAPTER 6

SIMPLE/DUAL FLUORESCENCE IN AMINOPYRIMIDINES

6.1 Introduction

Aminopyrimidines are molecules of increasing interest because of their important role as underlying constituents of several nucleobases (adenine, guanine and cytosine) and its presence in a large number of natural products [153] such as vitamin B1[154]. Amino substituted pyrimidines are also present in agrochemicals, pharmaceutical agents [155] and are common in material science [156–160].

As part of nucleobasis, pyrimidines are essential monomers to code genetic information. They show interesting photochemical properties and likely play an important role in some of the photochemical processes undergone by DNA. DNA and RNA bases absorb strongly in the UV range, but photoisomerization and subsequent photodegradation are rarely observed since the excess energy is efficiently dissipated through non radiative decay channels and transferred to the environment. These ultrafast decay pathways that enhance the photostability of these molecules are believed to be shared by all nucleobases. The deactivation seems to be deeply connected with the electronic structure of the pyrimidine ring. To un-

derstand the photophysics and photochemistry of DNA and RNA polymers, it is therefore advisable to consider the electronic excited states of single nucleobases as a first step. This strategy is reinforced by the fact that the multiconfigurational nature of the excited states makes necessary the use of expensive computational methods, not applicable to large molecules due to the current development of computational chemistry.

Due to the substitution of one or several pyrimidine hydrogen by amino or functionalized amino groups, aminopyrimidines are susceptible to undergo intramolecular charge transfer processes (ICT), because of the ability of the amino group to act as electron donor and of the acceptor character of the aromatic heterocycle. Since these two moieties are linked by a single bond, the state with charge separation can be favoured by rotation of the donor and the acceptor moieties and be further stabilized by an appropriate environment like a polar solvent [131, 161**?** –163].

If the CT species is stable enough, it can undergo radiative deactivation and produce an anomalous fluorescence band. The competition between the species responsible of the normal fluorescence, usually the locally excited, and the CT, gives raise to different luminescence patterns.

In the work presented in this chapter, we study the photochemistry of several aminopyrimidines that show different fluorescent characteristics. We will try to explain the differences observed experimentally by the differences found in the energetics and topology of the PES of the lowest excited states of these molecules.

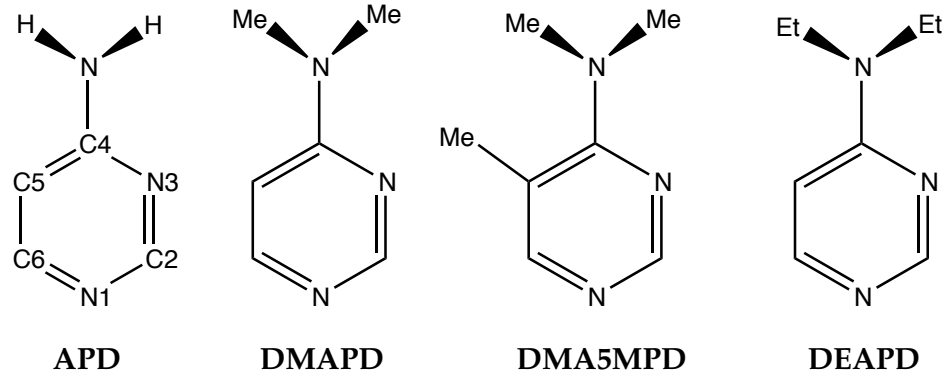

Figure 6.1: Structure of some aminopyrimidine derivatives

The systems studied, collected in Figure 6.1, have been chosen to be as similar

as possible, but having different fluorescence patterns, to show up the factors that determine the luminescent behaviour. For instance, whereas 4-aminopyrimidine (APD) does not exhibit any fluorescence even in highly polar aprotic solvents, 4-dimethylaminopyrimidine (DMAPD) shows only the normal fluorescence band in gas phase as well as in polar solvents. On the other hand, the 5-methyl substituted molecule 4-dimethylamino-5-methylpyrimidine (DMA5MPD) present normal fluorescence in gas phase and only anomalous fluorescence in polar aprotic solvents. Intriguingly, 4-diethyl-APD (DEAPD) shows only the normal band in gas phase, but dual fluorescence in highly polar aprotic solvents.

Hence, depending on structural or environmental factors, the fluorescence spectrum can show only the normal fluorescence band, the red-shifted anomalous band, or both, taking then place the so called dual fluorescence. Therefore nature and position of the substituents affects the photochemical properties of APDs. These results have been explained qualitatively by the twisted intramolecular CT (TICT) model and steric interactions between the substituents, although the reason for the different behaviour between DMAPD and DEAPD among other things is still obscure [31, 32].

In spite of the interesting properties of this kind of molecules, for some time they have not attracted much attention, probably because main efforts have been directed towards the aminobenzonitrile family of compounds, which present a very promising solvent dependent fluorescence.[164, 165]. However, more recently the discovery of the several possible deactivation pathways for adenine [166] has renewed the interest in aminopyrimidines and some theoretical studies have already been addressed to the deactivation pathways of aminopyrimidine [29, 30].

In the adenine case, the deactivation can take place via out of plane ring deformation or by means of specific bond-breaking processes but, according to energetic considerations, the first hypothesis seems to be more probable [166–169]. Concerning aminopyrimidine, recent studies pointed out the existence of several excited states of $^1(\pi - \pi^*)$ and $^1(n - \pi^*)$ character which play a role in the deactivation pathways. In particular, in the latest studies by Barbatti et al. [30], these authors found several stable intermediates in the S_1 PES of the $^1(n - \pi^*)$ state, the one populated by the initial excitation. They also found a $^1(\pi - \pi^*)/S_0$ crossings seam, obviously involved in the deactivation mechanisms, and located in it several minimum energy points. The different connexion between the minima and the cross-

ings points give place to several possible deactivation paths, some of them almost barrierless, allowing an ultrafast deactivation taking place. Some of the structures optimized by the authors show planar rings while in others different C atoms of the ring appears puckering. These works though do not study the charge transfer reaction of aminopyrimidines, nor the luminescent processes that can occur in these systems.

Scope

The aim of the work presented in this chapter is to understand in detail the photochemistry of the aminopyrimidines, studying the ICT mechanism and the competitive photodeactivation pathways to rationalize the effect of the substituents in the photochemical properties of this family of molecules. At the same time, we perform a exhaustive analysis of the nature of the excited states to rationalize the character of the S_1 stable species located and the origin of out of plane crossing seams. Hence the work developed can be structured in several steps:

- First we have carried out a complete study of the photochemistry of the prototype molecule APD.
- In a second stage, we have analysed the effect of the substituents in the study of the derivatives DMAPD and DMA5MPD in gas phase and in a polar solvent.
- Finally, we have performed some calculations on the DEAPD derivative to explain its intriguing luminescent behaviour.

6.2 Computational details

With the computer resources available today, it is not possible to treat a system of this size without rather drastic compromises regarding basis set as well as treatment of electron correlation. The problems of basis set deficiency and of insufficient inclusion of correlation effects are interrelated, and both are aggravated by the need of describing several electronic states, of quite dissimilar nature, in a balanced way.

The ground state and the six lower singlet excited states for APD, DMAPD, DEAP and DMA5MPD have been studied using the CASSCF/CASPT2 strategy we have used before [61, 100]. The basis set employed was the double zeta plus polarization 6-31G* basis set [101] for all the atoms. State averaged CASSCF calculations were run. The number of states average was determined after testing (see the Appendix of this chapter).

Full geometry optimizations were performed without any symmetry constraint and numerical frequency calculations were run to determine the nature of the stationary points at the CASSCF level. Conical intersections were optimized by using state-averaged orbitals without including the orbital rotation derivative correction to the gradient, which is usually small.

The energies presented and discussed along this chapter are those calculated at the MS-CASPT2 level, unless otherwise stated. The imaginary level shift technique [107] was used with a shift parameter of 0.3 au. The effect of the dynamic correlation in the energy is not the same for all the excited states considered. As a consequence, the magnitude of the energy difference between states change substantially when calculated at the CASSCF or at the MS-CASPT2 level [113, 170]. This affects mainly to the CIs, whose location becomes a highly non-trivial task, since the standard procedure is to locate the minimum energy point of degeneracy at the CASSCF level. When the energies of the states involved in the CI located are recalculated at the MS-CASPT2 level, the states can become non-degenerate, and in some cases the energy difference can be quite large. Given that the cost of the CI optimization at the MS-CASPT2 level is not computationally affordable as a routine procedure, to estimate the position and energy of the crossing when the CASSCF description is not accurate enough, linear interpolated internal reaction coordinate (LIIRC) paths are calculated at the MS-CASPT2 level between the minima of the crossing states, to get the energetic profiles of the states of interest along this path, and with them the points of crossing.

The active space employed in these calculations consists of 12 electrons and 11 orbitals (CAS(12,11)), which include the seven orbitals of the aminopyrimidine π system, the two N lone pairs of the in-ring N atoms (n_N), and two additional diffuse n_N pair type orbitals (see Figure 6.2). These two n_N orbitals were included in the active space after analysis of the state average molecular orbitals and the contribution of the configuration state functions (CSF) obtained at CASSCF/MS-

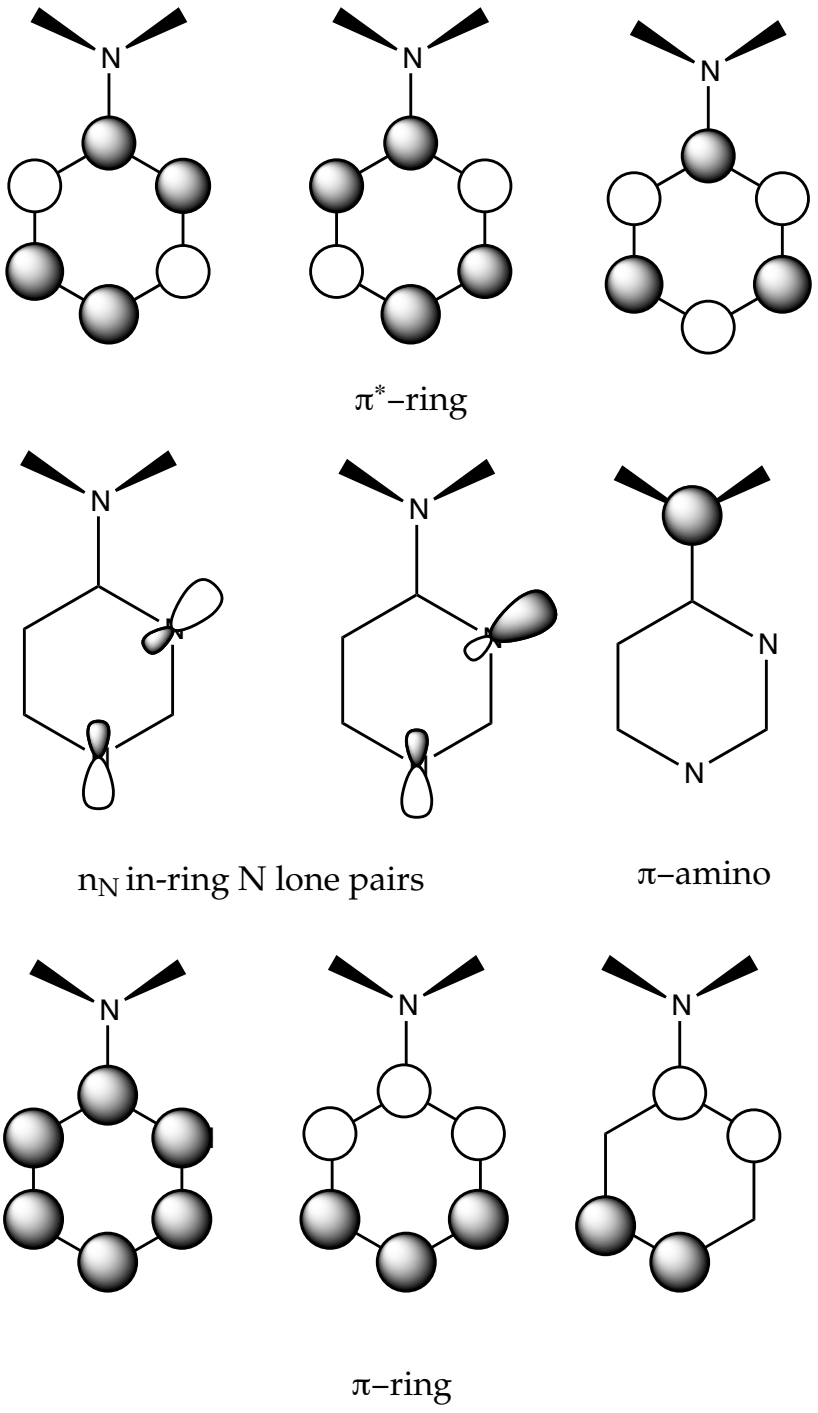

Figure 6.2: Schematic representation of the orbitals included in the CAS(12,9) calculations. The two extra orbitals included in the CAS(12,11) calculations are of the in-ring N lone pairs type

CASPT2 level with the smaller active space (12,9) for the ground state minimum and the lower singlet states in the Franck Condon region. This analysis, explained in detail in the Appendix of this chapter, shows an important mixing at the MS-CASPT2 level between the states involving the n_N. The strategy of increasing the CAS size to (12,11) allows the correlation associated with such lone pairs to be included already at the CASSCF level, and consequently the obtained energies are more accurate and the mixing between states is removed, so the physical analysis of the results becomes clearer [113, 170, 171].

The CASSI protocol and the PM-CAS-CI functions were used to compute transition dipole moments and oscillator strengths.

To take into account the solvent effects in the photochemistry of the APD derivatives, the reaction field formalism was used and a Conductor Polarizable Continuum Model (C-PCM) [172–174] was employed. The solvent parameters correspond to acetonitrile, to try to reproduce the usual experimental conditions, and the size of the tesserae of the solute cavity was set to 0.4 $Å^2$. Since the object of study is the emission of S_1 intermediates, the second root is used to generate the solvation charges, which will perturb the rest of the states considered.

In the presentation of the results and discussion of the physical nature of the states, only the configurations that contribute most to the results are taken into account. However, the data were generated using all the possible configurations necessary to get an accurate description of the states.

6.3 Results and Discussion

6.3.1 Parent system APD

The study of the parent system ADP, the smallest of the series of molecules studied, has been the first one and the most exhaustively developed. With this more detailed study, we have determined the most adequate computational parameters to get the best rate precision/cost and to get an adequate description of the states that provides a clear physical analysis of the results. We also analyse here which are the key areas of the PES that determine the photochemistry, and consequently the areas where we will focus our attention in the study of the derivatives.

FC energies and nature of excited states

First of all, we computed the energy and analysed the nature of the singlet lowest energy excited states at the optimized geometry of the ground state of APD. We found several types of excited states, schematize in Figure 6.3. To achieve this simplified description of the physical nature of the states, a detailed analysis of the results derived from several sets of test calculations was performed. This analysis is described in the Appendix of this chapter.

The character of the 6 lowest energy excited states found can be described as follow:

- a locally excited state state, LE, originated by an (π-π^*) excitation in the ring.
- four states generated by excitations of the n_N in ring lone pairs to the lowest π^*-ring orbitals, labelled NS and NA to indicate excitation from the symmetric (NS) or antisymmetric (NA) combination of n_N orbitals.
- a charge transfer state (CT), characterized by the transition of charge from the amino group to the π^*-ring orbitals.

Table 6.1 shows the energy of these states at the FC region obtained at different levels of calculation using a SA7-CASSCF(12,11) reference wave function. At the CASSCF level, the lack of dynamic correlation precludes a correct calculation of the energy of the CT state, which appears as the 5^{th} excited state. On the other hand, at this level of calculation the LE state is favoured and it appears to be the 1st excited state.

Table 6.1: CASSCF(12,11), SS-CASPT2(12,11) and MS-CASPT2(12,11) vertical energies (in kcal·mol^{-1}), oscillator strengths (f), and dipole moments (μ in Debyes) obtained using SA7-CASSCF(12,11) reference function for APD.

State	CASSCF	SS-State	SS-CASPT2	PM-State	MS-CASPT2	μ	f
S_0	0.0	S_0	0.0	S_0	0.0	3.09	
LE	124.0	NA1	117.2	NA1	116.5	1.75	0.0043
NA1	133.2	LE	121.3	LE	122.3	3.17	0.0141
NA2	138.6	NA2	123.0	NA2	124.7	1.89	0.0097
NS1	168.8	CT	144.7	CT	146.9	5.68	**0.1887**
CT	173.9	NS1	150.3	NS1	151.5	1.58	0.0046
NS2	176.8	NS2	157.8	NS2	159.6	2.50	0.0043

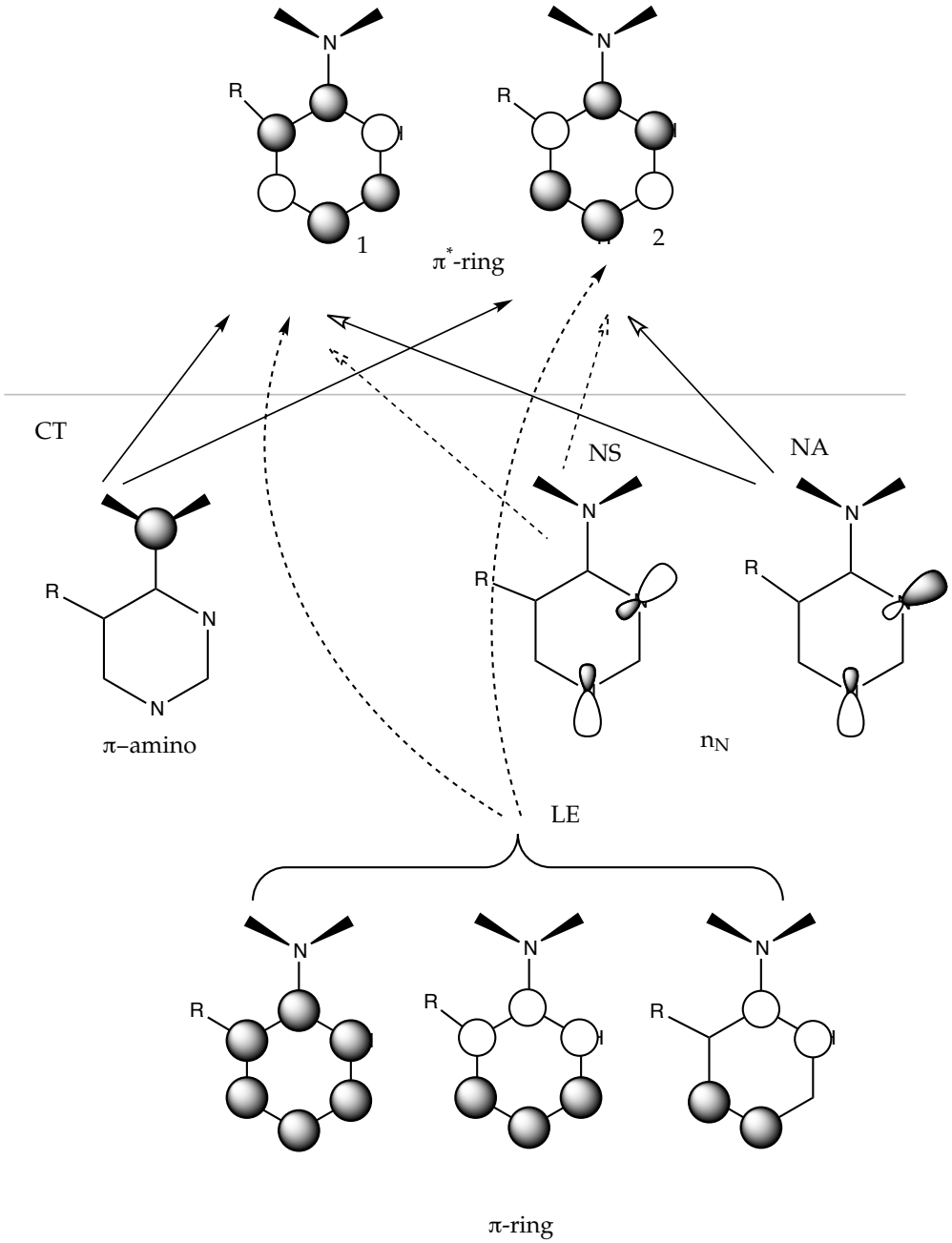

Figure 6.3: Schematic representation of the calculated excitations. The grey line separates the occupied orbitals (below the line) and the virtual π^* orbitals (labelled 1 and 2), which are responsible for the main excitations. The type of transition is also labelled: CT stands for charge transfer (solid lines and arrows), LE for local excitation (dashed lines and solid arrows) and NS and NA, for the excitations arising from the two possible combinations of the N lone pair orbitals (hollowed arrows).

When dynamic correlation is taken into account, the most noteworthy change is the large reduction of the CT state excitation energy. This large stabilization is not completely unexpected. Apart from the possible dynamic correlation effect, the orbitals that were used to describe the states at the CASSCF level were computed in a state-average procedure where the CT state was averaged with others of very different character. Consequently, these orbitals are not well adapted to describe the CT charge distribution. Part of the effect of the perturbation is to "relax" the orbitals to better describe each specific charge distribution (this is actually an effect hidden inside the perturbation), stabilizing preferentially the CT state: the LE state is stabilized only by 2.7 kcal·mol^{-1}, NA and NS states by 16.0 kcal·mol^{-1} and 18.5 kcal·mol^{-1} respectively and CT by 29.2 kcal·mol^{-1}.

When SA-CASSCF states interact via dynamic correlation at the MS-CASPT2 level, the PM-CAS-CI wave functions are obtained in terms of the SA-CASSCF wave functions. The composition of the PM-CAS-CI functions is showed in Table 6.2.

Table 6.2: Eigenvectors of the MS-CASPT2(12,11) effective Hamiltonian matrix diagonalitzation of the first seven low lying states in APD. PM-CAS-CI wave functions are named PM-CI.

	7 state averaged						
States	1 (GS) PM-CI	2 PM-CI	3 PM-CI	4 PM-CI	5 PM-CI	6 PM-CI	7 PM-CI
	Eigenvectors						
GS	**-0.9966**	-0.0010	-0.0118	-0.0052	0.0819	0.0015	0.0007
2	-0.0058	0.1423	**0.9869**	0.0121	0.0748	-0.0023	-0.0001
3	0.0016	**0.9149**	0.1271	**0.3634**	-0.0089	-0.1210	-0.0032
4	-0.0026	**0.3562**	-0.0644	**0.9263**	0.0220	-0.0250	0.0992
5	-0.0005	-0.1253	0.0151	-0.0020	0.0099	**-0.9643**	0.2326
6	-0.0827	0.0092	0.0731	0.0275	**-0.9929**	-0.0173	-0.0294
7	-0.0014	-0.0031	0.0049	-0.0949	-0.0349	0.2336	**0.9670**

Given that the standard procedure used in this work for geometry optimization uses CASSCF wave functions, it is important to check that the MS-CASPT2 states are described well enough at the CASSCF level in order to be able to considered the CASSCF geometries good enough approximations of the MS-CASPT2 ones. There is a certain extension of combination of the NA CASSCF states in the 2^{nd} and 4^{th} PM-CAS-CI functions, and of the NS states in the 6^{th} and 7^{th} ones, but still there is clearly a CASSCF function that predominates in each PM-CAS-CI function.

Finally regarding the absorption spectrum, MS-CASPT2 results indicate that the

initial excitation populates mainly the CT state, that is the fourth excited state, which shows an oscillator strength much larger than that of the rest of the states considered. This result is in good agreement with INDO/S results published by Herbich for this kind of molecules [31].

Ground state and excited state minima

The next step in this study was to locate and characterize the minima on the potential energy surfaces of the states of interest. Apart from the GS minimum and the S_0 surfaces, we located a LE, a CT, a NA2 and three NA1 minima on the S_1 surface (geometries shown in Figure 6.4, energies collected in Table 6.3).

Table 6.3: MS-CASPT2 energies relative to the S_0 minimum (ΔE), vertical energies to S_0 (both in kcal·mol^{-1}), dipole moments (in Debye) and oscillator strengths of the characterized S_1 minima for the APD molecule.

Minimum	ΔE	Vertical Energy	μ	f
LE	110.3	107.5	3.56	0.0310
NA2-C2	101.9	70.5	1.97	0.0013
NA1-C6	103.9	77.9	1.89	0.0079
NA1-C4	109.5	33.0	3.04	0.0004
NA1-TW	104.5	80.4	0.50	0.0087
TICT	116.3	74.0	7.76	0.0033

The unusual large number of minima on the lowest energy excited state PES of this system increases considerably the complexity of the photochemistry, given that the lifetime of this state is longer than that of the upper states, increasing the probabilities of reactivity and luminescence.

The LE minimum is totally planar except for the amino group, which is pyramidalized. It is computed to be 110.27 kcal·mol^{-1} above the ground state minimum and has a vertical energy with respect to the ground state of 107.5 kcal·mol^{-1}. The main contributions to the LE wave function are two CSF involving monoexitations to the π^*-ring orbitals 1 and 2 (see Figure 6.3), with coefficients 0.76 and 0.33 respectively. This is reflected in the geometry parameters with and enlarging of 0.061 Å of the C_5-C_6 distance due to antibonding character of the π^* orbitals between these atoms. Comparing with the wave function of this state at the FC geometry, there is an increase of the contribution of the monoexcitation to the π^*-ring 1 orbital.

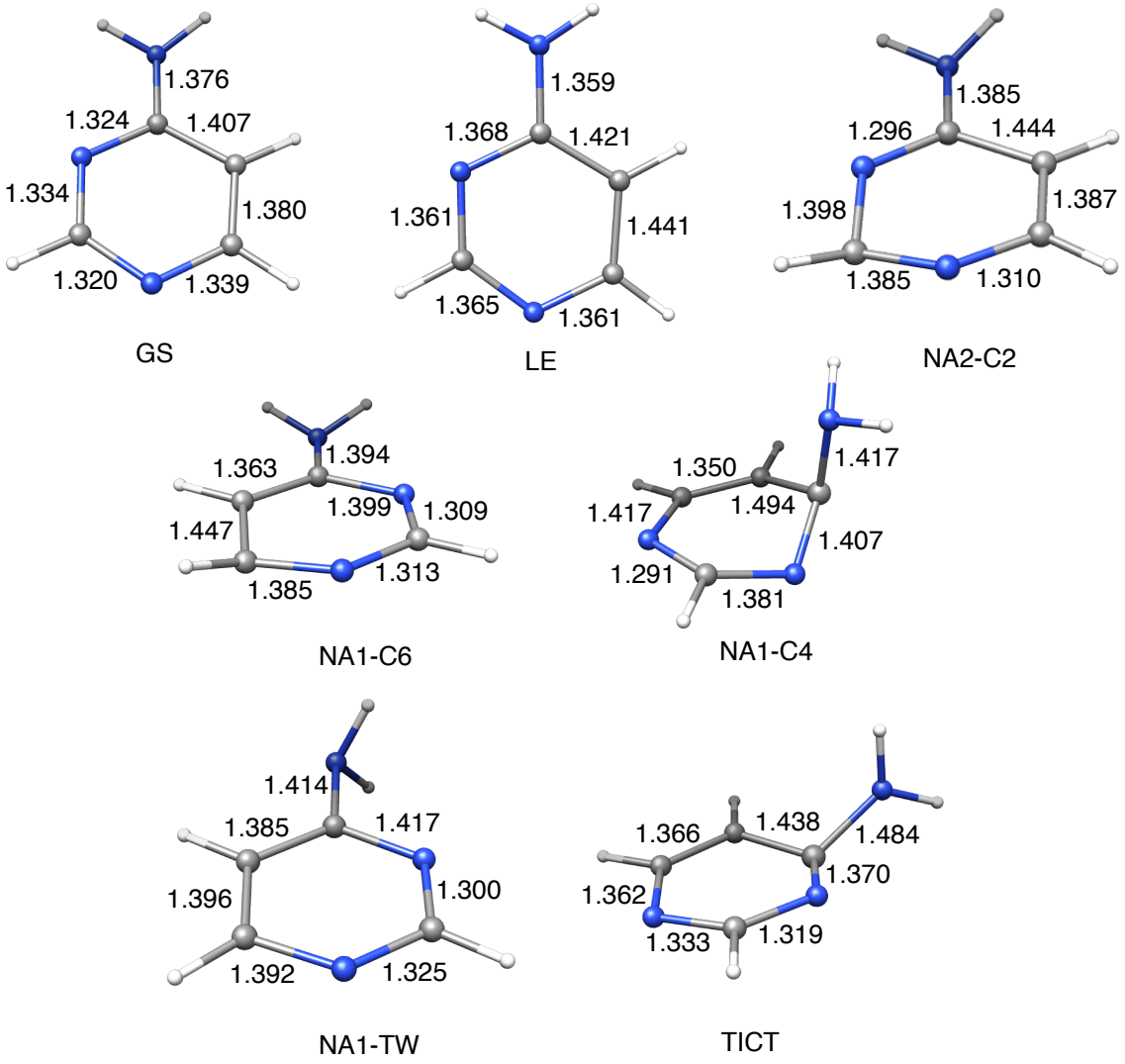

Figure 6.4: Optimized structures of S_0 and S_1 APD minima

The CT minimum lies 116.35 kcal·mol^{-1} over the ground state minimum and its geometry has the characteristics of a twisted ICT state (TICT), with the C-NH_2 group pyramidalized and twisted with respect to the ring plane. A significant increase of 0.108 Å can be observed in the bond distance of the amino group between the ground state and CT minima, according with the non bonding π character of the bond between donor and acceptor moieties in TICT states. Analysis of the wave function shows that it derives mainly from an excitation from the amino N lone pair orbital to the π^*-ring 1 orbital. The computed dipole moment of about 7.76 Debye confirms the CT nature of this species.

The NA2 minimum is 101.94 kcal·mol^{-1} above the ground state minimum. Its structure is C_2-puckered, since this deformation of the ring stabilizes the excitation from the NA orbital to the π^*-ring 2 orbital, given that this orbital shows antibonding character between C_2 and the adjacent C atoms. Furthermore N_3-C_4 distance is reduced by 0.028 Åand N_1-C_2 is enlarged by 0.065 Å in good agreement with the bonding character of N_3-C_4 and antibonding character of the N_1-C_2 bond of the π^*-ring 2 orbital.

The three NA1 minima found are associated to excitations from the NA orbital to the π^*-ring 1 orbital: a C_6-puckered minimum in which the amino group stays in the molecular plane (NA1-C6 in Figure 6.4), a similar C_4-puckered structure (NA1-C4), and a planar minimum with the amino group pyramidalized and perpendicularly oriented with respect to the ring plane (twisted geometry, NA1-TW). Their energies relative to the ground state minimum are 103.9, 109.5 and 104.5 kcal·mol^{-1} respectively.

The minimum C_6-puckered geometry can be explained like before in terms of the antibonding character of the double bond among adjacent bonded atoms and it is characterized by a large distances of 1.447 Å between C_5-C_6 and of 1.385 Å between N_1-C_6, in good agreement with the excitation to the π^*-ring 1 orbital.

NA1-C4 and NA1-TW are characterized by an increase of the distance between the amino group and the carbon ring up to 1.41 Å. Although the NA1-C4 lies high in energy, it can be relevant, because the ground state is only 33 kcal·mol^{-1} more stable than the NA1 state at this geometry (see Table 6.4) and the wave function obtained at the MS-CASPT2 level shows an important mixing of the NA1 and the ground state (see Table 6.5), what indicates that a conical intersection can be expected to be quite close to this NA1-C4 minimum. Consequently, if this minimum is populated, the system will easily reach a non-radiative deactivation channel to the ground state. This possibility will be discussed below.

On the other hand, the NA1-TW minimum does not seem to have an important role in APD photochemistry, but it can be important for the substituted amynopyrimidines photochemistry, as will also be discussed latter.

A intriguing difference between NA1-TW and TICT minima is the pyramidalization of the amino group. While in NA1-TW this group is pyrimidalized, in TICT it is not, but the bond with the ring is larger in the TICT structure than in NA1-TW.

Table 6.4: Vertical energies (in kcal·mol^{-1}) of SA7-CASSCF(12,11) in NA1-C4 minimum geometry of APD.

State	CASSCF	MS-CASPT2
	7 state averaged	
SO	98.9	76.48
NA1	104.4	109.46

Table 6.5: Largest coefficients of the first two eigenfunctions of the MS-CASPT2 effective Hamiltonian matrix diagonalitzation of the first two roots of the APD molecule at the geometry of the NA1-C4 minimum.

	7 state averaged	
States	1 (GS) PM-CI	2 PM-CI
	Eigenvectors	
GS	0.7775	-0.6287
2	0.6287	0.7775

The energy difference between the 1^{st} and the 2^{nd} excited states varies substantially on different minima of the S_1 surface (see Table 6.6) given that the nature of the second excited state also changes from one geometry to another. For example on the LE minimum the 2^{nd} excited state is NA1 in nature, and its energy is only 2.17 kcal·mol^{-1} higher. On the other hand at the NA1-C6 minimum, the S_2 surface correspond to the LE state, but this is 24.16 kcal·mol^{-1} higher in energy. At the CT minimum, the 2^{nd} excited state is of NA1 character and it is 13.38 kcal·mol^{-1} higher.

Table 6.6: MS-CASPT2 vertical energies (relative to the S_0 minimum) of first four low-lying states in S_1 minimum geometries.

	Minima					
Root	LE	Nature	NA2	Nature	NA1-C6	Nature
1	2.77	S_0	31.40	S_0	25.97	SO
2	110.27	LE	101.94	NA2	103.93	NA1
3	112.44	NA1	134.58	NA1	128.09	LE
4	127.02	NA2	136.81	LE	135.56	NA2
Root	NA1-C4	Nature	NA1-TW	Nature	CT	Nature
1	76.48	SO-NA1	24.07	SO	42.36	S_0
2	109.46	SO-NA1	104.48	NA1	116.35	CT
3	148.44	LE	128.51	NA2	129.73	NA1
4	155.24	NA2	145.16	LE	154.74	LE

The fact that the minima of the different excited states are all located on the S_1 surface and the small energy between them indicate that there must exist a large number of crossings between the corresponding PES. We will have to locate the lowest energy paths connecting the different minima to elucidate which ones can be populated from the first one populated after the initial excitation.

Deactivation paths: population of S_1 minima

We study here how the system will evolve from the FC region on the state populated after the initial excitation and discuss how the subsequent paths can populate other minima on the S_1 surface.

As we saw before, the state populated initially was the fourth excited state of CT character. One of the most probable events at this stage is the relaxation of this system on this PES. So we calculated a MEP on this surface at the CASSCF(8,7). Even starting with a CAS(8,7) which does not include the n_N orbitals, they come into play already at the early stages of the MEP and lead the system to a NA2 state. To check this result, we calculated a LIIRC path from the Franck-Condon region to the TICT minimum and calculated at the MS-CASPT2 level the profiles of the PES of the first five excited states (Figure 6.5), given the relevance of the dynamic correlation in the relative ordering of the states involved. The LIIRC path shows that, following the geometry relaxation path, the CT surface crosses the NA2, NA1 and LE surfaces. It means that there are direct paths to populate all this minima, but the most favoured one will be the path leading to the NA2 minima, because this is the first crossing in the CT relaxation path and because this minimum is the most stable one and consequently thermodynamically favoured. Nevertheless, given the small energy differences between some of the S_1 minima, if the barriers of these paths connecting minima are not too high, their populations will equilibrate along adiabatic paths on the S_1 surface. Therefore the population of all the S_1 minima have to be rationalized in terms of energies of conical intersections and transition states between states. For this reason we looked for CIs and TSs on the S_1 and S_2 PESs.

In a geometry near the FC region, and with a quasi planar conformation of the benzene ring and a C_5-C_6 bond distance between LE and NA2C2 minima, we found a conical intersection between the NA2 and LE states (see Figure 6.6), at 112.15

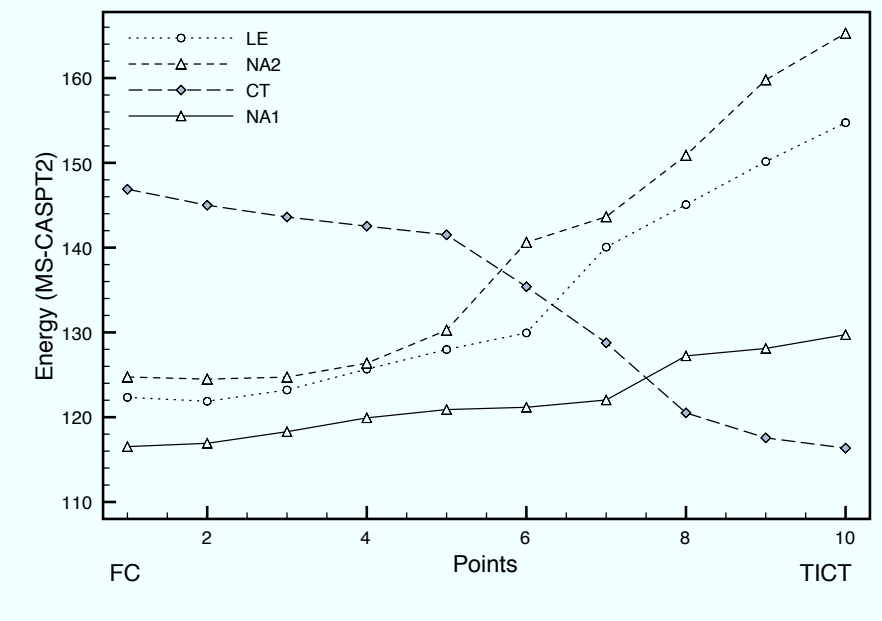

Figure 6.5: MS-CASPT2(12,11) LIIRC path from the FranckâĂŞCondon region to the TICT minimum. Profiles of the CT, NA2, NA1 and LE state are depicted. GS curve is not shown for the sake of clarity

kcal·mol^{-1} above the minimum of the ground state (Table 6.7). It is interesting to notice that it lies only 10.2 and 1.9 kcal·mol^{-1} above the NA2 and the LE minima respectively. Therefore if the LE is populated, an accessible non adiabatic path with a barrier of 1.9 kcal·mol^{-1} will shift the thermodynamic equilibrium towards NA2-C2 minimum.

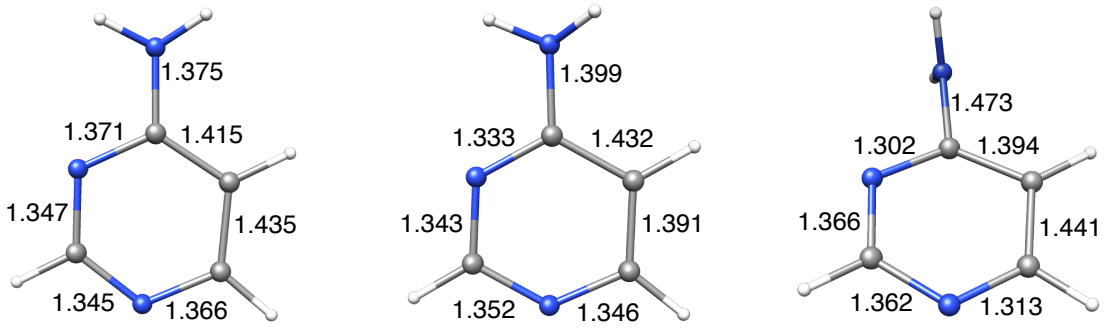

CI S_2/S_1 NA2/LE

CI S_2/S_1 NA1/NA2

CI S_2/S_1 CT/LE

Figure 6.6: Optimized CI $_2/S_1$ on the S_1 surface of APD

Table 6.7: Energies (in kcal·mol^{-1}) relative to the ground state minimum of optimized CIs and TS in the S_1 PES of APD.

State	MS-CASPT2
LE/NA2 CI	112.15
NA2/NA1 CI	110.05
TS NA1-C6/NA1-TW	104.7

Between the NA2 and NA1 states another CI was found at 110.05 kcal·mol^{-1} (see Figure 6.6). At its minimum energy point, the out-of-ring amino group is slightly more pyrimidalized than at the LE minimum. It is located 8.1 and 6.1 kcal·mol^{-1} over the NA2 and NA1-C6 minima respectively. This CI constitutes a low barrier that can be overcome with the excess of excitation energy that the system keeps after the initial absorption. Hence there is also a reaction path via a conical intersection between NA1 and NA2 leading to a thermodynamic equilibrium between these minima.

To analyse the population of NA1-TW minima, an exploration on the NA1 surface was done. A transition state between NA1-C6 and NA1-TW was found. Hence if the NA1-C6 minimum is populated, there is an adiabatic path through which the system can easily reach the NA1-TW minimum by overcoming an almost negligible barrier of 0.7 kcal·mol^{-1}. This transition state involves twisting of the out-of-ring amino group with respect to the benzene plane and planarization of the puckered C6. The transition vector is showed in Figure 6.7.

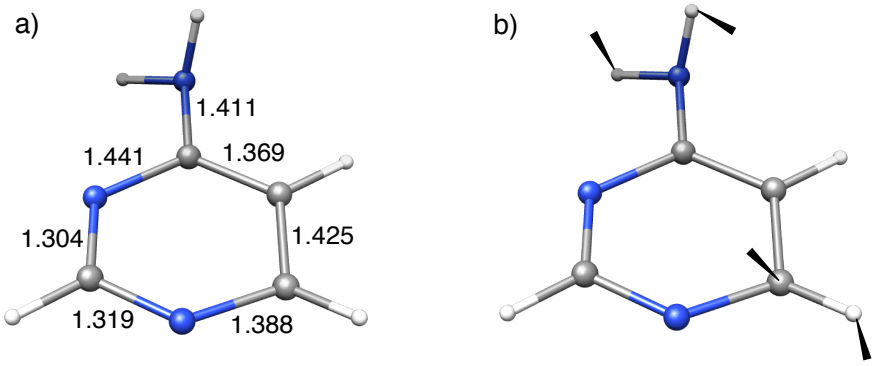

Figure 6.7: Optimized transition state on the S_1 surface between the NA1-TW and NA1-C6 minima. a) Geometry (distances in Å. b) transition vector.

The connection between the CT and LE states is a crucial point in other systems with ICT like the aminobezonitrile family [103**?**]. For this reason and for the sake of comparison, we also investigated this possible reaction path in APD.

Firstly we looked for a conical intersection between LE and CT states at CASSCF(12,11) level, however due to the different effect of dynamic correlation in the states studied (reasons commented in the Computational Details section) and the small energy differences between the low lying states, the optimization of the lowest energy crossing point between these states is not an easy task, and a CI at this level was not found.

A possible solution to reduce the number of low lying states involved in the calculations is the extraction of the N orbitals from the active space leading to a reduced (8,7) active space. So the only excited states described are LE and CT. In this way, a CI minimum between the LE and CT states was found, high above the LE minimum (34.7 kcal·mol^{-1} above at CASSCF(8,7) level). When the energies of both states were recalculated at the MS-CASPT2(12,11) level, thought, the LE and CT states were not degenerate any longer (Table 6.8), but continued being well above the LE minimum. This result points out that any crossing between the CT and the LE states is not easily accessible.

Table 6.8: CASSCF and MS-CASPT2 energies relative to the S_0 minimum (in kcal·mol^{-1}) and nature of states at the geometry of the CT/LE conical intersection optimized at the CASSCF(8,7) level in the APD molecule.

	CASSCF		MS-CASPT2
State	Nature	ΔE	ΔE
1	NA1	148.9	129.7
2	NA2	150.5	135.9
3	CT	156.0	143.0
4	CT	180.7	143.7
5	LE	182.1	151.0
6	NS2	194.7	176.3

In summary (Figure 6.8), since the energetic barriers connecting the S_1 LE and NA minima are low, all of them can be populated, although it is interesting to point out that the thermodynamic equilibrium favours the population of the NA minima rather than of the LE minimum.

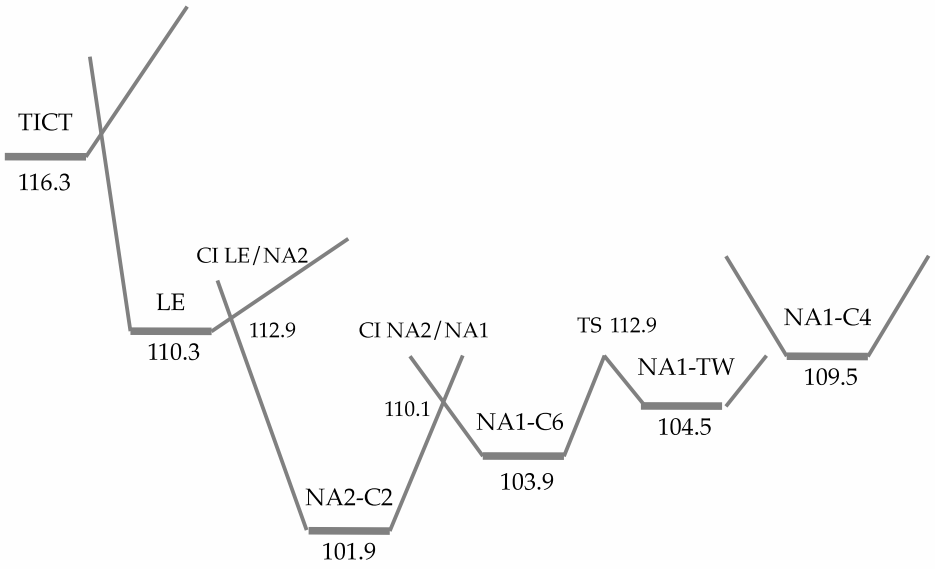

Figure 6.8: Schematic energy level diagram of the S_1 PES for APD.

Non-radiative deactivation paths

Once the possible population of S_1 minima were studied, the next step is analyse how the system can evolve from these minima. There are two competing channels: *a)* non radiative deactivation via conical intersection with the ground state and *b)* radiative fluorescence emission from them. If the first is energetically accessible through a path with small barriers, the lifetime of the excited state will be short and the system will not fluoresce. For this reason we look for CIs among the S_1 and S_0 PES.

We found three seams of degeneracy. The identification of the states crossing was made by an accurate analysis of the CSFs weights of the state wave functions of interest and the analysis of the pseudo-natural orbital occupancies. All the CIs located correspond to crossings of NA states with the ground state.

The minimum energy points of the CI are all located near S_1 minima of the NA states described in the previous section. We have labelled the CIs as NA1-C4/S_0

NA1-C6/S_0 and NA2-C2/S_0 CI according with their nature and geometry. All the CI minima structures (Figure 6.9) show greater puckering of the C atoms already puckered in the minima.

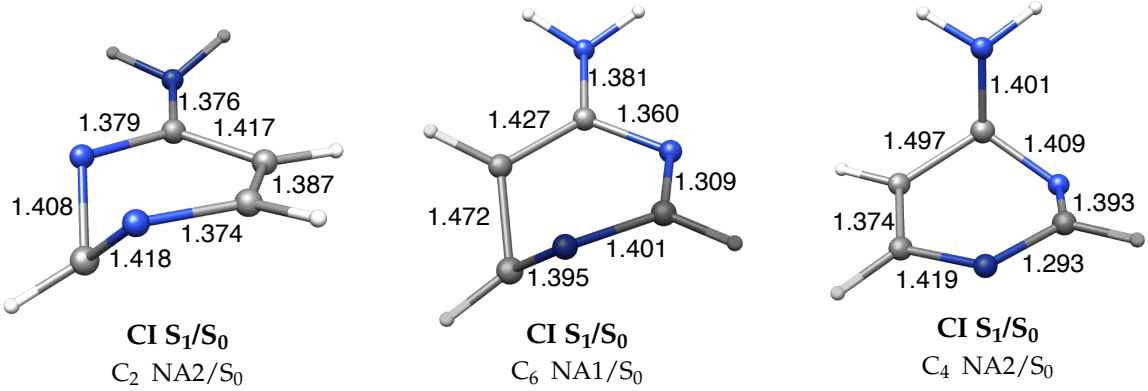

Figure 6.9: Optimized geometries of the S_1/S_0 CIs for APD.

Considering the conical intersections as the highest limit for the barrier for a state switch and comparing the energies of the S_1-NA minima with those of the CI, we find that the barrier for the radiationless decay from the NA2-C2 and NA1-C6 are 20.0 and 11.8 kcal·mol^{-1} respectively, while the path from NA1-C4 minimum can be considered barrierless. These radiationless deactivation paths open very efficient mechanisms for non radiative deactivation, being the one form the NA1-C4 minimum the most favourable.

Table 6.9: Energies (in kcal·mol^{-1}, relative to the S_0 minimum) of optimized S_1/S_0 CIs in APD.

State	MS-CASPT2
NA2/S_0 CI	121.9
NA1-C6/S_0 CI	115.7
NA1-C4/S_0 CI	109.0

In conclusion, we predict that the equilibrium between the different minima on the S_1 surface is possible and it will be displaced favouring the population of the NA minima. From there, taking into account the thermodynamic equilibrium between the NA state minima, the low oscillator strengths for NA states and the easily accessible CIs with the ground state, we predict that the non-radiative deactivation

is the most efficient channel. Consequently, no luminescence is expected from the APD, nor the normal band, neither the anomalous one. This is consistent with the absence of experimental data of luminescence for this molecule that eventually can be related to the high energy of the CT and LE states in the non substituted APDs. As it will be shown below, substituted aminopyrimidines behave very differently.

6.3.2 Absorption spectrum in substituted aminopyrimidines

To study how the substituents affect the luminescence of the members of the APD family, we center our attention in the regions of the PESs that proved to be crucial in the photochemistry of the parent system. That is, we will analyse the relative energies of the states at the Franck Condon region, the energetics of the most stable S_1 minima and the height of the barriers to equilibrate them in the substituted APDs. So as a first step we focus on in the FC region.

Ground state minima

To begin with, the geometry of the ground state minima was optimized for DMAPD, DMA5MPD and DEAPD (Figure 6.10).

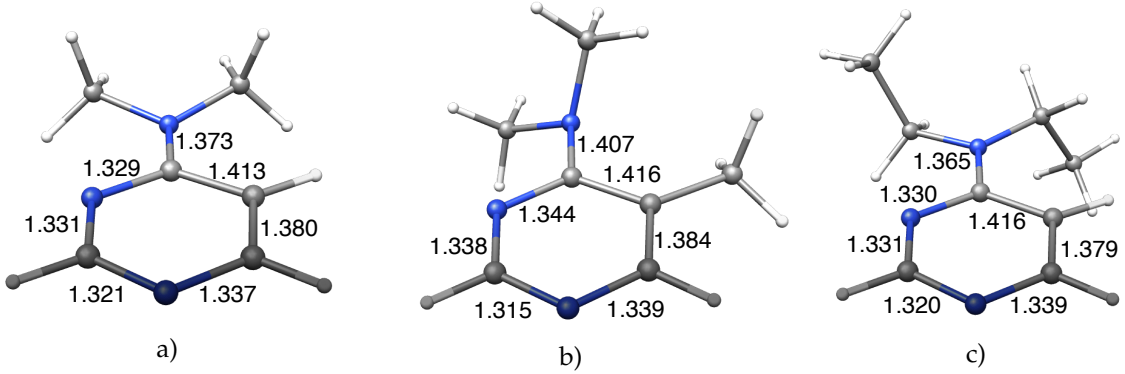

Figure 6.10: Optimized structures of S_0 minima of a) DMAPD b) DMA5MPD and c) DEAP. Distances in Angstroms.

Bond distances and angles remain nearly the same for all the studied compounds except the C-N distance as commented below. However, while DMAPD and DEAPD maintain a planar geometry, for the ortho-substituted DMA5MPD the

amino group is twisted and C_5 is slightly puckered. This distortion results in a torsion angle of about 39 ° between the methyl groups of the amino moiety and the ring, which is probably fair enough to lower the steric repulsion between the dimethylamino group and the methyl substituent placed in the ortho position.

Concerning the pyramidalization of the amino group (Table 6.10), it decreases as the donor ability and size of the substituents increases. Pyramidalization has been estimated by the average of the dihedral angles between the substituents of the amino group and the closest adjacent ring atom, and it varies from 23.3° for the non substituted APD to 13.9° and 12.3° for DMAPD and DEAPD respectively as shown in Table 6.10. The smaller pyramidalization allows for a larger coupling between the amino and π in-ring orbitals, giving place to a decrease of the C-N distance, from APD, to DMAPD and DEAPD, although the steric repulsions are larger. In the same way, the torsion of the amino group in DMA5MPD makes difficult the coupling of two moieties and the C-N distance is enlarged to 1.407 Å.

Table 6.10: Angle of amino group's pyramidalization (θ) and C-N out of ring distance (d(C-N)) for ground state minima of substituted and non substituted APDs.

Minima	θ	d(C-N_{out})
APD	23.3	1.376
DMAPD	13.9	1.373
DEAPD	12.3	1.365
DMA5MPD	-	1.407

Absorption spectrum

Next, the Franck Condon excitations were calculated for all the substituted APDs. Regarding DMA5MDP and DMAPD calculations, there are not important differences relative to APD (see Table 6.11). However, in the case of DMA5MPD, due to the loss of symmetry caused by the torsion of the amino group, the analysis of the states becomes more complex because the three kind of orbitals of the CAS depicted in Figure 6.2 (π-ring, N-amino and N lone pairs) are mixed. This mixing induces also difficulties in the MS-CASPT2 interpretation of the results, and it has been necessary to average more states than for APD (specifically 9 versus 7) in order

to uncouple the states S_4 and higher at the MS-CASPT2 level. The energetic ordering of the different excited states in all derivatives is basically the same than that found for APD at the MS-CASPT2 level, except for the LE and NA1 states, which swap their relative position, the LE state becoming the first excited state at MS-CASPT2 level as shown in Table 6.11. This is a crucial change of the fluorescence for the APD derivatives.

Table 6.11: CASSCF(12,11), SS-CASPT2(12,11) and MS-CASPT2(12,11) vertical energies (in kcal·mol*), oscillator strengths (f) and dipole moments (μ in Debyes) of DMAPD (8 states averaged), DEAPD (8 states averaged) and DMA5MPD (9 states averaged).

State	CASSCF	SS-State	SS-CASPT2	PM-State	MS-CASPT2	μ	f
			DMAPD				
SO	0.0	SO	0.0	SO	0.0	3.33	-
LE	121.4	LE	115.1	LE	109.8	3.94	0.0129
NA1	132.9	NA1	116.9	NA1	116.8	2.02	0.0214
NA2	140.1	NA2	123.4	NA2	124.7	1.96	0.0226
CT	163.1	CT	130.0	CT	132.4	7.23	0.3383
NS1	168.1	NS1	148.6	NS1	150.0	1.52	0.0041
NS2	176.8	NS2	156.9	NS2	158.9	2.64	0.0062
			DEAP				
SO	0.0	SO	0.0	SO	0.0	3.6	-
LE	119.8	LE	116.5	LE	113.3	4.66	0.0692
NA1	132.5	NA1	121.8	NA1	121.8	2.35	0.0041
NA2	141.1	NA2	131.2	NA2	132.4	1.96	0.0167
CT	160.5	CT	135.0	CT	136.5	7.57	0.3948
NS1	170.8	NS1	158.8	NS1	159.8	1.95	0.0032
CT2	176.8	CT2	158.6	CT2	163.5	6.44	0.0633
			DMA5MPD				
S_0	0.0	S_0	0.0	S_0	0.0		-
LE	104.0	LE	101.7	LE	99.0	4.29	0.05
NA1	120.5	NA1	112.6	NA1	113.4	1.5	0.01
NA2	139.7	CT	129.3	CT	128.9	6.8	0.26
CT	153.0	NA2	130.5	NA2	132.9	1.96	0.01
NS1	155.9	NS1	148.6	NS1	150.9	2.27	0.02
NS2	162.2	NS2	147.8	NS2	152.8	5.36	0.09

There is also an important lowering of the energy of the LE and CT states in the substituted analogues with respect to the unsubstituted APD. Actually, the CT

stabilization is already seen in absence of dynamic correlation, since it is already the fourth excited state at the CASSCF level. It is interesting to point out that at the FC region in these APD derivatives the ordering of the CASSCF and MS-CASPT2 states is the same.

In all cases, the value of the oscillator strength shows that the CT state is likely to absorb most of the irradiated light, as found for APD. However we found that the donor and esteric effects induce a larger oscillator strength for the CT state in DEAPD and DMAPD than for DMA5MPD and APD, proportional to the extension of the coupling between the donor and acceptor moieties. In the same way there is an increase of dipole moment from DMA5MPD, to DMAPD and DEAPD.

Thus for substituted aminopyrimidines the CT state lies at lower energy than for the small APD already in the Franck-Condon region and consequently this excited state is expected to be more accessible. For this reason TICT formation has been explored in more detail for DMAPD and DMA5MPD, to try to explain their luminescent behaviour in gas phase and in a polar solvent.

6.3.3 Normal or anomalous fluorescence

Like for the parent system, the fluorescent patterns of the APD derivatives are determined by the topology of the S_1 PES. Based on the results obtained for APD, we first looked more exhaustively for the minima of the lowest excited states of DMAPD and DMA5MPD. For DEAPD we limited to our study to the species shown in the previous cases to be determinant.

DMAPD S_1 minima

Table 6.12 collects information relative to the minima located on the S_1 PES for this system, and Figure 6.11 shows the geometries of the species found.

The energetic data show that, while the NA minima have about the same energy than in the APD analogues, the LE and CT intermediates undergo an important stabilization, which turn them into the most stable intermediates on the S_1 surface. This fact is consistent with the stabilization observed in the Franck-Condon region, and will have and important effect on the photophysical and photochemical pro-

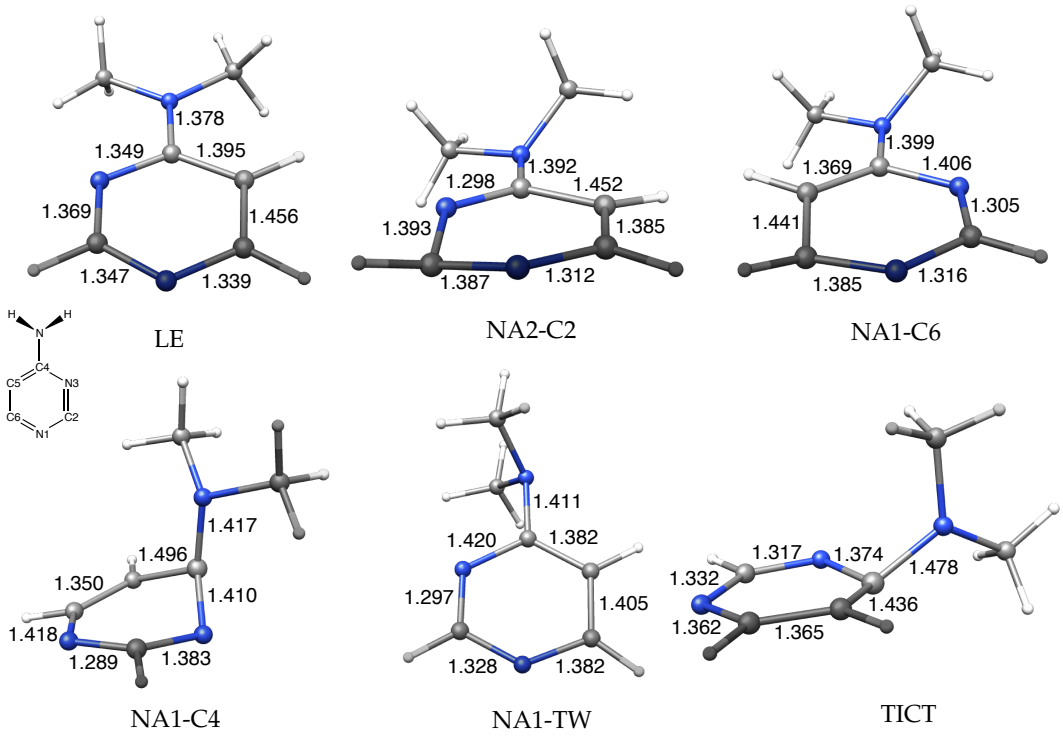

Figure 6.11: Geometries of the optimized S_1 minima for DMAPD

Table 6.12: MS-CASPT2 energies relative to the S_0 minimum (E), vertical energies to S_0 (both in kcal·mol^{-1}), dipole moments (in Debye) and oscillator strengths of the characterized S_1 minima for the DMAPD molecule.

Minimum	E	Vertical Energy	μ	f
LE	100.7	95.5	4.91	0.0602
NA2	102.4	69.2	1.50	0.0015
NA1-C6	103.8	78.0	1.32	0.0057
NA1-C4	109.9	34.3	2.30	0.0001
NA1-TW	104.8	81.6	0.55	0.0070
TICT	97.4	54.6	7.02	0.0009

cesses of DMAPD. The structures of all the S_1 species located are quite similar to those of ADP, with differences in the bond distances smaller than 0.01 Å, except for the case of the LE minimum.

In the LE minimum of this molecule, the out of ring amino group is not pyramidalized, in contrast with the LE geometry found for APD, due to the donor ability of the alkyl susbtituents of DMAPD. Concerning bond distances of in-ring atoms,

there are not significant differences between DMAPD and APD, however the out of ring C-N distance is enlarged from 1.359 Å in APD to 1.378 Å in DMAPD. While in APD the C-N distance is reduced relative to the ground state, this is not observed in DMAPD, perhaps due to steric effects of the bulkier amino substituents.

The LE species of DMAPD shows an increase of its dipole moment (4.91 D) with respect to the value for APD (3.56 D). In spite of the complex composition of the CSF that describes this state, the plot of the difference of electronic density between the excited state and the ground state, shown in Figure 6.12, reveal the LE character of these species. A certain transfer of charge accounts for its relative large dipole moment. In polar solvents the LE DMAPD will be stabilize further than the LE APD species, what can lead to differences in the fluorescence patterns of both systems.

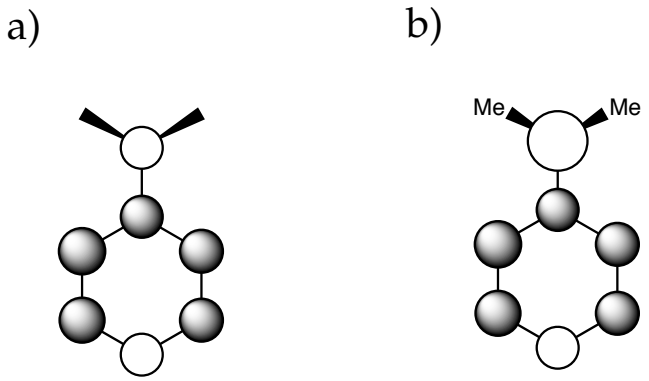

Figure 6.12: Plot of the electron density difference between the lowest excited states at the S_1-LE optimized geometries of a) APD and b) DMAPD.

DMA5MPD S_1 minima

The presence of the methyl substituent in C_5 originates a steric repulsion with the amino substituents, that is released by the rotation of the amino group. For this reason, new minima corresponding to twisted geometries of the planar species found for APD and DMAPD appear for DM5AMPD. Specifically we found a NA2-C2 Twisted (NA2-C2-TW) and a NA1-C6 Twisted (NA1-C6-TW) new minima, as shown in Table 6.13 and Figure 6.13.

In DM5MAPD, the CT minimum is stabilized with respect to the non substituted APD, probably due to the donor effect of the alkyl substituents in the amino group. On the other hand the LE minimum is less stabilized than in DMAPD,

Table 6.13: MS-CASPT2 energies relative to the S_0 minimum (E), vertical energies to S_0 (both in kcal·mol^{-1}), dipole moments (in Debye) and oscillator strengths of the characterized S_1 minima for the DMA5MPD molecule.

Minimum	E	Vertical Energy	μ	f
LE	107.0	99.1	4.61	0.0503
NA2-C2	107.1	76.1	1.60	0.0007
NA1-C6	109.0	89.7	1.13	0.0089
NA1-C4	115.9	89.5	2.00	0.0102
NA1-C6-TW	104.0	83.5	0.44	0.0088
NA2-C2-TW	109.8	69.3	0.45	0.0008
NA1-C4-TW	108.2	60.5	1.67	0.0054
TICT	105.4	68.6	6.94	0.0054

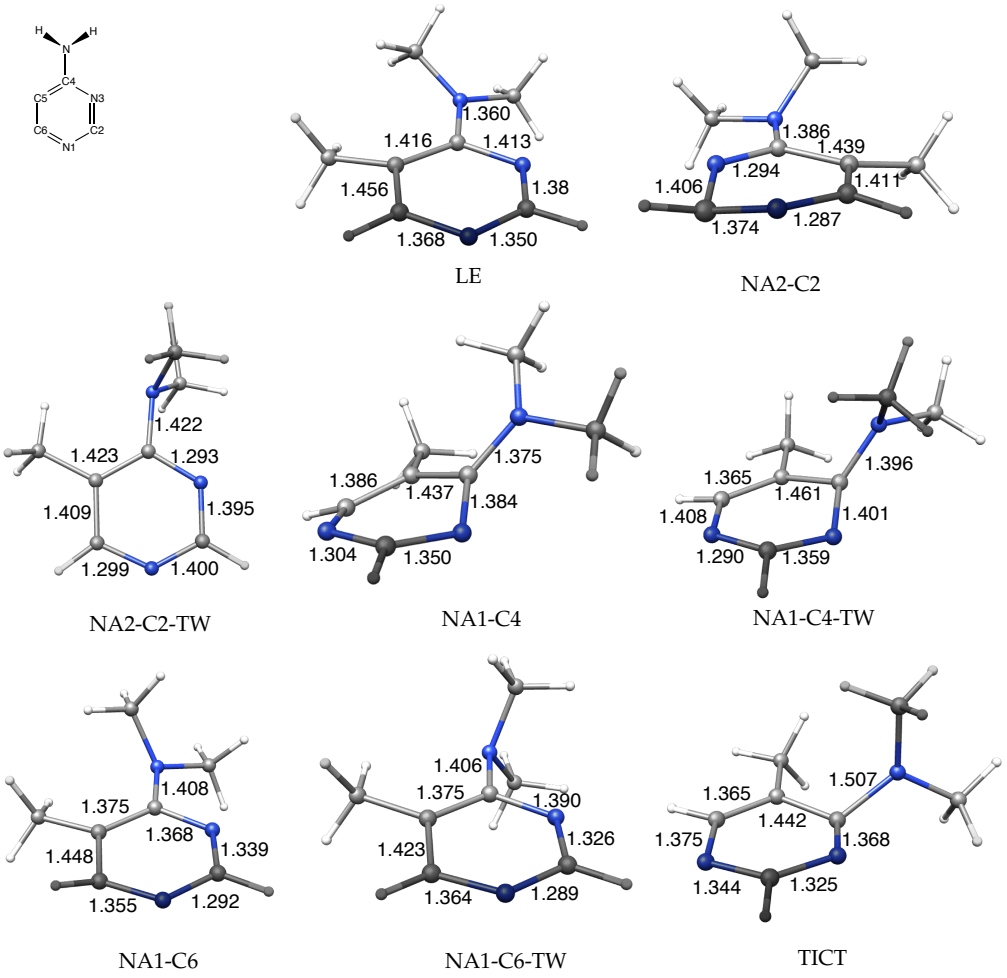

Figure 6.13: Geometries of the optimized S_1 minima for DMA5MPD

likely because of its tendency to adopt a planar geometry, where the mentioned steric repulsions is larger and because a certain tension of the amino group, that is not pyrimidalized in this structure. The opposite effect must be the reason of the stabilization of the twisted NA1 minima found, which are about 3-8 kcal·mol^{-1} more stable than its planar analogues.

The geometrical parameters of the different S_1 minima of DMA5MPD show the same trends as in DMAPD and APD, except for the case of the LE minimum. In this case, the C_4-N_3 distance increases relative to that of the ground state. The out of ring C-N distances follow the same trend as in APD (and opposite to DMAPD), probably due to the small pyramidalization of the amino group found in the LE geometry of DMAPD (see Figure 6.11).

DEAPD S_1 minima

The study of the topology of the S_1 PES performed for DMAPD and DMA5MPD and explained in the next section, show that the main role in the photophysics of APD derivatives is played by the LE and CT species. For this reason for DEAPD the study of the S_1 minima was limited to these two structures. It is worth to remember that DEAPD shows only the normal band in the gas phase but dual fluorescence in polar environments. For DEAPD we have located the LE and CT minima on the S_1 surface and calculated their energies in gas phase. Geometries are shown in Figure 6.14 and energies in Table 6.14.

Table 6.14: MS-CASPT2 energies relative to the S_0 minimum (E), vertical energies (both in kcal·mol^{-1}), dipole moments (in Debye) and oscillator strengths of the characterized S_1 minima for the DEAPD molecule.

Minimum	E	Vertical Energy	μ	f
		Gas phase		
LE	105.9	97.5	4.95	0.0558
TICT	101.3	62.7	7.78	0.0007

Concerning geometrical parameters, as other aminopyrimidines, there are not any significant differences on distances among in ring atoms. On the other hand, in the LE minimum compared with DMAPD, out of ring C-N distance is enlarged by almost 0.02 Å, and C_4 is less pyramidalized. This can be attributed to a larger

steric effect of the amino substituents, that enlarges the C-N distance, and a larger donating ability, that favours the planarity of this geometry. In the case of the TICT minima, due to the lack of coupling in the twisted structure, the steric effect of the ethyl substituents produces a large pyramidalization of C_4 instead of an elongation of the bond distance.

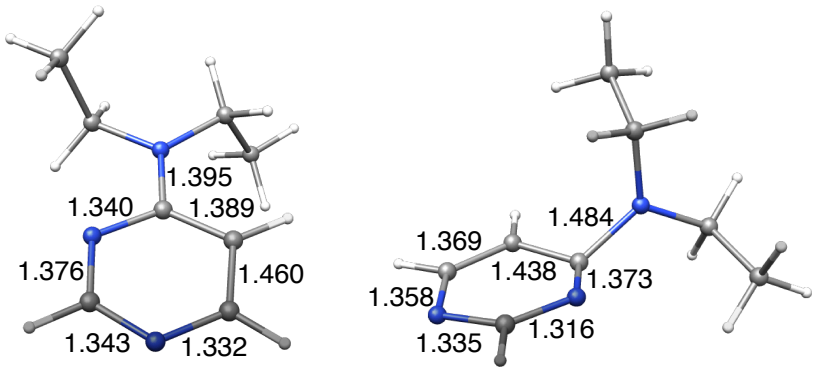

Figure 6.14: Geometries of the optimized LE and TICT minima for DEAPD.

Topology of the S_1 PES and luminescent patterns

In order to focus and limit the study of the reactive channels of the S_1 PES, we took into account several considerations:

- The CT state is the one preferentially populated after the initial excitation.
- The lowest energy minima of the S_1 surface correspond to the LE and CT states. It is necessary to know if these minima are connected through an accessible channel.
- The NA and NS minima have similar energies, only a little more inestable than the LE and CT ones. The accessibility of these minima will be checked only for some particular cases, assuming than a further connection between NS and NA minima is possible.
- Special attention should be paid to twisted species, preferentially stabilized in those derivatives with bulky amino substituents.

The particular results for each APD derivative are described next.

DMAPD

For this compound the CT minimum is more stable than the LE one, but at the Franck Condon region these states are inverted. It means that there must be a crossing of the corresponding PES that opens a channel for connecting these two S_1 minima, of almost the same energy, and equilibrate their populations. To characterize this channel we looked for a conical intersection.

Given that for this system the ordering of the states obtained at the MS-CASPT2 level is the same than at the CASSCF level, in principle it should be possible to locate and minimize this intersections at the CASSCF level. Several trials were made using different active spaces ((8,7) and (12,9)) and different number of states averaged (more detailed information in the Annex of this chapter). Although the optimizations could be finished (geometries shown in Figure 6.15), the mixed composition of the wave functions obtained preclude a not clear determination of the states involved in the crossing. Moreover, when dynamical correlation was included in the energy calculation, the states were not degenerate any longer.

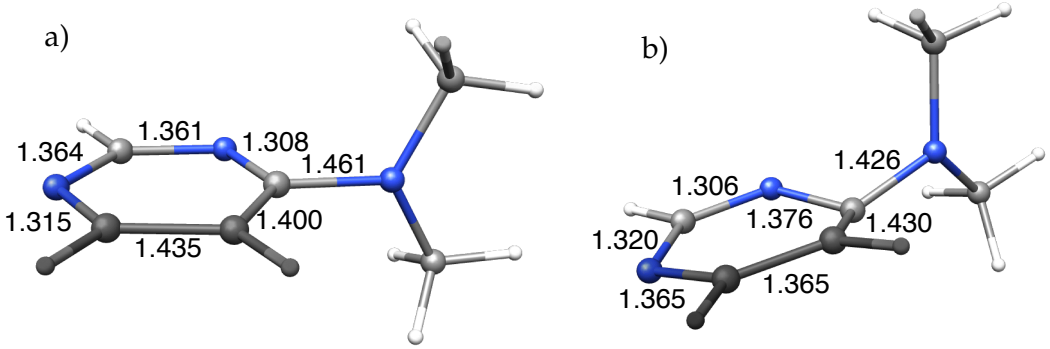

Figure 6.15: Optimized structures of CT/LE CIs at a) CASSCF(8,7) level and b) CASSCF(12,9) level for DMAPD.

For this reason, a LIIRC path between the LE and CT minima was obtained and the energy for the CT and the LE states calculated along this path. The energy profiles obtained are shown in Figure 6.16. The height of the crossing point relative to the minima is not negligible, but the LE minimum can be populated when the

conical intersection is reached in the relaxation path of the CT state from the Franck-Condon region. A latter equilibrium can be established between both minima if the system conserves the excess of excitation energy. To corroborate these hypothesis dynamics calculations should be run, but they are out of the scope of this work.

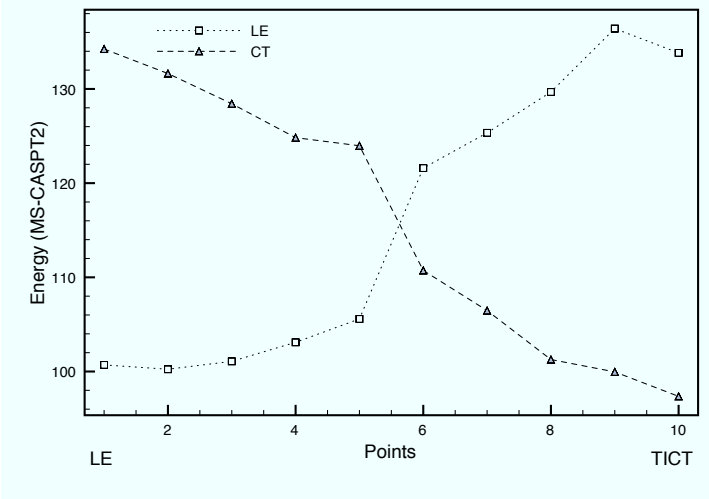

Figure 6.16: Computed MS-CASPT2(12,11) LE-CT path for DMAPD. Energies in kcal·mol^{-1}.

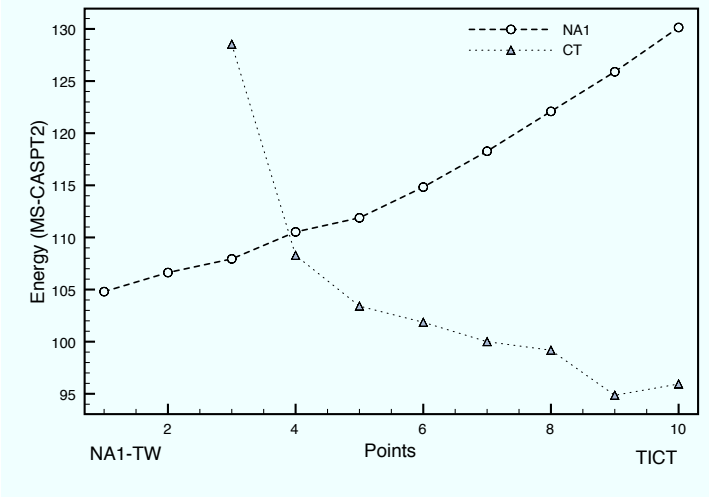

Figure 6.17: Computed MS-CASPT2(12,11) NA1-TW/CT path for DMAPD. Energies in kcal·mol^{-1}.

The NA1-TW minimum has a geometry quite close to that of the CT minimum, reason why we investigated the possible population of the NA1-TW minimum from the CT one. Hence, a LIIRC path was built between these two minima and the

energies were calculated at the MS-CASPT2 level. The profiles represented in Figure 6.17 show that the barrier is almost negligible relative to the NA1-TW minimum, but the energy difference between minima will displace the equilibrium towards the CT species.

For APD, conical intersections of the excited states with the ground state were located only for NA states. Assuming that the same feature holds for DMAPD, and given that in this case the CT and LE state minima are the ones thermodynamically and mechanistically favoured, we can suppose that there is not accessible non-radiative deactivation paths for DMAPD, and luminescence becomes the only possible deactivation channel. Although both LE and CT minima can be populated, the oscillator strength for the transition to the ground state calculated for the CT state (0.0009) is two orders of magnitude smaller than that of the LE state (0.0602). This can be explained by the overlap of the molecular orbitals that describe the excitation of the CT state, because when the electron is transferred from the donor to the acceptor moiety, the orbitals are decoupled by the torsional coordinate, so the transition becomes overlap forbidden. Consequently, the thermodynamic equilibrium has to be highly favourable towards the TICT minimum, in order to populate it for a large lifetime and allow the ICT fluorescence emission. In fact the same would happen with the other NA and NS minima: even if they were populated, given that their oscillator strengths are also very small, radiative transition to the ground state would not take place. This explains the fact that the DMAPD only shows the normal fluorescence band in gas phase.

DMA5MPD

Regarding the paths connecting the S_1 minima, the CT-LE and CT-NA1-TW LIIRC's paths were also obtained for DM5MAPD. The energetic profiles obtained are shown in Figures 6.18 and 6.19.

The global characteristics are almost the same that those found for DMAPD, but in this case the NA1-TW is almost isoenergetic with the CT minima and, given that the barrier connecting them is small, both minima can be equally populated. Nevertheless, in DM5AMPD we found again that the oscillator strength for the transition to the ground state is much larger for the LE state (although in this case only one order of magnitude larger) that those of the CT and NA1-TW states, for the

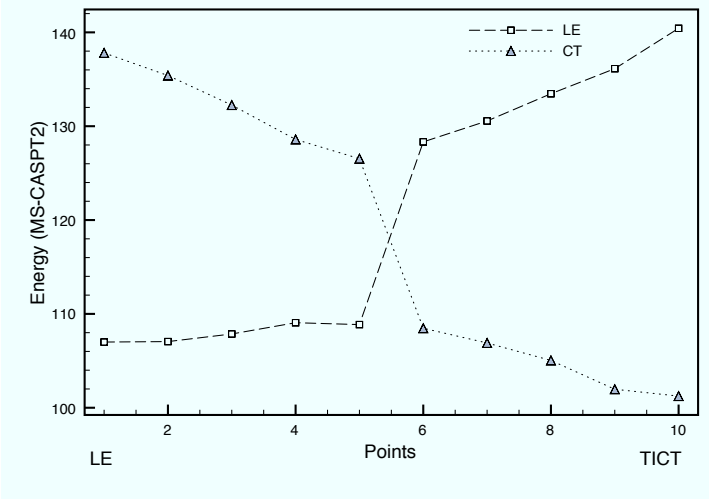

Figure 6.18: Computed MS-CASPT2(12,11) LE-CT path for DMA5MPD. Energies in kcal·mol^{-1}.

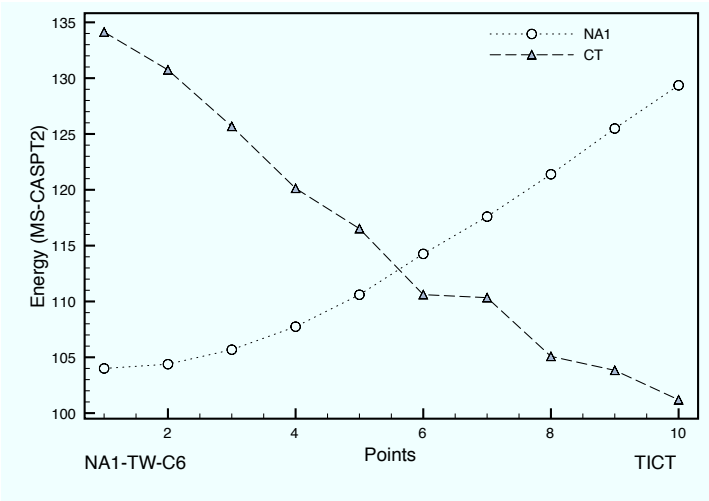

Figure 6.19: Computed MS-CASPT2(12,11) NA1-TW-C6/CT path for DMA5MPD. Energies in kcal·mol^{-1}.

same reasons exposed for DMAPD. Consequently, also in this case the luminescent deactivation will take place only from the LE minimum, and the NA1-TW and TICT states will be depopulated trying to keep the equilibrium with the LE state.

DEAPD

For this derivative the CT minimum is only 4 kcal·mol^{-1} more stable than the LE one (see Table 6.14), an energy difference similar to the ones found for DMAPD

and DMA5MPD, and also here the oscillator strength of the emission to the GS from the LE minimum is two orders or magnitude larger than the one from the CT minimum. Again, for this compound, like in the previous cases, only the normal band is observed in gas phase.

6.3.4 Fluorescence in polar solvent environments

As we already commented in the introduction, DMAPD, DMA5MPD and DEAP show all only normal fluorescence in gas phase while in polar aprotic solvents DMAPD shows only normal fluorescence, DMA5MPD only anomalous fluorescence and DEAP dual fluorescence. Due to this interesting difference and trying to explain it, we have also studied the effect of a polar aprotic solvent (acetonitrile) on the S_1 PES of these three APD derivatives by means of the PCM model.

Results are summarized in Tables 6.15, 6.16 and 6.17. The results for DMAPD and DMA5MPD show that in both cases the environment stabilizes the TICT and LE minima.

Table 6.15: MS-CASPT2 energies relative to the S_0 minimum (E), vertical energies to S_0, solvent stabilization energy (S.S.E, energy difference between gas phase and solution) (all kcal·mol^{-1}), dipole moments (in Debye) and oscillator strengths of the characterized S_1 minima for the DMAPD molecule in acetonitrile obtained with PCM.

Minimum	ΔE	Vertical Energy	S.S.E	μ	f
LE	90.8	89.1	9.9	8.25	0.0533
NA2	98.8	70.4	3.6	2.20	0.0017
NA1-C6	100.6	77.6	6.1	2.13	0.0053
NA1-TW	113.6	80.3	-	**12.20**	0.0001
TICT	89.0	40.7	8.4	11.24	0.0007

Due to the induced dipole moment by the solvent's reaction field, the solute molecule will possess a dipole moment larger in the solvent than in the gas phase. The largest difference is in LE and CT states. In the case of DMAPD a shift from 4.91 D to 8.25 D and from 7.02 D to 11.24 D respectively is observed. Changes in DEAPD are also rather noticeable: from 4.95 D to 7.47 D in the LE state and from 7.78 D to 12.39 in the CT state. In contrast, in DMA5MPD the change of dipole

Table 6.16: MS-CASPT2 energies relative to the S_0 minimum (E), vertical energies to S_0, solvent stabilization energy (S.S.E, energy difference between gas phase and solution) (all in kcal·mol^{-1}), dipole moments (in Debye) and oscillator strengths of the characterized S_1 minima for the DMA5MPD molecule in acetonitrile obtained with PCM.

Minimum	ΔE	Vertical Energy	S.S.E	μ	f
LE	102.5	96.2	4.5	6.11	
NA2	107.7	77.4	-0.6	2.04	
NA2-TW	110.3	71.5	-0.5	0.77	
NA1-C4TW	111.8	65.4	-3.5	2.31	
NA1-C6	114.4	92.1	-5.4	1.40	
NA1-TW	108.7	87.6	-4.7	0.59	
TICT	85.0	39.6	20.5	12.93	

Table 6.17: MS-CASPT2 energies relative to the S_0 minimum (E), vertical energies to S_0 (both in kcal·mol^{-1}), solvent stabilization energy (S.S.E, energy difference between gas phase and solution), dipole moments (in Debye) and oscillator strengths of the characterized S_1 minima for the DEAPD molecule in acetonitrile obtained with PCM.

Minimum	ΔE	Vertical Energy	S.S.E	μ	f
LE	97.5	95.1	7.47	8.4	0.0540
TICT	87.7	41.6	12.39	13.6	0.0030

moment in the LE state (from 4.61 D to 6.11) is not as severe as in DMAPD , but the CT state shows the same trend, with a change from 6.94 D to 12.93 D.

Similarly the molecular wave function and other molecular properties differ significantly from the gas phase calculations. Hence possible changes in oscillator strengths were analysed, but the emission of LE and CT state show the same trends as in gas phase.

It is interesting to point out that the smallest SSE corresponds to DMAPD, that is the derivative that does not change the fluorescence patterns from the gas phase to a polar environment. In this system the stabilizations is similar for the LE and CT states, but in DMA5MPD and DEAPD the CT state is more stabilized than the LE state. In the NA1-TW minimum of DMAPD marked in bold in Table 6.15, the CT state becomes the first excited state in solvent, as can be seen by the high dipole

moment. As a whole, the CT and LE minima continue being the most stable minima of the S_1 PES in a polar solvent, with larger energy differences relative to NA and NS minima.

In gas phase, the small energetic difference between the LE and TICT minima (about 3.3 and 1.6 kcal·mol^{-1} in DMAPD and DM5MAPD respectively) did not compensate the difference in the magnitude of the oscillator strength of the radiative transition to the ground state so only emission from the LE minimum was observed in both cases. In a polar solvent, this situation does not change for DMAPD, because the energy difference between the LE and TICT minima continue being very small (1.8 kcal·mol^{-1}), so again only the normal fluorescence band is expected (in agreement with experimental results). But for DMA5MPD the situation in acetonitrile is different, because the TICT minimum is strongly stabilized, becoming 17.5 kcal·mol^{-1} more stable than the LE minimum. In this case the thermodynamic equilibrium is well displaced towards the TICT minimum and, despite the lower oscillator strength of the transition to the ground state, the TICT species can emit being the ICT band the only one observed.

For DEAPD the LE-CT energy difference increases up to 9.8 kcal·mol^{-1}, which is smaller than the one found for DMA5MPD but larger than that of DMAPD. It can be due to the donor effect of the diethyl groups that stabilizes the CT minimum more than the methyl groups do in DMAPD and DMA5MPD. As a result, the equilibrium in DEAPD is only partially displaced towards the CT minimum, keeping the LE minimum also partially populated. The larger oscillator strength of the transition to the ground state from the LE minimum (f=0.056) allows this species to emit, in spite of its smaller population, and the larger population of the TICT minimum allows this other species also to emit, in spite of its smaller oscillator strength (f=0.0007). The dual fluorescence observed for DEAPD in polar solvents is in this way explained.

6.4 Summary

In this work we have studied the photochemistry of APD and three derivatives to elucidate the factors that determine the luminescent properties of this family of compounds and how the substituents affect it.

To do so, we have studied first in more extension the excited states of the parent system, APD, to determine the factors that are crucial in the photochemical processes that lead to final deactivation of the system after photoexcitation. In a second step, we have analysed these factors for the DMAPD, DEAPD and DMA5MPD derivatives looking for the differences that explain the different luminescent behaviour. Finally we have taken into account the effect of a polar solvent to understand how this environmental change affects the luminescent of these compounds.

In the study developed for the parent system, APD, the results show that the photochemistry is determined by the relative stability of the minima on the S_1 PES of the different types of excited states and the paths connecting them. The substituents of the derivative systems affect the relative stability of these minima. First of all, the alkyl substituents of the amino group stabilize preferentially the LE and CT excited states of the system. This is due to the donor effect of the alkyl substituents, which also reduces the pyramidalization of the amino group. In fact, for the unsubstituted APD the amino group is pyramidalized, while for the rest of derivatives the structure of the LE minima is nearly planar. In addition, when there is a bulky substituent in the ortho position, the steric repulsion between the substituents destabilizes the planar LE minimum, favouring the CT excited state.

Regarding the luminescent behaviour, if the NA minima on S_1 are more stable than the LE and CT ones, the most effective reactive channel is the non-radiative deactivation through the very accessible conical intersections that exist between the NA excited states and the ground state. In this case, like for example for APD, luminescent will not be observed.

On the other hand, if the CT and LE minima on the S_1 surface are more stable that the NA minima, the non-radiative deactivation channels are not accessible, and the deactivation of the system occurs necessarily through emission. The radiative species is determined by two factors: the relative stability of the LE/CT minima, and the value of the oscillator strength for the radiative transition to the ground state. Given that this oscillator strength is much larger for the LE state than for the CT one, the CT minima must be much more stable than the LE one to be competitive in the radiative deactivation process.

For the three derivatives DMAPD, DMA5MPD and DEAPD in gas phase, the NA minima are less stable that the LE and CT ones, being the last two almost

isoenergetics (CT-LE energy differences: 3.4, 1.6 and 4.6 kcal·mol^{-1} respectively). This leads to a common luminescent pattern, where only the normal fluorescence band is observed.

Polar solvents stabilize preferentially the CT minimum relative to the LE one, and the size of this relative stabilization depends partially on the magnitude of the dipole moment of both species in the different compounds. As a whole, the stabilization is larger for the DMA5MPD, where ICT-LE energy difference is 17.5 kcal·mol^{-1}. This difference is large enough to lead to luminescence exclusively from the CT minima. Consequently, for this compound only the anomalous fluorescence band is observed in polar solvents. The DEAPD is the intermediate case, where the ICT-LE is only of 9.9 kcal·mol^{-1}. In this case, both radiative deactivation are competitive and dual fluorescence is observed in polar solvents. For DMAPD, the ICT-LE energy difference is only 1.8 kcal·mol^{-1} so, like in gas phase, only the normal fluorescence band is observed.

The good agreement between the computational results and the experimental observations support the hypothesis proposed in this work, where the luminescent behaviour of several members of the aminopyrimidine family is justified.

A3 Appendix: Description of electronic states

The results shown in this chapter are based on calculations which parameters were decided after the exploratory computations described in this Appendix.

First of all the initial calculations of the vertical spectra at the ground state optimized geometry were performed averaging 7 states at the CASCSF level, using a 6-31G* basis set and an active space of 12 electrons in 9 orbitals. It comprises 6 p in ring orbitals and the out of ring p amino group orbital which describes the ($\pi - \pi^*$) excitations, and the two nitrogen in ring lone pairs that give rise to ($n - \pi^*$) excitations. The vertical energies of the first 7 states obtained at several levels of calculations are shown in Table 6.18.

Table 6.18: Vertical energies (in kcal·mol^{-1}), oscillator strengths (f), and dipole moments (μ in Debyes) obtained at different levels of calculation, all based on SA7-CASSCF(12,9) reference wave function for APD.

State	CASSCF	SS-CASPT2	PM-State	MS-CASPT2
S_0	0.0	0.0	S_0	0.0
LE	121.1	122.7	NA1	114.9
NA1	128.4	117.5	NA2	122.9
NA2	134.6	120.9	LE	123.8
NS1	163.5	147.7	CT	149.8
NS2	173.1	155.5	NS1	150.0
CT	176.7	147.0	NS2	158.9

The states of Table 6.18 are labelled according to the nature of the excitations that give them rise. Given that this assignation is a key point in the development of our work, it is interesting to explain how it has been done. To make the description easier, we will use from this moment the labels that were assigned at the end of the analysis described here (see Figure 6.3).

As a first step, to understand the nature of the excited states, we looked at the composition of the CASSCF functions given as combinations of configuration state functions (CSF) by the Molcas package. We found that all the NA and NS states were mainly described by only one CFS while in the LE and CT states two CSF had large weights. Given that in all cases the CFS corresponded mainly to monoexcitations, it is possible to interpret the nature of states looking at the orbitals

involved in the transitions.

Let's now analyse the MS-CASPT2 results. The composition of the PM-CAS-CI wave functions, shown in Table 6.19, reflects that the description of some states at the MS-CASPT2 level is given by combination of zero order wave functions, the states described at CASSCF level. The first and second PM-CAS-CI excited states are a combination of 3-SA-CASSCF and 4-SA-CASSCF states. Both are excitations from the NA orbital. The 6^{th} and 7^{th} PM-CAS-CI excited states are a combination of 5-SA-CASSCF and 6-SA-CASSCF states, both generated by a promotion of electronic density in the NS orbital. This mixture of states makes difficult the physical interpretation of the nature of the excited states, and introduces a margin of error given that the optimization procedure is based on CASSCF wave functions, that in this case are shown not to be a good approximation to the PM-CAS-CI wave functions.

Table 6.19: Eigenvectors of the MS-CASPT2(12,9) effective Hamiltonian matrix diagonalitzation of the first seven low-lying states in APD

	7 state averaged						
States	1 (GS) PM-CI	2 PM-CI	3 PM-CI	4 PM-CI	5 PM-CI	6 PM-CI	7 PM-CI
				Eigenvectors			
GS	-0.9957	-0.0009	0.0044	0.0127	-0.0875	-0.0268	0.0000
2	0.0028	-0.0874	-0.0146	0.9903	0.0996	0.0385	-0.0002
3	0.0015	0.8023	0.5577	0.0790	0.0694	-0.1798	0.0440
4	0.0021	0.5433	0.8094	-0.0386	-0.0167	0.1094	0.1898
5	0.0007	0.2311	-0.0444	0.0138	-0.2775	0.8723	0.3263
6	0.0028	0.0080	0.1774	0.0029	-0.1191	0.3149	-0.9247
7	0.0924	-0.0095	0.0154	0.1056	-0.9414	-0.3056	0.0206

To better clarify the nature of the excited states, we run two set of calculations. In the first set we localized the orbitals of the active space and calculated the occupation number of these orbitals in the different excited states at CASSCF(12,9) level. These results are collected in Table 6.20. The change of occupation reflects the excitation undergone in each excited state. The procedure to locate orbitals minimizes the overlapping of the orbitals centred in different atoms, but not between orbitals on the same centre. For this reason the atomic *p* and *n* orbitals of the nitrogen of the ring are not described separately and we consider the occupation on the nitrogen atoms as a whole.

Table 6.20: Orbital occupation numbers of the seven lowest states at CASSCF(12,9) with localized orbitals.

Orbitals	SO	LE	NA1	NA2	NS1	NS2	CT
π -amino	1.86	1.80	1.88	1.87	1.87	1.88	1.64
N1	3.12	3.05	2.91	2.84	2.82	3.09	3.27
p-C2	0.92	0.96	0.93	1.13	1.00	1.11	1.00
N3	3.16	3.14	3.02	3.00	3.04	2.78	3.17
p-C4	0.90	0.96	1.00	0.95	0.95	1.05	0.93
p-C5	1.08	1.00	1.09	1.21	1.14	1.19	1.10
p-C6	0.92	1.00	1.13	0.94	1.13	0.91	0.86

Regarding these occupation numbers, the CT state is well characterized by a decrease in the occupation of the off-ring N of 0.22, in agreement with the donor character of the amino group. The charge transferred to the ring is located mainly in N_1 and C_2. On the other hand, in the LE state the occupation number of the off-ring N orbital hardly change, and the changes in the occupation numbers of the orbitals located on the atoms of the ring are appreciably smaller that those observed in the CT state. NS and NA states show a decrease of the occupations of N_1 and N_3 that varies between 0.1 and 0.4, but always involving both Nitrogen atoms. It is not possible then to describe these states at the CASSCF level by single excitations (from a unique nitrogen orbital), and consequently the nature of the states described by the PM-CAS-CI functions, where the CASSCF functions are mixed, is even more difficult to elucidate. We can conclude that localized orbitals do not help in getting a simple description of the NA and NS states.

Another option to analyse the nature of the excitations is to calculate the difference of electron density between the ground state and each excited state. The 3D plots of this electron density differences can help to understand the change in the electronic distribution under the excitation. Figure 6.20 shows in no filled areas where the electronic density decreases and in filled areas where this density increases under the excitation. Again in this representation the nature of the CT and LE states are clear, but in the NA and NS states the changes of electronic density are always located in both in-ring nitrogen atoms, as was expected from the results of the analysis performed with localized orbitals. Nevertheless it is interesting to observe the similarity between the results for NA1 and NS1, whose wave functions only differs in the sign of the combination of the nitrogen orbitals.

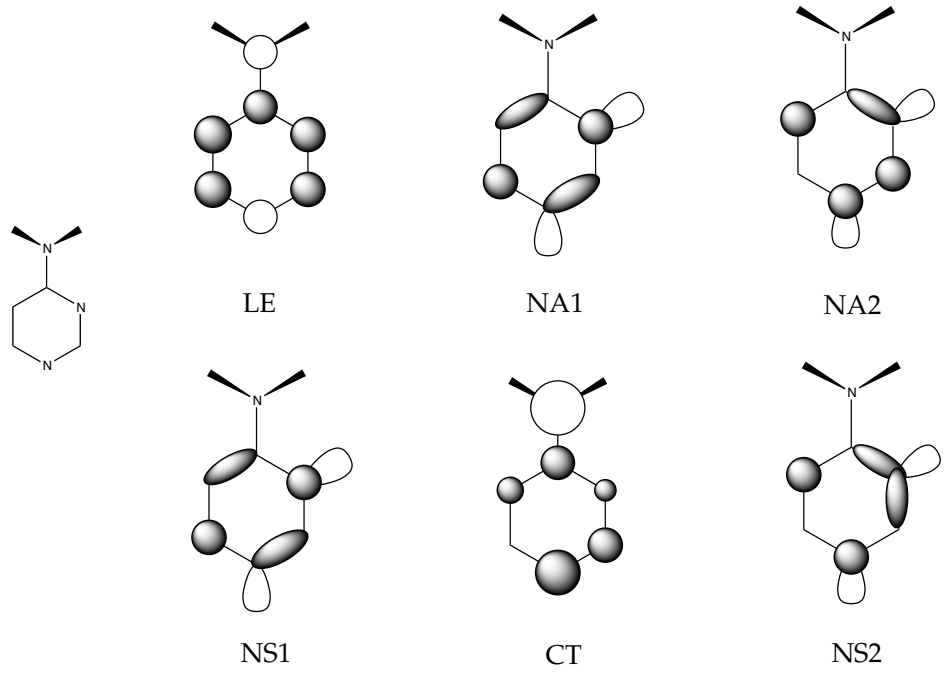

Figure 6.20: Difference for electron density between ground state and each of the first 6 excited states of APD. Filled areas are those where the electronic density increases for excited states, while in no filled areas the electron density decreases.

If SA-CASSCF wave functions are not quite correct to an accurate description of aminopyrimidines states, the optimization procedure carried out at this level could be incorrect. It is then convenient to minimize the mixing of CASSCF states at the MS-CASPT2 level as much as possible. To apply efficient strategies to minimize the mixing, it is convenient to try to understand the origin of the problem.

We have to consider the possibility of having some low energy Rydberg states in this system that can play a role in our results, even if they will be poorly described by a 6-31G* basis set. Given that the dynamic correlation in valence states is in general larger that in Rydberg states, the energies of both type of states calculated at the CASCF level (that will result in an artificial increase of the relative energy of the valence states) can become similar. If they are close enough, the states can mix. This artificial mixing due to the poor description of the CASSCF wave function will not be removed with the inclusion of perturbation at the SS-CASPT2 level, only at the MS-CASPT2 level the mixing will be removed and the energies obtained correctly, but the corresponding PM-CAS-CI wave functions will mix the zero order CASSCF states.

To check this possibility we took advantage of one of the differential characteristic of a Rydberg state, the large extension of its electronic distribution, due to the occupancy of diffuse orbitals. Valence states will have an orbital extension similar to the ground state while Rydberg states will be more diffuse. Diffuseness is generally measured by $< x^2 >$, the expectation value of $x^2 = \sum_i^n x^2(i)$ (n number of electrons). We will analyse the nature of the states described at the CASSCF and CASPT2 level through the values of the computed second order Cartesian moments, collected in Table 6.21. The values for the excited states calculated are similar to those of the ground state, so these results indicate that all the excited states calculated here are valence states. Besides, it is evident that there are not significant differences between the values obtained at the CASSCF and at the CASPT2 level. With this results we can conclude that there are not mixing of valence and Rydberg states at the CASSCF.

Table 6.21: Nature of states and second cartesian (XX, YY and ZZ) moments in atomic units of the lowest states of APD calculated at CASSCF(12,9)/6-31G* level.

State	CASSCF			SS-CASPT2		
	XX	YY	ZZ	XX	YY	ZZ
SO	-28.08	-31.32	-28.84	-27.99	-31.4	-28.72
LE	-27.66	-31.25	-29.3	-27.69	-31.32	-29.16
NA1	-26.58	-32.36	-27.48	-26.71	-32.4	-27.63
NA2	-26.45	-32.43	-27.12	-26.69	-32.45	-27.17
NS1	-25.06	-32.37	-28.24	-25.46	-32.44	-28.35
NS2	-28.84	-32.37	-26.14	-28.59	-32.41	-26.52
CT2	-27.04	-31.26	-28.65	-27.16	-31.47	-28.61

Once ruled out a possible mixing between valence and Rydberg states, we tried to improve the calculations in several ways to try to minimize the mixing of states observed in the PM-CAS-CI wave functions. First of all, in order to have a better description of the states generated by n_N excitations (NS and NA excited states), the basis set was enlarged including diffuse functions for the in-ring N atoms. This change in the basis set led to small quantitative differences in the relative energies (of less than 5 kcal $\cdot$ mol^{-1} in CASPT2 results, see Table 6.22). The composition of the PM-CAS-CI wave functions (see Table 6.23) exhibit a soaring mixing between CASSCF states in comparison with the previous results and there is an enlargement of the second order cartesian moments relative to previous results (Table 6.24), in

agreement with the diffuse character of the new orbitals included in the basis set. Thus no qualitative changes were observed when diffuse functions were added and the mixing in the PM-CAS-CI wave functions persisted.

Table 6.22: Vertical energies (in kcal·mol^{-1}) of the lowest states obtained at different levels of calculation, based on a SA7-CASSCF reference function for APD with diffuse functions.

State	CASSCF	SS-CASPT2	PM-State	MS-CASPT2
SO	0.0	0.0	SO	0.0
LE	124.2	121.6	NA-1	118.1
NA-1	134.3	119.0	NA-2	122.7
NA-2	139.4	123.1	LE	125.1
NS-1	169.5	151.3	CT	144.7
NS-2	172.3	142.5	NS-1	152.4
CT	176.8	157.4	NS-2	159.4

Table 6.23: Eigenvectors of the MS-CASPT2(12,9) effective Hamiltonian matrix diagonalitzation of the first seven low-lying states in APD obtained with diffuse functions.

	7 state averaged						
States	1 (GS) PM-CI	2 PM-CI	3 PM-CI	4 PM-CI	5 PM-CI	6 PM-CI	7 PM-CI
	Eigenvectors						
GS	0.996	-0.0007	-0.0077	-0.0053	0.0855	0.0011	0.0004
2	-0.0040	-0.1592	-0.9860	-0.0180	-0.0440	0.0025	0.0005
3	-0.0016	0.8756	-0.1330	-0.4476	-0.0113	-0.1214	-0.0148
4	0.0023	0.4366	-0.0879	0.8883	0.0241	-0.0435	0.0999
5	0.0005	-0.1304	0.0187	-0.0125	0.0043	-0.9498	0.2833
6	0.0859	0.0069	0.042	0.0292	-0.994	-0.0106	-0.0187
7	0.0007	0.0068	0.0029	-0.0957	-0.0236	0.2847	0.9535

The second possible strategy to improve the description of the valence states at the CASSCF level is to enlarge the active space to include more dynamic correlation. After checking different active spaces, two more virtual (diffuse) in-ring N orbitals were incorporated in the active space (obtaining a (12,11) active space), and the first seven lowest energy singlet states of APD calculated. The PM-CAS-CI wave functions are shown in Table 6.2 of the main text of this chapter and second cartesian moments are shown in Table 6.25. The description of states at MS-CASPT2 level shows that the studied states are fairly the same at CASSCF and MS-CASPT2 level.

Table 6.24: Nature of states and second cartesian (XX, YY and ZZ) moments in atomic units of the lowest states of APD calculated at CASSCF(12,9)/6-31G* adding diffuse functions.

State	CASSCF(12,9)		
	XX	YY	ZZ
SO	-28.63	-31.78	-29.24
LE	-28.26	-31.71	-29.71
NA1	-26.98	-32.78	-27.85
NA2	-27.02	-32.9	-27.39
NS1	-25.63	-32.8	-28.58
NS2	-29.32	-32.86	-26.52
CT2	-27.47	-31.74	-29.05

We can conclude that using a active space (12,11) the initial description of the system made initially at the CASSCF level will be a good approximation of the description done subsequently at the MS-CASPT2 level.

Table 6.25: Nature of states and second cartesian (XX, YY and ZZ) moments in atomic units of the lowest states of APD calculated at CASSCF(12,11)/6-31G* level.

State	SS-CASPT2(12,11)		
	XX	YY	ZZ
SO	-28.08	-31.32	-28.84
LE	-27.66	-31.25	-29.30
NA1	-26.58	-32.36	-27.48
NA2	-26.45	-32.43	-27.12
NS1	-25.06	-32.37	-28.24
CT	-28.84	-32.37	-26.14
NS2	-27.04	-31.26	-28.65

The character of valence excited states described using a CAS(12,9) is kept in the results obtained with CAS(12,11). It is interesting to point out that when using a CAS(12,11), NA and NS are the only excited states that have contributions of CSF with excitations to N virtual orbitals with coefficients about 0.06-0.07.

While the NS and NA transitions can be described as monoexcitations, the excitation that give place to the LE state involves depopulation of all three π-ring orbitals of the active space and occupation of the two π^*-ring orbitals, although the totally symmetric π-ring orbital undergoes a minor change in its occupation (from

1.96 to 1.88) and the main contribution comes from the other two π-ring orbitals, whose population changes from 1.91 to 1.31 and 1.59 at the CASSCF level.

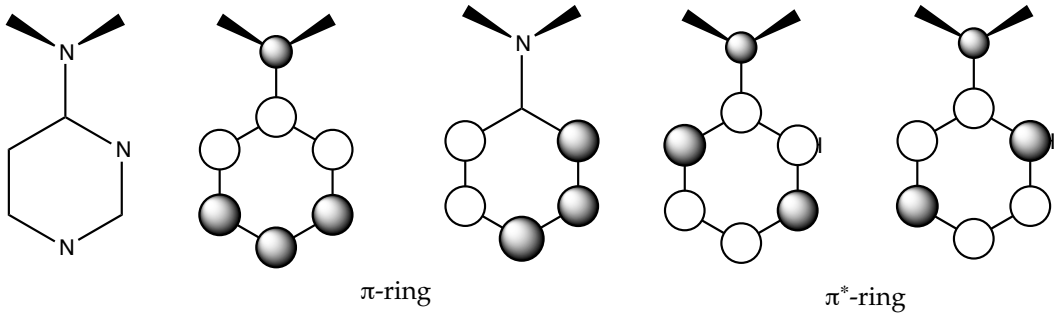

Figure 6.21: Delocalized molecular orbitals

Concerning the CT state, it is characterized by the promotion of an electron from a π-ring orbital with a nodal plane to a π^*-ring orbital delocated on the same atoms (Figure 6.21). With this description of the excitation, the only hint that points to this states as one of CT character, is its dipole moment, of the order of 6 D to be compared with the dipole of around 3 D of the other states. But the difference electron density plot between the CT state and ground state show a transference from the out of ring amino group to the ring (Figure 6.20) and SA-CASSCF(12,9) calculations with localized orbitals verified this transference of charge (see Table 6.20).

The MS-CASPT2(12,11) results are considered as final results to discuss in this chapter.

CHAPTER 7

CONCLUSIONS

The more outstanding conclusions have already been highlighted in previous chapters. However, it seems adequate to summarize them now.

Photosensitization by Phenalenone

Phenalenone (PN) is a very efficient singlet oxygen sensitiser in a wide range of solvents. The mechanism for populating the triplet state of PN responsible for this reaction, the $^3(\pi - \pi^*)$ state, and photochemical competitive pathways are studied.

- After the initial population of the S_2 excited state of $^1(\pi - \pi^*)$ character, the system undergoes an internal conversion to the $^1(n - \pi^*)$ state.
- After populating the dark S_1 state, the system relaxes to the $^1(n - \pi^*)$ minimum, but rapidly populates the triplet manifold through a very efficient intersystem crossing to the $^3(\pi - \pi^*)$ state.
- Although the population of the minimum of this triplet state is strongly favoured, a conical intersection with the $^3(n - \pi^*)$ surface opens an internal conversion channel to this state, a path accessible only at high temperatures.

- Radiationless deactivation processes are ruled out on the basis of the high-energy barriers found for the crossings between the excited states and the ground state.
- In the case of the frequency of fluorescence, this is the first time that these data have been theoretically predicted in good agreement with the experimental results.

Charge transfer in Aminobenzonitriles

Different reaction pathways of radiation and radiationless deactivation of 4-aminobenzonitrile (ABN) and 2,3,5,6-tetrafluoro-4-aminobenzonitrile (ABN-4F), which differ each other in the kind of emission spectra and in the fluorescence quantum yield, have been theoretically investigated. Two photoprocess mediated by ICT mechanisms that populate the LE state are proposed in this work.

- After the initial excitation to the ICT(Q) state there are two accessible paths along two different coordinates, giving place to the twist-ICT and rehybridized-ICT photoprocesses.
- A bend-geometry reaction coordinate permits the access to a conical intersection ICT(Q)/ICT(CN) populating the $(\pi - \sigma^*)$ state, but a ICT(CN)/LE conical intersection can be then reached, populating finally the minimum of the LE state.
- There is also an accessible adiabatic path between ICT(Q) and LE minima.
- Four different S_1/S_0 radiationless decay pathways have been localized, three of them from the LE state and one mediated by an ICT state.

ABN – After population of the locally excited (LE) minimum, the large activation barriers found explain that in this molecule the internal conversion only becomes an important decay channel above room temperature. In this system the equilibrium between LE and ICT(Q) minima is strongly displaced towards the S_1 -LE specie, from where the normal fluorescence band will be produced.

ABN-4F – Our results show that the topology of the potential energy surfaces in ABN-4F do no change in comparison with its counterpart ABN. The main changes occur in the energetics of the different species. In the case of ABN-4F the dominating process is the internal conversion to the ground state, where the system passes through a S_0/S_1 conical intersection in an almost barrierless process, precluding the emission that gives place to the normal fluorescence band. The process from the S_1-LE minimum to the S_1-ICT(Q) minimum is endoergic, with a small activation barrier. Consequently the S_1-ICT(Q) minimum can be populated temporarily leading to the appearance of the ICT anomalous band. We found that the intramolecular charge transfer (ICT) emission in ABN-4F takes place from a twisted structure on the ICT(Q) state.

Simple/dual fluorescence in aminopyrimidines

We have studied several members of this family that exhibit different fluorescence patterns to try to explain their photochemistry. This study has helped to understand the effect of the substituents and the environment. In the derivatives studied it has been observed not fluorescence at all, only a fluorescence band, normal or anomalous or dual fluorescence, depending on the substituents and on the environment (gas phase vs. polar solvents).

- We have located minima of several excited states (local excited (LE), charge transfer (CT) and $n_N-\pi^*$ states) on the lowest excited potential energy surface (S_1).
- The relative energy of these minima is the determinant factor of the luminescent behaviour.
- If the more stable S_1 minima are of $n_N-\pi^*$ character, a non radiative deexcitation channel is the most efficient reaction path and the system shows no fluorescence. If the more stable minima are the CT and/or the LE states, the non radiative deactivation channel is not accessible and the system fluoresces.

- The relative energies of the CT and LE minima (affected by substituents and by the presence of a polar solvent) and the different magnitude of the oscillator strength for the radiative transition to the ground state determine which emission is more efficient, giving place to normal, anomalous or dual fluorescence.

Our computational results satisfactorily explain the experimental findings and are in very good agreement with the experimental data available.

BIBLIOGRAPHY

[1] J. Ordoñez, V Navarro, and J. M. Sánchez. *Historia de la ciencia*. Alianza editorial, Madrid, 2005.

[2] Sadiku. M. N. O. *Elements of electromagnetism*. Oxford University Press, Oxford, 2001.

[3] P. Thuillier. *De arquimedes a Einstein*. Alianza editorial, Madrid, 1990.

[4] F. L. Pilar. *Elementary Quantum Chemistry*. McGraw-Hill, New York, 1968.

[5] E. Schrodinger. *Phys. Rev*, 28:1049, 1926.

[6] C. Schweitzer and R. Schmidt. *Chem. Rev.*, 103:1685–1757, 2003.

[7] C.S. Foote and E. L. Clennan. *Active Oxygen in Chemistry*. Chapman and Hall, London, 1995.

[8] C. Flors, M. J. Fryer, J. Waring, B. Reeder, U. Bechtold, P. M. Mullineaux, S. Nonell, M.T Wilson, and N. R. Baker. *J. Exp. Bot.*, 57:1725–34, 2006.

[9] R. W. Redmond and I. E. Kochevar. *Photochem. Photobiol.*, 82:1178–1186, 2006.

[10] L. I. Grossweiner. *The Science of Phototherapy: An Introduction*. Springer, Netherlands, 2005.

[11] J. Arnbjerg, M. J. Paterson, C. B. Nielsen, M. Jörgensen, O. Christiansen, and P. R. Ogilby. *J. phys. Chem. A*, 111:5756–67, 2007.

[12] C. Marti, O. Jürgens, O. Cuenca, M. Casals, and S. Nonell. *J. Photochem. and Photobiol. A*, 97:11–18, 1996.

[13] E. Oliveros, S. H. Bossmann, S. Nonell, C. Marti, G. Heit, A. Neuner, and M. Brauna. *New J. Chem.*, 23:85–93, 1999.

[14] C. Bosshard, K. Sutter, P. Pretre, J. Hulliger, M. Florsheimer, P. Kaatz, and P. Gunter. *Organic Nonlinear Optical Materials, Advances in Nonlinear Optics*. Gordon and Breach Publishers, New York, 1995.

[15] B. Kippelen, H. S. Lackritz, and R. O. Claus. *Organic Nonlinear Optical Materials and devices*. Materials Research Society, Warrendale, 1999.

[16] J. P. Lakowicz. *Principles of Fluorescence Spectroscopy*. Kluwer Academic, Hongham, 1999.

[17] J. J. La Chair. *Angew. Chem., Int. Ed. Engl.*, 38:3047–3050, 1999.

[18] J. J. La Chair. *Angew. Chem., Int. Ed. Engl.*, 37:325–329, 1998.

[19] J. J. La Chair. *Angew. Chem., Int. Ed. Engl.*, 110:339, 1998.

[20] Z. R. Grabowski, K. Rotkiewicz, and W. Rettig. *Chem. Rev.*, 103:3899–4030, 2003.

[21] V. Rettig. *Angew. Chem. Int.*, 25:971–988, 1986.

[22] Z. R. Grabowski, K. Rotkiewicz, and K. H. Grellman. *Chem. Phys. Lett.*, 19: 315–318, 1973.

[23] K. A. Zachariasse, M. Grobys, T. Vonderhaar, A. Hebecker, Y. Ilichev, Y. Jiang, O. Morawski, and W. Künhle. *J, Photochem. Photobiol. A*, 102:59–70, 1996.

[24] K. A. Zachariasse. *J. Photochem. Photobiol. A*, 105:373–383, 1997.

[25] S. I. Druzhinin, N. P. Ernsting, S. A Kovalenko, L. P. Lustres, T. A Senyushkina, and K. A Zachariasse. *J. Phys. Chem. A*, 110:2955–69, 2006.

[26] W. Schuddeboom, S. A. Jonker, J. H. Warman, U. Leinhos, W. Künhle, and K. A. Zachariasse. *J. Phys. Chem.*, 96:10809, 1992.

[27] K. A. Zachariasse, T. Von Der Haar, A. Hebecker, U. Leinhos, and W. Künhle. *Pure Appl. Chem.*, 65:1745, 1993.

[28] S. I. Druzhinin, Y. Jiang, A. Demeter, and K. A. Zachariasse. *Phys. Chem. Chem. Phys.*, 3:5213–5221, 2001.

[29] G. Zechmann and M. Barbatti. *Int. J. Quantum Chem.*, 108:1266–1276, 2008.

[30] M. Barbatti, M. Ruckenbauer, J. J. Szymczak, A. J. A Aquino, and H. Lischa. *Phys. Chem. Chem. Phys.*, 10:482–494, 2008.

[31] J. Herbich, Z. R. Grabowski, H. Wójtowicz, and K. Golankiewicz. *J. Phys. Chem.*, 93:3439–3444, 1989.

[32] J. Herbich, F. P. Salgado, R. P. H. Rettschnick, Z. R. Grabowski, and H. Wójtowicz. *J. Phys. Chem.*, 95:3491–3497, 1991.

[33] R. Pou-Amérigo, M. Merchán, and E. Ortíz. *J. Chem. Phys.*, 110:9536, 1999.

[34] V. Molina and M. Merchán. *J. Phys. Chem. A*, 105:3745–3751, 2001.

[35] D. J Tannor. *Introduction to quantum mechanics: a time dependent perspective*. University Science Books, California, 2006.

[36] R. Englman. *The Jahn-Teller effect in molecules and cristals*. Wiley-Interscience, New Jersey, 1992.

[37] I. B. Bersuker. *The Jahn-Teller effect*. Cambridge University Press, Cambridge, 2006.

[38] J. Franck and E. G. Dymond. *Trans. Faraday Soc.*, 21:536–542, 1926.

[39] W. A. Noyes. *Rev. Mod. Phys.*, 5:280–287, 1933.

[40] E. Condon. *Phys. Rev.*, 28:1182–1201, 1926.

[41] F. Bernardi, M. Olivucci, and M. A. Robb. *Chem. Soc. Rev.*, 25:321–328, 1996.

[42] M. Garavelli. *Theo. Chem. Acc.*, 116:87–105, 2006.

[43] M. Kasha. *Faraday Discussions*, 9:14–19, 1050.

[44] M. Olivucci. *Computational photochemistry, volume 16*. Elsevier, Siena, 2005.

[45] G.A Worth and L.S. Cederbaum. *Ann. Rev. Phys. Chem.*, 55:127–158, 2004.

[46] M. Olivucci F. Bernardi. *Chem. Soc. Rev.*, 1:321, 1996.

[47] J. von Neumann and E. P. Wigner. *Physik Z*, 30:467, 1929.

[48] H. C. Longuet Higuins G. Herberz. *Disc. Faraday Soc.*, 35:77, 1963.

[49] H. C. Longuet-Higgins. *Proc. R. Soc. Lond. A.*, 344:147–156, 1975.

[50] I. N. Ragazos and M. A. Robb. *Chem. Phys. Lett.*, 197:217–221, 1992.

[51] Gregory J. Atchity, Sotirios S. Xantheas, and Klaus Ruedenberg. *J. Chem. Phys.*, 95:1862–1876, 1991.

[52] B. Heß, C. M. Marian, U. Wahlgren, and O. Gropen. *Chem. Phys. Lett.*, 251: 365–371, 1996.

[53] J. M. Anglada and J. M. Bofill. *J. Comput. Chem.*, 18:992–1002, 1996.

[54] A. Szabo and N. S. Ostlund. *Modern Quantum Chemistry: Introduction to Advanced Electronic Structure Theory*. Dover Publications, New York, 1982.

[55] F. Jensen. *Introduction to Computational Chemistry*. Wiley-Blackwell, West Sussex, 2006.

[56] G. Karlstrom. *Comput. Mat. Sci.*, 28:222–239, 2003.

[57] M. J. Frisch, G. W. Trucks, H. B. Schlegel, G. E. Scuseria, M. A. Robb, J. R. Cheeseman, J. A. Montgomery, Jr., T. Vreven, K. N. Kudin, J. C. Burant, J. M. Millam, S. S. Iyengar, J. Tomasi, V. Barone, B. Mennucci, M. Cossi, G. Scalmani, N. Rega, G. A. Petersson, H. Nakatsuji, M. Hada, M. Ehara, K. Toyota, R. Fukuda, J. Hasegawa, M. Ishida, T. Nakajima, Y. Honda, O. Kitao, H. Nakai, M. Klene, X. Li, J. E. Knox, H. P. Hratchian, J. B. Cross, V. Bakken, C. Adamo, J. Jaramillo, R. Gomperts, R. E. Stratmann, O. Yazyev, A. J. Austin, R. Cammi, C. Pomelli, J. W. Ochterski, P. Y. Ayala, K. Morokuma, G. A. Voth, P. Salvador, J. J. Dannenberg, V. G. Zakrzewski, S. Dapprich, A. D. Daniels, M. C. Strain, O. Farkas, D. K. Malick, A. D. Rabuck, K. Raghavachari, J. B. Foresman, J. V. Ortiz, Q. Cui, A. G. Baboul, S. Clifford, J. Cioslowski, B. B. Stefanov, G. Liu, A. Liashenko, P. Piskorz, I. Komaromi, R. L. Martin, D. J.

Fox, T. Keith, M. A. Al-Laham, C. Y. Peng, A. Nanayakkara, M. Challacombe, P. M. W. Gill, B. Johnson, W. Chen, M. W. Wong, C. Gonzalez, and J. A. Pople. Gaussian 03, Revision C.02. Gaussian, Inc., Wallingford, CT, 2004.

[58] C. C. J. Roothaan. *Rec. Mod. Phys.*, 23:69–89, 1951.

[59] G. G. Hall. *Proc. R. Soc. A*, 205:541–552, 1951.

[60] P. Malmqvist, A. Rendell, and B. O. Roos. *J. Phys. Chem.*, 94:5477–5482, 1990.

[61] B. O. Roos. *Advances in Chemical Physics, Volume 69*. Wiley Interscience, New York - p. 339, 1987.

[62] B. O. Roos. *Lecture Notes in Quantum Chemistry*. Springer, Berlin - p. 117, 1992.

[63] P. A. Siegbahn, B. O. Roos, and B. Levy. *Phys. Scripta*, 21:323–327, 1980.

[64] B. Levy and G. Berthier. *Intern. J. Quantum Chem*, 2:307–319, 1968.

[65] A. Banerjee and F. Grein. *J. Chem. Phys*, 66:1054, 1977.

[66] P. Pulay. *Chem. Phys. Lett.*, 73:393–398, 1980.

[67] T. P. Hamilton and P. Pulay. *J. Chem. Phys.*, 84:5728–5734, 1986.

[68] K. N. kudin, G. E. Scuseria, and E. Cancès. *J. Chem. Phys.*, 116:8255–8261, 2002.

[69] K. Andersson, P. A. Malmqvist, and B. O. Roos. *J. Chem. Phys.*, 96:1218–1226, 1992.

[70] H. F. Schaefer. *Methods of Electronic Structure Theory (Modern theoretical chemistry)*. Plenum, New York, 1977.

[71] K Andersson and B. O. Roos. *Int. J. Quantum Chem*, 45:591–607, 1993.

[72] G. Ghigo, B. O. Roos, and P. A. Malmqvist. *Chem. Phys. Lett.*, 396:142–149, 2004.

[73] N. Forsberg and P. A. Malmqvist. *Chem. Phys. Lett.*, 155:189–194, 1989.

[74] N. Forsberg and Malmqvist P. *Chem. Phys. Lett.*, 274:196–204, 1997.

[75] J. Finley, P. A. Malmqvist, B. O. Roos, and L. Serrano-Andrés. *Chem. Phys. Lett.*, 288:299–306, 1998.

[76] M. A. El-Sayed. *J. Chem. Phys.*, 38:2834–2838, 1963.

[77] J. Tatchen and C. M. Marian. *Chem. Phys. Lett.*, 313:351–357, 1999.

[78] P.A. Malmqvist, B. O. Roos, and B. Schimmelpfennig. *Chem. Phys. Lett.*, 357: 230–240, 2002.

[79] C. Reichardt. *Solvents and Solvent Effects in Organic Chemistry*. VCH, Weihein, 1990.

[80] J. Tomasi and M. Persico. *Chem. Rev.*, 94:2027–2094, 1994.

[81] V. Barone and J. Cossi. *J. Chem. A*, 102:1995–2001, 1998.

[82] V. Barone, M. Cossi, and J. Tomasi. *J. Chem. Phys.*, 107:3210–3221, 1997.

[83] J. A. Leary, A. L. Lafleur, H. L Liber, and K. Blemann. *Anal. Chem.*, 55:758–761, 1983.

[84] K. Winters, J. C Batterton, and C. Van Baalen. *Environ. Sci. Technol.*, 11:270–272, 1977.

[85] R. G. Cooke and J. M. Edwards. *Prog. Chem. Org. Nat. Prod.*, 40:153–190, 1981.

[86] J. G. Luis, W. Quiñones, F. Echeverri, T. A. Grillo, M. P. Kishi, F. Garcia-Garcia, F. Torres, and G. Cardona. *Phytochem.*, 41:753–757, 1996.

[87] J. G. Luis, W. Q. Fletcher, F. Echeverri, and T. A. Grillo. *Tetrahedron*, 50:10963–10970, 1994.

[88] J. Z. Xiao, S. Kumazawa, H. Tomita, N. Yoshikawa, C. Kimura, and Mikawa. T. *J. Antibiot.*, 46:1570–1574, 1993.

[89] C. Flors and S. Nonell. *Acc. Chem. Res.*, 39:293–300, 2006.

[90] C. Flors, P. Ogilby, J. G. Luis, T. A. Grillo, L. R Izquierdo, P. Gentili, L. Bussoti, and S. Nonell. *Photochem. Photobiol.*, 82:95–103, 2006.

[91] T. J. Dougherty, C. J. Gomer, B. W. Henderson, G. Jori, D. Kessel, M. Korbelik, J Moan, and Q. Peng. *J. Natl. Cancer Inst.*, 90:889–905, 1998.

[92] L. Serrano-Andrés, R. Pou-Amérigo, M. P. Fülscher, and A. C. Borin. *J. Chem. Phys.*, 117:1649–1660, 2002.

[93] T. Okutsu, S. Noda, S. Tanaka, A. Kawai, K. Obi, and H. Hiratsuka. *J. Photochem. Photobiol. A*, 132:37–41, 2000.

[94] C. Flors and S. Nonell. *Helv. Chim. Acta.*, 84:2533–2539, 2001.

[95] C. Flors and S. Nonell. *J. Photochem. Photobiol. A*, 163:9–12, 2004.

[96] M. C. Daza, M. Doerr, S. Salzmann, C. M. Marian, and W. Thiel. *Phys. Chem. Chem. Phys.*, 11:1688–96, 2009.

[97] A. P. Darmanyan and C. S. Foote. *J. Phys. Chem.*, 97:4573–4576, 1993.

[98] G. Porter and P. Suppan. *Trans. Far. Soc.*, 61:1664, 1965.

[99] G. Porter and P. Suppan. *Trans. Far. Soc.*, 62:3375, 1996.

[100] K. Anderson, P. A. Malmqvist, and B. O. Roos. *J. Chem. Phys.*, 96:1218, 1992.

[101] W. J. Herhe, R. Ditchfield, and J. A. Pople. *J. Chem. Phys.*, 56:2257–2261, 1972.

[102] M. Reguero, M. Olivucci, F. Bernardi, and M. A. Robb. *J. Am. Chem. Soc.*, 116: 2103–2114, 1994.

[103] I. Gomez, M. Reguero, M. Boggio-Pasqua, and M. A. Robb. *J. Am. Chem. Soc.*, 127:7119–7129, 2005.

[104] M. Merchán, R. González-Luque, T. Climent, L. Serrano-Andrés, E. Rodríguez, M. Reguero, and D. Peláez. *J. Phys. Chem. B*, 110:26471–26476, 2006.

[105] P. O. Widmark, P. A. Malmqvist, and B. O. Roos. *Theo. Chim. Acta*, 77:291–306, 1990.

[106] M. Merchan and B. O. Roos. *Theo. Chim. Acta*, 87:227, 1995.

[107] B. O. Roos and K. Anderson. *Chem. Phys. Lett.*, 245:215–223, 1995.

[108] L. Serrano-Andrés, M. Merchán, and A. C. Borin. *Proc. Natl. Acad. Sci.*, 103: 8691–8696, 2006.

[109] K. N. Walzl, F. Koerting, and A. Kuppermann. *J. Chem . Phys.*, 87:3796–3803, 1987.

[110] M. Klessinger and J. Milch. *Excited states and photochemistry of organic molecules*. VCH, New York, 1995.

[111] E. Oliveros, P. Suardi-Murasecco, T. Aminian-Saghafi, and A. M. Braun. *Helv. Chim. Acta*, 74:79–90, 1991.

[112] R. Schmidt, C. Tanielian, R. Dunsbach, and C. Wolf. *J. Photochem. Photobiol. A*, 79:11–17, 1994.

[113] C. Angeli. *Int. J. Quantum Chem.*, 110:2436–2447, 2010.

[114] J. Woning and R. Bonneau. *J. Am. Chem. Soc.*, 113:6245–6255, 1991.

[115] E. García-Expósito, M. J. Bearpark, R. M. Ortuño, V. Branchadell, M. A. Robb, and S. Wilsey. *J. Org. Chem.*, 66:8811–8814, 2001.

[116] R. Nelson and L. Pierce. *J. Mol. Spectrosc.*, 18:344–352, 1965.

[117] A. A Gorman, I. Hamblett, and M. A. J Rodgers. *J. Am. Chem. Soc.*, 106: 4679–4682, 1984.

[118] S. E. Braslavsky and G. E. Heibel. *Chem. Rev.*, 92:1381–1410, 1992.

[119] E. Lippert, W. W. Lüder, F. Moll, W. Nägele, H. Boos, H. Prigge, and I. Seybold-Blankestein. *Angew. Chem.*, 73:695, 1961.

[120] K. A. Zachariasse, S. I. Druzhinin, W. Bosch, and R. Machinek. *J. Am. Chem. Soc.*, 126:1705–1715, 2004.

[121] A. Sobolewski. *Chem. Phys. Lett.*, 259:119–127, 1996.

[122] A. Sobolewski. *Chem. Phys. Lett.*, 250:428–436, 1996.

[123] S. I. Druzhinin, N. P. Enrsting, S. A. Kovalenko, L. Pérez Lustres, T. A. Senyushkina, and K. A. Zachariasse. *J. Phys. Chem. A*, 110:2955–2969, 2006.

[124] J-K Lee, T. Fujiwara, W. G. Kofron, M. Z. Zgierski, and E. C. Lim. *J. Chem. Phys.*, 128:164512–164512, 2008.

[125] R. Ramos, T. Fujiwara, M. Z. Zgierski, and E. C. Lim. *J. Phys. Chem. A*, 109: 7121–7126, 2005.

[126] A. L. Sobolewski, W. Sudholt, and W. Domcke. *J. Phys. Chem. A*, 102:2716–2722, 1998.

[127] T. Gustavsson, P. B. Coto, L. Serrano-Andrés, T. Fujiwara, and E. C. Lim. *J. Chem. Phys.*, 131:031101, 2009.

[128] T. Fujiwara, M. Z. Zgierski, and E. C. Lim. *Phys. Chem. Chem. Phys.*, 2011.

[129] W. W. Schuddeboom, S. A. Jonker, J. M. Warman, U. Leinhos, W. Kühnle, and K. A. Zachariasse. *J. Phys. Chem.*, 96:10809–10819, 1992.

[130] W. M. Kwok, C. Ma, D. Phillips, P. Matousek, A. W. Parker, and M. Towrie. *J. Phys. Chem. A*, 104:4188–4197, 2000.

[131] Z.R. Grabowski, K. Rotkiewicz, A. Siemiarczuk, D. J. Cowley, and W Baumann. *Nouv. J. Chim.*, 3:443–454, 1979.

[132] I. Gómez, Y. Mercier, and M. Reguero. *J. Phys. Chem. A*, 110(40):11455–61, 2006.

[133] U. Leinhos. *Chem. Inform.*, 95:2013–2021, 1991.

[134] R. O. Loutfy. *Can. J. Chem*, 54:1454–1463, 1976.

[135] J. N. Muller. *The theory of the Electronic Spectra of Organic Molecules*. Methuen, London, 1963.

[136] V. A. Galievsky, S. I. Druzhinin, A. Demeter, Y. Jiang, S. A. Kovalenko, L. P. Lustres, K. Venugopal, N. P. Ernsting, X. Allonas, M. Noltemeyer, R. Machinek, and K. A. Zachariasse. *Chem. Phys. Chem.*, 6:2307–2323, 2005.

[137] S. Murali, V. Kharlanov, W. Rettig, A. I. Tolmachev, and A. V Kropachev. *J. Phys. Chem. A*, 109:6420–6427, 2005.

[138] S. I. Druzhinin, V. A. Galievsky, and K. A. Zachariasse. *J. Phys. Chem. A*, 109: 11213–23, 2005.

[139] S. I. Druzhinin, A. Demeter, V. A. Galievsky, T. Yoshihara, and K. A. Zachariasse. *J. Phys. Chem. A*, 107(40):8075–8085, 2003.

[140] T. H. Dunning. *J. Chem. Phys.*, 90:1007–1023, 1989.

[141] L. Blancafort, P. Celani, M. J. Bearpark, and M. A. Robb. *Theor. Chem. Acc. Theor. Comput. Model. Theor. Chim. Acta*, 110:92–99, 2003.

[142] C. Gonzalez and B. J. Schlegel. *J. Phys. Chem.*, 94:5523–5527, 1990.

[143] A. Heine, R. Herbst-Irmer, D. Stalke, W. Kühnle, and K. A. Zachariasse. *Acta Crystallogr.*, B50:363–373, 1994.

[144] J. Dreyer and A. J. Kumrow. *J. Am. Chem. Soc.*, 122:2577–2585, 2000.

[145] U. Lommatzsch and B. Brutschy. *Chem. Phys.*, 234:35–57, 1998.

[146] L. Serrano-Andres, M. Merchan, B. O. Roos, and R. Lindh. *J. Am. Chem. Soc.*, 117:3189–3204, 1995.

[147] J. Platt. *J. Chem. Phys.*, 17:484–495, 1949.

[148] Y. V. Il'ichev, W. Kühnle, and K. A. Zachariasse. *J. Phys. Chem.*, 102:5670–5680, 1998.

[149] K. A. Zachariasse, S. I. Druzhinin, S. A. Kovalenko, and T. Senyushkina. *J. Chem. Phys.*, 131:224313–224322, 2009.

[150] W. Fuss, K. K. Pushpa, W. Rettig, W. E. Schmid, and S. A. Trushin. *Photochem. Photobiol. Sci.*, 1:255–262, 2002.

[151] S. A. Trushin, T. Yatsuhashi, W. Fuss, and W. E. Schmid. *Chem. Phys. Lett.*, 376:282, 2003.

[152] W. Fuss, W. E. Schmid, K. Kuttan Pushpa, S. A. Trushin, and T. Yatsuhashi. *Phys. Chem. Chem. Phys.*, 9:1151–1169, 2007.

[153] I. M. Lagoja. *Chem. Biodivers.*, 2:1–50, 2005.

[154] A. Schellenberger, G. Hubner, and H. Neef. *Methods Enzymol.*, 278:131–146, 1997.

[155] B. Roth and C. C. Cheng. *Prog. Med. Chem.*, 19:268–330, 1982.

[156] A. El-Ghayoury, A. P. H. J. Schenning, P. A. Van Hal, J. K. J. Van Duren, R. A. J. Janssen, and E. W. Meijer. *Angew. Chem.*, 113:3772–3775, 2001.

[157] El-Ghayoury A., Schenning A. P.H. J., P. A. Van Hal, J. K. J. Van Duren, R. A. J. Janssen, and E. W. Meijer. *Angew. Chem. Int. Ed.*, 40:3660–3663, 2001.

[158] Y. J. Kim, Kim J. H., M. S. Kang, M. J. Lee, J. Won, J. C. Lee, and Kang Y. S. *Adv. Mater.*, 16:1753–1757, 2004.

[159] C. H. Huang, N. D. McClenaghan, A. Kuhn, Bravic G., and D. M. Bassani. *Tetrahedron*, 62:2050–2059, 2006.

[160] T. Hegmann, J. Kain, S. Diele, B. Schubert, H. Bogel, and C. Tschierske. *J. Mater. Chem.*, 13:991–1003, 2003.

[161] P. Calza, C. Medana, C. Baiocchi, and E. Pelizzetti. *Appl. Catal. B*, 52:267–274, 2004.

[162] J. E. Hoffman, H. Cheng, A. L. Rheingold, A. DiPasquale, and A. Yanovsky. *Acta Cryst. E*, 65:02374, 2009.

[163] C. Li and A. Rosenau. *Tetrahedron Lett.*, 50:5888–5893, 2009.

[164] W. Rettig. *Angew. Chem. Int. Ed. Engl.*, 25:971–988, 1986.

[165] S. Cogan, S Zilberg, and Y. Haas. *J. Am. Chem. Soc.*, 128:3335–3345, 2006.

[166] M. Barbatti and H. Lischka. *J. Phys. Chem.. A*, 111:2852–2858, 2007.

[167] C. E Crespo-Hernández, C. Boiko, P. M. Hare, and B. Kohler. *Chem. Rev.*, 104: 1977–2019, 2004.

[168] S. Perun, A. L. Sobolewski, and W. Domcke. *Chem. Phys.*, 313:107–112, 2005.

[169] L. Blancafort, B. Cohen, P. M. Hare, and M. A. Robb. *J. Phys. Chem. A*, 109: 4431–4436, 2005.

[170] C. Angeli. *J. Comput. Chem.*, 30:1319–1333, 2009.

[171] Malmqvist P. A., B.O. Roos, Fulscher M. P., and A. P. Rendell. *Chem. Phys.*, 162:359–367, 1992.

[172] V. Barone and M. Cossi. *J. Phys. Chem. A*, 102:1995–2001, 1998.

[173] M. Cossi, N. Rega, G. Scalmani, and V. Barone. *J. Chem. Phys.*, 114:5691–5701, 2001.

[174] J Tomasi, B. Mennucci, and R. Cammi. *Chem. Rev.*, 105:2999–3093, 2005.

GLOSSARY

f Oscillator strength

μ Dipole moment

E Energy

X_1 Gradient Difference

X_2 Derivative coupling

Φ_Δ Singlet oxygen quantum yield

Φ_f Quantum yield of fluorescence

ABN Aminobenzonitrile

ABN-4F 2,3,5,6-tetrafluoro-4-aminobenzonitrile

ACS Apparent Surface Charge

AMFI Atomic Mean-Field Integrals

ANO Atomic Natural Orbital

APD Aminopyrimidine

BO Born Oppenheimer

BOA Born Oppenheimer Approximation

CASPT2 Complete Active Space with 2^{nd} Order Perturbation

CASSCF Complete Active Space Self Consistent Field

CASSI Complete Active Space State Interaction

CI Conical Intersection

CSF Configuration state function

CT Charge Transfer

DEAPD 4-diethyl-aminopyrimidine

DIIS Direct Inversion in the Iterative Subspace

DMAPD 4-dimethylaminopyrimidine

DMA5MPD 4-dimethylamino-5-methylpyrimidine

DNA Deoxyribonucleic acid

ESA Excited State Absorption

FC Franck-Condon

FCI Full Configuration Interaction

GS Ground State

$\hat{H}$ Hamiltonian

HF Hartree Fock

IC Internal Conversion

ICT Intramolecular Charge Transfer

IPEA Ionization Potential-Electron Affinity

ISC Intersystem Crossing

LE Locally Excited

LCAO Linear Combination of Atomic Orbitals

LIIRC Linear Interpolated Internal Reaction Coordinate

LS Level Shift

MCSCF Multi-Configuration Self Consistent Field

MEP Minimum Energy Path

MP2 Moller Pleset with 2^{nd} Order Perturbation

MS-CASPT2 Multi State-Complete Active Space with 2^{nd} Order Perturbation

MXS minimum in the crossing seam

NR Newton Raphson

PCM Polarizable continuum models

PDT Photodynamic Therapy

PES Potential Energy Surface

PICT Intramolecular Charge Transfer

PM-CAS-CI Perturbed Modified-Complet Active Space-Configuration Interaction

PN Phenalenone

PS Photosensitizer

RICT Rehybridized Intramolecular Charge Transfer

RNA RiboNucleic Acid

SA State Average

SCF Self Consistent Field

SOC Spin Orbit Coupling

SSE Solvent Stabilization Energy

STC Singlet Triplet Crossing

super-CI Super Configuration Interaction

SS-CASPT2 Single State-Complete Active Space with 2^{nd} Order Perturb

TA Transient Absorption

TDDFT Time Dependent Density Functional Theory

TDM Transition Dipole Moment

TDSE Time Dependent Schrödinger Equation

TICT Twisted Intramolecular Charge Transfer

TISE Time Independent Schrödinger Equation

TS Transition State

UV Ultra Violet

ANNEX TO CHAPTER 5

Data for 4-aminobenzonitrile

Table 7.1: CASSCF, SS-CASPT2 and MS-CASPT2/cc-pVDZ energies relative to S_0 (in kcal·mol^{-1}) and dipole moments (in Debye) of the characterized ABN minima optimized at CASSCF/6-31G* level. All CASSCF calculations were done with the number fo roots avaraged showed in Root column.

Minimum	Root	Nature	CASSCF	SS-CASPT2	Dipol	MS-CASPT2
LE	1	S_0	5.73	1.38	5.10	1.38
	2	LE	105.81	102.1	5.37	101.77
RICT	1	S_0	42.13	30.64	4.88	30.64
	2	LE	148.6	134.43	4.55	122.2
	3	ICT	154.33	122.22	9.87	134.45
TICT	1	S_0	40.86	33.36	3.8	33.36
	2	LE	135.84	125.98	4.59	113.07
	3	ICT	162.77	126.41	10.7	139.32
PICT	1	S_0	13.26	4.94	6.71	3.74
	2	LE	116.22	105.74	5.93	105.74
	3	ICT	146.15	115.79	11.23	116.99

Table 7.2: CASSCF, SS-CASPT2 and MS-CASPT2/cc-pVDZ energies relative to S_0 (in kcal·mol^{-1}), dipole moments (in Debye) and oscillator strengths calculed with PM-CAS-CI wave functions of the characterized ABN minima optimized at CASSCF/cc-pVDZ. All CASSCF calculations were done with the number of roots avaraged showed in Root column.

Geom	State	SS-CASPT2	μ	Nature	MS-CASPT2	f
LE	S_0	2.01	5.37	S_0	2.01	
	LE	102.73	5.1	LE	102.4	0.00687
RICT	S_0	31.02	4.86	S_0	31.02	
	LE	134.62	4.55	ICT	122.14	0.00099
	ICT	122.15	10.45	LE	134.64	
TICT	S_0	33.26	3.82	S_0	33.26	
	LE	125.86	4.56	ICT	112.94	0.00514
	ICT	125.87	10.76	LE	138.8	
PICT	S_0	4.94	6.71	S_0	3.74	
	LE	105.74	5.93	LE	105.74	
	ICT	115.79	11.23	ICT	116.99	-

Table 7.3: Eigenvectors of the SA2-MS-CASPT2 effective hamiltonian matrix diagonalitzation at the optimized geometry of the LE species at CASSCF/cc-pVDZ level.

2 state averaged		
States	1 (GS) PM-CI	2 PM-CI
	Eigenvectors	
GS	1.00000000	0.00000424
2	-0.00000424	1.00000000

Table 7.4: Eigenvectors of the SA3-MS-CASPT2 effective hamiltonian matrix diagonalitzation at the optimized geometry of the RICT species at CASSCF/cc-pVDZ.

3 state averaged			
States	1 (GS) PM-CI	2 PM-CI	3 PM-CI
		Eigenvectors	
GS	-0.99999911	-0.00007639	0.00133412
2	0.00133599	-0.03541349	0.99937185
3	0.00002909	-0.99937274	-0.03541356

Table 7.5: Eigenvectors of the SA3-MS-CASPT2-cc-PVDZ effective hamiltonian matrix diagonalitzation at the optimized geometry of the PICT species at CASSCF/cc-pVDZ level.

3 state averaged			
States	1 (GS) PM-CI	2 PM-CI	3 PM-CI
		Eigenvectors	
GS	0.99467065	0.00000017	-0.10310337
2	-0.00001245	-0.99999999	-0.00012171
3	0.10310337	-0.00012235	0.99467064

Table 7.6: Eigenvectors of the SA3-MS-CASPT2 effective hamiltonian matrix diagonalitzation at the optimized geometry of the TICT specie at CASSCF/cc-pVDZ.

3 state averaged			
States	1 (GS) PM-CI	2 PM-CI	3 PM-CI
		Eigenvectors	
GS	1.00000000	0.00003587	0.00001400
2	-0.00001548	0.70729949	-0.70691402
3	-0.00003526	0.70691402	0.70729949

Table 7.7: CASSCF, SS-CASPT2 and MS-CASPT2/cc-pVDZ energies relative to S_0 (in kcal·mol^{-1}) and dipole moments (in Debye) of S_0me critical points of ABN obtained at CASSCF/6-31G* level.

Critical Points	CASSCF	SS-CASPT2	Dipol	MS-CASPT2
		S_3/S_2 CI		
CT-Q/RICT	154.9	124.52	11.18	124.18
	173.89	160.47	5.87	160.81
		S_2/S_1 CI		
CT-Q/LE	132.2	106.35	7.61	106.35
	133.85	124.53	3.95	124.53
RICT/LE	150.74	121.52	9.45	118.14
	151.09	132.19	5.34	135.57
		Transition States		
LE-TICT	56	48.04	5.11	46.16
	140.6	132.48	9.17	111.66
	155.49	114.34	3.93	137.04

Table 7.8: CASSCF, SS-CASPT2 and MS-CASPT2/cc-pVDZ energies relative to S_0 (in kcal·mol^{-1}) and dipole moments (in Debye) of some critical points of ABN obtained at CASSCF/cc-pVDZ level. Calculation are performed with SA2-CASSCF basis except TS with SA3-CASSCF basis.

Critical Points	CASSCF	SS-CASPT2	Dipol	MS-CASPT2
		S_3/S_2 CI		
CT-Q/RICT	156.92	126.65	11.58	126.64
	157.02	129.48	13.05	129.49
CT-Q/CT-AQ	166.55	151.37	7.28	140.39
	166.58	142.36	10.24	153.34
		S_2/S_1 CI		
CT-Q/LE	156.92	116.5	6.21	98.75
	157.02	113.08	6.91	130.82
RICT/LE	149.15	122.15	9.45	118.77
	149.5	132.82	5.34	136.2
		Transition States		
LE-TICT	56	48.04	5.11	46.16
	140.6	132.48	9.17	111.66
	155.49	114.34	3.93	137.04

Table 7.9: MS-CASPT2/cc-pVDZ energies relative to the S_0 minimum (in kcal·mol^{-1}. Calculated with *a)* SA2-CASSCF and *b)* SA3-CASSCF reference function.

Geom	MS-CASPT2
S_2/S_1 CI RICT/LE	$127.48^{(a)}$
TS LE-TICT	$111.66^{(b)}$

Table 7.10: CASSCF, SS-CASPT2 and MS-CASPT2/cc-pVDZ energies relative to the S_0 minimum (in kcal·mol^{-1}) and dipole moments (in Debye) of the radiationless deactivation of ABN obtained at CASSCF/6-31G* level.

Critical Points	Nature	CASSCF	SS-CASPT2	Dipol	MS-CASPT2
		S_1/S_0 CI			
C1	S_0	128.78	108.06	6.57	107.1
	LE	129.47	120.92	4.84	121.89
C2	ICT(Q)	108.63	80.36	9.60	79.99
	S_0	111.17	100.72	3.62	101.09
C3	S_0	128.74	122.71	4.86	122.46
	LE	129.15	122.46	5.15	122.71
C4	S_0	127.22	106.83	7.05	106.32
	LE	127.61	115.36	5.03	115.87
		Transition states			
TS2		129.05	114.45	4.71	116.25
TS3		130.11	126.53	4.77	126.53

Data for 2,3,5,6-tetrafluoro-4-aminobenzonitrile

Table 7.11: MS-CASPT2/cc-pVDZ energies relative to the S_0 minimum (in kcal·mol^{-1}) of some critical points of ABN-4F obtained at CASSCF/6-31G* level.

Critical Points	MS-CASPT2
S_3/S_2 CI	
CT-Q/RICT	130.98
S_2/S_1 CI	
CT-Q/LE	113.79
RICT/LE	135.31
Transition States	
LE-TICT	112.59

Table 7.12: MS-CASPT2/cc-pVDZ average energies of the involved states of the crossing relative to the S_0 minimum (in kcal·mol^{-1}) of the radiationless deactivation critical points of ABN-4F located at CASSCF/6-31G* level.

Critical Points	MS-CASPT2
S_1/S_0 CI	
C1	98.52
C2	93.98
C3	126.21
C4	117.08
Transition states	
TS1	103.9
TS2	115.86

ANNEX TO CHAPTER 6

CT/LE conical intersection in 4-dimethylaminopyrimidine

The computing of the crossing channel connecting LE and CT state is a difficult task in APD. However a CI was found at CASSCF(8,7) and CASSCF(12,9) in DMPAD due to stabilitzation of CT already at CASSCF level. The optimized geometries of both actives spaces show big differences (Figure 7.1), the most noticiable is the enlarging of C_4 pirimidalization on CASSCF(12,9) calculation in comparison with that of CASSCF(8,7) . The CT/LE CI optimized at CASSCF(8,7) level show the same trends like CT/LE CI geometry optimized at CASSCF(12,11) level for ABN.

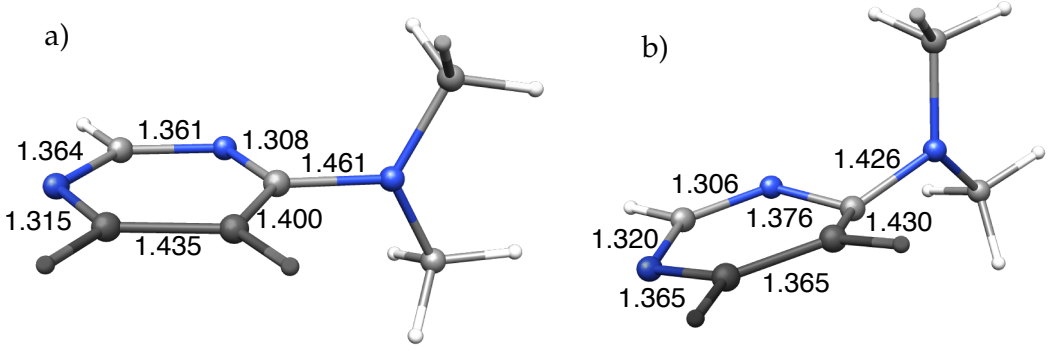

Figure 7.1: Optimized structures CT/LE CIs at CASSCF(8,7) and CASSCF(12,9).

Final CASSCF(12,11) results must be calculted within different number of av-

eraged states due to small energy differences between states and root flipping in several state average scenarios. Firstly an stateaverage of seven states was used in optimized CASSCF(12,9) and CASSCF(8,7) geometries (Table 7.13 and 7.14).

Table 7.13: CASSCF/MS-CASPT2/cc-pVDZ energies (both in kcal·mol^{-1}) relative to the S_0 minimum at the optimized CASSCF(8,7) CT/LE CI geometry in DMAPD.

Root	Nature	SA7-CASSCF(12,11)	Nature	MS-CASPT2(12,11)
1	SO	30.18	S_0	26.81
2	LE	151.04	NA-2+CT	113.73
3	NA-1	151.28	CT	119.72
4	NA-2	153.66	NA-1	130.75
5	CT	156.79	NA-(1+2) CT	139.02
6	CT	158.18	LE	151.41
7	NS-1	195.88	NS-1	176.96

Table 7.14: CASSCF/MS-CASPT2/cc-pVDZ energies (both in kcal·mol^{-1}) relative to the S_0 minimum at the optimized CASSCF(12,9) CT/LE CI geometry in DMAPD

Root	Nature	SA7-CASSCF(12,11)	Nature	MS-CASPT2(12,11)
1	SO	29.49	SO	31.36
2	NA-1	130.75	CT + LE	102.15
3	LE	143.91	NA-1	121.00
4	CT	148.69	CT	139.52
5	NA-2	164.34	NA-2	147.95
6	NS-1	175.46	LE+NA-1	149.01
7	CT	186.65	NS-1	161.58

However, at this level of calculation there is a mixing of the three N lone pair orbitals that preclude a clear determination of the nature of the states involved in the crossing (Figure orbitals, 7.2). Moreover, when the dynamical correlation was included in the energy calculation, the states were not degenerate any longer.

Secondly observing the degenerancy of NA1, LE and CT in these geometries, a state average of second, third and fourth state was used to improve the CI energy. NA-1 is stabilized and LE is placed higher in energy. As is expected when dynamical correlation is incorporated these states become no degenerated, furthermore the analysis of MS-CASPT2 results show an important mixing of states.

For this reason, in order to have a more clearer general picture, is necessary the

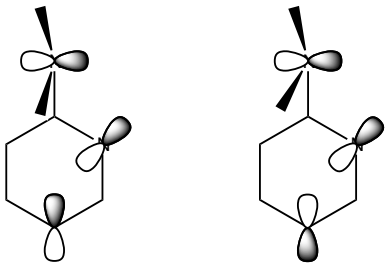

Figure 7.2: Mixing of orbitals at SA-CASSCF(12,11) level in CI CT/LE.

Table 7.15: Vertical energies (both in kcal·mol^{-1}) relative to the S_0 minimum at the optimized CASSCF(12,9) CT/LE CI geometry in DMAPD

Root	Nature	SA234-CASSCF(12,11)	MS-CASPT2(12,11)
2	NA-1+CT	130.69	104.48
3	NA-1+CT	137.28	128.56
4	NS-1	142.42	147.30

Table 7.16: Eigenvectors of the MS-CASPT2 effective hamiltonian matrix diagonalitzation of an average of SA2-SA3-SA4-CASSSCF in CT/LE CI geometry optimized at CASSCF(12,9).

3 state averaged			
States	2 PM-CI	3 PM-CI	4-PM-CI
	Eigenvectors		
2	0.479485	0.862270	-0.163045
3	0.864398	-0.496121	-0.081719
4	0.151355	0.101752	0.983228

calculation of the LIIRC path between LE and CT minima at MS-CASPT2(12,11) level.

In the natural science we are not only observers we are always part of the system